DATA-DRIVEN MHD: NOVEL APPLICATIONS TO THE SOLAR ATMOSPHERE

EDITED BY: Abhishek Kumar Srivastava, Robertus Erdelyi, Stefaan Poedts,
Peng-Fei Chen and Yihua Yan

PUBLISHED IN: Frontiers in Astronomy and Space Sciences and Frontiers in Physics

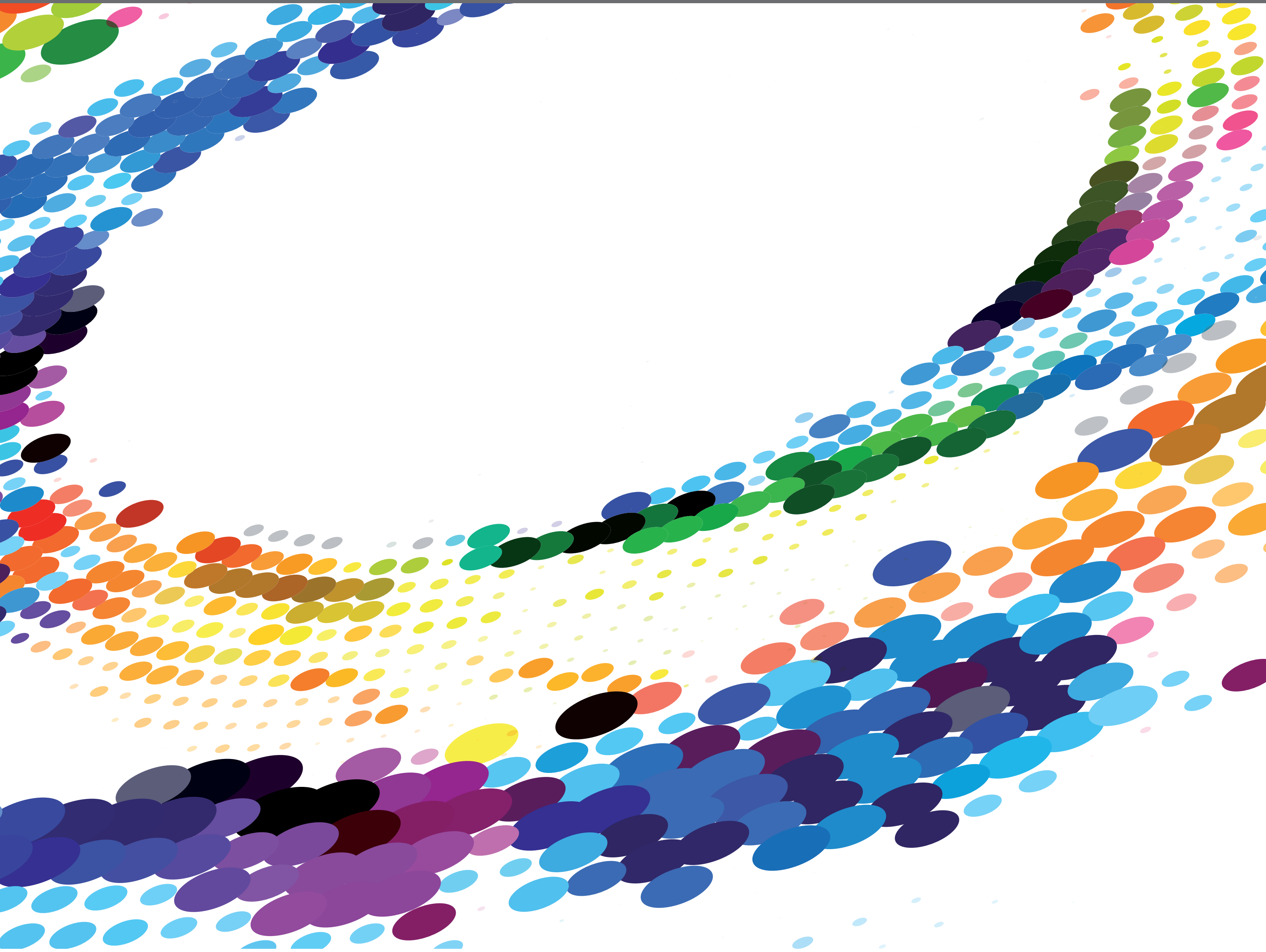

frontiers Research Topics

ISSN 1664-8714
ISBN 978-2-88971-837-5
DOI 10.3389/978-2-88971-837-5

About Frontiers

Frontiers is more than just an open-access publisher of scholarly articles: it is a pioneering approach to the world of academia, radically improving the way scholarly research is managed. The grand vision of Frontiers is a world where all people have an equal opportunity to seek, share and generate knowledge. Frontiers provides immediate and permanent online open access to all its publications, but this alone is not enough to realize our grand goals.

Frontiers Journal Series

The Frontiers Journal Series is a multi-tier and interdisciplinary set of open-access, online journals, promising a paradigm shift from the current review, selection and dissemination processes in academic publishing. All Frontiers journals are driven by researchers for researchers; therefore, they constitute a service to the scholarly community. At the same time, the Frontiers Journal Series operates on a revolutionary invention, the tiered publishing system, initially addressing specific communities of scholars, and gradually climbing up to broader public understanding, thus serving the interests of the lay society, too.

Dedication to Quality

Each Frontiers article is a landmark of the highest quality, thanks to genuinely collaborative interactions between authors and review editors, who include some of the world's best academicians. Research must be certified by peers before entering a stream of knowledge that may eventually reach the public - and shape society; therefore, Frontiers only applies the most rigorous and unbiased reviews.
Frontiers revolutionizes research publishing by freely delivering the most outstanding research, evaluated with no bias from both the academic and social point of view. By applying the most advanced information technologies, Frontiers is catapulting scholarly publishing into a new generation.

What are Frontiers Research Topics?

Frontiers Research Topics are very popular trademarks of the Frontiers Journals Series: they are collections of at least ten articles, all centered on a particular subject. With their unique mix of varied contributions from Original Research to Review Articles, Frontiers Research Topics unify the most influential researchers, the latest key findings and historical advances in a hot research area! Find out more on how to host your own Frontiers Research Topic or contribute to one as an author by contacting the Frontiers Editorial Office: frontiersin.org/about/contact

DATA-DRIVEN MHD: NOVEL APPLICATIONS TO THE SOLAR ATMOSPHERE

Topic Editors:
Abhishek Kumar Srivastava, Indian Institute of Technology (BHU), India
Robertus Erdelyi, The University of Sheffield, United Kingdom
Stefaan Poedts, KU Leuven, Belgium
Peng-Fei Chen, Nanjing University, China
Yihua Yan, National Astronomical Observatories (CAS), China

Citation: Srivastava, A. K., Erdelyi, R., Poedts, S., Chen, P.-F., Yan, Y., eds. (2021). Data-driven MHD: Novel Applications to the Solar Atmosphere. Lausanne: Frontiers Media SA. doi: 10.3389/978-2-88971-837-5

Table of Contents

04 ***Editorial: Data-Driven MHD - Novel Applications to the Solar Atmosphere***
A. K. Srivastava, R. Erdélyi, S. Poedts, P. F. Chen and Y. Yan

09 ***Oscillation and Evolution of Coronal Loops in a Dynamical Solar Corona***
David J. Pascoe, Christopher R. Goddard and Tom Van Doorsselaere

21 ***Domain of Influence Analysis: Implications for Data Assimilation in Space Weather Forecasting***
Dimitrios Millas, Maria Elena Innocenti, Brecht Laperre, Joachim Raeder, Stefaan Poedts and Giovanni Lapenta

44 ***A Comparison Study of Extrapolation Models and Empirical Relations in Forecasting Solar Wind***
Sandeep Kumar, Arghyadeep Paul and Bhargav Vaidya

60 ***Significance of Cooling Effect on Comprehension of Kink Oscillations of Coronal Loops***
Daria Shukhobodskaia, Alexander A. Shukhobodskiy, Chris J. Nelson, Michael S. Ruderman and Robert Erdélyi

73 ***Testing and Validating Two Morphological Flare Predictors by Logistic Regression Machine Learning***
M. B. Korsós, R. Erdélyi, J. Liu and H. Morgan

81 ***MHD Modeling of Solar Coronal Magnetic Evolution Driven by Photospheric Flow***
Chaowei Jiang, Xinkai Bian, Tingting Sun and Xueshang Feng

frontiers
in Astronomy and Space Sciences

EDITORIAL
published: 18 October 2021
doi: 10.3389/fspas.2021.739264

Editorial: Data-Driven MHD - Novel Applications to the Solar Atmosphere

A. K. Srivastava[1]*, *R. Erdélyi*[2,3,4], *S. Poedts*[5,6], *P. F. Chen*[7,8] *and Y. Yan*[9]

[1]*Department of Physics, Indian Institute of Technology (BHU), Varanasi, India,* [2]*Solar Physics and Space Plasma Research Centre, University of Sheffield, Sheffield, United Kingdom,* [3]*Department of Astronomy, Eötvös Loránd University, Budapest, Hungary,* [4]*Gyula Bay Zoltán Solar Observatory (GSO), Hungarian Solar Physics Foundation (HSPF), Gyula, Hungary,* [5]*Centre for Mathematical Plasma Astrophysics, Department of Mathematics, KU Leuven, Leuven, Belgium,* [6]*Institute of Physics, University of Maria Curie-Skłodowska, Lublin, Poland,* [7]*School of Astronomy and Space Science, Nanjing University, Nanjing, China,* [8]*Key Lab of Modern Astronomy and Astrophysics (Nanjing University), Ministry of Education, Nanjing, China,* [9]*National Astronomical Observatory, Chinese Academy of Sciences, Beijing, China*

Keywords: magnetohydrodynamics, corona, MHD waves, magnetic field, flares, Sun

Editorial on the Research Topic

Data-driven MHD: Novel Applications to the Solar Atmosphere

Edited and reviewed by:
Scott William McIntosh,
National Center for Atmospheric Research (UCAR), United States

****Correspondence:***
A. K. Srivastava
asrivastava.app@iitbhu.ac.in

Specialty section:
This article was submitted to Stellar and Solar Physics, a section of the journal Frontiers in Astronomy and Space Sciences

Received: *10 July 2021*
Accepted: *11 August 2021*
Published: *18 October 2021*

Citation:
Srivastava AK, Erdélyi R, Poedts S, Chen PF and Yan Y (2021) Editorial: Data-Driven MHD - Novel Applications to the Solar Atmosphere. Front. Astron. Space Sci. 8:739264. doi: 10.3389/fspas.2021.739264

1 INTRODUCTION

The joint action of the complex magnetic field and ionised hot plasma leads to a range of dynamical processes, including magnetohydrodynamic (MHD) waves in the Sun's atmosphere at disparate spatial, temporal and spectral scales (Andries et al., 2009; Mathioudakis et al., 2013; Li et al., 2020; Van Doorsselaere et al., 2020; Srivastava et al., 2021; Wang et al., 2021). Different observatories have been employed since past several decades, both in space and at the ground, which put up a notably revamped knowledge about the physical processes transporting energy and mass in the Sun's magnetised atmosphere at diverse spatio-temporal scales (De Pontieu et al., 2004; Jess et al., 2009; Srivastava et al., 2017; Grant et al., 2018; Srivastava et al., 2018; Liu et al., 2019; Li et al., 2020; Van Doorsselaere et al., 2020). Remarkably, at the large spatial-scales, the key progress in understanding the origin of impulsive transient/eruptive phenomena such as energetic flares and bulky coronal mass ejections [CMEs, (Chen, 2011),], the related plasma processes detected at multi-wavelength radiative emissions varying from Gamma rays, X-rays to radio wave frequencies, as well as their space weather reverberations have illustrated a cardinal significance in the context of magnetohydrodynamics (MHD) modelling in recent era (Guo et al., 2019; Korsós et al.; Millas et al.; Samara et al., 2021). Besides the evolution of current age telescopes and their back-end cutting edge instruments for observing the dynamical plasma processes, noteworthy progress has been made in the theory of MHD waves, magnetic instabilities, global and local configurations of the magnetic fields and their energy build-up/release processes in the solar atmosphere. The novel science is emerged in understanding the wave processes, spontaneous/forced reconnection, and eruptive phenomena in the context of MHD. The leap forward advancements in the observations, coupled with theory, have emerged in form of front-line scientific progress in the field of solar astrophysics. These progresses have put down the basic preliminaries for current (e.g., 4m-DKIST (Rimmele et al., 2020; Rast et al., 2021); Parker Solar Probe (Bale et al., 2016); Solar Orbiter (Müller et al., 2020; GarcíaMarirrodriga et al., 2021)) and forthcoming high resolution new generation observatories (e.g., 4m-EST (Jurčák et al., 2019); 2.5m-WeHoT (Fang et al., 2019); 2m-NLST (Hasan et al., 2010); Aditya-L1 (Raghavendra Prasad et al., 2017; Tripathi et al., 2017), CHASE (Li et al., 2019), etc.) to explore extensively the magnetic coupling of different layers of the Sun's atmosphere, their localised energy and mass transport phenomena, physical processes supporting a variety of eruptive events and space weather. The large cohort of observational data, once assimilated, will pave the way to realistic and stringent MHD modelling, whose novel scientific results may further match with the observations to solve numerous outstanding problems in solar and heliospheric physics.

The present special research topic has provided an opportunity to the solar physicists and space scientists to publish timely review articles and original novel scientific results on the exclusive theme of "*Data-driven MHD: Novel Applications to the Solar Atmosphere*". The guest editors solicited the scientific articles that put forward the way to the front-line observational data and associated data-driven MHD modelling collectively to answer the fundamental but earnest topics of the solar atmosphere. The objective of this topical issue is to put forward a novel insights into the solar and heliospheric physics community, particularly when the epoch of fine spatio-temporal resolution observations is on our horizon (Erdélyi et al., 2019; Erdélyi et al.,; Matthews et al., 2019; McCrea et al., 2019; Rast et al., 2021). Key scientific themes include, but are not limited to:

- The potential role of MHD waves in the hot and magnetized solar atmosphere (Pascoe et al.; Shukhobodskaia et al.);
- The dynamical plasma processes in the solar active regions, and their modelling in the framework of MHD (Jiang et al.);
- Prediction of the space weather candidates (e.g., solar flares and CMEs) (Korsós et al., 2021);
- Study of the MHD oscillations and solar magneto-seismology (SMS) utilizing cutting-edge photospheric, chromospheric, transition region and coronal observations from both space and ground (Pascoe et al.; Shukhobodskaia et al.);
- Modelling the large-scale solar eruptive and transient phenomena (e.g., flares, CMEs, solar wind) and their space weather and heliospheric consequences (Kumar et al.; Millas et al.).

The present special issue and collection of the articles bring a novel set of new scientific results, which are summarised in the next subsection.

2 NOVEL SCIENTIFIC OUTCOMES OF THE TOPICAL ISSUE

1) The complex plasma dynamics and energetics of the solar atmosphere are governed by the combined interplay of the plasma and magnetic fields. The current trends of the understanding of Sun's magnetic field origin and its data driven modelling are at the fore-front of the solar research, and there are extensive attempts made in recent days on this very important scientific theme (Bobra et al., 2008; Cheung and DeRosa, 2012; Kliem et al., 2013; Dalmasse et al., 2019; Zhou et al., 2020; Yardley et al., 2021). The paper titled "*MHD Modelling of Solar Coronal Magnetic Evolution Driven by Photospheric Flow*" by Jiang et al. depicted a cutting edge perspective of the data-driven MHD simulations of magnetic fields generated in the solar active region (AR). To the extent of our knowledge, this is the first result to develop the observational data enabled full MHD model that utilises directly the flow field at the solar photosphere measured with the DAVE4VM technique. They establish an MHD equilibrium gleaned on one vector magnetogram by utilising an MHD-relaxation model with an adeptly less kinetic viscosity. They further apply the reported MHD equilibrium as an initial condition for ensuing a data-driven evolution. Thereafter, they derive the plasma flows at the solar photosphere from the time series of the observed magnetograms derived from DAVE4VM method. In the present study, the surface plasma flows are ultimately employed as an input in the time sequence to the bottom boundary of the reported MHD model. It concordantly upgrade the magnetic field at each time step by directly solving the magnetic induction equation at the bottom boundary of the numerical simulation box. They apply this MHD model to understand the generation of the solar magnetic field in AR 12158 whose sources are observed by SDO/HMI vector magnetograms in their paper. Their numerical model brings out a quasi-static stress of the magnetic line of forces primarily via the rotational flows of the leading sunspot of solar active region. This process creates the core magnetic field lines to constitute a coherent S-shape resemblance with the sigmoidal structure as often observationally detected in the solar atmosphere. The total magnetic energy acquired in the numerical model seen equalising closely to the stored magnetic energy as estimated straight away from the original vector magnetogram using the estimated optical flow fields by DAVE4VM. Such a new data-driven magnetic field model possesses potential scientific implications in the field of solar physics to study that how the Sun's magnetic fields, as driven by the slow plasma flow fields at the photosphere, get into an unstable state and run into the gigantic eruptions.
2) Kink mode oscillations are ubiquitously evident in a variety of magnetic structures in the solar atmosphere (Andries et al., 2009). In the paper titled "Oscillation and Evolution of Coronal Loops in a Dynamical Solar Corona", Pascoe et al. (Pascoe et al.) perform the numerical simulations in order to understand the oscillation and evolution of solar coronal loops in the dynamical solar atmosphere. They have investigated the observational evidences of the magnetoacoustic kink oscillations and the Kelvin-Helmholtz (KH) instability both using high-resolution seismological and spatial data analysis methods. The exclusive finding elucidates that low amplitude kink oscillations may play a role in giving rise the significant changes in the loop profile. This may influence the measurements of the transverse loop inhomogeneity based on the seismological and forward modelling methods. The influence on forward modelling estimates in the present work may also result for the previous observational signatures advocating loops having a wider

inhomogeneous layer. Such diagnostics are very crucial to understand the diagnostics and in understanding the dissipative processes of such waves in coronal loops.

3) As stated in (Mathioudakis et al., 2013), the kink oscillations of the solar magnetic loops have been extensively explored, both in the observational data and in the theoretical models, since the last couple of decades. Recently, this is demonstrated that most of the observationally detected driven kink oscillations of the coronal loops are subjected to the damping with either exponential or Gaussian profiles. A variety of physical mechanisms/processes are now well studied to understand the damping phenomenon of the kink oscillations (Shukhobodskaia et al.). However, some of the driven kink oscillations are noted to be evolved in such a way that they may not be modelled by using a Gaussian or exponential damping profiles. This is due to the fact that the amplification of kink oscillations are even observed at several instances in the coronal loops. A variety of recent scientific results in this context have delineated that including the joint effects of coronal loop expansion, cooling, and resonant absorption may result in the significant departure from the Gaussian and exponential damping profiles of the fast magnetoacoustic kink oscillations. It significantly describes the increase in oscillation amplitude w.r.t. time in many observed cases. In the paper titled "Significance of Cooling Effect on Comprehension of Kink Oscillations of Coronal Loops" (Shukhobodskaia et al.), authors examined ten driven kink oscillations in the coronal loops to further probe on the ability of expansion and cooling to expound the complicated damping profiles of these oscillations. Their results do not reckon on fitting a periodicity to these transverse oscillations by considering the complexities in both the temporal (i.e., change in the period) and spatial (i.e., change in the amplitude) variations. This can be considered for in a sophisticated and easy course of action. Additionally, this approach may also permit authors to theorise some important diagnostic information (e.g., the density ratio at the loop footpoints where kink oscillations were evolved) from the oscillation profile alone. This diagnostics does not require any comprehensive measurements of the loop as well as complex numerical modelling. The derived scientific results suggest the correlations between the density ratio at the loop footpoints and the amplitudes and periods of the kink oscillations. Ultimately, the authors compare their obtained results to the previous models, specifically the purely Gaussian and exponential damping profiles of the kink oscillations, through the estimations of Ξ^2 values. Therefore, they find that the inclusion of cooling can produce better fits to the damped kink oscillations in some cases. The present scientific findings suggest that the temperature evolution must be incorporated in the kink-mode oscillation models to best understand these oscillations which are not purely Gaussian or exponential in nature.

4) It is extensively studied in the literature that the most dynamic solar active-regions (ARs) are well-known to give rise the gigantic flares rapidly, where this frequency varies with the solar cycle. The prediction of these flares is a difficult task, and a wide range of methodologies is applied to proceed. Machine learning approaches seem to have strong potentials (Bobra and Couvidat, 2015; Kusano et al., 2020). In this topical issue the paper titled "Testing and Validating Two Morphological Flare Predictors by Logistic Regression Machine Learning" (Korsós et al.) addresses a stringent method that is developed to investigate and assess numerical measures of the mixed states of ARs with opposite magnetic field polarities. By evaluating two morphological parameters, i.e., the separation parameter, as well as the sum of the horizontal magnetic field gradient, the present study delivers engrossing evidences for the hypothesised relation between the level of mixed states of the studied active region (AR) and the level of the solar eruption probability within it. The efficiency of these two parameters as flare predictors, or flare-pre-cursors, is tested on a archetypal sample of randomly selected ARs, based on the SOHO/MDI-Debrecen Data (SDD) and the SDO/HMI - Debrecen Data (HMIDD) sunspot catalogues. The selected data satisfy well-defined selection criteria. Over 1,000 ARs were analysed to confirm the combined forecasting abilities of these two morphological parameters. The logistic regression machine learning method was employed to carry out the study. It is shown that the two pre-cursors with their threshold values act as excellent interrelated predictors. The conditional forecasting probability of the investigated pre-cursors is found to be at least 70% a day ahead of flare onset. This is certainly an improvement when compared to the currently available similar studies.

5) The space weather refers to the physical conditions in the interplanetary medium and in the solar terrestrial environment. It is basically generated by the solar activity, inclusive of the variable ambient solar wind, energetic flares, and huge and massive coronal mass ejections (CMEs) (Guo et al., 2019; Korsós et al., 2020; Millas et al.; Samara et al., 2021). Mitigation of the adverse space weather effects with economic and social benefits needs an improved knowledge of the Sun-Earth relation. Data and models are the basis for effective space weather forecasting. The paper entitled "Domain of Influence Analysis: Implications for Data Assimilation in Space Weather Forecasting" (Millas et al.), contains a description of the famous and frequently utilised space weather forecast models as well as the most suitable locations for space weather data gathering. The authors used three models that simulate different stages of the connection of the Sun to the Earth and applied Representer Analysis (RA) on them. They also performed a Domain of Influence (DOI) analysis to the same models. The models considered are OpenGGCM and Tsyganenko, which focus on the interplay of the supersonic solar wind with the planetary magnetosphere, and PLUTO which is applied to numerically model the propagation of the coronal mass ejections (CMEs) in the interplanetary space. Their model based analysis is favourable for the studies of space weather dynamics for the multitude of reasons. On the first instance, they get quantitative understanding of the most utilitarian locations of the observation points, e.g., solar wind monitors. For the illustration, they describe that the absolute values of

the Domain of Influence (DOI) are exceptionally lower in the magnetospheric plasma sheet at the Earth's outer atmosphere. Given the fact that the understanding of this specific subsystem is pivotal for the space weather, an effective and augmented monitoring of the region will be highly advantageous. On the other hand, they are accomplished to better characterise the numerical models. Even if the present analysis aims on spatial correlations compared to the temporal correlations, they infer that the time-independent numerical models are less useful for the Data Assimilation pursuit compared to the time-dependent numerical models. Finally, they get hold of the first exclusive stride toward enterprising objectives of pin pointing the most pertinent heliospheric parameters for modelling the CME propagation in the heliosphere, their arrival time, and exclusively their geoeffectiveness at the Earth's magnetosphere. The present work clearly improves the data acquisition and modelling capabilities of the interplanetary responses of the space-weather candidates.

6) CMEs and sporadic solar jets set out as perturbations to the ambient supersonic solar wind, and their joint effects exhibit a vital inference in the space weather associated dynamical plasma processes. Consequently, a vigorous foundation for precise forecast of the background solar wind properties is a most essential pathway towards the progress of any space weather prediction. In the paper titled "A Comparison Study of Extrapolation Models and Empirical Relations in Forecasting Solar Wind" (Kumar et al.), the authors studied on the application and comparison of different numerical models which are crucial to the prediction of a steady state high-speed solar wind. Notably, the authors carry out the case studies on Carrington rotations 2053, 2082, and 2104. Thereafter, they have evaluated the performance of magnetic field extrapolation models in concurrence with the velocity empirical formulations. This further helps in predicting the physical properties of the solar wind at the Lagrangian point "L1". The two completely distinct models to extrapolate the solar wind from the Sun's corona to the inner-heliospheric space are described by the authors. The first model is related with the kinematics based Heliospheric Upwind eXtrapolation (HUX) model. The second model is a physics based model. With the PLUTO open-source code, the physics-based model solves a set of hydrodynamic equations in the conservative form, and the numerical results can also estimate and forecast the thermal parameters of the solar wind. The predictions of the solar wind parameters by different models are quantitatively assessed by comparing with statistical observations. Moreover, they extend such a developed modelling framework to forecast the polarities of interplanetary magnetic fields near the Earth. Their model performs pretty well, for example, the comparison between their predictions and the observations leads to a remarkable correlation coefficient up to ~0.73–0.81, with a root mean square error of ~75–90 km s^{-1}. In addition, they compare the physics-based model and the hourly time-scale OMNI solar wind data. It is found that the standard deviation is similar to each other and the solar wind proton temperatures match very well between predictions and *in-situ* measurements.

3 CONCLUSION

The present topical collection brings some state-of-art scientific articles on the study of physical understanding of the MHD wave modes and their behaviour in the non-adiabatic solar atmosphere; their numerical simulations in magnetic loops. Moreover, the stringent active region modelling and the flare prediction models provide novel scientific understanding on the dynamics of eruptive phenomena and their predictions in the framework of space weather research. A comparative study of the extrapolation models and empirical relations in predicting the solar wind also put forward a comprehensive study on magnetic extrapolation models and their role in understanding and forecasting the physical properties of the solar wind over the Carrington rotations. The role of the MHD modelling and data assimilation in space weather forecasting is also emphasised in this collection. Given the fact that new as well as forthcoming observatories from ground and space in the modern era of solar and heliospheric physics are focusing on understanding energy and mass transport processes at diverse spatio-temporal scales as well as space weather studies, the present topical issue serves significantly with some selective front-line research papers and their thematic contents in demonstrating the cutting-edge progress in these research fields.

AUTHOR CONTRIBUTIONS

All authors listed have made a substantial, direct, and intellectual contribution to the work and approved it for publication.

FUNDING

RE acknowledge to the Science and Technology Facilities Council (STFC, grant number ST/M000826/1) United Kingdom and the Royal Society for enabling this research. RE also acknowledges the support received by the CAS Presidents International Fellowship Initiative Grant No. 2019VMA052. PC is supported by NSFC (11961131002). AS and RE acknowledge the support from UKIERI (Indo-UK) Project Grant (2018–2021; 184-1/2018(IC)).

ACKNOWLEDGMENTS

RE also acknowledges the warm hospitality received at USTC, Hefei, where part of his contribution was made.

REFERENCES

Andries, J., van Doorsselaere, T., Roberts, B., Verth, G., Verwichte, E., and Erdélyi, R. (2009). Coronal Seismology by Means of Kink Oscillation Overtones. *Space Sci. Rev.* 149, 3–29. doi:10.1007/s11214-009-9561-2

Bale, S. D., Goetz, K., Harvey, P. R., Turin, P., Bonnell, J. W., Dudok de Wit, T., et al. (2016). The FIELDS Instrument Suite for Solar Probe Plus. *Space Sci. Rev.* 204, 49–82. doi:10.1007/s11214-016-0244-5

Bobra, M. G., and Couvidat, S. (2015). Solar Flare Prediction Usingsdo/hmi Vector Magnetic Field Data with a Machine-Learning Algorithm. *ApJ* 798, 135. doi:10.1088/0004-637X/798/2/135

Bobra, M. G., van Ballegooijen, A. A., and DeLuca, E. E. (2008). Modeling Nonpotential Magnetic Fields in Solar Active Regions. *ApJ* 672, 1209–1220. doi:10.1086/523927

Chen, P. F. (2011). Coronal Mass Ejections: Models and Their Observational Basis. *Living Rev. Solar Phys.* 8, 1. doi:10.12942/lrsp-2011-1

Cheung, M. C. M., and DeRosa, M. L. (2012). A Method for Data-Driven Simulations of Evolving Solar Active Regions. *ApJ* 757, 147. doi:10.1088/0004-637X/757/2/147

Dalmasse, K., Savcheva, A., Gibson, S. E., Fan, Y., Nychka, D. W., Flyer, N., et al. (2019). Data-optimized Coronal Field Model. I. Proof of Concept. *ApJ* 877, 111. doi:10.3847/1538-4357/ab1907

De Pontieu, B., Erdélyi, R., and James, S. P. (2004). Solar Chromospheric Spicules from the Leakage of Photospheric Oscillations and Flows. *Nature* 430, 536–539. doi:10.1038/nature02749

Erdélyi, R., Amari, T., Belucz, B., Berrilli, F., Bogachev, S., Bolsée, D., et al. (2019). *HiRISE – High Resolution Imaging and Spectroscopy Explorer – Ultrahigh Resolution, Interferometric and External Occulting Coronagraphic Science: Great Leap in Solar Physics*. ESA Voyage. 2050 White Paper.

Erdélyi, R., Damé, L., Fludra, A., Mathioudakis, M., Amari, T., Belucz, B., et al. . HiRISE – High-Resolution Imaging and Spectroscopy Explorer – Ultrahigh Resolution, Interferometric and External Occulting Coronagraphic Science. *J. Exp. Astron.* (under review).

Fang, C., Gu, B., Yuan, X., Ding, M., Chen, P., Dai, Z., et al. (2019). 2.5 M Wide-Field and High-Resolution Telescope. *Sci. Sin.-Phys. Mech. Astron.* 49, 059603. doi:10.1360/SSPMA2018-00313

García Marirrodriga, C., Pacros, A., Strandmoe, S., Arcioni, M., Arts, A., Ashcroft, C., et al. (2021). Solar Orbiter: Mission and Spacecraft Design. *A&A* 646, A121. doi:10.1051/0004-6361/202038519

Grant, S. D. T., Jess, D. B., Zaqarashvili, T. V., Beck, C., Socas-Navarro, H., Aschwanden, M. J., et al. (2018). Alfvén Wave Dissipation in the Solar Chromosphere. *Nat. Phys.* 14, 480–483. doi:10.1038/s41567-018-0058-3

Guo, Y., Xia, C., Keppens, R., Ding, M. D., and Chen, P. F. (2019). Solar Magnetic Flux Rope Eruption Simulated by a Data-Driven Magnetohydrodynamic Model. *ApJ* 870, L21. doi:10.3847/2041-8213/aafabf

Hasan, S. S., Soltau, D., Kärcher, H., Süß, M., and Berkefeld, T. (2010). NLST: India's National Large Solar Telescope. *Astron. Nachr.* 331, 628–635. doi:10.1002/asna.201011389

Jess, D. B., Mathioudakis, M., Erdélyi, R., Crockett, P. J., Keenan, F. P., and Christian, D. J. (2009). Alfven Waves in the Lower Solar Atmosphere. *Science* 323, 1582–1585. doi:10.1126/science.1168680

Jurčák, J., Collados, M., Leenaarts, J., van Noort, M., and Schlichenmaier, R. (2019). Recent Advancements in the EST Project. *Adv. Space Res.* 63, 1389–1395. doi:10.1016/j.asr.2018.06.034

Kliem, B., Su, Y. N., van Ballegooijen, A. A., and DeLuca, E. E. (2013). Magnetohydrodynamic Modeling of the Solar Eruption on 2010 April 8. *ApJ* 779, 129. doi:10.1088/0004-637x/779/2/129

Korsós, M. B., Georgoulis, M. K., Gyenge, N., Bisoi, S. K., Yu, S., Poedts, S., et al. (2020). Solar Flare Prediction Using Magnetic Field Diagnostics above the Photosphere. *ApJ* 896, 119. doi:10.3847/1538-4357/ab8fa2

Kusano, K., Iju, T., Bamba, Y., and Inoue, S. (2020). A Physics-Based Method that Can Predict Imminent Large Solar Flares. *Science* 369, 587–591. doi:10.1126/science.aaz2511

Li, B., Antolin, P., Guo, M.-Z., Kuznetsov, A. A., Pascoe, D. J., Van Doorsselaere, T., et al. (2020). Magnetohydrodynamic Fast Sausage Waves in the Solar Corona. *Space Sci. Rev.* 216, 136. doi:10.1007/s11214-020-00761-z

Li, C., Fang, C., Li, Z., Ding, M.-D., Chen, P.-F., Chen, Z., et al. (2019). Chinese Hα Solar Explorer (CHASE) - a Complementary Space mission to the ASO-S. *Res. Astron. Astrophys.* 19, 165. doi:10.1088/1674-4527/19/11/165

Liu, J., Nelson, C. J., Snow, B., Wang, Y., and Erdélyi, R. (2019). Evidence of Ubiquitous Alfvén Pulses Transporting Energy from the Photosphere to the Upper Chromosphere. *Nat. Commun.* 10, 3504. doi:10.1038/s41467-019-11495-0

Mathioudakis, M., Jess, D. B., and Erdélyi, R. (2013). Alfvén Waves in the Solar Atmosphere. *Space Sci. Rev.* 175, 1–27. doi:10.1007/s11214-012-9944-7

Matthews, S., Baker, D., Bloomfield, D. S., Browning, P. K., Calcines, A., Del Zanna, G., et al. (2019). *Solar Particle Acceleration, Radiation & Kinetics (SPARK)*. ESA Voyage 2050 White Paper.

McCrea, I., Davies, J., Dunlop, M., Erdélyi, R., Forsyth, C., Harra, L., et al. (2019). *"The Grand European Heliospheric Observatory" – an Integrated ESA Approach to Challenges in Solar and Solar-Terrestrial Physics*. ESA Voyage 2050 White Paper.

Müller, D., St. Cyr, O. C., Zouganelis, I., Gilbert, H. R., Marsden, R., Nieves-Chinchilla, T., et al. (2020). The Solar Orbiter mission. *A&AA&A* 642, A1. doi:10.1051/0004-6361/202038467

Raghavendra Prasad, B., Banerjee, D., Singh, J., Nagabhushana, S., Kumar, A., Kamath, P. U., et al. (2017). Visible Emission Line Coronagraph on Aditya-L1. *Curr. Sci.* 113, 613. doi:10.18520/cs/v113/i04/613-615

Rast, M. P., Bello González, N., Bello González, N., Bellot Rubio, L., Cao, W., Cauzzi, G., et al. (2021). Critical Science Plan for the Daniel K. Inouye Solar Telescope (DKIST). *Sol. Phys.* 296, 70. doi:10.1007/s11207-021-01789-2

Rimmele, T. R., Warner, M., Keil, S. L., Goode, P. R., Knölker, M., Kuhn, J. R., et al. (2020). The Daniel K. Inouye Solar Telescope - Observatory Overview. *S Solar Phys.* 295, 172. doi:10.1007/s11207-020-01736-7

Samara, E., Pinto, R. F., Magdalenić, J., Wijsen, N., Jerčić, V., Scolini, C., et al. (2021). Implementing the MULTI-VP Coronal Model in EUHFORIA: Test Case Results and Comparisons with the WSA Coronal Model. *A&A* 648, A35. doi:10.1051/0004-6361/202039325

Srivastava, A. K., Ballester, J. L., Cally, P. S., Carlsson, M., Goossens, M., Jess, D. B., et al. (2021). Chromospheric Heating by Magnetohydrodynamic Waves and Instabilities. *J. Geophys. Res. Space Phys.* 126, e029097. doi:10.1029/2020JA029097

Srivastava, A. K., Murawski, K., Kuźma, B., Wójcik, D. P., Zaqarashvili, T. V., Stangalini, M., et al. (2018). Confined Pseudo-shocks as an Energy Source for the Active Solar corona. *Nat. Astron.* 2, 951–956. doi:10.1038/s41550-018-0590-1

Srivastava, A. K., Shetye, J., Murawski, K., Doyle, J. G., Stangalini, M., Scullion, E., et al. (2017). High-frequency Torsional Alfvén Waves as an Energy Source for Coronal Heating. *Sci. Rep.* 7, 43147. doi:10.1038/srep43147

Tripathi, D., Ramaprakash, A. N., Khan, A., Ghosh, A., Chatterjee, S., Banerjee, D., et al. (2017). The Solar Ultraviolet Imaging Telescope On-Board Aditya-L1. *Curr. Sci.* 113, 616. doi:10.18520/cs/v113/i04/616-619

Van Doorsselaere, T., Srivastava, A. K., Antolin, P., Magyar, N., Vasheghani Farahani, S., Tian, H., et al. (2020). Coronal Heating by MHD Waves. *Space Sci. Rev.* 216, 140. doi:10.1007/s11214-020-00770-y

Wang, T., Ofman, L., Yuan, D., Reale, F., Kolotkov, D. Y., and Srivastava, A. K. (2021). Slow-Mode Magnetoacoustic Waves in Coronal Loops. *Space Sci. Rev.* 217, 34. doi:10.1007/s11214-021-00811-0

Yardley, S. L., Mackay, D. H., and Green, L. M. (2021). Simulating the Coronal Evolution of Bipolar Active Regions to Investigate the Formation of Flux Ropes. *Sol. Phys.* 296, 10. doi:10.1007/s11207-020-01749-2

Zhou, Y. H., Chen, P. F., Hong, J., and Fang, C. (2020). Simulations of Solar Filament fine Structures and Their Counterstreaming Flows. *Nat. Astron.* 4, 994–1000. doi:10.1038/s41550-020-1094-3

Conflict of Interest: The authors declare that the research was conducted in the absence of any commercial or financial relationships that could be construed as a potential conflict of interest.

frontiers
in Astronomy and Space Sciences

ORIGINAL RESEARCH
published: 09 September 2020
doi: 10.3389/fspas.2020.00061

Oscillation and Evolution of Coronal Loops in a Dynamical Solar Corona

David J. Pascoe[1]*, Christopher R. Goddard[2] and Tom Van Doorsselaere[1]

[1] Centre for Mathematical Plasma Astrophysics, Department of Mathematics, KU Leuven, Leuven, Belgium,
[2] Max-Planck-Institut für Sonnensystemforschung, Göttingen, Germany

Observations have revealed two regimes of kink oscillations of coronal loops. Large amplitude oscillations excited by impulsive energy releases such as coronal mass ejections are characterized by their strong damping by resonant absorption. Lower amplitude oscillations may also be excited and sustained by the ubiquitous motions present in the corona and so are characterized as being decayless. We perform numerical simulations to study the oscillation and evolution of coronal loops in a dynamical environment. We investigate the observational signatures of kink oscillations and the Kelvin-Helmholtz instability in terms of high-resolution seismological and spatial data analysis techniques. We find that low amplitude kink oscillations are capable of generating significant changes in the loop profile which can affect estimates of the transverse loop inhomogeneity based on seismological and forward modeling methods. The disparity between methods may be indicative of non-linear evolution of coronal loops. The influence on forward modeling estimates could also account for previous observational evidence favoring loops having wider inhomogeneous layers.

Keywords: magnetohydrodynamics (MHD), sun - corona, sun - magnetic fields, sun - oscillations, waves and instabilities

Edited by:
Yihua Yan,
National Astronomical Observatories (CAS), China

Reviewed by:
Jose Luis Ballester,
University of the Balearic Islands, Spain
Petra Kohutova,
University of Oslo, Norway

****Correspondence:***
David J. Pascoe
david.pascoe@kuleuven.be

Specialty section:
This article was submitted to Stellar and Solar Physics, a section of the journal Frontiers in Astronomy and Space Sciences

Received: *05 June 2020*
Accepted: *03 August 2020*
Published: *09 September 2020*

Citation:
Pascoe DJ, Goddard CR and Van Doorsselaere T (2020) Oscillation and Evolution of Coronal Loops in a Dynamical Solar Corona. Front. Astron. Space Sci. 7:61. doi: 10.3389/fspas.2020.00061

1. INTRODUCTION

Kink oscillations of coronal loops are periodic displacements of the loop axis. They were first observed using the Transition Region And Coronal Explorer (TRACE; Handy et al., 1999) in an active region perturbed by a solar flare (Aschwanden et al., 1999; Nakariakov et al., 1999). Hundreds of observations of standing kink modes have now been studied (e.g., catalogs by Goddard et al., 2016; Nechaeva et al., 2019), aided by the full disk coverage and enhanced temporal resolution of the Atmospheric Imaging Assembly (AIA) on board the Solar Dynamics Observatory (SDO; Lemen et al., 2012).

Large amplitude kink oscillations are observed to be strongly damped which is attributed to the process of resonant absorption (e.g., De Moortel et al., 2016, and references therein). This is a robust damping mechanism since it only requires that the transition between a higher density coronal loop and the lower density background plasma occurs over a finite spatial scale. In analytical and numerical models this transition is usually described in terms of a boundary layer surrounding the core of the loop. The inhomogeneous layer width (commonly normalized by the loop radius to produce the parameter ϵ) represents a transverse spatial scale which is also important for other physical processes such as phase mixing (Heyvaerts and Priest, 1983) and the Kelvin-Helmholtz instability. It is therefore a key physical parameter but difficult to observe directly, which motivates its seismological inference through the damping of kink oscillations.

The length L of a coronal loop is typically much larger than its radius R. Under this thin tube approximation, the phase speed of the kink mode is the kink speed C_k, which is a density-weighted average of the internal and external Alfvén speeds. Under the further thin boundary approximation corresponding to the limit $\epsilon \to 0$, the period of oscillation for the fundamental standing kink mode is then $P = 2L/C_\mathrm{k}$. However, parametric studies (Van Doorsselaere et al., 2004; Soler et al., 2014; Pascoe et al., 2019a) find that the period of oscillation does also depend on the width of the boundary layer when it is sufficiently large.

The boundary layer of a coronal loop provides a continuous variation of the local Alfvén speed, and the resonance condition is satisfied where the kink mode frequency matches the local Alfvén frequency. A transfer of wave energy from collective kink motions to localized azimuthal perturbations ($m = 1$ Alfvén waves) will appear as a damping of the periodic loop displacement. The azimuthal motions will typically appear as unresolved Doppler velocity perturbations due to line-of-sight (LOS) integration of multiple waves and structures (e.g., De Moortel and Pascoe, 2012; Pant et al., 2019). Although this transfer is a linear and ideal process, subsequent phase-mixing of the Alfvén waves in the inhomogeneous layer can generate small spatial scales which enhance dissipative processes such as viscosity and resistivity (e.g., Pagano and De Moortel, 2017; Pagano et al., 2018).

Initial descriptions of the resonant absorption of kink oscillations took the form of exponential damping profiles (Goossens et al., 2002, 2012; Ruderman and Roberts, 2002; Arregui et al., 2007) based on analytical derivations for the asymptotic state of the system under the thin tube thin boundary (TTTB) approximation. Numerical simulations (Pascoe et al., 2012) found poor agreement with exponential damping behavior at early times, where a Gaussian damping profile appeared more suitable. The analytical description of Hood et al. (2013) accounted for this Gaussian damping regime as an approximation for the initial behavior of the kink mode, with exponential damping behavior at a later stage. The switch from Gaussian to exponential damping behavior was shown to depend on the loop density contrast ratio ζ, which was confirmed by the parametric study by Pascoe et al. (2013). It was also used to propose a general damping profile (GDP), combining both the Gaussian and exponential damping regimes, as a convenient approximation for seismology. The Gaussian damping behavior was initially studied for propagating kink waves but is also applicable to standing waves (e.g., Ruderman and Terradas, 2013; Magyar and Van Doorsselaere, 2016a; Pagano et al., 2018). In particular, Pascoe et al. (2019a) performed 300 numerical simulations to produce a lookup table (LUT) as a convenient means of estimating the damping profile beyond the applicability of the thin boundary approximation. Resonant absorption therefore accounts not only for the strong damping of kink oscillations but also the observational evidence for their non-exponential damping behavior (De Moortel et al., 2002; Ireland and De Moortel, 2002; Goddard et al., 2016; Morton and Mooroogen, 2016; Pascoe et al., 2016c), and allows the seismological inference of the transverse density profile of the loop (Pascoe et al., 2016b, 2017a, 2018).

The Kelvin-Helmholtz instability (KHI; e.g., Browning and Priest, 1984; Ofman et al., 1994) has been demonstrated by numerous numerical studies to cause redistribution of loop plasma during kink oscillations (e.g., Terradas et al., 2008a; Soler et al., 2010; Antolin et al., 2014; Karampelas and Van Doorsselaere, 2018). Since the rate of the instability depends on the shear flows it is also affected by the width of the inhomogeneous layer (e.g., Magyar and Van Doorsselaere, 2016a; Goddard et al., 2018). The "decayless" regime of kink oscillations refers to low amplitude oscillations which appear to be undamped (Anfinogentov et al., 2013, 2015; Nisticò et al., 2013) or even growing (Wang et al., 2012), in contrast with the large amplitude and strongly damped oscillations discussed above. Only coronal loops with a discontinuous boundary would not exhibit damping due to resonant absorption. However, the strong shear velocities that would be present in such a scenario would also lead to the rapid development of KHI and the establishment of an effective boundary layer by mixing of internal plasma. Forward modeling of EUV emission from coronal loops (e.g., Van Doorsselaere et al., 2016) suggests observational effects associated with KHI might contribute to the appearance of weak damping in some circumstances (Antolin et al., 2016, 2017), but generally the presence of damping by resonant absorption must be compensated by the driving mechanism, such as persistent footpoint oscillations (e.g., Afanasyev et al., 2019, 2020; Karampelas et al., 2019) or flows (Nakariakov et al., 2016; Karampelas and Doorsselaere, 2020). Decayless kink oscillations might be connected with the observation of propagating transverse velocity perturbations (e.g., Tomczyk et al., 2007; Tomczyk and McIntosh, 2009; Verth et al., 2010; Pascoe et al., 2015) since both appear to be ubiquitous and require a persistent source of wave energy, though spatial analysis of the decayless kink modes confirms they are indeed standing modes (Duckenfield et al., 2018) as does the period of oscillation being proportional to the loop length (Anfinogentov et al., 2015).

In this paper we consider the effect of the Kelvin-Helmholtz instability on the distortion of the loop density profile and its appearance in optically thin EUV images. Our simulation of a coronal loop experiencing multiple perturbations which excite and maintain standing kink oscillations approximating the decayless regime is presented in section 2. In section 3, we consider the observational signature of our simulation and compare the results with a statistical study of the density profiles of coronal loops. Conclusions are presented in section 4.

2. NUMERICAL SIMULATION OF NON-LINEAR EVOLUTION

In this section, we describe our numerical simulation of a coronal loop which experiences multiple low-amplitude impulsive perturbations designed to excite the fundamental standing kink mode. Our use of multiple perturbations as opposed to a continuous driver facilitates analysis of the evolution of the loop and its oscillation in time by enabling us to use established techniques for the damping behavior of impulsively-generated decaying oscillations. The coronal loop is modeled as a straight flux tube embedded in a uniform magnetic field with no gravitational stratification. The only non-uniformity is thus provided by the coronal loop. We use a linear density profile in the inhomogeneous layer for comparison with previous work, in particular the parametric study by Pascoe et al. (2019a) which describes the effect of a thick inhomogeneous layer. We note that the numerical simulations in that paper studied the linear regime of kink oscillations and used cylindrical coordinates, with the assumption of $m = 1$ symmetry for the azimuthal dependence corresponding to the kink oscillation and Alfvén waves generated by resonant absorption (e.g., Pascoe et al., 2010). In this paper, we study non-linear evolution of the loop, which includes the breaking of $m = 1$ azimuthal symmetry by the development of KHI (e.g., the large deformations in Karampelas and Van Doorsselaere, 2018). We use LARE3D (Arber et al., 2001) which solves the non-linear MHD equations in Cartesian geometry.

The loop has a length of 100 Mm, radius of 1 Mm, and the uniform magnetic field strength corresponds to an external Alfvén speed of 1 Mm/s. The loop has a density contrast ratio of $\zeta = 3$ for which the TTTB estimate for the period of oscillation of the fundamental kink mode is $P_{\mathrm{k}} \approx 283$ s, allowing several cycles of the oscillation to be observed between each perturbation (1,000 s apart). However, each subsequent perturbation will be applied at a time which does not correspond to a zero in the oscillation of the current oscillation. The numerical domain extends to $[-4, 4]$ Mm in the x and y directions perpendicular to the loop axis with a resolution of $400 \times 400 \times 200$ grid points. Numerical tests indicate this is sufficient for the problem, and the need for significantly higher resolution in the transverse directions. Boundary conditions are periodic in the x- and y-directions, and line-tied in z. We consider a low-beta plasma ($\beta = 0.001$) and the loop is initially set in pressure balance, corresponding to a cooler loop. We do not consider non-adiabatic effects (e.g., Aschwanden and Terradas, 2008; Magyar et al., 2015; Ruderman et al., 2019).

An impulsive fundamental standing kink mode perturbation is applied to the x-component of the plasma velocity every 1,000 s. Our aim is to demonstrate the evolution of the loop and oscillation parameters over several iterations of the perturbation. For this purpose we use a inhomogeneous layer width $\epsilon = 0.3$ which is sufficiently large to provide significant (readily measurable) damping for the oscillation while not too large as to inhibit the development of KHI. Similarly, the amplitude of the velocity perturbations is approximately 1% of the Alfvén speed to allow KHI to develop at a moderate rate. Our density profile parameters $\zeta = 3$ and $\epsilon = 0.3$ are reasonable for a coronal loop, for example the loop analyzed on 2012-03-09 by Pascoe et al. (2017c) was estimated to have $\zeta = 2.93^{+2.40}_{-0.85}$ and $\epsilon = 0.35^{+0.23}_{-0.12}$ (values correspond to the median and 95% credible interval). They are also similar to the values used in numerical simulations performed by Goddard et al. (2018) and Karampelas et al. (2019).

Our driver is intended to efficiently generate the fundamental standing kink mode in the loop, but does not correspond to the exact eigenfunction which would generally be unknown as the loop evolves during the simulation. We use the spatial form

$$v_x = A\mathrm{sech}^{\nu}\left(r/R\right)\cos\left(kz\right) \tag{1}$$

with $A = 0.015$ Mm/s, $k = \pi/L$ corresponding to the fundamental longitudinal harmonic, and $\nu = 3$ providing an appropriate spatial scale in the radial ($r = \sqrt{x^2 + y^2}$) direction. We note that the form of our driver and loop also excludes higher harmonics which can be readily generated by a broadband footpoint driver (e.g., Afanasyev et al., 2020). A persistent footpoint driver is likely more realistic but makes it difficult to accurately measure the period of oscillation due to the presence of the driver spectrum in addition to the natural frequencies. The presence of longitudinal stratification due to gravity, expansion, or curvature leads to coupling of longitudinal harmonics (e.g., Pascoe et al., 2009; Pascoe and Nakariakov, 2016) and changes to the ratio of their periods (e.g., Andries et al., 2005; McEwan et al., 2006; Safari et al., 2007; Verth and Erdélyi, 2008; Arregui et al., 2013) but does not significantly affect the damping rate due to resonant absorption (Arregui et al., 2005; Dymova and Ruderman, 2006). The period ratio for harmonics has been observed in many studies of large-amplitude oscillations (e.g., Verwichte et al., 2004; De Moortel and Brady, 2007; Van Doorsselaere et al., 2007; Pascoe et al., 2016a, 2017a; Duckenfield et al., 2019) and recently in decayless oscillations (Duckenfield et al., 2018).

Figure 1 shows the evolution of the transverse loop density profile at the middle of the coronal loop, i.e., the anti-node for the fundamental standing kink mode. The panels show the density profile in normalized units (external density $\rho_{\mathrm{e}} = 1$). The cross symbols in **Figure 1** denote the center of mass of the loop. The dashed line represents the contour for which the local Alfvén speed matches the kink speed. **Figure 2** demonstrates the evolution of the coronal loop and its oscillation during our simulation. The evolution of the loop profile is characterized by fitting the transverse density profile with a model based on a circular cross-section and linear density profile in the inhomogeneous layer, which is satisfied exactly for the initial condition but otherwise an approximation. They therefore correspond to a value which is averaged in the azimuthal direction, whereas it is known from previous work (e.g., Barbulescu et al., 2019; Hillier and Arregui, 2019) and our **Figure 1** that KHI causes density perturbations to develop which exhibit the same $m = 1$ symmetry as the kink mode. For example, the loop becomes extended in the direction of its displacement (e.g., Karampelas and Van Doorsselaere, 2018). We note that this method for estimating loop parameters is only possible with simulation data, whereas the observational signatures will be considered in section 3.

The top left panel of **Figure 2** shows the position of the coronal loop based on our fitting of the density profile (solid line). The dashed line is the position of the center of mass of the loop which is in good agreement. We apply a perturbation at $t = 0$ s and every 1,000 s thereafter, indicated by the vertical dotted lines. The subsequent increase in amplitude of the oscillation depends on whether the perturbation is aligned with or opposed to the current direction of motion (which we choose arbitrarily to demonstrate both cases). We note that the abrupt changes in phase is a consequence of our driving mechanism, which is chosen for convenience of our analysis, and is not observed in decayless oscillations. The clear signature

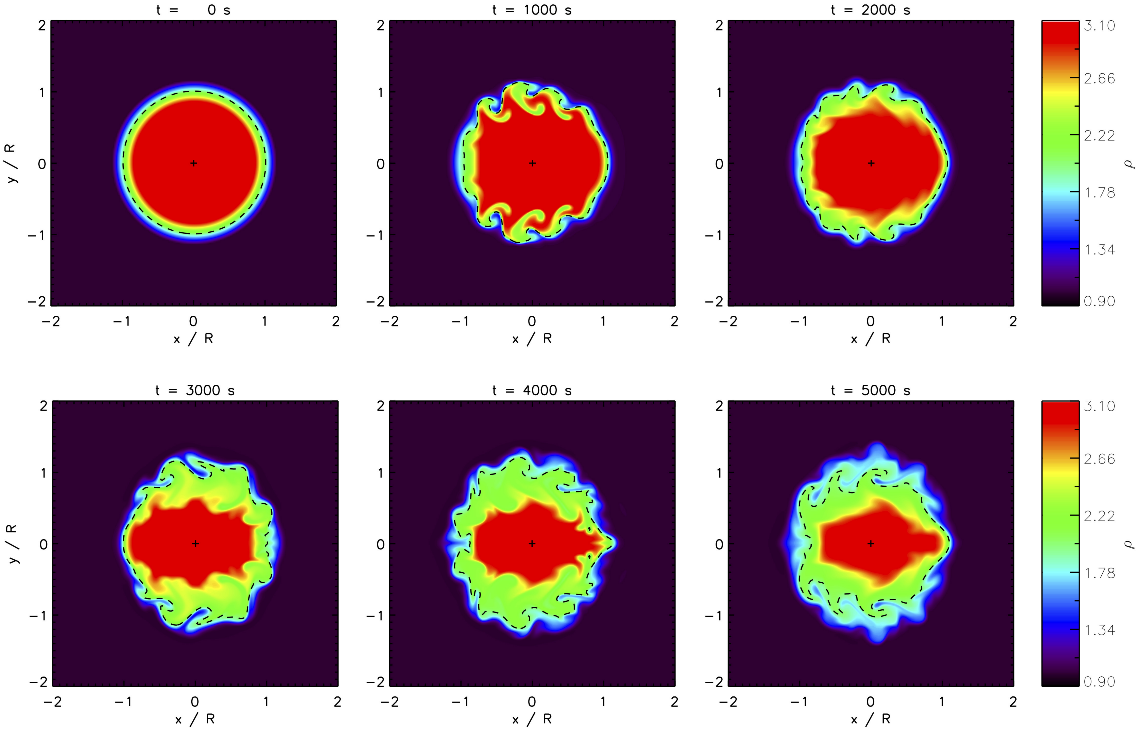

FIGURE 1 | Evolution of the loop density profile in time. The panels show the density in normalized units at the middle ($z = 50$ Mm) of the coronal loop. The cross symbols denote the position of the loop. The dashed line represents the contour for which the local Alfvén speed matches the kink speed.

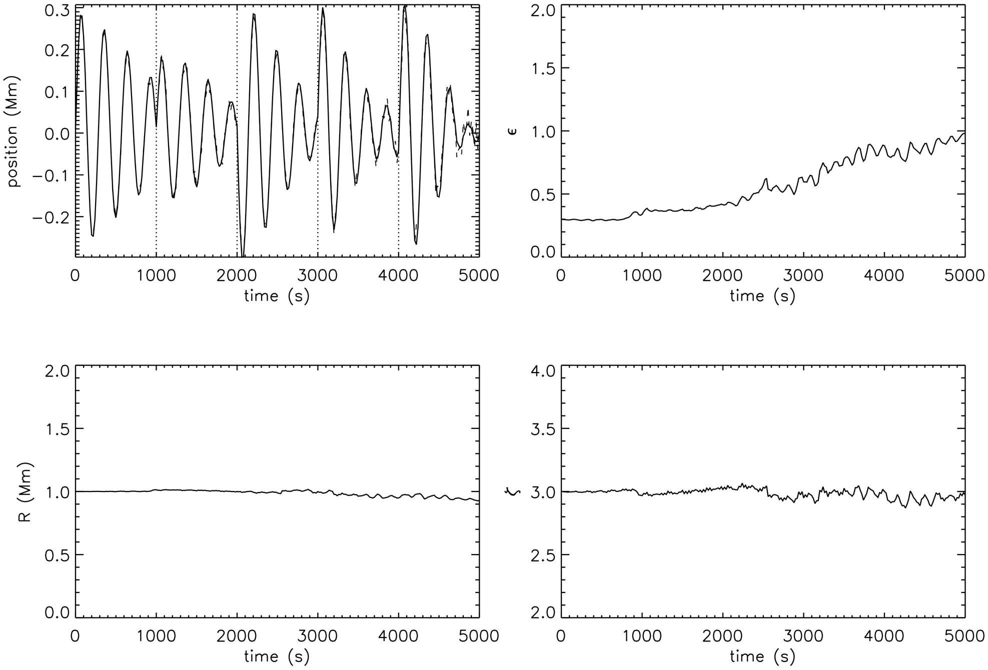

FIGURE 2 | Oscillation of the coronal loop and evolution of the transverse loop density profile parameters taken at the middle of the loop during our numerical simulation; loop position **(top left)**, normalized inhomogeneous layer width **(top right)**, loop radius **(bottom left)**, and density contrast ratio **(bottom right)**.

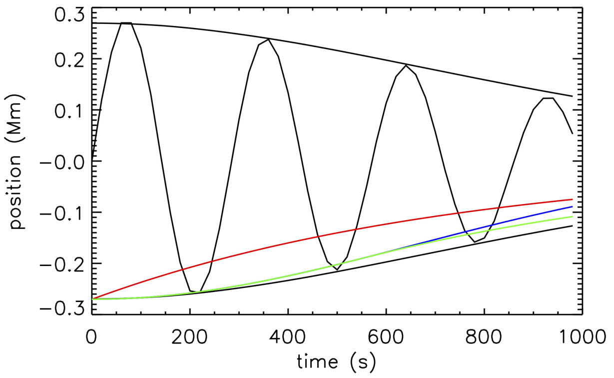

FIGURE 3 | Damping of the kink oscillation after the first applied perturbation. The damping envelopes correspond to the LUT (black), GDP (green), Gaussian (blue), and exponential (red) damping profiles.

of damping and then an increase in amplitude also does not represent decayless oscillations with an approximately constant amplitude, although we have deliberately chosen a sufficiently long interval between perturbations to allow seismological analysis and this effect would be reduced by more frequent and lower amplitude perturbations.

The maximum amplitude of 0.3 Mm is consistent with the decayless regime of kink oscillations which is lower than 1 Mm and an average of approximately 0.2 Mm (Anfinogentov et al., 2015). It is evident that the damping rate at the end of the simulation is greater than that at the start of the simulation (further discussion below). The other panels in **Figure 2** show the evolution of the loop parameters. There is no significant change in the loop radius R or density contrast ratio ζ. The main effect of KHI is the increase in the width of the inhomogeneous layer, from its initial value of 0.3 to approximately 1 at the end of our simulation. The onset of this increase occurs after several cycles of the oscillation due to the time required for KHI to develop. The widening inhomogeneous layer and unchanged loop radius are consistent with the study of non-linear evolution of loops by Goddard et al. (2018), although that paper considered the changes in the transverse intensity profile rather than the density profile here. Goddard et al. (2018) also reported a decrease in the peak intensity of the loop, whereas our analysis here indicates an unchanged density contrast ratio. There is no inconsistency in these two results since the decrease in intensity can also be associated with the mixing of plasmas of different temperatures by KHI, and numerical simulations such as those in Goddard et al. (2018) typically impose temperature profiles which decrease inside the loop to maintain pressure balance.

Figure 3 shows the oscillation of the coronal loop after the first applied perturbation and before the second. During this time there are minimal effects due to the non-linear evolution of the loop (see **Figure 2**) and so the damping rate is consistent with the black envelopes representing the linear solution calculated with the lookup table (LUT) of Pascoe et al. (2019a). The LUT envelope contains the correction for the boundary layer not being thin, whereas each of the colored envelopes are based on the thin boundary approximation and so overestimate the damping of the kink oscillation, particularly the exponential damping profile (red) which does not account for the Gaussian damping behavior during the first couple of cycles of the oscillation. For the general damping profile (GDP) the switch from a Gaussian profile (blue) to an exponential profile occurs after 2 cycles for a density contrast ratio of $\zeta = 3$. The damping rate during subsequent cycles is increased due to KHI, as studied by Magyar and Van Doorsselaere (2016a). We also note that the fitted period of oscillation is $P \approx 1.01P_{\mathrm{k}}$, consistent with the small increase due to the presence of a non-thin boundary layer also found in numerical simulations by Pascoe et al. (2019a), and contrary to the decrease in period reported by Soler et al. (2013) and Soler et al. (2014).

Figure 4 shows the results of wavelet analysis (Torrence and Compo, 1998) of the oscillation of the loop axis (left panel). The contours for the wavelet power suggests a small decrease in the period of oscillation in time. This effect is also found by fitting the oscillation as a series of damped perturbations with a time-varying period of oscillation and inhomogeneous layer width (right panel) based on the LUT damping profile. The fitted period of oscillation starts as slightly larger than the TTTB approximation (dashed line in left panel) due to the thickness of the inhomogeneous layer as discussed above. The period of oscillation then decreases during the simulation, due to the non-linear evolution, to a value slightly less than the TTTB approximation. Overall, the TTTB approximation remains a good approximation for the period of oscillation.

The seismological estimate for ϵ is based on the damping due to resonant absorption calculated for different density profile parameters (ζ, ϵ) by Pascoe et al. (2019a) and summarized in the LUT[1]. This accounts for the effect of a thick inhomogeneous layer and the presence of the non-exponential damping regime. The loop model used in this paper is the same as that used to generate the LUT, and so the results may be directly compared with the relevant physical difference being the non-linear evolution due to finite amplitude kink oscillations. We fit our oscillation with a sinusoidal oscillation comprised of five segments (corresponding to each of the applied perturbations) but a period of oscillation and inhomogeneous layer width which vary (as quadratic polynomials) continuously across all segments. The solid lines in **Figure 4** represent the fitted dependence of $P(t)$ and $\epsilon(t)$ required to account for the period and damping in our simulation. Within each individual segment the damping profile is calculated from the LUT using $\zeta = 3$ and the local average for $P(t)$ and $\epsilon(t)$.

The increase in ϵ required to account for the increase in damping rate in time is much larger (approximately twice) than the estimate based on fitting the transverse density profile. On the other hand, it is evident from **Figure 1** that the smaller estimate is more reasonable since the loop has not become fully inhomogeneous by the end of the simulation as the seismological

---

[1] https://github.com/djpascoe/kinkLUT

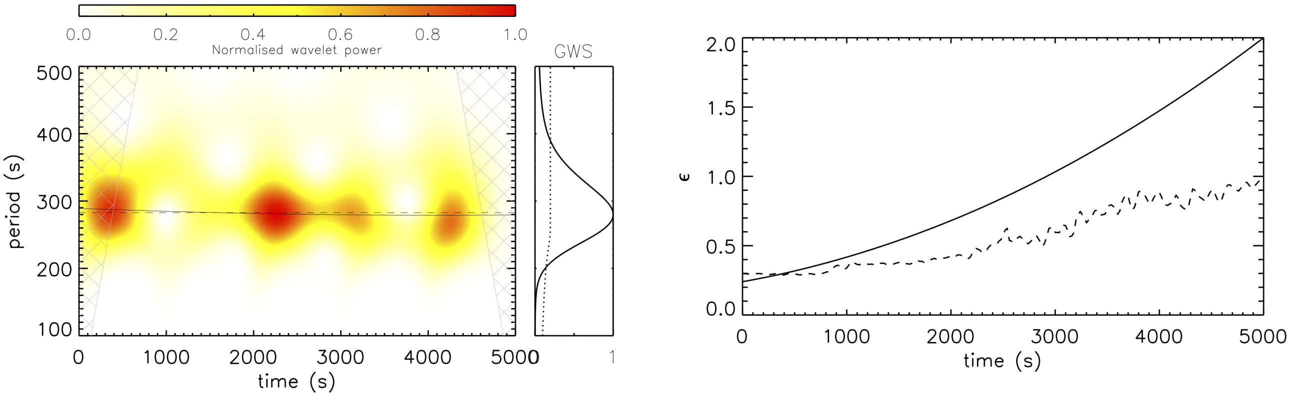

FIGURE 4 | Wavelet analysis of the loop oscillation (left panel). The solid line in the normalized wavelet power represents the fitted variation of the period of oscillation in time. The dashed line denotes the estimate based on the TTTB approximation. The hatched region represents the cone of influence. The global wavelet spectrum (GWS) is shown with the dotted line corresponding to the 90% significance level. The right panel shows the seismologically determined variation in inhomogeneous layer width (compared with the estimate in **Figure 2** shown as a dashed line).

analysis with $\epsilon \rightarrow 2$ suggests. We can therefore conclude that the non-linear evolution increases the damping rate of kink oscillations above the level suggested by the increasing inhomogeneous layer width. This is not unexpected since our estimate of the inhomogeneous layer width only describes the large scale broadening effect of KHI due to the mixing of loop plasma and external plasma, while KHI is also known to generate small scale structures ("TWIKH rolls").

Figure 1 shows that these TWIKH rolls also modify the location where the condition for resonant absorption to occur is satisfied (dashed lines). In particular, near the locations of maximum mode coupling ($x = 0, y = \pm R$), the TWIKH rolls cause the resonant contour to double back on itself, presenting additional locations at which resonant absorption can occur. Accordingly, we can caution that the seismologically-inferred value of ϵ is likely to be an overestimate in the case of loop oscillations with strong development of KHI. Previous studies have also estimated ϵ independently of seismological analysis using the transverse intensity profile of the loop. In the following section we consider how this estimate is also affected by the development of KHI.

The seismological model discussed above used a constant density contrast ratio and varying inhomogeneous width based on our understanding of the evolution of the loop due to KHI such as the results in **Figure 2**. However, approaching the oscillation from a purely seismological point of view, we could consider an alternative analysis of the increase in damping rate as due to a varying density contrast ratio with ϵ remaining constant. We find that this would require a significant increase to $\zeta > 15$ and so could readily be refuted by a lack of brightening in EUV intensity images and due to a mechanism for large increases in loop mass (or decrease in surrounding plasma) to be theoretically accounted for. Such a large change in ζ would also significantly change the period of oscillation unless somehow balanced by a corresponding change in the magnetic field strength.

3. OBSERVATIONAL SIGNATURE OF LOOP EVOLUTION

In this section, we consider the evolution of our simulated coronal loop in terms of the established observational method to estimate the inhomogeneous layer width based on the shape of transverse intensity profile. The appearance of a coronal loop in optically thin EUV intensity images can be approximated using the square of the density integrated along the line-of-sight. This method was previously used by Aschwanden et al. (2003) and Aschwanden and Nightingale (2005) who modeled TRACE 171 Å data using a density profile with a sinusoidal inhomogeneous layer. It was extended by Aschwanden et al. (2007) to also consider rectangular (step) function and Gaussian density profiles, although these were found to typically be indistinguishable from the density profile with a sinusoidal inhomogeneous layer for TRACE data when including the smoothing effect of the instrumental point-spread function.

More recently, a similar method was applied by Pascoe et al. (2017b) to estimate the inhomogeneous layer width of a coronal loop observed using SDO/AIA 171 Å. The density profiles used in that study included a step function, Gaussian profile, and a inhomogeneous layer with a linear profile. Bayesian analysis found very strong evidence for the linear transition over the step profile (and very strong evidence for the step profile over the Gaussian), indicative of a small but finite inhomogeneous layer in the loop, and consistent with the separate seismological studies of the same loop by Pascoe et al. (2016b, 2017a). A technique using both the seismological and intensity modeling methods simultaneously to estimate the inhomogeneous layer width of an oscillating coronal loop was produced by Pascoe et al. (2018).

Goddard et al. (2017) performed a statistical study of 233 coronal loops comparing the step, Gaussian, and linear inhomogeneous layer density profiles. For 58% of cases there was strong evidence for the existence of an inhomogeneous layer, and there were no cases of strong evidence against there being an inhomogeneous layer. The inhomogeneous layer widths

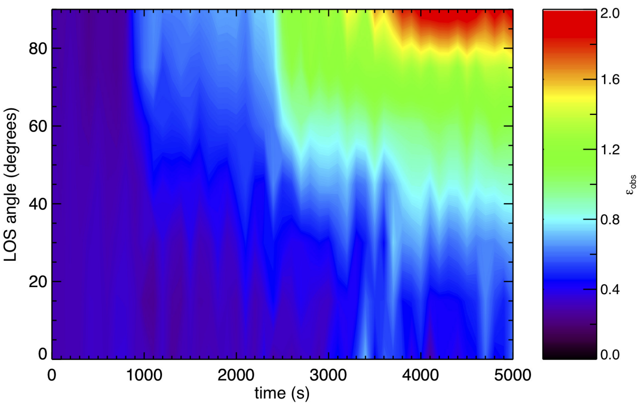

FIGURE 5 | The inhomogeneous layer width based on the transverse intensity profile of the coronal loop in our numerical simulation. Near the start of the simulation the initial value of 0.3 is measured for all LOS angles, but at later times the observed value increases.

observed covered the full range of 0 to 2 and had no correlation with the loop radius.

Figure 5 shows the value of inhomogeneous layer width inferred from our numerical simulation using the same method applied to observational data (Goddard et al., 2017; Pascoe et al., 2017b). This is calculated from the numerical data with the EUV intensity approximated as the square of the density integrated along the LOS, which we vary between 0 and 90 degrees relative to the plane of the loop oscillation. The observationally inferred value $\epsilon_{\rm obs}$ increases with time due to the non-linear evolution of the loop by development of KHI, as in Goddard et al. (2018), and with the LOS angle since the density perturbations associated with this evolution reflect the $m = 1$ symmetry of the kink mode driving it (see **Figure 1**).

Large LOS angles show the strongest variation in $\epsilon_{\rm obs}$ but would also exhibit the smallest transverse displacements. In such cases, the presence of kink oscillations could therefore be inferred indirectly by the increase of the inhomogeneous layer width in time, and directly using Doppler shift observations. For smaller LOS angles the increase in the inhomogeneous layer width is weaker but the transverse perturbations are larger, corresponding to the scenario for which decayless oscillations are detected by EUV imaging such as SDO/AIA. The estimate of ϵ presented in **Figure 2** shows ϵ increasing to approximately 1 by the end of the simulation. This increase corresponds to an LOS angle of approximately 55 degrees in **Figure 5**. We can therefore expect that studies which consider the evolution of the loop coinciding with detectable oscillations (displacements) in EUV would typically underestimate the evolution which has actually taken place in terms of the evolution of the EUV intensity profile. This is in contrast to the results of the previous section which demonstrate how the seismologically-inferred value of ϵ would typically be an overestimate due to the generation of small scale density perturbations by KHI. Such a discrepancy between seismological and forward modeling estimates could therefore be indicative of non-linear evolution of the loop due to KHI, motivating further study to exclude other potential sources of discrepancy such as the influence of multiple loops along the LOS.

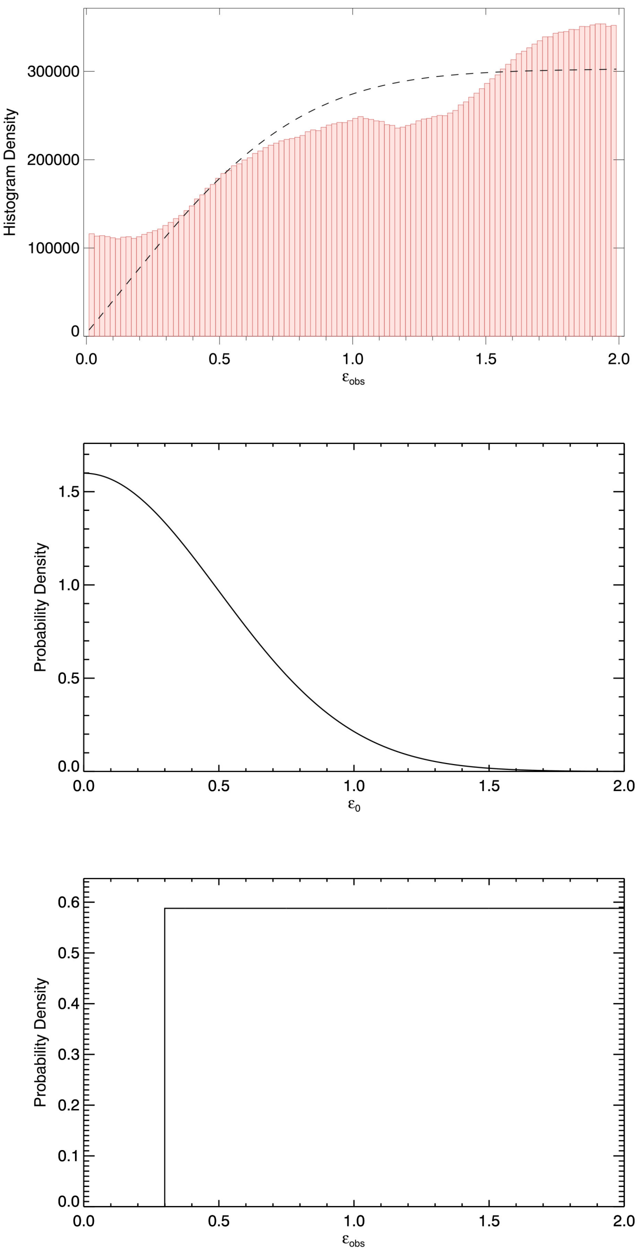

FIGURE 6 | Histogram for the inhomogeneous layer width $\epsilon_{\rm obs}$ based on observations of 233 coronal loops **(top)**. The dashed line represents a model for the observed distribution of $\epsilon_{\rm obs}$ based on loops being created with some initial distribution ϵ_0 **(middle)**, and $\epsilon_{\rm obs}$ being some value greater than ϵ_0 (shown in **bottom** panel for the case of $\epsilon_0 = 0.3$).

In **Figure 6**, we present a simple model to use the results of our numerical simulation to interpret an ensemble of observational data for a large number of loops such as the statistical study by Goddard et al. (2017). Those loops were chosen for a study of the transverse density profile with no consideration for oscillation. On the other hand, it has been established that decayless oscillations are ubiquitous in coronal loops (Anfinogentov et al., 2015). We can therefore consider that these loops will have undergone some range of non-linear evolution due to decayless oscillations, and that they also represent a range of LOS angles.

The top panel of **Figure 6** shows a histogram of the observed value of the inhomogeneous layer width based on the study by Goddard et al. (2017). We note that in **Figure 3** of that paper the values of ϵ correspond to the median value of the posterior probability distribution returned using Bayesian analysis with Markov chain Monte Carlo (MCMC) sampling (Anfinogentov et al., 2020). Here we also wish to consider the uncertainty associated with those values and so sum the full posterior probability distributions for all 233 loops. The study of each loop is based on 10^5 MCMC samples and the plotted histogram uses 100 bins hence the average histogram density being $233 \times 10^5/100 \sim 200,000$.

Our model distribution for ϵ_{obs}, shown as the dashed line in the top panel, is the combination of two probability distributions described below. We consider that for a loop with initial inhomogeneous layer ϵ_0, the observed value ϵ_{obs} may be any value greater than ϵ_0 (up to 2 by definition) depending on the amount of non-linear evolution and LOS angle as demonstrated in **Figure 5**. This is shown in the bottom panel for the example of $\epsilon = 0.3$, with a uniform distribution assumed for simplicity. The middle panel represents the initial distribution of ϵ_0. This will be determined by the mechanism which creates coronal loops and is presently unknown. We assume a half-normal distribution with the width of the distribution taken to be a free parameter which we fit by comparing our final model distribution to that from our observational data. The fitted width of approximately 0.5 implies loops are only required to have small initial inhomogeneous layer widths to account for the observed values, assuming the observational results are influenced by non-linear evolution similar to that shown in **Figure 5**.

The largest difference between the model and observational data is in the limit $\epsilon_{\text{obs}} \rightarrow 0$. However, we note that the observational data is based on Bayesian analysis with a posterior probability density broadened to include values of 0 by observational error, whereas there is no consideration of errors in our model. The original statistical study by Goddard et al. (2017) found no cases for which the Bayesian evidence favored the step function density profile which corresponds to $\epsilon = 0$. On the other hand, our assumption of a uniform probability distribution for ϵ_{obs} under-represents the expected peak at ϵ_0 and especially penalizes the limit of $\epsilon_0 \rightarrow 0$ for which the range $\epsilon_0 \leq \epsilon_{\text{obs}} \leq 2$ is greatest.

This simple model therefore demonstrates how observational results supporting larger values of inhomogeneous layer width are compatible with loops being generated with initially small values of ϵ under the assumption that the non-linear evolution of loops due to decayless oscillations acts only to increase the observed value of ϵ_{obs}. This analysis also demonstrates how future observational studies might provide information about the mechanism by which coronal loops are generated if the probability distribution for ϵ_0 could be related to a theoretical model as opposed to our assumption of a half-normal distribution.

4. CONCLUSIONS

In this paper we have simulated the non-linear evolution of a coronal loop due to KHI and investigated the effect on the corresponding observational signatures. To facilitate analysis of the results our driver is impulsive which is typically associated with large amplitude decaying kink oscillations. On the other hand, the low amplitude of our driver corresponds to the decayless regime of kink oscillations and the repetitive perturbations may be considered as an approximation of some intermittent driving mechanism, for example, random buffeting of loop footpoints by photospheric motions. However, it is unlikely that decayless oscillations are actually generated in this way since it introduces abrupt changes in the phase of the oscillation which are typically not observed. Our resulting oscillation is decayless over the longer term, as kink mode energy lost by resonant absorption is replaced by subsequent additional perturbations. We find that these low amplitude kink oscillations approximating the decayless regime are capable of generating significant changes in the loop profile which can affect both the seismological and spatial estimates for the inhomogeneous layer width by different amounts. This can potentially be used to infer the presence of non-linear evolution of loop profiles through any disparity in estimates, although care would be required to ensure the direction and magnitude of the disparity is consistent with the physical model and observational conditions. Furthermore, we demonstrate that this effect could account for the observed distribution of inhomogeneous layer widths favoring larger values even if the mechanism by which loops are generated were to favor thin layers. This is similar to the argument by Magyar and Van Doorsselaere (2016b) for the non-existence of multi-stranded coronal loops due to the mixing of plasma by KHI, but with the transverse plasma inhomogeneity being in the form of a boundary layer as opposed to a large number of small structures throughout the loop.

We can use the results of this paper to reconsider the case of a coronal loop which has been previously studied independently using seismological and spatial methods to determine to loop profile, and which exhibited both decayless and decaying kink oscillations. The seismological analysis of the loop, based on the large amplitude decaying oscillation, found an inhomogeneous layer width $\epsilon = 0.49^{+0.23}_{-0.12}$ (Pascoe et al., 2017a) (the density contrast ratio was also estimated to be 3 as used in this paper). The spatial estimate based on forward modeling the transverse intensity profile produced a value of $\epsilon = 0.59^{+0.14}_{-0.15}$ (Pascoe et al., 2017b). The loop was observed from the side, i.e., a LOS angle close to zero (see, e.g., Figure 1 of Pascoe et al., 2016b) and so a minimal increase in the width would be expected by studying the evolution of the intensity profile. The spatial study by Pascoe et al. (2017b) uses the loop intensity profile at the start of the large amplitude oscillation, however decayless oscillations were also detected in the same loop before, during and after the large amplitude oscillation; Nisticò et al. (2013)

detected approximately 12 cycles of decayless oscillation before the onset of the large amplitude perturbation, while Pascoe et al. (2017a) estimated the amplitude of the decayless component as approximately 0.14 Mm (compared with a loop radius of approximately 3 Mm).

We can therefore consider two scenarios. Firstly, no KHI took place during the decayless regime, and so the spatial estimate of the inhomogeneous layer width is an accurate representation of the loop structure. Its consistency with the seismological estimate is due to the onset of any KHI arising from the large amplitude decaying oscillation being delayed by at least one cycle. Alternatively, KHI did take place during the decayless oscillations and in time to influence the results obtained for the large amplitude oscillation. The corresponding evolution of the loop profile means that the damping rate and inhomogeneous layer width would be overestimated by the seismological analysis, whereas the inhomogeneous layer width would be underestimated by the spatial analysis which has a very low LOS angle. The consistency of the two estimates for ϵ suggests the first scenario in which there was no KHI arising from the initial decayless stage of the oscillation. A recent study of the evolution of the temporal evolution of loops following large amplitude oscillations (Goddard and Nisticò, 2020) also found no clear evidence of KHI, but all loops analyzed did display changes after the onset of the oscillation. The extent to which this is due to observational issues, rather than genuine evolution of the loops, remains to be determined. That study was also based on DEM analysis which is known to produce overly broad spectra (e.g., Van Doorsselaere et al., 2018; Pascoe et al., 2019b) which may conceal the signatures of KHI.

The disparity between the abundant evidence for KHI in simulations compared to the lack of evidence in loop oscillations therefore remains to be accounted for. For the particular example considered above, the width of the loop being approximately three times larger than in our simulation may account for the apparent much slower evolution, with the non-linearity parameter being the displacement amplitude normalized by the loop radius (e.g., Van Doorsselaere et al., 2020). This reduces the 12 decayless cycles observed by Nisticò et al. (2013) to the equivalent of approximately 4 in our simulation, which is sufficiently early that the non-linear evolution would not influence either the seismological or spatial results, and so they would remain consistent with each other and an accurate representation of the actual loop structure.

Our simulation demonstrates that the development of KHI is associated with an increasing damping rate and decreasing period of oscillation. However, the variation in the period of oscillation is small (approximately 3% during our entire simulation) and likely to be surpassed in observations by additional effects, such as changes in loop length or plasma properties, which can cause larger changes and either increases or decreases (e.g., Ireland and De Moortel, 2002; Nisticò et al., 2013; White et al., 2013; Pascoe et al., 2017c). Recent analysis of standing kink oscillations excited by two solar flares found the later oscillations damped faster than the earlier ones, consistent with KHI, while the period of oscillation increased by approximately 20% during the observation (Pascoe et al., 2020). The insensitivity of the period of oscillation to the transverse loop structure is consistent with the kink oscillation being a collective fast magnetoacoustic mode (e.g., Díaz et al., 2005; Pascoe et al., 2007). Previous studies have demonstrated that the damping of kink oscillations by resonant absorption is also not sensitive to loops being multi-stranded (Terradas et al., 2008b; Pascoe et al., 2011). However, the presence of such structuring is of interest since it can lead to a significant underestimation of the wave energy estimated using Doppler measurements (De Moortel and Pascoe, 2012; Pant et al., 2019) or an overestimation of the broadness of DEM spectra (Van Doorsselaere et al., 2018). Due to LOS integration of optically thin EUV emission it is difficult to interpret fine structure in transverse intensity profiles, particularly when using a single channel as may be the case for coronal loops which are often identifiable only in the 171 Å channel of SDO/AIA. Observations using higher resolution instruments such as CRisp Imaging Spectro-Polarimeter (CRISP; Antolin et al., 2012; Scullion et al., 2014) and the High-Resolution Coronal Imager (Hi-C; Aschwanden and Peter, 2017; Williams et al., 2020) reveal that loop structuring indeed exists below the resolution of SDO/AIA. Our results demonstrate that the non-linear evolution of the loop profile by KHI produces a time-dependent (increasing) damping rate for kink oscillations that would not be expected for structuring due to loops being multi-stranded. This is due to KHI concentrating the changes to the loop profile in the inhomogeneous layer near the locations where resonant absorption occurs.

More generally, our results demonstrate the need for detailed comparison of non-linear numerical simulations and forward modeled observable signatures (preferably multi-channel) to assist in the interpretation of physical effects such as KHI. The confirmation, or otherwise, of such effects allows additional physical conditions to be revealed, for example the inhibition of KHI due to the presence of magnetic twist (Terradas et al., 2018).

DATA AVAILABILITY STATEMENT

The raw data supporting the conclusions of this article will be made available by the authors, without undue reservation.

AUTHOR CONTRIBUTIONS

DP and TV contributed conception and design of the study. CG and DP performed the observational data analysis. DP wrote the first draft of the manuscript and received input from all co-authors.

FUNDING

DP and TV were supported by the GOA-2015-014 (KU Leuven) and the European Research Council (ERC) under the European Union's Horizon 2020 research and innovation programme (grant agreement no. 724326).

REFERENCES

Afanasyev, A., Karampelas, K., and Van Doorsselaere, T. (2019). Coronal loop transverse oscillations excited by different driver frequencies. *Astrophys. J.* 876:100. doi: 10.3847/1538-4357/ab1848

Afanasyev, A. N., Van Doorsselaere, T., and Nakariakov, V. M. (2020). Excitation of decay-less transverse oscillations of coronal loops by random motions. *Astron. Astrophys*. 633:L8. doi: 10.1051/0004-6361/201937187

Andries, J., Arregui, I., and Goossens, M. (2005). Determination of the coronal density stratification from the observation of harmonic coronal loop oscillations. *Astrophys. J. Lett*. 624, L57–L60. doi: 10.1086/430347

Anfinogentov, S., Nisticò, G., and Nakariakov, V. M. (2013). Decay-less kink oscillations in coronal loops. *Astron. Astrophys*. 560:A107. doi: 10.1051/0004-6361/201322094

Anfinogentov, S. A., Nakariakov, V. M., and Nisticò, G. (2015). Decayless low-amplitude kink oscillations: a common phenomenon in the solar corona? *Astron. Astrophys*. 583:A136. doi: 10.1051/0004-6361/201526195

Anfinogentov, S. A., Nakariakov, V. M., Pascoe, D. J., and Goddard, C. R. (2020). Solar Bayesian Analysis Toolkit – a new Markov chain Monte Carlo IDL code for Bayesian parameter inference. *arXiv Preprints* arXiv:2005.05365. Available online at: https://ui.adsabs.harvard.edu/abs/2020arXiv200505365A

Antolin, P., De Moortel, I., Van Doorsselaere, T., and Yokoyama, T. (2016). Modeling observed decay-less oscillations as resonantly enhanced kelvin-helmholtz vortices from transverse MHD waves and their seismological application. *Astrophys. J. Lett*. 830:L22. doi: 10.3847/2041-8205/830/2/L22

Antolin, P., De Moortel, I., Van Doorsselaere, T., and Yokoyama, T. (2017). Observational signatures of transverse magnetohydrodynamic waves and associated dynamic instabilities in coronal flux tubes. *Astrophys. J*. 836:219. doi: 10.3847/1538-4357/aa5eb2

Antolin, P., Vissers, G., and Rouppe van der Voort, L. (2012). On-Disk Coronal Rain. *Solar Phys*. 280, 457–474. doi: 10.1007/s11207-012-9979-7

Antolin, P., Yokoyama, T., and Van Doorsselaere, T. (2014). Fine strand-like structure in the solar corona from magnetohydrodynamic transverse oscillations. *Astrophys. J. Lett*. 787:L22. doi: 10.1088/2041-8205/787/2/L22

Arber, T., Longbottom, A., Gerrard, C., and Milne, A. (2001). A staggered grid, Lagrangian-Eulerian remap code for 3-d MHD simulations. *J. Comput. Phys*. 171, 151–181. doi: 10.1006/jcph.2001.6780

Arregui, I., Andries, J., Van Doorsselaere, T., Goossens, M., and Poedts, S. (2007). MHD seismology of coronal loops using the period and damping of quasi-mode kink oscillations. *Astron. Astrophys*. 463, 333–338. doi: 10.1051/0004-6361:20065863

Arregui, I., Asensio Ramos, A., and Diaz, A. J. (2013). Bayesian analysis of multiple harmonic oscillations in the solar corona. *Astrophys. J. Lett*. 765:L23. doi: 10.1088/2041-8205/765/1/L23

Arregui, I., Van Doorsselaere, T., Andries, J., Goossens, M., and Kimpe, D. (2005). Resonantly damped fast MHD kink modes in longitudinally stratified tubes with thick non-uniform transitional layers. *Astron. Astrophys*. 441, 361–370. doi: 10.1051/0004-6361:20053039

Aschwanden, M. J., Fletcher, L., Schrijver, C. J., and Alexander, D. (1999). Coronal loop oscillations observed with the transition region and coronal explorer. *Astrophys. J*. 520, 880–894. doi: 10.1086/307502

Aschwanden, M. J., and Nightingale, R. W. (2005). Elementary loop structures in the solar corona analyzed from TRACE triple-filter images. *Astrophys. J*. 633, 499–517. doi: 10.1086/452630

Aschwanden, M. J., Nightingale, R. W., Andries, J., Goossens, M., and Van Doorsselaere, T. (2003). Observational tests of damping by resonant absorption in coronal loop oscillations. *Astrophys. J*. 598, 1375–1386. doi: 10.1086/379104

Aschwanden, M. J., Nightingale, R. W., and Boerner, P. (2007). A statistical model of the inhomogeneous corona constrained by triple-filter measurements of elementary loop strands with TRACE. *Astrophys. J*. 656, 577–597. doi: 10.1086/510232

Aschwanden, M. J., and Peter, H. (2017). The width distribution of loops and strands in the solar corona–are we hitting rock bottom? *Astrophys. J*., 840:4. doi: 10.3847/1538-4357/aa6b01

Aschwanden, M. J., and Terradas, J. (2008). The effect of radiative cooling on coronal loop oscillations. *Astrophys. J. Lett*. 686:L127. doi: 10.1086/592963

Barbulescu, M., Ruderman, M. S., Van Doorsselaere, T., and Erdélyi, R. (2019). An analytical model of the Kelvin-Helmholtz instability of transverse coronal loop oscillations. *Astrophys. J*. 870:108. doi: 10.3847/1538-4357/aaf506

Browning, P. K., and Priest, E. R. (1984). Kelvin-Helmholtz instability of a phased-mixed Alfven wave. *Astron. Astrophys*. 131, 283–290.

De Moortel, I., and Brady, C. S. (2007). Observation of higher harmonic coronal loop oscillations. *Astrophys. J*. 664, 1210–1213. doi: 10.1086/518830

De Moortel, I., Hood, A. W., and Ireland, J. (2002). Coronal seismology through wavelet analysis. *Astron. Astrophys*. 381, 311–323. doi: 10.1051/0004-6361:20011659

De Moortel, I., and Pascoe, D. J. (2012). The effects of line-of-sight integration on multistrand coronal loop oscillations. *Astrophys. J*. 746:31. doi: 10.1088/0004-637X/746/1/31

De Moortel, I., Pascoe, D. J., Wright, A. N., and Hood, A. W. (2016). Transverse, propagating velocity perturbations in solar coronal loops. *Plasma Phys. Controlled Fusion* 58:014001. doi: 10.1088/0741-3335/58/1/014001

Díaz, A. J., Oliver, R., and Ballester, J. L. (2005). Fast magnetohydrodynamic oscillations in a multifibril Cartesian prominence model. *Astron. Astrophys*. 440, 1167–1175. doi: 10.1051/0004-6361:20052759

Duckenfield, T., Anfinogentov, S. A., Pascoe, D. J., and Nakariakov, V. M. (2018). Detection of the second harmonic of decay-less kink oscillations in the solar corona. *Astrophys. J. Lett*. 854:L5. doi: 10.3847/2041-8213/aaaaeb

Duckenfield, T. J., Goddard, C. R., Pascoe, D. J., and Nakariakov, V. M. (2019). Observational signatures of the third harmonic in a decaying kink oscillation of a coronal loop. *Astron. Astrophys*. 632:A64. doi: 10.1051/0004-6361/201936822

Dymova, M. V., and Ruderman, M. S. (2006). Resonantly damped oscillations of longitudinally stratified coronal loops. *Astron. Astrophys*. 457, 1059–1070. doi: 10.1051/0004-6361:20065051

Goddard, C. R., Antolin, P., and Pascoe, D. J. (2018). Evolution of the transverse density structure of oscillating coronal loops inferred by forward modeling of EUV intensity. *Astrophys. J*. 863:167. doi: 10.3847/1538-4357/aad3cc

Goddard, C. R., and Nisticò, G. (2020). Temporal evolution of oscillating coronal loops. *Astron. Astrophys*. 638:A89. doi: 10.1051/0004-6361/202037467

Goddard, C. R., Nisticò, G., Nakariakov, V. M., and Zimovets, I. V. (2016). A statistical study of decaying kink oscillations detected using SDO/AIA. *Astron. Astrophys*. 585:A137. doi: 10.1051/0004-6361/201527341

Goddard, C. R., Pascoe, D. J., Anfinogentov, S., and Nakariakov, V. M. (2017). A statistical study of the inferred transverse density profile of coronal loop threads observed with SDO/AIA. *Astron. Astrophys*. 605:A65. doi: 10.1051/0004-6361/201731023

Goossens, M., Andries, J., and Aschwanden, M. J. (2002). Coronal loop oscillations. An interpretation in terms of resonant absorption of quasi-mode kink oscillations. *Astron. Astrophys*. 394:L39–L42. doi: 10.1051/0004-6361:20021378

Goossens, M., Soler, R., Arregui, I., and Terradas, J. (2012). Analytic approximate seismology of propagating magnetohydrodynamic waves in the solar corona. *Astrophys. J*. 760:98. doi: 10.1088/0004-637X/760/2/98

Handy, B. N., Acton, L. W., Kankelborg, C. C., Wolfson, C. J., Akin, D. J., Bruner, M. E., et al. (1999). The transition region and coronal explorer. *Solar Phys*. 187, 229–260. doi: 10.1023/A:1005166902804

Heyvaerts, J., and Priest, E. R. (1983). Coronal heating by phase-mixed shear Alfven waves. *Astron. Astrophys*. 117, 220–234.

Hillier, A., and Arregui, I. (2019). Coronal cooling as a result of mixing by the nonlinear Kelvin-Helmholtz instability. *Astrophys. J*. 885:101. doi: 10.3847/1538-4357/ab4795

Hood, A. W., Ruderman, M., Pascoe, D. J., De Moortel, I., Terradas, J., and Wright, A. N. (2013). Damping of kink waves by mode coupling. I. Analytical treatment. *Astron. Astrophys*. 551:A39. doi: 10.1051/0004-6361/201220617

Ireland, J., and De Moortel, I. (2002). Application of wavelet analysis to transversal coronal loop oscillations. *Astron. Astrophys*. 391, 339–351. doi: 10.1051/0004-6361:20020643

Karampelas, K., and Doorsselaere, T. V. (2020). Generating transverse loop oscillations through a steady-flow driver. *Astrophys. J*. 897:L35. doi: 10.3847/2041-8213/ab9f38

Karampelas, K., and Van Doorsselaere, T. (2018). Simulations of fully deformed oscillating flux tubes. *Astron. Astrophys*. 610:L9. doi: 10.1051/0004-6361/201731646

Karampelas, K., Van Doorsselaere, T., Pascoe, D. J., Guo, M., and Antolin, P. (2019). Amplitudes and energy fluxes of simulated decayless kink oscillations. *Front. Astron. Space Sci.* 6:38. doi: 10.3389/fspas.2019.00038

Lemen, J. R., Title, A. M., Akin, D. J., Boerner, P. F., Chou, C., Drake, J. F., et al. (2012). The atmospheric imaging assembly (AIA) on the solar dynamics observatory (SDO). *Solar Phys*. 275, 17–40. doi: 10.1007/978-1-4614-3673-7_3

Magyar, N., and Van Doorsselaere, T. (2016a). Damping of nonlinear standing kink oscillations: a numerical study. *Astron. Astrophys*. 595:A81. doi: 10.1051/0004-6361/201629010

Magyar, N., and Van Doorsselaere, T. (2016b). The instability and non-existence of multi-stranded loops when driven by transverse waves. *Astrophys. J*. 823:82. doi: 10.3847/0004-637X/823/2/82

Magyar, N., Van Doorsselaere, T., and Marcu, A. (2015). Numerical simulations of transverse oscillations in radiatively cooling coronal loops. *Astron. Astrophys*. 582:A117. doi: 10.1051/0004-6361/201526287

McEwan, M. P., Donnelly, G. R., Díaz, A. J., and Roberts, B. (2006). On the period ratio $P_1/2P_2$ in the oscillations of coronal loops. *Astron. Astrophys*. 460, 893–899. doi: 10.1051/0004-6361:20065313

Morton, R. J., and Mooroogen, K. (2016). Model fitting of kink waves in the solar atmosphere: Gaussian damping and time-dependence. *Astron. Astrophys*. 593:A59. doi: 10.1051/0004-6361/201628613

Nakariakov, V. M., Anfinogentov, S. A., Nisticò, G., and Lee, D.-H. (2016). Undamped transverse oscillations of coronal loops as a self-oscillatory process. *Astron. Astrophys*. 591:L5. doi: 10.1051/0004-6361/201628850

Nakariakov, V. M., Ofman, L., Deluca, E. E., Roberts, B., and Davila, J. M. (1999). TRACE observation of damped coronal loop oscillations: implications for coronal heating. *Science* 285, 862–864. doi: 10.1126/science.285.5429.862

Nechaeva, A., Zimovets, I. V., Nakariakov, V. M., and Goddard, C. R. (2019). Catalog of decaying kink oscillations of coronal loops in the 24th solar cycle. *Astrophys. J. Suppl. Ser*. 241:31. doi: 10.3847/1538-4365/ab0e86

Nisticò, G., Nakariakov, V. M., and Verwichte, E. (2013). Decaying and decayless transverse oscillations of a coronal loop. *Astron. Astrophys*. 552:A57. doi: 10.1051/0004-6361/201220676

Ofman, L., Davila, J. M., and Steinolfson, R. S. (1994). Nonlinear studies of coronal heating by the resonant absorption of Alfvén waves. *Geophys. Res. Lett*. 21, 2259–2262. doi: 10.1029/94GL01416

Pagano, P., and De Moortel, I. (2017). Contribution of mode-coupling and phase-mixing of Alfvén waves to coronal heating. *Astron. Astrophys*. 601:A107. doi: 10.1051/0004-6361/201630059

Pagano, P., Pascoe, D. J., and De Moortel, I. (2018). Contribution of phase-mixing of Alfvén waves to coronal heating in multi-harmonic loop oscillations. *Astron. Astrophys*. 616:A125. doi: 10.1051/0004-6361/201732251

Pant, V., Magyar, N., Van Doorsselaere, T., and Morton, R. J. (2019). Investigating "dark" energy in the solar corona using forward modeling of MHD waves. *Astrophys. J*. 881:95. doi: 10.3847/1538-4357/ab2da3

Pascoe, D. J., Anfinogentov, S., Nisticò, G., Goddard, C. R., and Nakariakov, V. M. (2017a). Coronal loop seismology using damping of standing kink oscillations by mode coupling. II. additional physical effects and Bayesian analysis. *Astron. Astrophys*. 600:A78. doi: 10.1051/0004-6361/201629702

Pascoe, D. J., Anfinogentov, S. A., Goddard, C. R., and Nakariakov, V. M. (2018). Spatiotemporal analysis of coronal loops using seismology of damped kink oscillations and forward modeling of EUV intensity profiles. *Astrophys. J*. 860:31. doi: 10.3847/1538-4357/aac2bc

Pascoe, D. J., Goddard, C. R., Anfinogentov, S., and Nakariakov, V. M. (2017b). Coronal loop density profile estimated by forward modelling of EUV intensity. *Astron. Astrophys*. 600:L7. doi: 10.1051/0004-6361/201730458

Pascoe, D. J., Goddard, C. R., and Nakariakov, V. M. (2016a). Spatially resolved observation of the fundamental and second harmonic standing kink modes using SDO/AIA. *Astron. Astrophys*. 593:A53. doi: 10.1051/0004-6361/201628784

Pascoe, D. J., Goddard, C. R., Nisticò, G., Anfinogentov, S., and Nakariakov, V. M. (2016b). Coronal loop seismology using damping of standing kink oscillations by mode coupling. *Astron. Astrophys*. 589:A136. doi: 10.1051/0004-6361/201628255

Pascoe, D. J., Goddard, C. R., Nisticò, G., Anfinogentov, S., and Nakariakov, V. M. (2016c). Damping profile of standing kink oscillations observed by SDO/AIA. *Astron. Astrophys*. 585:L6. doi: 10.1051/0004-6361/201527835

Pascoe, D. J., Hood, A. W., de Moortel, I., and Wright, A. N. (2012). Spatial damping of propagating kink waves due to mode coupling. *Astron. Astrophys*. 539:A37. doi: 10.1051/0004-6361/201117979

Pascoe, D. J., Hood, A. W., De Moortel, I., and Wright, A. N. (2013). Damping of kink waves by mode coupling. II. Parametric study and seismology. *Astron. Astrophys*. 551:A40. doi: 10.1051/0004-6361/201220620

Pascoe, D. J., Hood, A. W., and Van Doorsselaere, T. (2019a). Coronal loop seismology using standing kink oscillations with a lookup table. *Front. Astron. Space Sci*. 6:22. doi: 10.3389/fspas.2019.00022

Pascoe, D. J., and Nakariakov, V. M. (2016). Standing sausage modes in curved coronal slabs. *Astron. Astrophys*. 593:A52. doi: 10.1051/0004-6361/201526546

Pascoe, D. J., Nakariakov, V. M., and Arber, T. D. (2007). Sausage oscillations in multishell coronal structures. *Solar Phys*. 246, 165–175. doi: 10.1007/s11207-007-9055-x

Pascoe, D. J., Nakariakov, V. M., Arber, T. D., and Murawski, K. (2009). Sausage oscillations in loops with a non-uniform cross-section. *Astron. Astrophys*. 494, 1119–1125. doi: 10.1051/0004-6361:200810541

Pascoe, D. J., Russell, A. J. B., Anfinogentov, S. A., Simões, P. J. A., Goddard, C. R., Nakariakov, V. M., et al. (2017c). Seismology of contracting and expanding coronal loops using damping of kink oscillations by mode coupling. *Astron. Astrophys*. 607:A8. doi: 10.1051/0004-6361/201730915

Pascoe, D. J., Smyrli, A., and Van Doorsselaere, T. (2019b). Coronal density and temperature profiles calculated by forward modeling EUV emission observed by SDO/AIA. *Astrophys. J*. 884:43. doi: 10.3847/1538-4357/ab3e39

Pascoe, D. J., Smyrli, A., and Van Doorsselaere, T. (2020). Tracking and seismological analysis of multiple coronal loops in an active region. *Astrophys. J*. 898:126. doi: 10.3847/1538-4357/aba0a6

Pascoe, D. J., Wright, A. N., and De Moortel, I. (2010). Coupled Alfvén and Kink oscillations in coronal loops. *Astrophys. J*. 711, 990–996. doi: 10.1088/0004-637X/711/2/990

Pascoe, D. J., Wright, A. N., and De Moortel, I. (2011). Propagating coupled Alfvén and Kink oscillations in an arbitrary inhomogeneous corona. *Astrophys. J*., 731:73. doi: 10.1088/0004-637X/731/1/73

Pascoe, D. J., Wright, A. N., De Moortel, I., and Hood, A. W. (2015). Excitation and damping of broadband kink waves in the solar corona. *Astron. Astrophys*. 578:A99. doi: 10.1051/0004-6361/201321328

Ruderman, M. S., and Roberts, B. (2002). The damping of coronal loop oscillations. *Astrophys. J*. 577, 475–486. doi: 10.1086/342130

Ruderman, M. S., Shukhobodskaya, D., and Shukhobodskiy, A. A. (2019). Resonant damping of propagating kink waves in non-stationary, longitudinally stratified, and expanding solar waveguides. *Front. Astron. Space Sci*. 6:10. doi: 10.3389/fspas.2019.00010

Ruderman, M. S., and Terradas, J. (2013). Damping of coronal loop kink oscillations due to mode conversion. *Astron. Astrophys*. 555:A27. doi: 10.1051/0004-6361/201220195

Safari, H., Nasiri, S., and Sobouti, Y. (2007). Fast kink modes of longitudinally stratified coronal loops. *Astron. Astrophys*. 470, 1111–1116. doi: 10.1051/0004-6361:20065997

Scullion, E., Rouppe van der Voort, L., Wedemeyer, S., and Antolin, P. (2014). Unresolved fine-scale structure in solar coronal loop-tops. *Astrophys. J*. 797:36. doi: 10.1088/0004-637X/797/1/36

Soler, R., Goossens, M., Terradas, J., and Oliver, R. (2013). The behavior of transverse waves in nonuniform solar flux tubes. I. Comparison of ideal and resistive results. *Astrophys. J*. 777:158. doi: 10.1088/0004-637X/777/2/158

Soler, R., Goossens, M., Terradas, J., and Oliver, R. (2014). The behavior of transverse waves in nonuniform solar flux tubes. II. Implications for coronal loop seismology. *Astrophys. J*. 781:111. doi: 10.1088/0004-637X/781/2/111

Soler, R., Terradas, J., Oliver, R., Ballester, J. L., and Goossens, M. (2010). Kelvin-Helmholtz instability in coronal magnetic flux tubes due to azimuthal shear flows. *Astrophys. J*. 712, 875–882. doi: 10.1088/0004-637X/712/2/875

Terradas, J., Andries, J., Goossens, M., Arregui, I., Oliver, R., and Ballester, J. L. (2008a). Nonlinear instability of kink oscillations due to shear motions. *Astrophys. J. Lett*. 687:L115. doi: 10.1086/593203

Terradas, J., Arregui, I., Oliver, R., Ballester, J. L., Andries, J., and Goossens, M. (2008b). Resonant absorption in complicated plasma configurations:

applications to multistranded coronal loop oscillations. *Astrophys. J.* 679, 1611–1620. doi: 10.1086/586733

Terradas, J., Magyar, N., and Van Doorsselaere, T. (2018). Effect of magnetic twist on nonlinear transverse Kink oscillations of line-tied magnetic flux tubes. *Astrophys. J.* 853:35. doi: 10.3847/1538-4357/aa9d0f

Tomczyk, S., and McIntosh, S. W. (2009). Time-distance seismology of the solar corona with CoMP. *Astrophys. J.* 697, 1384–1391. doi: 10.1088/0004-637X/697/2/1384

Tomczyk, S., McIntosh, S. W., Keil, S. L., Judge, P. G., Schad, T., Seeley, D. H., et al. (2007). Alfvén waves in the solar corona. *Science* 317:1192. doi: 10.1126/science.1143304

Torrence C., and Compo G. P. (1998). A Practical Guide to Wavelet Analysis. *Bull. Am. Meteorol. Soc.* 79, 61–78.

Van Doorsselaere, T., Andries, J., Poedts, S., and Goossens, M. (2004). Damping of coronal loop oscillations: calculation of resonantly damped Kink oscillations of one-dimensional nonuniform loops. *Astrophys. J.* 606, 1223–1232. doi: 10.1086/383191

Van Doorsselaere, T., Antolin, P., and Karampelas, K. (2018). Broadening of the differential emission measure by multi-shelled and turbulent loops. *Astron. Astrophys.* 620:A65. doi: 10.1051/0004-6361/201834086

Van Doorsselaere, T., Antolin, P., Yuan, D., Reznikova, V., and Magyar, N. (2016). Forward modelling of optically thin coronal plasma with the FoMo tool. *Front. Astron. Space Sci.* 3:4. doi: 10.3389/fspas.2016.00004

Van Doorsselaere, T., Li, B., Goossens, M., Hnat, B., and Magyar, N. (2020). Wave pressure and energy cascade rate of kink waves computed with Elsässer variables. *Astrophys. J.* 899:100. doi: 10.3847/1538-4357/aba0b8

Van Doorsselaere, T., Nakariakov, V. M., and Verwichte, E. (2007). Coronal loop seismology using multiple transverse loop oscillation harmonics. *Astron. Astrophys.* 473, 959–966. doi: 10.1051/0004-6361:20077783

Verth, G., and Erdélyi, R. (2008). Effect of longitudinal magnetic and density inhomogeneity on transversal coronal loop oscillations. *Astron. Astrophys.* 486, 1015–1022. doi: 10.1051/0004-6361:200809626

Verth, G., Terradas, J., and Goossens, M. (2010). Observational evidence of resonantly damped propagating Kink waves in the solar corona. *Astrophys. J. Lett.* 718:L102–L105. doi: 10.1088/2041-8205/718/2/L102

Verwichte, E., Nakariakov, V. M., Ofman, L., and Deluca, E. E. (2004). Characteristics of transverse oscillations in a coronal loop arcade. *Solar Phys.* 223, 77–94. doi: 10.1007/s11207-004-0807-6

Wang, T., Ofman, L., Davila, J. M., and Su, Y. (2012). Growing transverse oscillations of a multistranded loop observed by SDO/AIA. *Astrophys. J. Lett.* 751:L27. doi: 10.1088/2041-8205/751/2/L27

White, R. S., Verwichte, E., and Foullon, C. (2013). Anti-phase signature of flare generated transverse loop oscillations. *Astrophys. J.* 774:104. doi: 10.1088/0004-637X/774/2/104

Williams, T., Walsh, R. W., Winebarger, A. R., Brooks, D. H., Cirtain, J. W., De Pontieu, B., et al. (2020). Is the high-resolution coronal imager resolving coronal strands? Results from AR 12712. *Astrophys. J.* 892:134. doi: 10.3847/1538-4357/ab6dcf

Conflict of Interest: The authors declare that the research was conducted in the absence of any commercial or financial relationships that could be construed as a potential conflict of interest.

frontiers
in Astronomy and Space Sciences

ORIGINAL RESEARCH
published: 08 October 2020
doi: 10.3389/fspas.2020.571286

Domain of Influence Analysis: Implications for Data Assimilation in Space Weather Forecasting

Dimitrios Millas[1,2]*, *Maria Elena Innocenti*[1]*, *Brecht Laperre*[1], *Joachim Raeder*[3], *Stefaan Poedts*[1,4] *and Giovanni Lapenta*[1]

[1] Department of Mathematics, Centre for Mathematical Plasma Astrophysics, KU Leuven, Leuven, Belgium, [2] Department of Physics and Astronomy, University College London, London, United Kingdom, [3] Institute for the Study of Earth, Oceans and Space, University of New Hampshire, Durham, NH, United States, [4] Institute of Physics, University of Maria Curie-Skłodowska, Lublin, Poland

OPEN ACCESS

Edited by:
Xueshang Feng,
National Space Science Center (CAS), China

Reviewed by:
Grant David Meadors,
Los Alamos National Laboratory (DOE), United States
Matthew Lang,
University of Reading, United Kingdom
Siegfried Gonzi,
Met Office, United Kingdom

***Correspondence:**
Dimitrios Millas
dimitrios.millas@ucl.ac.uk
Maria Elena Innocenti
mariaelena.innocenti@kuleuven.be

Specialty section:
This article was submitted to Stellar and Solar Physics, a section of the journal Frontiers in Astronomy and Space Sciences

Received: *10 June 2020*
Accepted: *28 August 2020*
Published: *08 October 2020*

Citation:
Millas D, Innocenti ME, Laperre B, Raeder J, Poedts S and Lapenta G (2020) Domain of Influence Analysis: Implications for Data Assimilation in Space Weather Forecasting. Front. Astron. Space Sci. 7:571286. doi: 10.3389/fspas.2020.571286

Solar activity, ranging from the background solar wind to energetic coronal mass ejections (CMEs), is the main driver of the conditions in the interplanetary space and in the terrestrial space environment, known as space weather. A better understanding of the Sun-Earth connection carries enormous potential to mitigate negative space weather effects with economic and social benefits. Effective space weather forecasting relies on data and models. In this paper, we discuss some of the most used space weather models, and propose suitable locations for data gathering with space weather purposes. We report on the application of *Representer analysis (RA)* and *Domain of Influence (DOI) analysis* to three models simulating different stages of the Sun-Earth connection: the OpenGGCM and Tsyganenko models, focusing on solar wind—magnetosphere interaction, and the PLUTO model, used to simulate CME propagation in interplanetary space. Our analysis is promising for space weather purposes for several reasons. First, we obtain quantitative information about the most useful locations of observation points, such as solar wind monitors. For example, we find that the absolute values of the DOI are extremely low in the magnetospheric plasma sheet. Since knowledge of that particular sub-system is crucial for space weather, enhanced monitoring of the region would be most beneficial. Second, we are able to better characterize the models. Although the current analysis focuses on spatial rather than temporal correlations, we find that time-independent models are less useful for Data Assimilation activities than time-dependent models. Third, we take the first steps toward the ambitious goal of identifying the most relevant heliospheric parameters for modeling CME propagation in the heliosphere, their arrival time, and their geoeffectiveness at Earth.

Keywords: solar wind, coronal mass ejections (CMEs), magnetohydrodynamics (MHD), numerical simulations, statistical tools, domain of influence, observations

1. INTRODUCTION

Solar activity affects the terrestrial environment with a constantly present but highly variable solar wind and with higher energy, transient events, such as flares and Coronal Mass Ejections (CMEs).

"Space weather" (Bothmer and Daglis, 2007) is the discipline that focuses on the impact of these solar drives on the solar system and in particular on the Earth and its near space environment.

Space weather events can have serious effects on the health of astronauts and on technology, with potentially large economic costs (Eastwood et al., 2017). The importance of space weather forecasting has grown with societal dependence on advanced space technology, on communication and on the electrical grid. For example, the Halloween 2003 solar storms that impacted Earth between 19th of October 2003 and 7th of November 2003 caused an hour long power outage in Sweden (Pulkkinen et al., 2005), forced airline flight reroutes, and affected communication and satellite systems (Plunkett, 2005). The "great geomagnetic storm" of March 13–14, 1989 caused, among other disruptions, a blackout of up to 9 h in most of Quebec Province, due to a massive failure experienced by the power grid Hydro-Quebec Power Company (Allen et al., 1989).

In order to improve space weather forecasting, accurate models of the Sun-Earth connection are needed. Such forecasts are challenging because of the complexity of the processes involved and the large range of spatial and temporal scales. Commonly the heliosphere is divided into sub-systems, where each one is simulated with a different model, such that the models feed into each other (Luhmann et al., 2004; Tóth et al., 2005). These models can be either physics-based or empirical. Empirical models (such as, in the solar domain, Altschuler and Newkirk, 1969; Schatten et al., 1969; Schatten, 1971; Wang and Sheeley Jr, 1992; Nikolić, 2019) usually require less computational resources, enabling faster forecasts. They can also serve as a baseline for physics-based models (Siscoe et al., 2004). However, empirical models lack the sophistication of more expensive first-principles based numerical models. Recently, machine learning methods have emerged, that can provide a new approach to space weather forecasting (Camporeale, 2019; Laperre et al., 2020). Most of these methods, while promising, must still undergo extensive validation.

The technique of Data Assimilation (DA) was developed to improve model predictions by properly initializing models from data and by keeping a model on track during its time evolution (Kalnay, 2003; Bouttier and Courtier, 1999; Evensen, 2009). DA methods were originally applied to atmosphere and ocean models, which exhibit a large degree of inertia. The latter is also true for the solar wind, but not for the magnetosphere-ionosphere system, which is strongly driven and dissipative. Therefore, in space weather forecasting, DA aims not only at initializing the models, but also at using information from various observations to bring the evolution of a system as predicted from a model closer to the real system evolution (Kalman, 1960; Bouttier and Courtier, 1999; Bishop and Welch, 2001; Evensen, 2009; Le Dimet and Talagrand, 1986; Innocenti et al., 2011), making up for model deficiencies in the terms of resolution and incomplete physical description.

The quantity and quality of available data is a critical factor in the effectiveness of Data Assimilation. This is the reason why fields where data can be obtained more easily and continuously have shown early successes in DA implementations. Examples of these fields are meteorology and oceanography, and, in space sciences, ionospheric and radiation belt physics (Bennett, 1992; Ghil and Malanotte-Rizzoli, 1991; Egbert and Bennett, 1996; Kalnay, 2003; Rigler et al., 2004; Schunk et al., 2004; Kondrashov et al., 2007). Examples of DA applications targeting specifically the interplanetary space environments are Schrijver and DeRosa (2003), Mendoza et al. (2006), Arge et al. (2010), Innocenti et al. (2011), Skandrani et al. (2014), Lang and Owens (2019), and Lang et al. (2020).

Representer analysis (RA) and Domain of Influence analysis (DOI) (Bennett, 1992; Egbert and Bennett, 1996; Echevin et al., 2000; Evensen, 2009; Skandrani et al., 2014), briefly summarized in section 2, are powerful statistical tools used to estimate the effectiveness of DA techniques when applied to a specific model, without assimilating actual data. Such analysis can be used in several ways. It allows us to optimize assimilation strategies, it may uncover model biases that can then be addressed by further model development, and it may be used to optimize the observation systems that provide operational data for DA. For example, RA/DOI can be used to optimize locations for solar wind monitors, such as locations proposed near the L5 Lagrangian point (Vourlidas, 2015; Lavraud et al., 2016; Pevtsov et al., 2020).

In the present paper, the RA and DOI analysis is applied to three models: the OpenGGCM magnetosphere—ionosphere model (section 3.1), two of the empirical Tsyganenko magnetosphere magnetic field models (section 3.2), and a solar wind simulation based on the PLUTO code (section 3.3). These models simulate critical sub-systems in the Sun-Earth connection with a focus on the terrestrial magnetosphere and Coronal Mass Ejection propagation.

The present paper provides insights into the locations of the terrestrial magnetosphere that should be prioritized (ideally, in absence of orbital constraints) for space weather forecasting and monitoring activity. We compare a time-dependent, physics based model (e.g., OpenGGCM) and time-independent, empirical (e.g., Tsyganenko) models in terms of the expected benefits that DA can provide. We conclude that time-dependent models should be preferentially chosen for DA. We take the first steps toward the goal if understanding the main physical parameters, close to the Sun and in interplanetary space, that control CME propagation and hence their arrival time at Earth.

This manuscript is organized as follows: in section 2 we introduce the theoretical background on RA and the DOI; section 3 discusses the application of the method to the different models; in section 4 we summarize the results and discuss potential improvements and new applications.

2. REPRESENTER ANALYSIS AND DOMAIN OF INFLUENCE ANALYSIS

This section introduces the mathematical basis of RA and DOI analysis. The reader is referred to Skandrani et al. (2014) and references therein for an in depth derivation.

Let us start from a system described by the state variable vector $\mathbf{x}_t \in \mathbb{R}^n . \mathbf{x}_t$ is a vector containing the n state variables that describe the system at a time t. Let us assume that the evolution of the system can be described as a discrete-time process controlled by an evolution law $\mathbf{A}$. The state of the system then evolves as follows: $\mathbf{x}_t = \mathbf{A}(\mathbf{x}_{t-1}) + \mathbf{w}_{t-1}$, where $\mathbf{w} \in \mathbb{R}^n$ is process noise. The process noise is assumed to be Gaussian and with covariance matrix Q.

If a model $\mathbf{M}$ (for example, a simulation model) of the evolution law $\mathbf{A}$ is available, we can obtain, following Kalman (1960) and Evensen (2009), a prior estimate $\hat{\mathbf{x}}_t^-$ of the state variable $\mathbf{x}_t$ through the simulation model as

$$\hat{\mathbf{x}}_t^- = \mathbf{M}(\hat{\mathbf{x}}_{t-1}^-) + \mathbf{w}_{t-1}. \tag{1}$$

Assume now that we have m observational values or measurements $\mathbf{z}_t \in \mathbb{R}^m$. These measurements can be mapped to the current state $\mathbf{x_t}$ through the so-called observation operator $\mathbf{H} \in \mathbb{R}^{m \times n}$, such that $\mathbf{z}_t = \mathbf{H}\mathbf{x}_t + \nu_t$. Here, ν is the (assumed Gaussian) measurement noise, with a covariance matrix $\mathbf{R}$.

It can be then shown (Bishop and Welch, 2001) that a posterior estimate of the state ($\hat{\mathbf{x}}_t$) can be obtained from the prior estimate of the state ($\hat{\mathbf{x}}_t^-$), obtained from Equation (1), as follows:

$$\hat{\mathbf{x}}_t = \hat{\mathbf{x}}_t^- + \mathbf{K}_t \left(\mathbf{z}_t - \mathbf{H}\hat{\mathbf{x}}_t^-\right). \tag{2}$$

Here, the term $\left(\mathbf{z}_t - \mathbf{H}\hat{\mathbf{x}}_t^-\right)$ is called the "innovation," and represents the difference between the measurements and their expected values, calculated by applying the observation operator to the prior state estimate. The Kalman gain $\mathbf{K}_t$ is obtained by minimizing the posterior error covariance matrix. This is the "correction" step of the Kalman filter, where the Kalman gain is calculated and the estimate and error covariance matrix of the posterior state are updated. The "prediction" (forecast) phase of the filter results in the calculation of the prior state estimate and prior error covariance matrix (used to compute the Kalman gain).

The prior and posterior error covariance matrices are respectively defined as

$$\mathbf{P}_t^- = \mathbb{E}\left[\left(\mathbf{x}_t - \hat{\mathbf{x}}_t^-\right)\left(\mathbf{x}_t - \hat{\mathbf{x}}_t^-\right)^T\right], \quad \mathbf{P}_t = \mathbb{E}\left[\left(\mathbf{x}_t - \hat{\mathbf{x}}_t\right)\left(\mathbf{x}_t - \hat{\mathbf{x}}_t\right)^T\right], \tag{3}$$

where $\mathbb{E}$ is the expected value, $\mathbf{x}_t$ is the "real," unknown system state and $\epsilon^- = \left(\hat{\mathbf{x}}_t^- - \mathbf{x}_t\right)$ and $\epsilon = \left(\hat{\mathbf{x}}_t - \mathbf{x}_t\right)$ are the prior and posterior errors, calculated as the difference between the prior ($\hat{\mathbf{x}}_t^-$)/posterior ($\hat{\mathbf{x}}_t$) state and the real state, $\mathbf{x}_t$. Notice that, although these are the definitions of the error covariances, this is not how they are computed in the filter, since the real state is not known.

The formula for the calculation of the posterior state, Equation (2), can be written as

$$\hat{\mathbf{x}}_t = \hat{\mathbf{x}}_t^- + \mathbf{r}\mathbf{b} \tag{4}$$

where $\mathbf{r} \in \mathbb{R}^{n \times m}$ and $\mathbf{b} \in \mathbb{R}^m$ are defined as

$$\mathbf{r} = \mathbf{P}^- \mathbf{H}^T, \qquad \mathbf{b} = \left(\mathbf{H}\mathbf{P}^-\mathbf{H}^T + \mathbf{R}\right)^{-1}\left(\mathbf{z} - \mathbf{H}\hat{\mathbf{x}}^-\right), \tag{5}$$

with $\mathbf{R}$ the measurement noise covariance matrix. The time index t has been dropped for ease of reading.

We will from now on assume that the system (and in particular, the observation operator $\mathbf{H}$) is linear. Then, each column of the matrix $\mathbf{r}$, denoted as $\mathbf{r}_j$ with $j = 1, \ldots, m$, is the representer associated to a given observation z_j (remember that $\mathbf{z}$ is the vector with m observations), and gives a measure of the impact of that observation in "correcting" the prior state estimate. If we further assume that each observation j is located at grid point k_j, and is associated to a state variable, then each column $\mathbf{r}_j$ (now $\mathbf{r}_{k_j}$, given the assumption mentioned above) contains the covariances ("cov") between the prior errors at the observation point k_j and at every other grid node, for all the state variables.

Since the real state is not available for error covariance calculations, an ensemble of simulations can be used to estimate the prior errors instead. An ensemble (Evensen, 2009) can be generated by perturbing one or several of the sources of model errors. In this work, ensembles are generated for each model by perturbing the respective initial/boundary conditions. Once the ensemble is available, the covariances of the prior errors at a certain simulated time can be approximated as the ensemble covariances ("cov^{ens}") of the prior errors. These in turn become the ensemble covariances of the simulated state variables, if one assumes that the prior errors are unbiased. The ensemble covariance between the state variable x and y is defined as

$$\mathrm{cov}^{ens}(x, y) = \frac{1}{N}\sum_{s=1}^{N}\left[\left(x_s^- - \frac{1}{N}\sum^{N} x_s^-\right)\left(y_s^- - \frac{1}{N}\sum_{s=1}^{N} y_s^-\right)\right] \tag{6}$$

where N is the number of members in the ensemble, and x and y represent two state variables (notice that, for ease of reading, we indicate here two state variables as x and y, while earlier we indicated as vector $\mathbf{x}$ all the state variables).

In a set of simulations, the prior state variables are the simulation results at a specific time. Being able to calculate the representers associated to observations from the ensemble rather than from assimilating observations simplifies the RA significantly.

Following the discussion of the representer term $\mathbf{r}$ in the calculation of the posterior state, Equations (4) and (5), we now examine the term $\mathbf{b}$. Assuming that the only observation point for observation j is at grid node k_j (i.e., the row j of the matrix $\mathbf{H}$ has only the term k_j different from zero), the element of $\mathbf{b}$ associated to the observation at grid point k_j, denoted as b_{k_j}, becomes, from Equation (5):

$$b_{k_j} = \frac{z_{k_j} - \hat{x}_{k_j}^-}{cov\left(\epsilon_{k_j}^-, \epsilon_{k_j}^-\right) + cov\left(\epsilon_{k_j}^z, \epsilon_{k_j}^z\right)}, \tag{7}$$

where we have made use of the simplified form of the matrix **H** and where $\epsilon^z_{k_j}$ is the observation error associated with the observation z_{k_j}.

If x_i is one of the state variables at grid node i, the correction to x_i brought by the assimilation of the measure z_{k_j}, following Equations (4), (5), (7) and some straightforward manipulation based on the definitions of covariance, variance, correlation, can be written as (Skandrani et al., 2014)

$$\hat{x}_i - \hat{x}_i^- = \mathrm{corr}^{ens}\left(\hat{x}_{k_j}^-, \hat{x}_i^-\right) F\left(z_{k_j}\right). \tag{8}$$

Here, $F(z_{k_j})$ is the modulation factor and $\mathrm{corr}^{ens}\left(\hat{x}_{k_j}^-, \hat{x}_i^-\right)$ the correlation. The correlation is computed from the ensemble, and is calculated between the state variable at node k_j and at node i. This correlation reflects how a change at node k_j, caused, e.g., by the assimilation of the measurement z_{k_j}, will influence the node i, and is what we call the DOI. The correlation over the ensemble is defined, using the dummy variables x and y for brevity, as:

$$\mathrm{corr}^{ens}(x, y) = \frac{\mathrm{cov}^{ens}\left(x, y\right)}{\sqrt{\mathrm{var}\left(x\right)\mathrm{var}\left(y\right)}}. \tag{9}$$

The modulation factor $F(z_{k_j})$ in Equation (8) depends, among other things, on the measurement z_{k_j} and on the error associated to the measure z_{k_j}. Hence Data Assimilation has to be performed to calculate this term. The $\mathrm{corr}^{ens}\left(\hat{x}_{k_j}^-, \hat{x}_i^-\right)$ term reflects how large we can expect the area that will be affected by the assimilation of z_{k_j} to be. But to know how large the difference between the posterior and prior state, $\hat{x}_i - \hat{x}_i^-$, will be, we need to know the modulation factor as well.

So now the DOI of the measurement z_{k_j} on the state variable at grid point i, x_i, can be defined as

$$DOI(z_{k_j}, x_i) = \mathrm{corr}^{ens}\left(\hat{x}_{k_j}^-, \hat{x}_i^-\right). \tag{10}$$

One can see from its definition that the DOI can be calculated *before assimilation* by computing the ensemble correlation of the state variable value at the grid point k_j with that at grid point i. Dropping the i index, i.e., examining the expected impact of measurement z_{k_j} on all the state variables $\mathbf{x}$ at all grid points, we obtain the more general definition of the DOI as

$$DOI(z_{k_j}) = \mathrm{corr}^{ens}\left(\hat{x}_{k_j}^-, \hat{\mathbf{x}}^-\right). \tag{11}$$

We can then draw "DOI maps" that show the correlation between a field at grid point k_j, the "observation point," and the other grid points.

Notice that in this derivation we have assumed, for simplicity, that the measurement z and the state variable x refer to the same field, for example, the x component of the magnetic field, or of the velocity. This simplifies the formulation of the numerator of Equation (7) and improves the readability of the derivation. Skandrani et al. (2014) shows examples where the DOI is calculated between different fields, e.g., magnetic field and velocity.

DOI analysis has the advantage that it can be calculated for all state variables and at any grid point without actual assimilation, i.e., without the need for measurements **z**. In order to compute the DOI at a time step t, we only require evolving the ensemble up to said time step t, and then performing the correlation over the ensemble between the state variable value at the observation point k_j and at all other grid points.

Because DOI values are derived from a correlation they are bounded between −1 and 1. $|DOI| \sim 1$ indicates that the field at that specific point significantly changes when the same field (or a different field, in the case of cross-correlation) varies at the observation point. $|DOI| \sim 0$ indicates the opposite, i.e., variation at the observation point have little or no effect. Thus, DOI analysis also provides information on how information propagates within the model, and therefore sheds light on the physical processes within the model. We will exploit this property in section 3.2.

We note that in this study we only focus on spatial correlations, neglecting temporal correlations. In other words, the following analysis (i.e., the calculation of variances, DOI, etc.) is restricted to specific instances in time, rather than examining correlations between fields at difference times as well. The dependence on time will be addressed in a future project.

The RA is applied to "artificial" data, obtained from ensembles of simulations focused on different processes of interest in the Sun-Earth connection: the interaction of the solar wind with the terrestrial magnetosphere (via OpenGGCM and Tsyganenko simulations) and the propagation of a CME-like event in the steady solar wind (PLUTO).

OpenGGCM and the Tsyganenko Geomagnetic Field Models both simulate the interaction of the solar wind with the magnetospheric system. OpenGGCM is a physics-based magnetohydrodynamic (MHD) model, while the Tsyganenko models are semi-empirical best-fit representations for the magnetic field, based on a large number of satellite observations (Tsyganenko, 1995, 2002a; Tsyganenko and Sitnov, 2005).

PLUTO is an MHD-modeling software used to simulate the propagation of a CME in the background solar wind. This software can be used to numerically solve the partial differential equations encountered in plasma physics problems, in conservative form, in different regimes (from hydrodynamics to relativistic MHD). The structure of the software is explained in Mignone et al. (2007, 2012). Full documentation and references can be found in the relevant web page: http://plutocode.ph.unito.it/.

Because the DOI analysis is an ensemble based technique the size of the ensemble and its properties matter. In order to test for sufficient size, we performed the DOI calculation using a limited, random subset of the ensemble, which we gradually expanded. We found that using at 25 runs were sufficient to obtain a consistent ensemble mean, variance, and DOI. We note, however, that this may change for different choices of simulation resolution and parameters used for the generation of the ensemble.

3. APPLICATIONS

3.1. Magnetospheric Applications I: OpenGGCM

The OpenGGCM (Open Geospace General Circulation Model) is a MHD based model that simulates the interaction of the solar wind with the magnetosphere-ionosphere-thermosphere system. OpenGGCM is available at the Community Coordinated Modeling Center at NASA/GSFC for model runs on demand (see: http://ccmc.gsfc.nasa.gov). This model has been developed and continually improved over more than two decades. Besides numerically solving the MHD equations with high spatial resolution in a large volume containing the magnetosphere, the model also includes ionospheric processes and their electrodynamic coupling with the magnetosphere.

The mathematical formulation of the software is described in Raeder (2003). The latest version of OpenGGCM, used here, is coupled with the Rice Convection Model (RCM) (Toffoletto et al., 2001), which treats the inner magnetosphere drift physics better than MHD and allows for more realistic simulations that involve the ring current (Cramer et al., 2017). The model is both modular and efficiently parallelized using the message passing interface (MPI). It is written in Fortran and C, and uses extensive Perl scripting for pre-processing. The software runs on virtually any massively parallel supercomputer available today.

OpenGGCM uses a stretched Cartesian grid (Raeder, 2003) that is quite flexible. There is a minimal useful resolution, about $150 \times 100 \times 100$ cells, that yields the main magnetosphere features but does not resolve mesoscale structures, such as FTEs or small plasmoids in the tail plasma sheet. At the other end, we have run simulations with grids as large as $\sim$1,000^3 (on some 20,000 cores). In terms of computational cost that is almost a 10^4 ratio. Here, we used a grid of $325 \times 150 \times 150$ cells which is sufficient for the purposes of this study and runs faster than real time on a modest number of cores.

OpenGGCM has been used for numerous studies of magnetospheric phenomena, such as storms (Raeder et al., 2001b; Raeder and Lu, 2005; Connor et al., 2016), substorms (Raeder et al., 2001a; Ge et al., 2011; Raeder et al., 2010), magnetic reconnection (Dorelli, 2004; Raeder, 2006; Berchem et al., 1995), field-aligned currents (Moretto et al., 2006; Vennerstrom et al., 2005; Raeder et al., 2017; Anderson et al., 2017), and magnetotail processes (Zhu et al., 2009; Zhou et al., 2012; Shi et al., 2014), to name a few.

The boundary conditions require the specification of the three components of the solar wind velocity and magnetic field, the plasma pressure and the plasma number density at 1 AU, which are obtained from ACE observations (Stone et al., 1998) and applied for the entire duration of the simulation at the sunward boundary.

We generate an ensemble of 50 OpenGGCM simulations by perturbing the v_x component of the input solar wind velocity. Changing this particular parameter guarantees a direct and easy way to interpret magnetospheric response.

First, we run a reference simulation using the observed solar wind values at 1 AU starting from May 8th, 2004, 09:00 UTC (denoted as t_0) until 13:00 UTC on May 8th, 2004. We choose this period because it is relatively quiet: no iCME were registered in the Richardson/Cane list of near-Earth interplanetary CMEs (Richardson and Cane, 2010), and as it is common during the declining phase of the solar cycle, geomagnetic activity is driven by Corotating Interaction Regions and High Speed Streams (Tsurutani et al., 2006). The study of outlier events, such as CME arrival at Earth, is left as future work.

To generate the ensemble, the solar wind compression is changed in each of the "perturbed" simulations. The perturbed velocity in the x (Earth-to-Sun) direction is set, for the entire duration of each simulation, to a *constant* value obtained by multiplying the average observed v_x^{avg} by a random number S sampled from a normal distribution with mean $\mu = 1$ and standard deviation $\sigma = 0.1$:

$$v_x = S v_x^{avg}, \text{ with } S \in \mathcal{N}(1, (0.1)^2). \tag{12}$$

The time period we use to calculate the average is the duration of the reference simulation, between 9:00 UTC and 13:00 UTC on May 8th, 2004.

Our choices for the generation of the ensemble are determined by the necessity to preserve both the Gaussian characteristic of the model error and the physical significance of the simulations: the solar wind compression in all ensemble members is not too far from the reference value. With such low standard deviation, the average of the obtained perturbed value plus/minus several sigmas are still within the typical range for the solar wind: the minimum and maximum values of the constant, perturbed input velocities are $|v_x| \sim 363$ km/s and $|v_x| \sim 583$ km/s, respectively. The solar wind velocity v_x is negative in the Geocentric Solar Ecliptic (GSE) coordinates used here. The v_x values that we obtain in this way are not supposed to be representative of the full range of values that v_x can assume; they are used to generate an ensemble of simulations "slightly perturbed" with respect to our reference simulation. We note that the real distribution of solar wind velocity is far from a normal distribution, with two distinct peaks and extreme outliers, and would not be appropriate to produce the required ensemble. We refer the reader to Fortin et al. (2014) for optimal procedures on how to choose the variance of the ensemble.

The ensemble analysis requires running 50 simulations to produce the ensemble members, plus the unperturbed reference simulation. Each run takes $\sim$12 h on 52 cores on the supercomputer Marconi-Broadwell (Cineca, Italy), for a total cost of $\sim$32,000 core hours.

We verify that the prior errors are unbiased (as assumed in the derivation of the method summarized in section 2) by comparing the reference simulation and the average of the ensemble. We note that the ensemble mean is an appropriate metric to use in this case because the perturbed simulations have not been generated in order to represent all possible solar wind velocity values, but small perturbations around the reference case.

Figure 1 shows this comparison in the xz plane for the x component of the velocity and of the magnetic field at a fixed time (172 min after the beginning of the simulation), for both the reference simulation (panels A,B) and the average of the ensemble (panels C,D). The magnetic field lines, depicted in

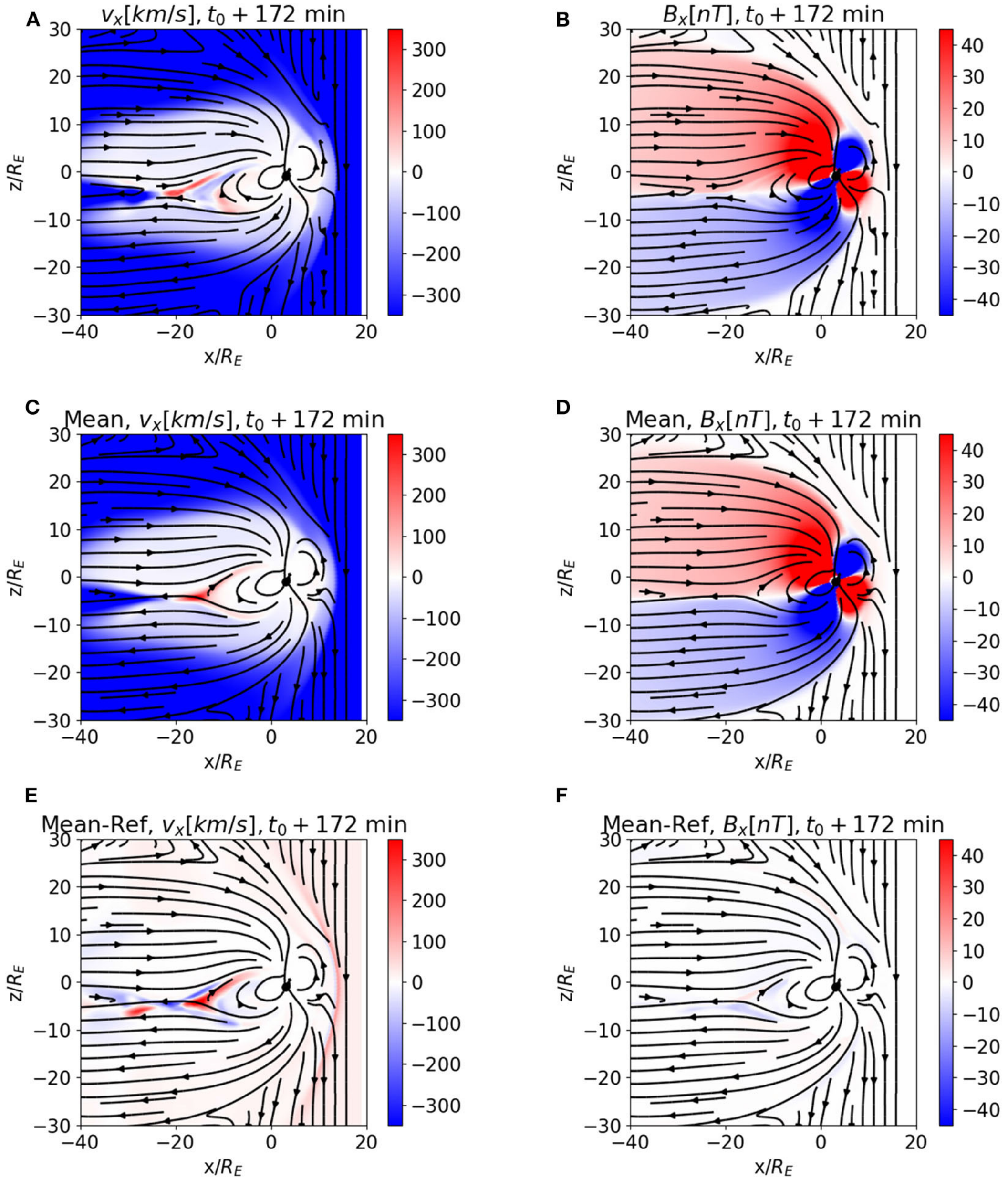

FIGURE 1 | Reference simulation **(A,B)**, ensemble mean **(C,D)**, and difference between the ensemble mean and the reference simulation results **(E,F)** for the ensemble of OpenGGCM magnetospheric simulations. The ensemble is generated by perturbing the v_x solar wind boundary condition. v_x is depicted in **(A,C,E)**, b_x in **(B,D,F)**. The coordinate system is GSE The depicted time is 172 min after the beginning of the simulation, May 8th 2004, 9:00 UTC. The boundary conditions at the sunward boundary of the "reference" simulation are observed solar wind values.

black, are calculated from the reference simulation in panels (A,B) and from the ensemble average in panels (C,D). The distances are normalized by the Earth radius R_E.

Visual inspection of panels (A–D) and of the difference between the ensemble mean and the reference simulation results, depicted in panels (E,F) for v_x and B_x, respectively, highlight the areas where the behavior differs most within the ensemble: the bow shock, the plasma sheet, and the neutral line. The former is a plasma discontinuity that moves back and forth in response to the changing solar wind Mach number, and thus gets smeared out in the ensemble. The latter is a region of marginal stability in the magnetosphere that reacts in a non-linear way to solar wind changes.

In order to determine if 50 ensemble members are sufficient for our analysis, we have compared corresponding plots of the difference between the ensemble mean and the reference simulation for v_x with decreasing number (40, 30, 20) of ensemble members. We find that, with decreasingly smaller

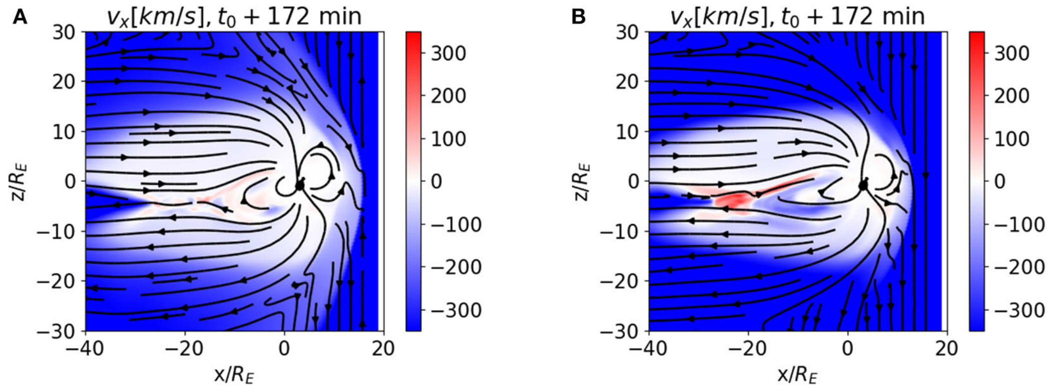

FIGURE 2 | v_x field component, at the same time as **Figure 1**, for the ensemble member with the lowest **(A)** and highest **(B)** absolute value of the perturbed, inflowing v_x velocity component in the OpenGGCM ensemble.

ensembles, the plasma sheet structure seen in **Figure 1E**, is only minimally affected. However, the differences around the bow shock become more pronounced. The velocity difference increases in the solar wind and magnetosheath as well, and the magnetic field structure at the magnetosphere/solar wind interface (as shown by the magnetic field lines, which are drawn for the average field in panels E,F and similar analysis) begin to change significantly with respect to the reference simulation. By comparing the plots with 50, 40, 30, and 20 ensemble members, we conclude that 30 is the minimum number of ensemble members that gives average fields compatible with the reference simulation, with our choice of perturbation to generate the ensemble.

Figures 1A,B show characteristic signatures of magnetic reconnection in the magnetotail, i.e., the X pattern and the formation of dipolarization fronts in the magnetic field lines, and the presence of earthward and tailward jets in v_x departing from the X point. We provide a movie showing the dynamic evolution in the **Supplementary Material** (ReferenceSimVx.avi). The movie shows the solar wind b_z time variation and the subsequent occurrence of several magnetopause/magnetotail reconnection events. The "formation" of the magnetosphere occurs during the first $\sim$ 30 min of the simulation and should be disregarded.

The movie MeanVx.avi, also in the **Supplementary Material**, shows how the global evolution changes in the ensemble mean: the magnetopause and magnetotail reconnection patterns are still overall visible, but smoothed out by the averaging procedure with respect to the reference simulation, since the different ensemble instances reconnect at different times and the smaller scale features of each single run are averaged away.

In **Figure 2** and movies LowerVx.avi and HigherVx.avi we compare the evolution of the members of the ensemble generated with the lower ($|v_x| \sim 363$ km/s, panel A) and higher ($|v_x| \sim 583$ km/s, panel B) absolute value of the v_x velocity component. The movies show that the velocity values and magnetic field line patterns are significantly different from the reference simulation and from the ensemble average, demonstrating that the perturbations are not trivial.

TABLE 1 | Coordinates of the observation points used in the DOI analysis.

	x/R_E	y/R_E	z/R_E
Solar wind	15	0	20
Magnetosheath	−10	0	20
Northern lobe	−10	0	5
Plasma sheet	−20	0	−3

We now discuss the RA and DOI analysis for a set of different observation points, depicted as white stars in the following figures, in the inflowing solar wind (A), in the magnetosheath (B), in the northern lobe (C), and in the plasma sheet (D), for the same plane and time as **Figure 1**. The coordinates of each of these points in the *xz*-plane are given in **Table 1**, the y coordinate being $y/R_E = 0$. **Figures 3**, **4** show the DOI maps for v_x and b_x, respectively. Note that the correlations which are displayed are not cross-correlations: the correlation is done between the value of a field at the observation point and the values of the same field at the other grid points.

Figures 3, **4** show that the correlations are mostly ordered by the principal regions of the magnetosphere, such as the lobes, the magnetosheath, and the plasma sheet. For example, **Figure 3** shows the results for the v_x correlations. The DOI values for the plasma sheet are different from those in the magnetosheath and the lobes in all panels. As expected, the stronger correlations are somewhat localized around the observation point, for example, the strongest correlations in panel (D), where the observation point is in the plasma sheet, are in the plasma sheet itself and its immediate surroundings. However, some other observation points have a much larger DOI, such as the ones in the solar wind and the magnetosheath. This makes physical sense, because v_x variations in those regions will propagate through much of the magnetosphere. **Figure 4** shows the B_x correlations. The northern and southern lobes clearly stand out, with opposite DOI values, and the magnetosheath stands out as well. Because the B_x values have opposite signs in the two lobes, the DOI values also have opposite signs. The correlation values depend on the variability of the field value at the observation point, thus the

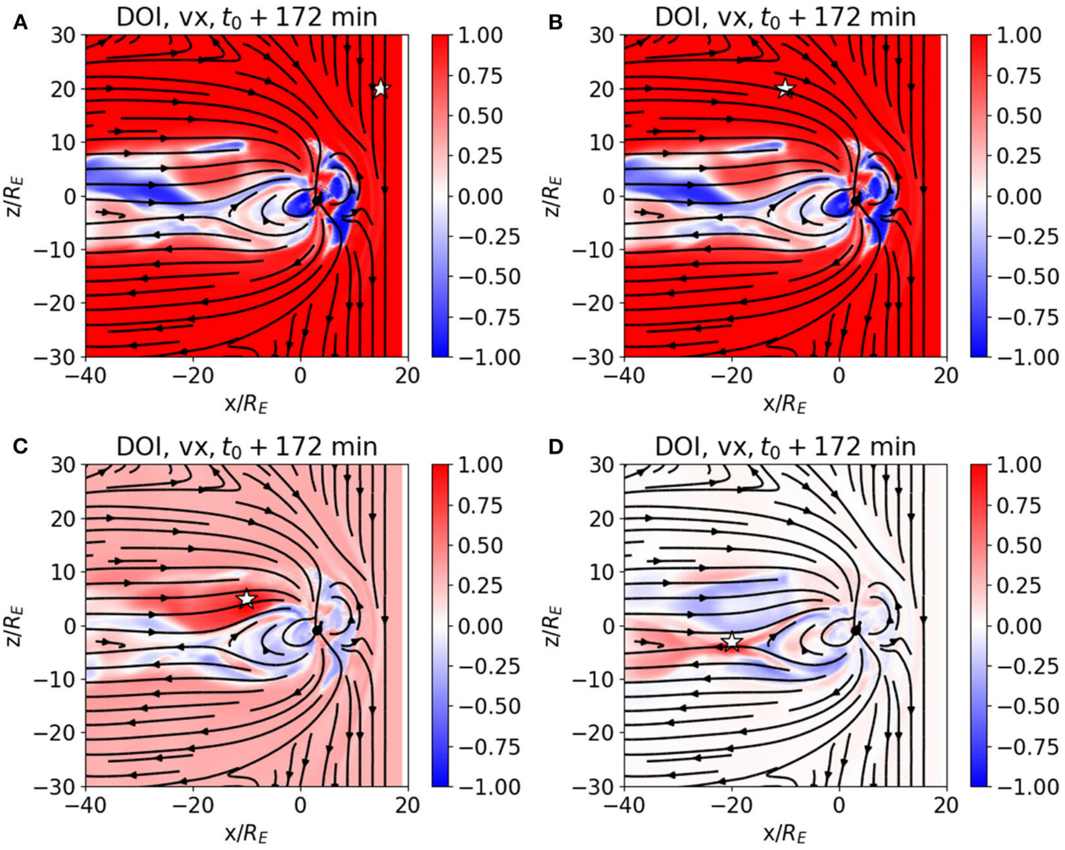

FIGURE 3 | DOI maps for v_x, computed from the correlation of an ensemble of OpenGGCM magnetospheric simulation, with observation points in the solar wind **(A)**, magnetosheath **(B)**, northern lobe **(C)**, plasma sheet **(D)**.

panels that exhibit lower correlations are those with observation point in the plasma sheet, where the intrinsic variance of both v_x and B_x is higher (see **Figure 1**) due to the different reconnection patterns in the different members of the ensemble. For example, in **Figure 3D**, the velocity value at the observation point in the plasma sheet exhibits little correlation with the v_x values outside of the plasma sheet and the neighboring areas. This is a consequence of the jet structure which is caused by internal magnetospheric dynamics rather than the solar wind driver.

The temporal dynamic DOI behavior is similar: the DOI maps of v_x and B_x with observation point in the plasma sheet exhibit higher temporal variability than those with a observation point in the magnetosheath, as can be seen in the DOI movies DOI_bx_bx_MSheath.avi, DOI_bx_bx_pSheet.avi, DOI_vx_vx_MSheath.avi, DOI_vx_vx_pSheet.avi and in **Figure 5**. The Figure shows the DOI map for v_x (panels A,B) and B_x (panels C,D) with observation point in the plasma sheet (panels A,C) and in the magnetosheath (panels B,D) at t_0 + 192 min. All the previous figures, **Figures 1–4**, were at t_0 + 172 min.

We note that the plots with observation points in the magnetosheath are not significantly different to earlier plots (see **Figures 3**, **4**), except for the plasma sheet plots, which differ profoundly.

To summarize and interpret the OpenGGCM results, the DOI analysis is well in line with our understanding of the terrestrial magnetosphere. In the v_x case, when the observation point is in the solar wind or in the magnetosheath, the $|DOI|$ values are very high in both the solar wind and the magnetosheath region. This is expected, because v_x in the solar wind is a correlation with itself (and thus a sanity test for the calculation), whereas the magnetosheath is largely driven by the interaction between solar wind and the bow shock, where the Rankine-Hugoniot conditions predict a positive correlation of the downstream velocity with the upstream velocity. When the observation points are in the solar wind and magnetosheath regions, the $|DOI|$ values in the plasma sheet are expected to be lower due to internal transient dynamics (e.g., reconnection events, bursty bulk flows) in the sheet which may be triggered by local plasma sheet dynamics, rather than solar wind compression. Local dynamics in the sheet is also the reason why, in **Figure 3D**, when the observation point is in the plasma sheet, the correlation with the solar wind and magnetosheath regions is close to zero. Even if, in global terms, magnetic reconnection in the plasma sheet were triggered by magnetopause dynamics, in any region of the plasma sheet v_x may flow sunward or anti-sunward, depending on the location of the reconnection site, and thus would be uncorrelated

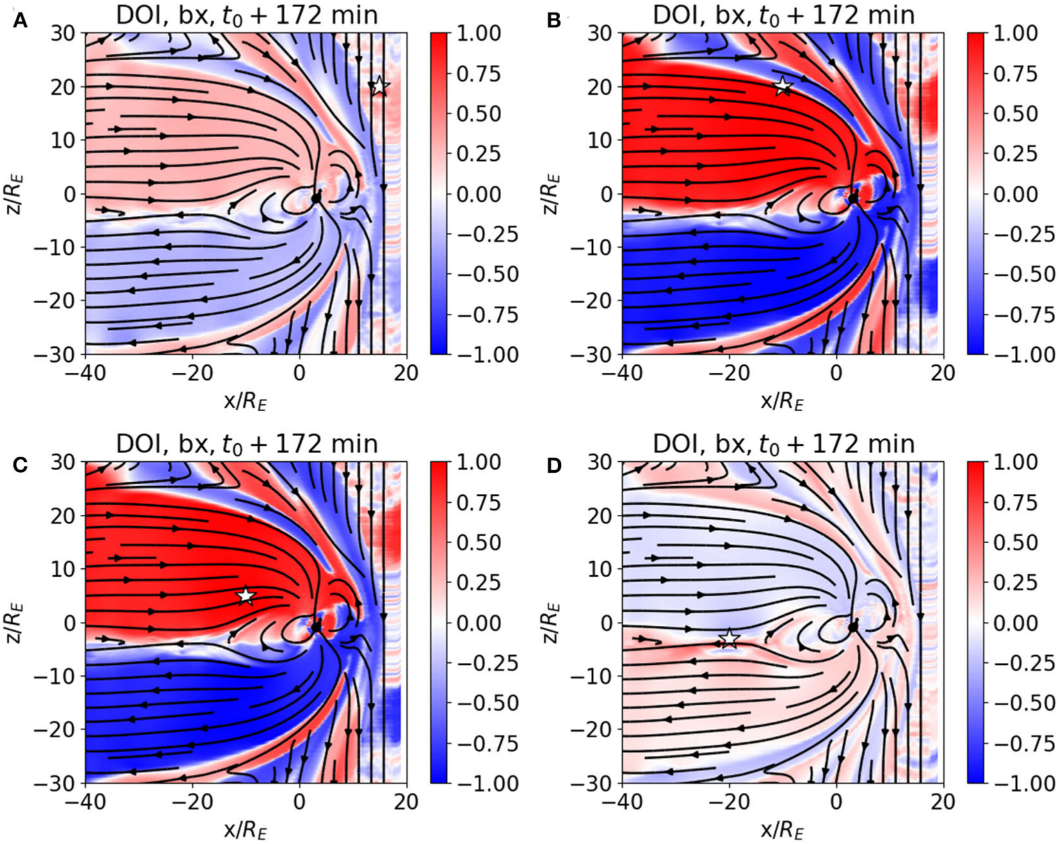

FIGURE 4 | DOI maps for b_x, computed from the correlation of an ensemble of OpenGGCM magnetospheric simulations, with observation points in the solar wind **(A)**, magnetosheath **(B)**, northern lobe **(C)**, plasma sheet **(D)**.

with the velocity in the solar wind or in the magnetosheath. The lobe magnetic field is expected to be directly driven by the solar wind dynamic pressure, and thus by v_x. As the dynamic pressure increases, the lobe flare angle decreases, and vice versa. As the flare angle decreases, the lobe field gets compressed. **Figures 4B,C** show that effect, as expected.

Similar consideration broadly apply to the B_x DOI results shown in **Figure 4**. There is, however, a significant difference between panel (A) in **Figures 3**, **4**. When the observation point is in the solar wind, high correlations are obtained in large parts of the magnetosphere for v_x, while B_x correlations are much lower. This can be attributed to the fact that B_x in the solar wind is not a major driver of magnetospheric dynamics, unlike the solar wind speed and solar wind dynamic pressure. The geo-effective component of the interplanetary magnetic field (IMF) is the B_z component, which controls reconnection at the magnetopause and thus the dominant energy input into the magnetosphere.

3.2. Magnetospheric Applications II: Tsyganenko Model

The Tsyganenko models are a family of empirical, static terrestrial magnetic field models (Tsyganenko, 1987, 1989, 1995, 2002a,b; Tsyganenko et al., 2003; Tsyganenko and Sitnov, 2005). The successive model versions (available at http://geo.phys.spbu.ru/~tsyganenko/modeling.html) reflect increasing knowledge of the magnetospheric systems and are based on an increasing amount of data from all regions in the magnetosphere.

The models are based on a mathematical description of the magnetosphere, which includes contributions from major magnetospheric current sources, such as the Chapman-Ferraro current, the ring current, the cross-tail current sheet and large-scale field-aligned currents. Terms are added to account for the magnetopause and for partial penetration of the IMF into the magnetosphere. The most recent versions can also take into account the dipole tilt, the dawn-dusk asymmetry, and allow for open magnetospheric configurations. The parameters of the models are derived from a regression to magnetic field observations, and keyed to magnetic indices and/or solar wind parameters. The model requires the user to specify a date and time for the dipole orientation. The other model parameters, either an index, such as the Kp, or solar wind variables, are to be given by the user. In more recent models, Tsyganenko also provides yearly input data files for his models. From these inputs, an approximation of the magnetosphere is created for the specified date and time. Notice that the Tsyganenko models are static, and only provides a snapshot of the magnetosphere. However, since the parameters are time dependent the model can be used in a quasi-dynamic mode.

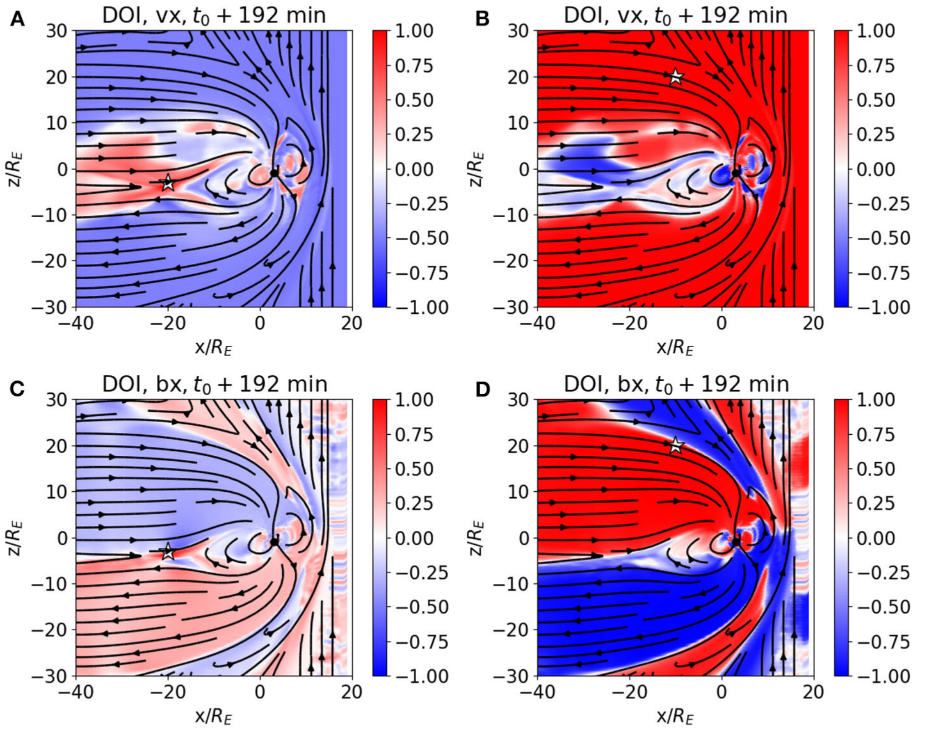

FIGURE 5 | DOI maps for v_x **(A,B)** and B_x **(C,D)** from an ensemble of OpenGGCM magnetospheric simulations with observation point in the plasma sheet **(A,C)** and in the magnetosheath **(B,D)**, at t_0+ 192 min. All previous Figures were at t_0+ 172 min.

Several versions of the Tsyganenko model have been tested over the years against observations and physics-based, MHD models (Thomsen et al., 1996; Huang et al., 2006; Woodfield et al., 2007). While the Tsyganenko models do not account for the Earth's internal magnetic field, methods are provided to add the internal field model as described in the above cited literature.

In order to simulate the evolution of the magnetosphere with the chosen Tsyganenko model, we create snapshots of the magnetosphere at different times. The time May 8th, 2004, 09:00 UTC is taken as t_0, the same time as the OpenGGCM simulations presented in section 3.1. The model is "evolved" by using a time series of the required input parameters, which are obtained from the OMNIWeb database (King and Papitashvili, 2005).

We use two versions of the Tsyganenko model, the T96 model (Tsyganenko, 1996) and the TA15 model (Tsyganenko and Andreeva, 2015). We generate the Tsyganenko ensembles in the same way as the OpenGGCM examples, by using a distribution of v_x values as described in section 3.1.

Before we analyse the results of the T96 ensemble, we show the magnetospheric configuration computed by the model using the original solar wind data. In **Figure 6**, the first row of figures shows the results of the "reference" simulation, e.g., the simulation without any perturbed inputs, at time $t_0 + 85$ min, for B_x (panel A) and B_z (panel B).

Unlike the OpenGGCM, the T96 model cannot model reconnection, although some approximation of reconnection is included in later Tsyganenko models (Tsyganenko, 2002a,b). Also, the day-side magnetospheric structure is only approximated with respect to physics-based models, and bow shock and magnetosheath are not clearly distinguishable. In **Figure 6**, the second row shows the average of the ensemble at the same time of the reference simulation, for B_x (panel C) and B_z (panel D). The results are similar to the reference simulation, as shown by the logarithm of the absolute difference between the reference and ensemble mean (e.g., **Figures 6E,F**). The only significant difference is located at the magnetopause, which is expected since varying the solar wind velocity changes the standoff distance.

Next we analyse the DOI maps of the T96 model. **Figure 7** shows the DOI maps for the B_x and B_z field components at time $t_0 + 85$ min. Although the T96 model is parameterized by the solar wind velocity, it only models the magnetic field in the magnetosphere. Because of this, we are only able to analyze the DOI maps of the magnetic field components. The observation points are placed in the northern lobe, in proximity to the current sheet, at the dayside magnetosphere, and in the southern lobe. Like in the OpenGGCM case, the DOI maps reflect the general regions of the magnetosphere as reproduced by the T96 model. However, the correlation only takes values of ±1 in the magnetosphere, and zero in the solar wind. The latter is simply a consequence of the fact that the model does not predict the IMF, which is therefore independent of the v_x variations of the

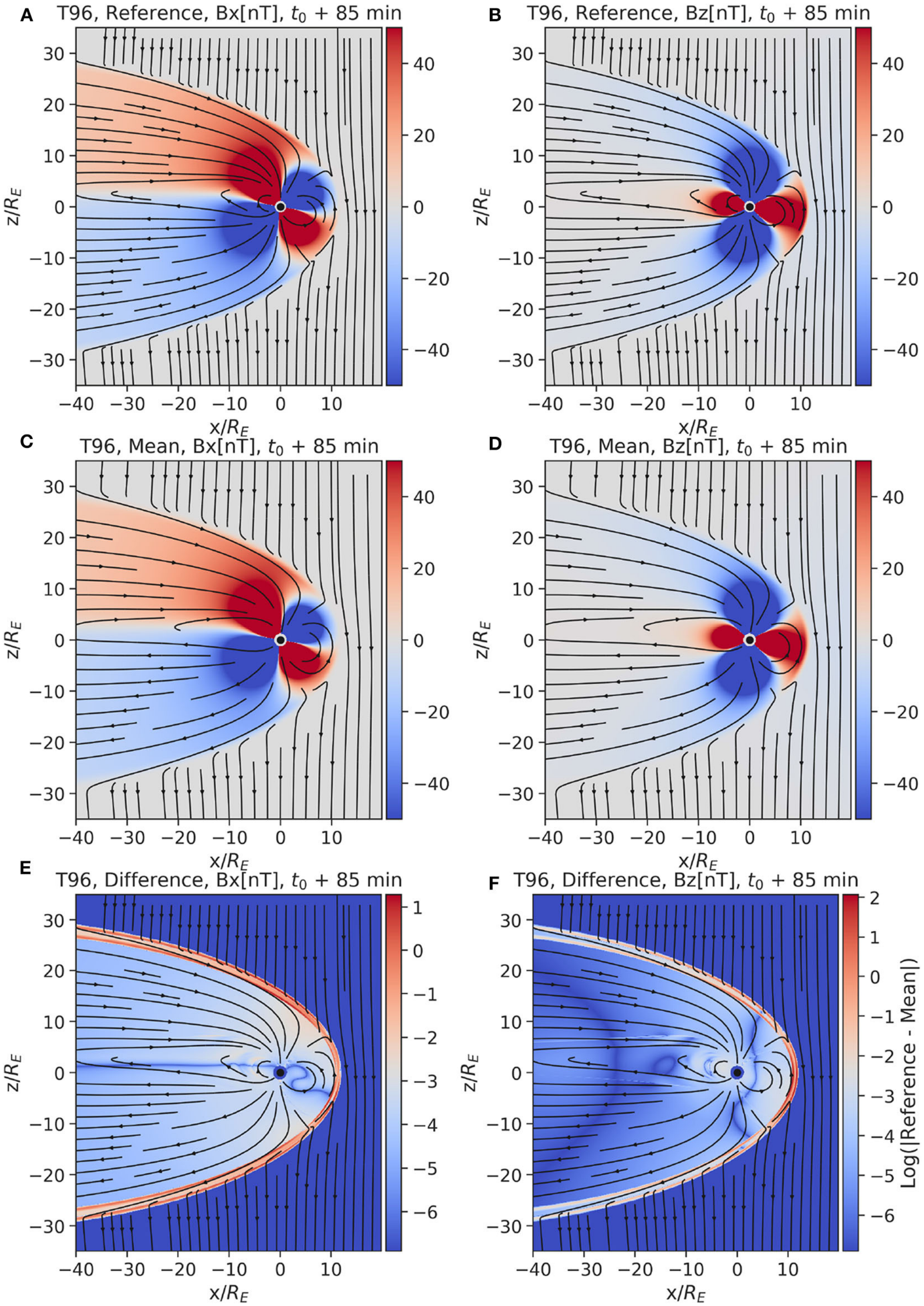

FIGURE 6 | Results from the T96 Tsyganenko model. The top row **(A,B)** shows the reference magnetic field (B_x and B_z component respectively) at time $t_0 + 85$ min, with a negative IMF. The middle row **(C,D)** shows the ensemble mean of the same magnetic field components at the same time $t_0 + 85$ min. We clipped the magnetic field values to $|50nT|$, in order to make variations in the tail better visible. The last row **(E,F)** shows the logarithm of the absolute difference between the reference simulation and the mean of the ensemble.

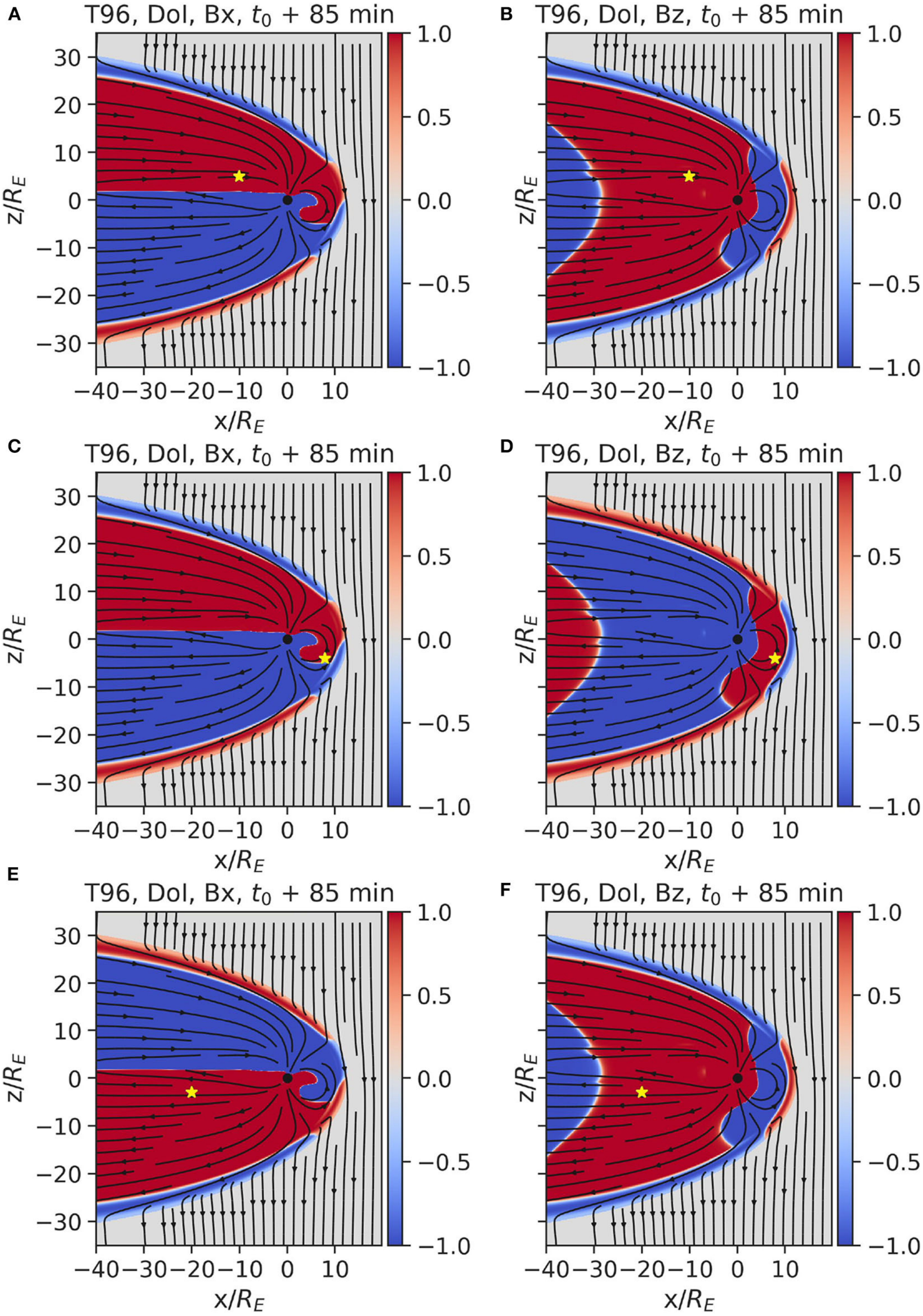

FIGURE 7 | Each row displays the DOI maps for B_x and B_z, from an ensemble of Tsyganenko model T96 simulations with observation point in the plasma sheet **(A,B)**, dayside magnetosphere **(C,D)** and southern lobe tail **(E,F)**, respectively.

ensemble. The former is due to the fact that the model has no intrinsic time dependence. Any variations of the solar wind affect the entire magnetosphere instantly and in proportion to the variation. Thus, after normalization, only the sign matters, i.e., whether a given change at the observation point leads to a positive or negative change at a different point.

Now we focus on the results of the TA15 model. **Figure 8** shows the reference simulation and ensemble mean for the B_x and B_z fields, with superimposed field lines, at time $t_0 + 85$ min, together with the difference between reference and ensemble mean. We observe that the reproduced dayside magnetosphere structure is improved compared to the T96 model, at the expense of unrealistically high magnetic field values in the inflowing solar wind, and correspondingly distorted magnetic field lines. These artificial boundary conditions in the Sunwards boundary are used to obtain an "open" magnetosphere which blends with the inflowing solar wind, without seeming to form a nightside magnetosheath. Notice also the high values at these artificial boundary conditions in the difference plot, indicating that there is a high variability in their values.

From the DOI maps in **Figure 9** (with observation points at the same positions as **Figure 7**), we can confirm that the modeled IMF is used to construct the internal magnetospheric solution. While in the T96 model the solar wind B_x and B_z values were uncorrelated with the magnetospheric values, here the absolute value (i.e., ignoring the sign) of the correlation is very high: the solar wind input strictly determines the inner magnetospheric solution, making the correlation practically unitary. This could be because of the deterministic analytical formula used to construct the magnetic field, where everything is exactly determined on a global scale.

Note that the correlations reported are spatial and not temporal, therefore no causality is implied. High correlation between the IMF and magnetospheric fields point to the fact that, in an ensemble generated by perturbing the solar wind input, the model is built in such a way that variations in the magnetic field are highly correlated through the system, apparently without highlighting the boundary regions that we were able to spot in the DOI maps for the OpenGGCM and Tsyganenko T96 simulations.

A last remark on the DOI analysis applied to the Tsyganenko models is the following. The analysis helps us understand and visualize how the different models are built, with regards to the relationship between the solar input and the magnetospheric solution. DA analysis then proves useful here as a model investigation tool.

It also highlights that caution should be used when deciding to apply DA techniques to a particular model, depending on the objectives of the investigation. The Tsyganenko models were built to provide time-independent, empirical-based insights into the structure of the magnetosphere at a particular instant in time. They do not aim at representing the state of the pristine solar wind, which is used only to better the magnetospheric solution (hence the somehow unrealistic solar wind patterns identified in **Figures 8**, **9**). Also, they do not intend to reproduce temporal dynamics in the magnetosphere. These factors result in DOI maps where the absolute value of the correlation is always either 1 or −1. When using DOI techniques with the purposes of identifying useful locations for satellite placement, these are not useful results: we are interested in the value of the DOI, not in the *sign*. Hence, caution should be used before using empirical, time-independent models for this particular purpose: more significant information will possibly be acquired from their physics-based, time-dependent counterparts. This consideration does not intend to diminish the importance of empirical, time-independent models for other scientific objectives such us, most importantly, quick forecasting.

3.3. Heliospheric Application: PLUTO

In this section, we study the propagation of a Coronal Mass Ejection in a solar meridional plane, which is defined by the rotation axis of the Sun and a radial vector in the equatorial plane. In all the runs of the ensemble, the computational domain is $1R_\odot \leq r \leq 216R_\odot$ and $0 \leq \theta \leq \pi$ in spherical coordinates, where $R_\odot$ is the solar radius and θ is the polar angle (or colatitude), corotating with the Sun. Assuming axisymmetry around the solar rotation axis, we may limit our analysis to 2.5D (pseudo 3D) simulations. The grid resolution is uniform in both directions, 384 × 384 cells, which is sufficient to capture the structure of the background solar wind while keeping the computational cost and output size manageable.

We simulate the background solar wind using a simple adiabatic model with effective polytropic index $\Gamma = 1.13$ (Keppens and Goedbloed, 2000). We also assume a time-independent dipole background magnetic field:

$$B_r = -2B_o \cos\theta / r^3, \tag{13}$$

$$B_\theta = -B_o \sin\theta / r^3, \tag{14}$$

where B_r, B_θ are the r, θ components of the magnetic field in spherical coordinates and B_o a constant used to scale the field to $B = 1.1$G on the solar equator. We impose the density distribution ρ as a function of the latitude θ at the inner boundary to achieve a "dead zone" of low velocity near the equator and a fast solar wind near the poles simultaneously (see Keppens and Goedbloed, 2000 and Chané et al., 2008). The differential rotation of the Sun is also taken into account, following Chané et al. (2005); this is achieved by imposing a varying azimuthal velocity $v_\phi = v_\phi(\theta)$ at the inflow boundary.

Once the simulation reaches a steady state, roughly after ∼ 2.5 days or $t = 10$ in normalized units, the radial velocity at 1 AU is ∼ 300 km/s near the equator and ∼ 850 km/s near the poles. This is consistent with the large-scale bimodal solar wind structure that is typically observed during solar minimum (McComas et al., 1998).

We create two ensembles of 100 simulations each. In the first ensemble, the velocity of the CME in each case is randomly selected from a Gaussian distribution with mean $\mu = 900$ km/s and standard deviation $\sigma = 25$ km/s. The resulting values are typical of strong CME events. In the second ensemble, the spatial extent of the boundary conditions that launch the CME varies as well, along with the velocity of the CME as described above. The half-width of this region is also randomly selected from a Gaussian distribution with $\mu = 10^\circ$ and $\sigma = 0.5^\circ$. All other parameters remain the same in every run.

The values of the CME widths that are used here are comparable to observed events. The choice of parameters in the second ensemble is less constrained by observations and leads to the appearance of very small values of variance. We thus

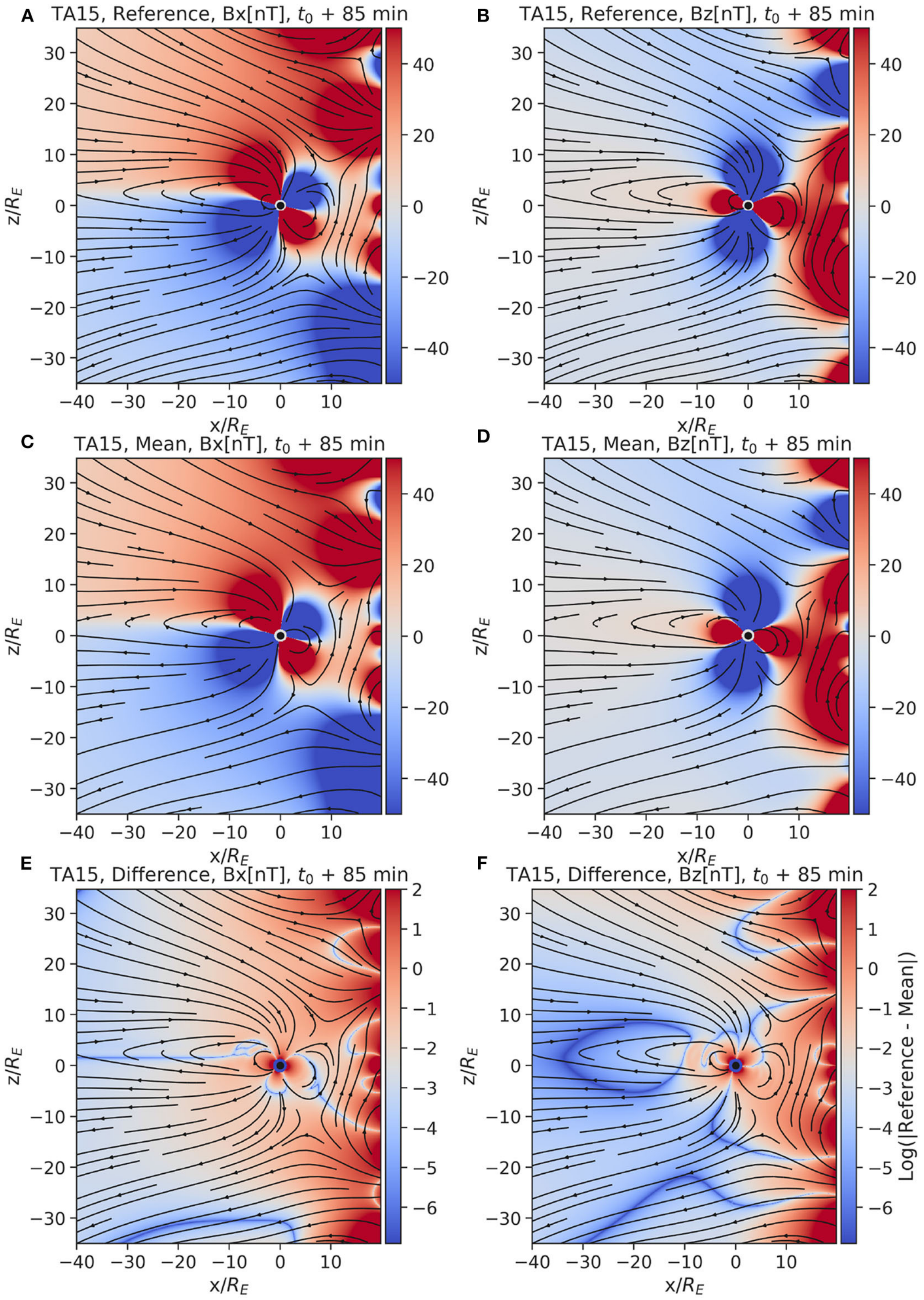

FIGURE 8 | The reference and mean magnetic field (B_x: **(A,C)** and B_z: **(B,D)** respectively) at time $t_0 + 85$ min from the Tsyganenko TA15 model are displayed in the top two rows of figures. Notice the non-realistic high magnetic field values in the inflowing solar wind (at $x/R_E > 10$). We assume these unrealistic values are necessary for the model to construct the day-side magnetosphere. The values of the magnetic field have been cut off in the top two rows of figures at $|50nT|$, to make sure the variations in the tail are visible. The last row **(E,F)** of figures shows the logarithm of the absolute error between the reference simulation and the mean of the ensemble.

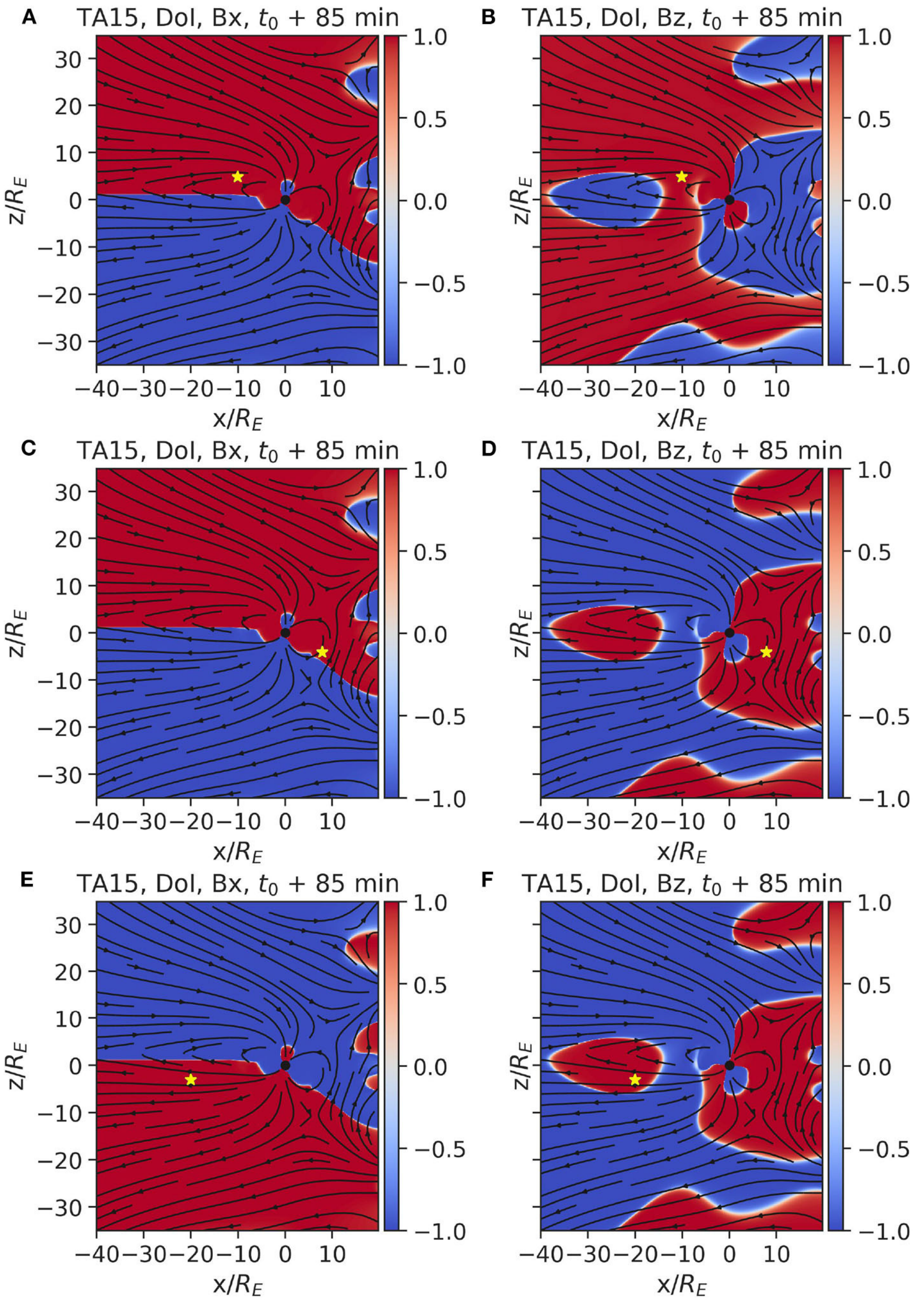

FIGURE 9 | DOI maps for B_x **(A,C,E)** And B_z **(B,D,F)**, computed from an ensemble of Tsyganenko TA15 simulations at $t_0 + 85$ min with observation points at the same position as **Figure 7**.

find large areas where the DOI $\sim$ 1, since the simulations in the ensemble do not differ significantly. This was confirmed by creating and analyzing a third ensemble, where the width of the CME is chosen from a Gaussian with $\mu = 20^\circ$ and $\sigma = 2.0^\circ$.

Figure 10 shows the evolution of the radial velocity average over the whole ensemble. Up to $t = 11$, i.e., before the CME is launched, all runs are identical. The CME is initialized similar to the simplified approach of Keppens and Goedbloed (2000), such that the boundary conditions on the solar surface are modified to represent a change of mass flux. In our case, we modify the boundary conditions at R=1R$_\odot$, in a given region around $\theta = 80^\circ$. A tracer (a passive scalar only present as an advected quantity within the flow, without effect on the plasma) is also injected with the CME, to facilitate monitoring its propagation. In the middle and right panel of **Figure 10** we show the ejection of the CME and its propagation. The CME front can be clearly distinguished at $t = 12$.

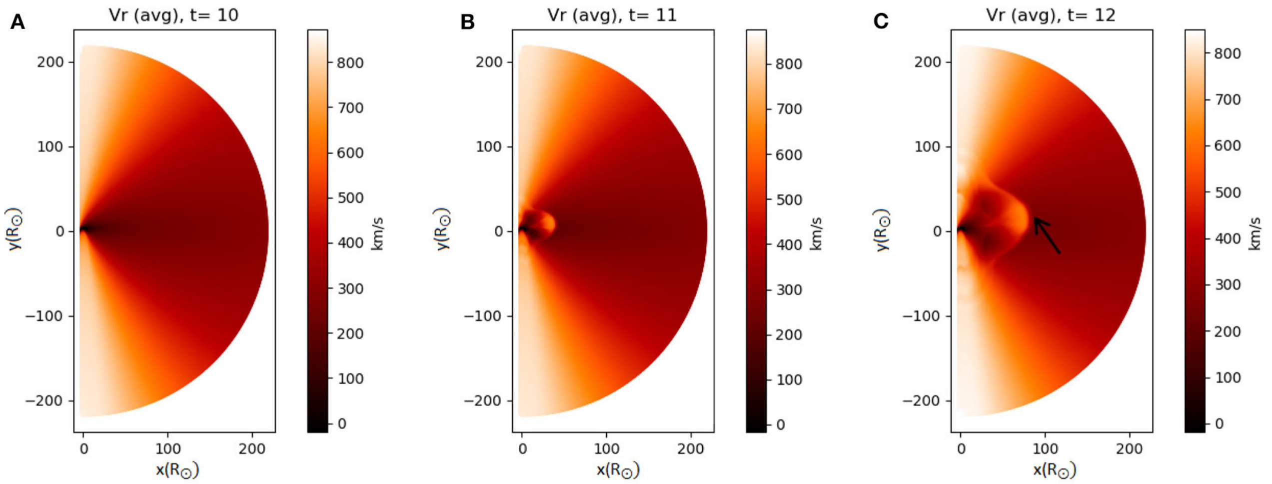

FIGURE 10 | Injection and propagation of a CME via the average radial velocity in the ensemble (in km/s). From **(A–C)**: relaxed solar wind (*t* = 10), injection and propagation of the CME (*t* = 11, *t* = 12). The leading edge (front shock) is prominent in the last panel, marked by a black arrow.

To apply the RA technique, as explained in section 2, we select a point of interest and perform the analysis based on (a) the plasma density, or (b) the radial velocity. We present results at t=14, when the CME has reached a distance of $\sim 150R_{\odot}$, for two detection points (at $R = 90$ and $R = 150R_{\odot}, \theta = 80°$). At times earlier than $t = 10$ (when the solar wind reaches a steady state and the CME is injected), the DOI is zero, since the observation point is disconnected from the rest of the domain before the CME reaches it.

The propagation of the CME can be monitored in the MHD simulations easily via, e.g., a tracer (or the radial velocity). The DOI map, when the tracer is used as a criterion, follows closely the CME propagation pattern observed in the MHD runs. However, this is of limited use, besides testing, as the tracer (in our case) does not represent a real physical quantity.

The DOI map for the first ensemble, where we perturb only the radial velocity of the CME, is shown in **Figure 11**. The regions where information from the CME front has not yet arrived have DOI = 0, as shown in the radial velocity DOI map (**Figure 11**). When only one parameter is modified (first ensemble), the density DOI map shows a very large area of the domain saturated with correlation $\simeq$1. This is probably due to variations in density of the background solar wind induced by the propagation of the CME. The regions with absolute value of the DOI $\simeq$ 1 that are located far from the CME propagation front (at small or large angles θ) are the areas of high radial velocity in **Figure 10**, where the information on the perturbation introduced when triggering the CME has already propagated. The density and radial velocity of all ensemble members are modified in a similar way, hence the large $|DOI|$ values.

In the second ensemble, where the width of the CME is also modified, the DOI map of the density shows smaller correlation values (compare especially panels B,D in the two figures) compared to the previous ensemble, because the differences between the runs of the ensemble are now larger (see **Figure 12**). This results in smaller regions where the DOI is close to unity compared to the first case.

The last ensemble, where the CME width and its perturbation are larger compared to the second case, is shown in **Figure 13**. The DOI pattern is qualitatively similar to **Figure 12**, but due to the larger values in the size of the CME and its perturbation, the regions with high DOI values (meaning the regions affected by CME propagation in at least one member of the ensemble) are slightly larger as well.

Additional analysis, not shown here, was carried out on subsets of the ensembles to ensure the ensemble size is sufficient. We found that in this case convergence was achieved if at least 25 ensemble members were used (as described in section 2); however, this number may differ in other cases, depending on the specifics of the ensemble.

The DOI analysis applied to the simulations performed with PLUTO are indicative of the versatility of the method. In all PLUTO ensembles, we can monitor the influence of the CME during its propagation and the response of the system via the DOI. Moreover, we can identify certain CME components, such as the leading edge, from the DOI maps. Differences in the response of the system due to the choice of the perturbation or parameters are captured as well. The resolution used here was sufficient to capture the CME injection and propagation within reasonable computational cost; the typical run time for simulating a member of the ensemble was of the order of $\sim 10'$ min on 28 cores.

However, some limitations of the model must be considered. The axisymmetric assumption simplifies the problem and allows to reduce computation costs, but with the drawback of not accounting for the three-dimensional CME structure. The limited angular resolution imposes a weak constraint on both the perturbed and unperturbed size of the CME that we can simulate. Runs with a higher resolution can remove this constraint at

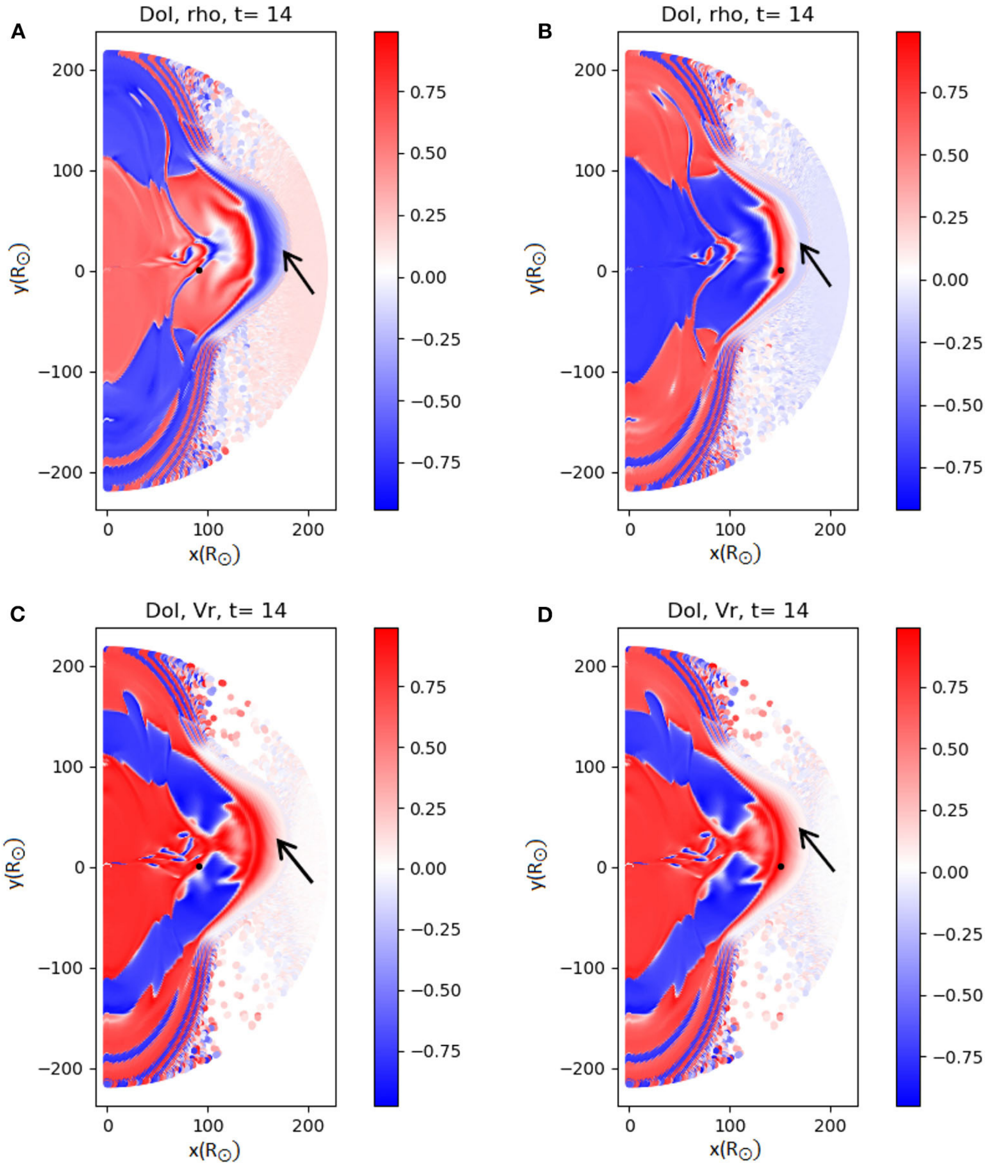

FIGURE 11 | DOI maps for the density **(A,B)** and the radial velocity **(C,D)**, from an ensemble of PLUTO simulations. The first column has the observation point at $R = 90R_{\odot}$ and the second column at $R = 150R_{\odot}$ (marked by the black dot). In this set we only perturb the radial velocity of the CME. The structure of the CME can be seen quite clearly in **(A,B)**, where the leading edge is evident and marked by a black arrow in all panels.

additional computational cost. Simulations in 3D will be part of future work in order to capture the full system, where also differences in the polar direction can be examined. Finally, a more realistic model for the background magnetic field should be used, rather than a simple static dipole. We focused mainly on calculating the DOI at different times and locations, but a similar approach can be used to estimate the arrival time of the CME, as described in Owens et al. (2020).

4. SUMMARY AND CONCLUSIONS

In this paper, we apply the Representer analysis and the Domain of Influence analysis to two fundamental components of the Sun-Earth connection: the interaction between the solar wind and the terrestrial magnetosphere, simulated with the OpenGGCM MHD code and with the empirical Tsyganenko models, and the propagation of CMEs in the background solar wind, simulated with the MHD PLUTO model.

In each case an ensemble is generated by appropriately perturbing initial/boundary conditions. Subsequently, the DOI analysis is applied over the ensemble. Localization methods, which can be used to reduce spurious correlations in the estimated prior covariance matrix (Anderson, 2007; Bishop and Hodyss, 2007; Sakov and Bertino, 2011), are not used at this stage.

Primarily, the DOI analysis is a first step in the application of Data Assimilation techniques to a model, and can be applied before assimilation itself to gain insight on the system and on the model. However,

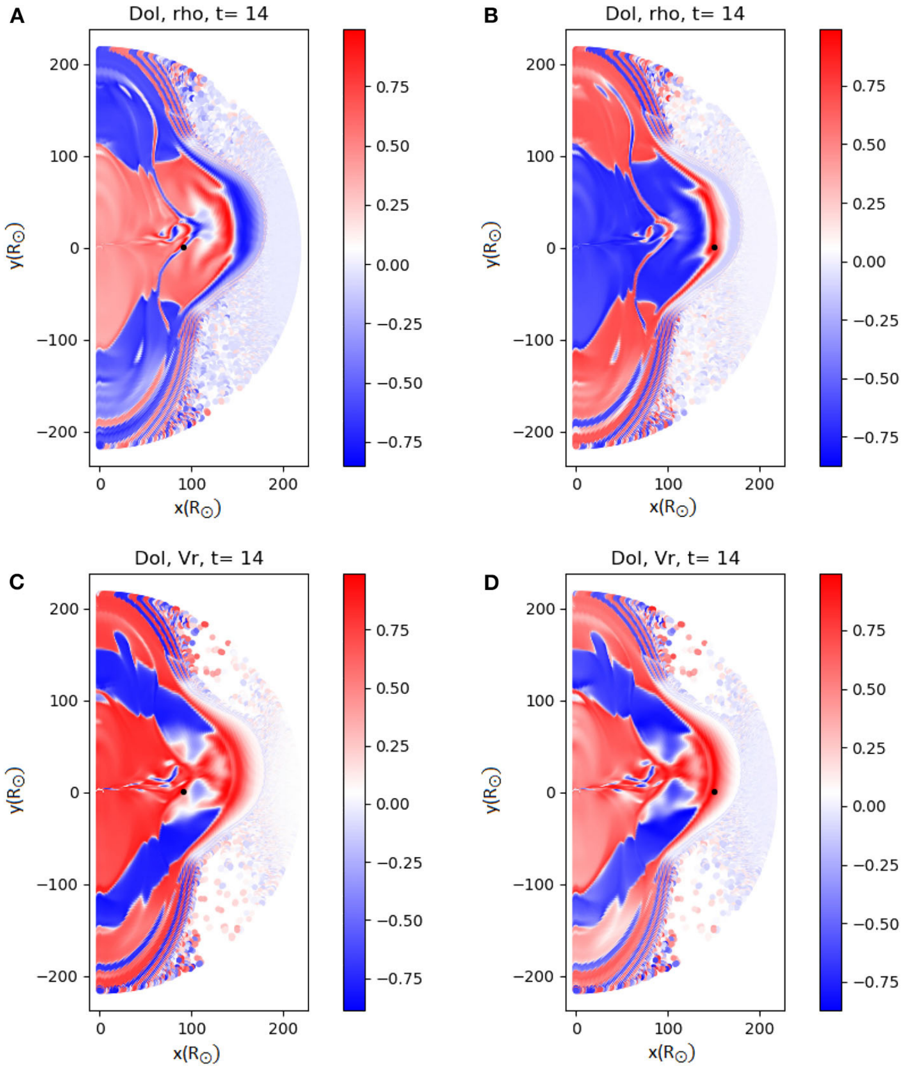

FIGURE 12 | DOI maps for the density **(A,B)** and the radial velocity **(C,D)**, computed from PLUTO simulation ensembles. The first column has a detection point at $R = 90R_{\odot}$ and the second column at $R = 150R_{\odot}$ (marked by the black dot). In this set we perturb two parameters, the radial velocity and the size of the CME.

the DOI analysis can also be used to gain physical insight, and to devise optimized observation systems, as discussed below.

Our main results are as follows.

First, we have demonstrated that DOI analysis can provide useful information on the most appropriate locations for future observation points, such as solar wind and magnetospheric monitors. Large absolute values of the DOI, calculated with respect to an observation point, means that observations at that location would provide significant information of that field in the specific, large $|DOI|$ area, but less so in areas with lower $|DOI|$. This can be used in two different ways. On one hand, DOI analysis can help to find observations points that are connected to large $|DOI|$ areas, in order to increase the amount of information brought in by a single new observation. On the other hand, the same information can be used for a different objective. Given a particular location, one can ask where observations need to be obtained to improve knowledge of that area. A useful example here is the plasma sheet in the OpenGGCM analysis, section 3.1. **Figures 3**, **4** show that $|DOI|$ values in the plasma sheet are consistently low, notwithstanding the field which is examined (v_x or B_x) and the location of the observation point. $|DOI|$ values in the plasma sheet are low even if the observation point is in the plasma sheet itself: $|DOI|$ values, which are of course 1 at the observation point itself, quickly become smaller even a small distance away. Since the plasma sheet is a location of particular importance for space weather forecasting, or basic research for that matter, single s/c in the plasma sheet are of limited use, and rather a constellation of satellites, such as proposed in Angelopoulos et al. (1998) and Raeder and Angelopoulos (1998) would be necessary.

Second, we have used the DOI analysis to improve our knowledge of the models we use, and in particular to investigate

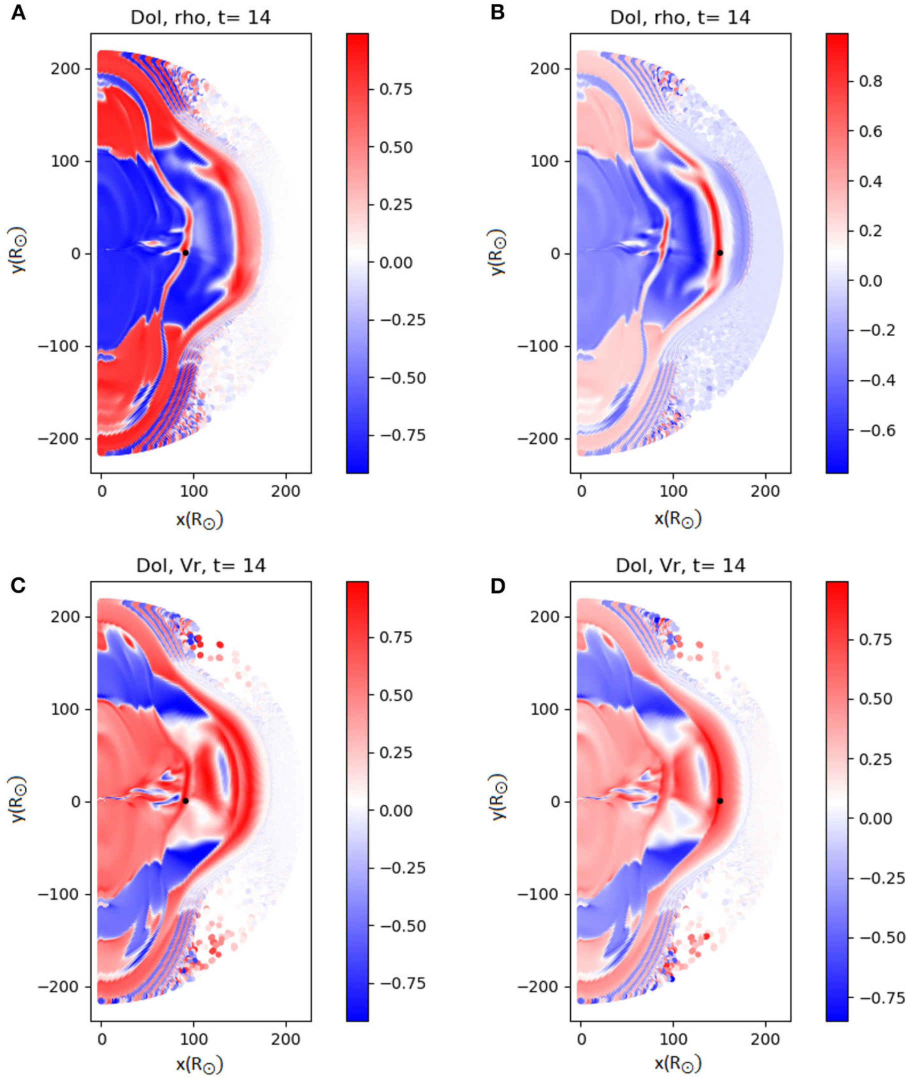

FIGURE 13 | DOI maps from ensembles of PLUTO simulations for the density **(A,B)** and the radial velocity **(C,D)**. The first column has a detection point at $R = 90R_{\odot}$ and the second column at $R = 150R_{\odot}$. In this set we perturb two parameters, the radial velocity and the size of the CME, with a larger perturbation in the size with respect to the second data set.

whether these models are appropriate for the implementation of Data Assimilation. The DOI analysis for the Tsyganenko models in section 3.2 powerfully highlights the model evolution from version T96 to version TA15. In version T96, the magnetosphere is a closed system, and solar wind conditions are not correlated (DOI ~ 0 in **Figure 7**) with the magnetospheric region. In version TA15, the magnetosphere opens up to solar wind driving, and the correlation between the solar wind region and the magnetosphere becomes very high (**Figure 9**). One should remember that the Tsyganenko models are supposed to be used to investigate the magnetospheric system, and the solar wind configuration is artfully modified as to give the best representation of the magnetosphere under the specified conditions.

One common aspect of the two versions of the Tsyganenko models is that (with the exception of the solar wind region in T96) the DOI values are always either 1 or -1, for all fields and regions examined. These results appear less realistic than the OpenGGCM results obtained in section 3.1, where DOI values have larger variability. The Tsyganenko models differ with respect to OpenGGCM in two fundamental aspects, in that they (a) empirically reconstruct the magnetospheric magnetic field from an array of observations and (b) that they are not time-dependent. Either of these two aspects can contribute to the unrealistically high correlations we observe. Investigations on other models, and specifically on empirical, time-dependent models, will possibly help disentangle the role of these two aspects. At this stage of the investigation, we advance the hypothesis that time-dependent models may be better suited than time-independent models as background models for Data Assimilation techniques.

Third, with this analysis we have highlighted a possible path for future, targeted improvements of global heliospheric models used, among other things, for simulations of CME propagation in the heliosphere. It has long been known that one of the critical aspects of the simulation of CME arrival time is the estimation of the physical parameters to use as initial conditions in the simulations. While some parameters can be easily estimated from remote sensing, others are more difficult to determine properly and their variability affects the accuracy of the forecast (Falkenberg et al., 2010). In this paper, we have shown that DOI analysis could constitute an important stage of a model analysis effort aimed at clarifying which aspects of a model should be prioritized in order to obtain more accurate simulations of CME propagation.

In this study, as a first step, we show DOI maps obtained from the correlations of a single variable calculated between the variable at the observation point and the same variable in the domain under investigation. As demonstrated in Skandrani et al. (2014), cross-correlations can be used to find the influence of one variable upon another.

The results of a DOI cross-correlation analysis can then be used to determine which quantities and areas in a simulation are most relevant in determining a certain observational quantity (such as the radial velocity of a CME in the case of CME propagation simulations). This analysis can then guide modelers on deciding which aspects of a model could be improved for more realistic results. It could help understanding, for example, if CME propagation in a model is mainly controlled by the background magnetic field configuration or by the properties of the CME itself at launch. In the first case, modeling efforts could be directed into accurate high resolution representation of the magnetic field configuration in the lower corona. In the second case, instead, modeling improvements could be focused on extracting better estimates of CME launch parameters (e.g., CME density, velocity, internal magnetic field configuration with respect to the background wind) from available observations.

The spatial correlations provided by DOI can also be of particular interest in evaluating the effect of actual measurements done at positions different from the traditional L1, such as, for example, missions planned for L5 or missions closer to the Sun.

Future work will extend this study to include temporal and cross correlations between different field components. This will further increase our knowledge of the models used to simulate such critical space weather processes.

The DOI analysis presented here can also be combined with an Observing System Simulation Experiment (OSSE), an approach already used in ionospheric and solar dynamo studies (Hsu et al., 2018; Dikpati, 2017) to help provide a cost-effective approach to the evaluation of the potential impact of new observations. OSSE requires that DA is already implemented and uses independently simulated "data" that are ingested into a different model or a different instance of the same model. The effect of DA can then be investigated, albeit with caveats, since the "data" are not real. DOI analysis would obviate the need to have DA implemented, which can be very costly. Instead, only ensemble runs with an unmodified model are required, and can provide a measure of the usefulness of a model and the available data for a specific situation.

DATA AVAILABILITY STATEMENT

The datasets generated for this study are available on reasonable request to the corresponding author.

AUTHOR CONTRIBUTIONS

MI, BL, and DM created the ensembles using OpenGGCM, Tsyganenko, and PLUTO, respectively, as they appear in the main body of the article, processed the data and presented the results of the analysis, and prepared the manuscript. JR provided the OpenGGCM and contributed to the interpretation of the magnetosphere model results. JR, GL, and SP provided the support during the analysis and the preparation of the article. All authors contributed to the article and approved the submitted version.

FUNDING

DM aknowledges support from AFRL (Air Force Research Laboratory)/USAF (US Air Force) project (AFRL Award No. FA9550-14-1-0375, 2014-2019) and partial support by UK STFC (Science and Technology Facilities Council) Consolidated Grant ST/S000240/1 (UCL-MSSL, University College London-Mullard Space Science Laboratory, Solar System). MI's work was supported by an FWO (Fonds voor Wetenschappelijk Onderzoek–Vlaanderen) post-doctoral fellowship. BL, MI, GL, and JR acknowledge funding from the European Union's Horizon 2020 research and innovation programme under grant agreement No. 776262 (AIDA, Artificial Intelligence for Data Analysis, www.aida-space.eu). JR also acknowledges support through AFOSR grant FA9550-18-1-0483 and from the NASA/THEMIS mission through a subcontract from UC Berkeley. SP and GL acknowledge funding from the European Union's Horizon 2020 research and innovation programme under grant agreement No. 870405. These results were also obtained in the framework of the projects C14/19/089 (C1 project Internal Funds KU Leuven), G.0A23.16N (FWO-Vlaanderen), C 90347 (ESA Prodex), and Belspo (Belgian Science Policy) BRAIN project BR/165/A2/CCSOM.

ACKNOWLEDGMENTS

The PLUTO simulations were performed using allocated time on the clusters Genius and Breniac. The computational resources and services used in this work were provided by the VSC (Flemish Supercomputer Center), funded by the Research Foundation Flanders (FWO) and the Flemish Government–Department EWI. The OpenGGCM simulations were performed on the supercomputer Marconi-Broadwell (Cineca, Italy) under a PRACE allocation. We acknowledge the NASA National Space Science Data Center, the Space Physics Data Facility, and the ACE

Principal Investigator, Edward C. Stone of the California Institute of Technology, for usage of ACE data. We acknowledge use of NASA/GSFC's Space Physics Data Facility's OMNIWeb service, and OMNI data.

SUPPLEMENTARY MATERIAL

The Supplementary Material for this article can be found online at: https://www.frontiersin.org/articles/10.3389/fspas.2020.571286/full#supplementary-material

Supplementary Video 1 | Temporal variation of b_z, reference run.

Supplementary Video 2 | Evolution of the ensemble mean.

Supplementary Video 3 | Evolution when $|v_x| \sim 363$ km/s.

Supplementary Video 4 | Evolution for $|v_x| \sim 583$ km/s.

Supplementary Video 5 | DOI for Bx, observation point in the plasmasheet.

Supplementary Video 6 | DOI for Vx, observation point in the plasmasheet.

Supplementary Video 7 | DOI for Bx, observation point in the magnethosheath.

Supplementary Video 8 | DOI for Vx, observation point in the magnethosheath.

1. Dynamic representation of the open magnetosphere scenario using OpenGGCM (shown in **Supplementary Video 1**), showing the temporal variation of the b_z component and reconnection events.
2. Global evolution of the ensemble mean (**Supplementary Video 2**), where the modified magnetopause-magnetotail reconnection pattern is visible.
3. Evolution of the members of the ensemble using different values for the v_x component. Two different values are tested, $|v_x| \sim 363$ km/s (**Supplementary Video 3**) and $|v_x| \sim 583$ km/s (**Supplementary Video 4**), resulting in two different magnetosheath patterns.
4. The DOI movies for the Bx and Vx with observation points in the plasma sheet (**Supplementary Videos 5**, **6**).
5. The DOI movies for the Bx and Vx with observation points in the magnetosheath (**Supplementary Videos 7**, **8**).

REFERENCES

Allen, J., Sauer, H., Frank, L., and Reiff, P. (1989). Effects of the march 1989 solar activity. *EOS Trans. Am. Geophys. Union* 70, 1479–1488. doi: 10.1029/89EO00409

Altschuler, M. D., and Newkirk, G. (1969). Magnetic fields and the structure of the solar corona. *Sol. Phys.* 9, 131–149. doi: 10.1007/BF00145734

Anderson, B. J., Korth, H., Welling, D. T., Merkin, V. G., Wiltberger, M. J., Raeder, J., et al. (2017). Comparison of predictive estimates of high-latitude electrodynamics with observations of global-scale birkeland currents. *Space Weather* 15, 352–373. doi: 10.1002/2016SW001529

Anderson, J. L. (2007). Exploring the need for localization in ensemble data assimilation using a hierarchical ensemble filter. *Phys. D* 230, 99–111. doi: 10.1016/j.physd.2006.02.011

Angelopoulos, V., Carlson, C. W., Curtis, D. W., Harvey, P., Lin, R. P., Mozer, F. S., et al. (1998). "On the necessity and feasability of a equatorial magnetospheric constellation," in *Science Closure and Enabling Technologies for Constellation Class Missions*, eds V. Angelopoulos and P. V. Panetta (Berkeley, CA: University of California, Berkeley; NASA Goddard Space Flight Center), 14.

Arge, C. N., Henney, C. J., Koller, J., Compeau, C. R., Young, S., MacKenzie, D., et al. (2010). Air force data assimilative photospheric flux transport (adapt) model. *AIP Conf. Proc.* 1216, 343–346. doi: 10.1063/1.3395870

Bennett, A. F. (1992). *Inverse Methods in Physical Oceanography*. Cambridge: Cambridge University Press.

Berchem, J., Raeder, J., and Ashour-Abdalla, M. (1995). "Reconnection at the magnetospheric boundary: results from global MHD simulations," in *Physics of the Magnetopause, Volume 90 of AGU Geophysical Monograph*, eds B. U. Sonnerup and P. Song (Washington, DC: American Geophysical Union), 205. doi: 10.1029/GM090p0205

Bishop, C. H., and Hodyss, D. (2007). Flow-adaptive moderation of spurious ensemble correlations and its use in ensemble-based data assimilation. *Q. J. R. Meteorol. Soc.* 133, 2029–2044. doi: 10.1002/qj.169

Bishop, G., and Welch, G. (2001). "An introduction to the Kalman filter," in *Proceedings of SIGGRAPH Course 8* (Chapel Hill, NC), 41.

Bothmer, V., and Daglis, I. A. (2007). *Space Weather: Physics and Effects*. Berlin: Springer Science & Business Media.

Bouttier, F., and Courtier, P. (1999). *Data Assimilation Concepts and Methods. Meteorological Training Course Lecture Series*. Reading: ECMWF.

Camporeale, E. (2019). The challenge of machine learning in space weather: nowcasting and forecasting. *Space Weather* 17, 1166–1207. doi: 10.1029/2018SW002061

Chané, E., Jacobs, C., van der Holst, B., Poedts, S., and Kimpe, D. (2005). On the effect of the initial magnetic polarity and of the background wind on the evolution of CME shocks. *Astron. Astrophys*. 432, 331–339. doi: 10.1051/0004-6361:20042005

Chané, E., Poedts, S., and van der Holst, B. (2008). On the combination of ACE data with numerical simulations to determine the initial characteristics of a CME. *Astron. Astrophys*. 492, L29–L32. doi: 10.1051/0004-6361:200811022

Connor, H. K., Zesta, E., Fedrizzi, M., Shi, Y., Raeder, J., Codrescu, M. V., et al. (2016). Modeling the ionosphere-thermosphere response to a geomagnetic storm using physics-based magnetospheric energy input: OpenGGCM-CTIM results. *J. Space Weather Space Clim.* 6:A25. doi: 10.1051/swsc/2016019

Cramer, W. D., Raeder, J., Toffoletto, F., Gilson, M., and Hu, B. (2017). Plasma sheet injections into the inner magnetosphere: two-way coupled OpenGGCM-RCM model results. *J. Geophys. Res. Space Phys.* 122, 5077–5091. doi: 10.1002/2017JA024104

Dikpati, M. (2017). "Ensemble Kalman filter data assimilation in a solar dynamo model," in *AGU Fall Meeting Abstracts, Volume 2017* (San Francisco, CA), SM14A-05.

Dorelli, J. C. (2004). A new look at driven magnetic reconnection at the terrestrial subsolar magnetopause. *J. Geophys. Res.* 109:16. doi: 10.1029/2004JA010458

Eastwood, J. P., Biffis, E., Hapgood, M. A., Green, L., Bisi, M. M., Bentley, R. D., et al. (2017). The economic impact of space weather: where do we stand? *Risk Anal.* 37, 206–218. doi: 10.1111/risa.12765

Echevin, V., De Mey, P., and Evensen, G. (2000). Horizontal and vertical structure of the representer functions for sea surface measurements in a coastal circulation model. *J. Phys. Oceanogr.* 30, 2627–2635. doi: 10.1175/1520-0485(2000)030<2627:HAVSOT>2.0.CO;2

Egbert, G., and Bennett, A. (1996). Data assimilation methods for ocean tides. *Elsevier Oceanogr. Ser.* 61, 147–179. doi: 10.1016/S0422-9894(96)80009-2

Evensen, G. (2009). *Data Assimilation: The Ensemble Kalman Filter*. Berlin: Springer Science & Business Media.

Falkenberg, T. V., Vršnak, B., Taktakishvili, A., Odstrcil, D., MacNeice, P., Hesse, M. (2010). Investigations of the sensitivity of a coronal mass ejection model (ENLIL) to solar input parameters. *Space Weather*. 8, 1–11.

Fortin, V., Abaza, M., Anctil, F., and Turcotte, R. (2014). Why should ensemble spread match the rmse of the ensemble mean? *J. Hydrometeorol.* 15, 1708–1713. doi: 10.1175/JHM-D-14-0008.1

Ge, Y. S., Raeder, J., Angelopoulos, V., Gilson, M. L., and Runov, A. (2011). Interaction of dipolarization fronts within multiple bursty bulk flows in global MHD simulations of a substorm on 27 February 2009. *J. Geophys. Res.* 116:A00I23. doi: 10.1029/2010JA015758

Ghil, M., and Malanotte-Rizzoli, P. (1991). Data assimilation in meteorology and oceanography. *Adv. Geophys.* 33, 141–266. doi: 10.1016/S0065-2687(08)60442-2

Hsu, C. T., Matsuo, T., and Liu, J. Y. (2018). Impact of assimilating the FORMOSAT-3/COSMIC and FORMOSAT-7/COSMIC-2 RO data on the midlatitude and low-latitude ionospheric specification. *Earth Space Sci.* 5, 875–890. doi: 10.1029/2018EA000447

Huang, C.-L., Spence, H. E., Lyon, J. G., Toffoletto, F. R., Singer, H. J., and Sazykin, S. (2006). Storm-time configuration of the inner magnetosphere: Lyon-Fedder-Mobarry MHD code, Tsyganenko model, and goes observations. *J. Geophys. Res. Space Phys.* 111:12. doi: 10.1029/2006JA011626

Innocenti, M. E., Lapenta, G., Vršnak, B., Crespon, F., Skandrani, C., Temmer, M., et al. (2011). Improved forecasts of solar wind parameters using the kalman filter. *Space Weather* 9, 1–15. doi: 10.1029/2011SW000659

Kalman, R. E. (1960). A new approach to linear filtering and prediction problems. *J. Basic Eng.* 82, 35–45. doi: 10.1115/1.3662552

Kalnay, E. (2003). *Atmospheric Modeling, Data Assimilation and Predictability*. Cambridge: Cambridge University Press.

Keppens, R., and Goedbloed, J. P. (2000). Stellar winds, dead zones, and coronal mass ejections. *Astrophys. J.* 530, 1036–1048. doi: 10.1086/308395

King, J., and Papitashvili, N. (2005). Solar wind spatial scales in and comparisons of hourly wind and ace plasma and magnetic field data. *J. Geophys. Res. Space Phys.* 110:8. doi: 10.1029/2004JA010649

Kondrashov, D., Shprits, Y., Ghil, M., and Thorne, R. (2007). A Kalman filter technique to estimate relativistic electron lifetimes in the outer radiation belt. *J. Geophys. Res. Space Phys.* 112:12. doi: 10.1029/2007JA012583

Lang, M., Owens, M., and Lawless, A. (2020). "Improving solar wind forecasts using data assimilation," in *EGU General Assembly Conference Abstracts EGU General Assembly Conference Abstracts* (Vienna), 10909. doi: 10.5194/egusphere-egu2020-10909

Lang, M., and Owens, M. J. (2019). A variational approach to data assimilation in the solar wind. *Space Weather* 17, 59–83. doi: 10.1029/2018SW001857

Laperre, B., Amaya, J., and Lapenta, G. (2020). Dynamic time warping as a new evaluation for dst forecast with machine learning. *arXiv* 2006.04667. doi: 10.3389/fspas.2020.00039

Lavraud, B., Liu, Y., Segura, K., He, J., Qin, G., Temmer, M., et al. (2016). A small mission concept to the sun-earth lagrangian l5 point for innovative solar, heliospheric and space weather science. *J. Atmos. Sol. Terres. Phys.* 146, 171–185. doi: 10.1016/j.jastp.2016.06.004

Le Dimet, F.-X., and Talagrand, O. (1986). Variational algorithms for analysis and assimilation of meteorological observations: theoretical aspects. *Tellus A Dyn. Meteorol. Oceanogr.* 38, 97–110. doi: 10.1111/j.1600-0870.1986.tb00459.x

Luhmann, J. G., Solomon, S. C., Linker, J. A., Lyon, J. G., Mikic, Z., Odstrcil, D., et al. (2004). Coupled model simulation of a sun-to-earth space weather event. *J. Atmos. Sol. Terres. Phys.* 66, 1243–1256. doi: 10.1016/j.jastp.2004.04.005

McComas, D. J., Bame, S. J., Barraclough, B. L., Feldman, W. C., Funsten, H. O., Gosling, J. T., et al. (1998). Ulysses' return to the slow solar wind. *Geophys. Res. Lett.* 25, 1–4. doi: 10.1029/97GL03444

Mendoza, O. B., De Moor, B., and Bernstein, D. (2006). Data assimilation for magnetohydrodynamics systems. *J. Comput. Appl. Math.* 189, 242–259. doi: 10.1016/j.cam.2005.03.030

Mignone, A., Bodo, G., Massaglia, S., Matsakos, T., Tesileanu, O., Zanni, C., et al. (2007). PLUTO: a numerical code for computational astrophysics. *Astrophys. J. Suppl.* 170, 228–242. doi: 10.1086/513316

Mignone, A., Zanni, C., Tzeferacos, P., van Straalen, B., Colella, P., and Bodo, G. (2012). The PLUTO code for adaptive mesh computations in astrophysical fluid dynamics. *Astrophys. J. Suppl.* 198:7. doi: 10.1088/0067-0049/198/1/7

Moretto, T., Vennerstrom, S., Olsen, N., Rastaetter, L., and Raeder, J. (2006). Using global magnetospheric models for simulation and interpretation of SWARM external field measurements. *Earth Planets Space* 58, 439–449. doi: 10.1186/BF03351940

Nikolić, L. (2019). On solutions of the pfss model with gong synoptic maps for 2006–2018. *Space Weather* 17, 1293–1311. doi: 10.1029/2019SW002205

Owens, M., Lang, M., Barnard, L., Riley, P., Ben-Nun, M., Scott, C. J., et al. (2020). A computationally efficient, time-dependent model of the solar wind for use as a surrogate to three-dimensional numerical magnetohydrodynamic simulations. *Sol. Phys.* 295:43. doi: 10.1007/s11207-020-01605-3

Pevtsov, A. A., Petrie, G., MacNeice, P., and Virtanen, I. I. (2020). Effect of additional magnetograph observations from different lagrangian points in sun-earth system on predicted properties of quasi-steady solar wind at 1 au. *Space Weather* 18:e2020SW002448. doi: 10.1029/2020SW002448

Plunkett, S. (2005). *The Extreme Solar Storms of October to November 2003*. Technical report, Naval Research Laboratory, Space Science Division, Washington, DC, United States.

Pulkkinen, A., Lindahl, S., Viljanen, A., and Pirjola, R. (2005). Geomagnetic storm of 29–31 october 2003: geomagnetically induced currents and their relation to problems in the swedish high-voltage power transmission system. *Space Weather* 3:19. doi: 10.1029/2004SW000123

Raeder, J. (2003). "Global magnetohydrodynamics–a tutorial," in *Space Plasma Simulation*, eds J. Büchner, C. T. Dum, and M. Scholer (Berlin; Heidelberg; New York, NY: Springer Verlag), 212–246. doi: 10.1007/3-540-36530-3_11

Raeder, J. (2006). Flux transfer events: 1. Generation mechanism for strong southward IMF. *Ann. Geophys.* 24, 381–392. doi: 10.5194/angeo-24-381-2006

Raeder, J., and Angelopoulos, V. (1998). "Using global simulations of the magnetosphere for multi-satellite mission planning and analysis," in *Science Closure and Enabling Technologies for Constellation Class Missions*, eds V. Angelopoulos and P. V. Panetta (Berkeley, CA: University of California, Berkeley; NASA Goddard Space Flight Center), 78.

Raeder, J., Cramer, W. D., Germaschewski, K., and Jensen, J. (2017). Using OpenGGCM to compute and separate magnetosphere magnetic perturbations measured on board low earth orbiting satellites. *Soc. Sci. Res.* 206, 601–620. doi: 10.1007/s11214-016-0304-x

Raeder, J., and Lu, G. (2005). Polar cap potential saturation during large geomagnetic storms. *Adv. Space Res.* 36, 1804–1808. doi: 10.1016/j.asr.2004.05.010

Raeder, J., McPherron, R. L., Frank, L. A., Paterson, W. R., Sigwarth, J. B., Lu, G., et al. (2001a). Global simulation of the geospace environment modeling substorm challenge event. *J. Geophys. Res.* 106:381. doi: 10.1029/2000JA000605

Raeder, J., Wang, Y. L., Fuller-Rowell, T. J., and Singer, H. J. (2001b). Global simulation of space weather effects of the Bastille Day storm. *Sol. Phys.* 204:325. doi: 10.1023/A:1014228230714

Raeder, J., Zhu, P., Ge, Y., and Siscoe, G. L. (2010). OpenGGCM simulation of a substorm: axial tail instability and ballooning mode preceding substorm onset. *J. Geophys. Res.* 115:A00l16. doi: 10.1029/2010JA015876

Richardson, I. G., and Cane, H. V. (2010). Near-earth interplanetary coronal mass ejections during solar cycle 23 (1996–2009): catalog and summary of properties. *Sol. Phys.* 264, 189–237. doi: 10.1007/s11207-010-9568-6

Rigler, E., Baker, D., Weigel, R., Vassiliadis, D., and Klimas, A. (2004). Adaptive linear prediction of radiation belt electrons using the kalman filter. *Space Weather* 2, 1–9. doi: 10.1029/2003SW000036

Sakov, P., and Bertino, L. (2011). Relation between two common localisation methods for the ENKF. *Comput. Geosci.* 15, 225–237. doi: 10.1007/s10596-010-9202-6

Schatten, K. H. (1971). Current sheet magnetic model for the solar corona," in *Solar Wind*. eds C. P. Sonett, P. J. Coleman and J. M. Wilcox (Washington: Scientific and Technical Information Office, National Aeronautics and Space Administration), 44.

Schatten, K. H., Wilcox, J. M., and Ness, N. F. (1969). A model of interplanetary and coronal magnetic fields. *Sol. Phys.* 6, 442–455. doi: 10.1007/BF00146478

Schrijver, C. J., and DeRosa, M. L. (2003). Photospheric and heliospheric magnetic fields. *Sol. Phys.* 212, 165–200. doi: 10.1023/A:1022908504100

Schunk, R. W., Scherliess, L., Sojka, J. J., Thompson, D. C., Anderson, D. N., Codrescu, M., et al. (2004). Global assimilation of ionospheric measurements (GAIM). *Radio Sci.* 39:11. doi: 10.1029/2002RS002794

Shi, Q. Q., Hartinger, M., Angelopoulos, V., Tian, A., Fu, S., Zong, Q.-G., et al. (2014). Solar wind pressure pulse-driven magnetospheric vortices and their global consequences. *J. Geophys. Res. Space Phys.* 119, 4274–4280. doi: 10.1002/2013JA019551

Siscoe, G., Baker, D., Weigel, R., Hughes, J., and Spence, H. (2004). Roles of empirical modeling within CISM. *J. Atmos. Sol. Terres. Phys.* 66, 1481–1489. doi: 10.1016/j.jastp.2004.03.028

Skandrani, C., Innocenti, M. E., Bettarini, L., Crespon, F., Lamouroux, J., and Lapenta, G. (2014). Flip-mhd-based model sensitivity analysis. *Nonlin. Process. Geophys.* 21, 539–553. doi: 10.5194/npg-21-539-2014

Stone, E. C., Frandsen, A., Mewaldt, R., Christian, E., Margolies, D., Ormes, J., et al. (1998). The advanced composition explorer. *Space Sci. Rev.* 86, 1–22. doi: 10.1023/A:1005082526237

Thomsen, M., McComas, D., Reeves, G., and Weiss, L. (1996). An observational test of the tsyganenko (t89a) model of the magnetospheric field. *J. Geophys. Res. Space Phys.* 101, 24827–24836. doi: 10.1029/96JA02318

Toffoletto, F., Spiro, R., Wolf, R., Birn, J., and Hesse, M. (2001). Modeling inner magnetospheric electrodynamics. *Space Weather* 125, 265–272. doi: 10.1029/GM125p0265

Tóth, G., Sokolov, I. V., Gombosi, T. I., Chesney, D. R., Clauer, C. R., De Zeeuw, D. L., et al. (2005). Space weather modeling framework: a new tool for the space science community. *J. Geophys. Res. Space Phys.* 110:21. doi: 10.1029/2005JA011126

Tsurutani, B. T., Gonzalez, W. D., Gonzalez, A. L., Guarnieri, F. L., Gopalswamy, N., Grande, M., et al. (2006). Corotating solar wind streams and recurrent geomagnetic activity: a review. *J. Geophys. Res. Space Phys.* 111. doi: 10.1029/GM167

Tsyganenko, N. (1987). Global quantitative models of the geomagnetic field in the cislunar magnetosphere for different disturbance levels. *Planet. Space Sci.* 35, 1347–1358. doi: 10.1016/0032-0633(87)90046-8

Tsyganenko, N. (1989). A magnetospheric magnetic field model with a warped tail current sheet. *Planet. Space Sci.* 37, 5–20. doi: 10.1016/0032-0633(89)90066-4

Tsyganenko, N. (2002a). A model of the near magnetosphere with a dawn-dusk asymmetry 1. Mathematical structure. *J. Geophys. Res. Space Phys.* 107:SMP-12. doi: 10.1029/2001JA000219

Tsyganenko, N. (2002b). A model of the near magnetosphere with a dawn-dusk asymmetry 2. Parameterization and fitting to observations. *J. Geophys. Res. Space Phys.* 107:SMP-10. doi: 10.1029/2001JA000220

Tsyganenko, N., and Andreeva, V. (2015). A forecasting model of the magnetosphere driven by an optimal solar wind coupling function. *J. Geophys. Res. Space Phys.* 120, 8401–8425. doi: 10.1002/2015JA021641

Tsyganenko, N., Singer, H., and Kasper, J. (2003). Storm-time distortion of the inner magnetosphere: how severe can it get? *J. Geophys. Res. Space Phys.* 108:18. doi: 10.1029/2002JA009808

Tsyganenko, N., and Sitnov, M. (2005). Modeling the dynamics of the inner magnetosphere during strong geomagnetic storms. *J. Geophys. Res. Space Phys.* 110:16. doi: 10.1029/2004JA010798

Tsyganenko, N. A. (1995). Modeling the earth's magnetospheric magnetic field confined within a realistic magnetopause. *J. Geophys. Res. Space Phys.* 100, 5599–5612. doi: 10.1029/94JA03193

Tsyganenko, N. A. (1996). "Effects of the solar wind conditions in the global magnetospheric configurations as deduced from data-based field models," in *International Conference on Substorms* (Versailles), 389:181.

Vennerstrom, S., Moretto, T., Rastaetter, L., and Raeder, J. (2005). Field-aligned currents during northward interplanetary field: morphology and causes. *J. Geophys. Res.* 110:A06205. doi: 10.1029/2004JA010802

Vourlidas, A. (2015). Mission to the sun-earth l5 lagrangian point: an optimal platform for space weather research. *Space Weather* 13, 197–201. doi: 10.1002/2015SW001173

Wang, Y.-M., and Sheeley, N. Jr. (1992). On potential field models of the solar corona. *Astrophys. J.* 392, 310–319. doi: 10.1086/171430

Woodfield, E., Dunlop, M., Holme, R., Davies, J., and Hapgood, M. (2007). A comparison of cluster magnetic data with the Tsyganenko 2001 model. *J. Geophys. Res. Space Phys.* 112:15. doi: 10.1029/2006JA012217

Zhou, X.-Z., Ge, Y. S., Angelopoulos, V., Runov, A., Liang, J., Xing, X., et al. (2012). Dipolarization fronts and associated auroral activities: 2. Acceleration of ions and their subsequent behavior. *J. Geophys. Res. Space Phys.* 117:1. doi: 10.1029/2012JA017677

Zhu, P., Raeder, J., Germaschewski, K., and Hegna, C. C. (2009). Initiation of ballooning instability in the near-earth plasma sheet prior to the 23 March 2007 THEMIS substorm expansion onset. *Ann. Geophys.* 27, 1129–1138. doi: 10.5194/angeo-27-1129-2009

Conflict of Interest: The authors declare that the research was conducted in the absence of any commercial or financial relationships that could be construed as a potential conflict of interest.

frontiers
in Astronomy and Space Sciences

ORIGINAL RESEARCH
published: 23 November 2020
doi: 10.3389/fspas.2020.572084

A Comparison Study of Extrapolation Models and Empirical Relations in Forecasting Solar Wind

Sandeep Kumar[1]*, **Arghyadeep Paul**[1] **and Bhargav Vaidya**[1,2]

[1]Discipline of Astronomy Astrophysics and Space Engineering, Indian Institute of Technology Indore, Indore, India, [2]Center of Excellence in Space Sciences India, Indian Institute of Science Education and Research Kolkata, Mohanpur, India

Coronal mass ejections and high speed solar streams serve as perturbations to the background solar wind that have major implications in space weather dynamics. Therefore, a robust framework for accurate predictions of the background wind properties is a fundamental step toward the development of any space weather prediction toolbox. In this pilot study, we focus on the implementation and comparison of various models that are critical for a steady state, solar wind forecasting framework. Specifically, we perform case studies on Carrington rotations 2,053, 2,082, and 2,104, and compare the performance of magnetic field extrapolation models in conjunction with velocity empirical formulations to predict solar wind properties at Lagrangian point L1. Two different models to extrapolate the solar wind from the coronal domain to the inner-heliospheric domain are presented, namely, a) Kinematics based [Heliospheric Upwind eXtrapolation (HUX)] model, and b) Physics based model. The physics based model solves a set of conservative equations of hydrodynamics using the PLUTO code and can additionally predict the thermal properties of solar wind. The assessment in predicting solar wind parameters of the different models is quantified through statistical measures. We further extend this developed framework to also assess the polarity of inter-planetary magnetic field at L1. Our best models for the case of CR2053 gives a very high correlation coefficient (~0.73–0.81) and has an root mean square error of (~75–90 km s^{-1}). Additionally, the physics based model has a standard deviation comparable with that obtained from the hourly OMNI solar wind data and also produces a considerable match with observed solar wind proton temperatures measured at L1 from the same database.

Keywords: solar wind, sun–earth connection, sun: magnetic fields, sun: heliosphere, method: numerical, space weather modeling

Edited by:
Stefaan Poedts,
KU Leuven, Belgium

Reviewed by:
Meng Jin,
Lockheed Martin Solar and Astrophysics Laboratory (LMSAL), United States
Jiansen He,
Peking University, China

Correspondence:
Sandeep Kumar
ssandeepsharma201@gmail.com

Specialty section:
This article was submitted to Stellar and Solar Physics, a section of the journal Frontiers in Astronomy and Space Sciences

Received: *12 June 2020*
Accepted: *16 October 2020*
Published: *23 November 2020*

Citation:
Kumar S, Paul A and Vaidya B (2020) A Comparison Study of Extrapolation Models and Empirical Relations in Forecasting Solar Wind. Front. Astron. Space Sci. 7:572084. doi: 10.3389/fspas.2020.572084

1. INTRODUCTION

Space weather refers to the dynamic conditions on the Sun and in the intervening Sun–Earth medium that can severely influence the functioning of space-borne and ground based technical instruments thereby affecting human life. Predicting the impact of space weather thereby becomes an essential task. In particular, explosive events on the Sun that include solar flares, coronal mass ejections (CMEs) and solar energetic particles play a crucial role in influencing space weather (Schwenn, 2006). The ambient solar wind being the medium in which the CMEs propagate also plays a significant role in influencing space weather, particularly, high speed solar wind streams which contribute to about 70% of geomagnetic activity outside of the solar maximum phase (Richardson et al., 2000). Therefore, understanding and predicting the key properties of the ambient solar wind is a crucial component of space weather modeling (Owens and Forsyth, 2013).

Magnetic field is a key ingredient that threads the solar plasma and governs the dynamical properties of solar wind. Observational measurements of field strengths in tenuous coronal environments is a challenging task even today. Thus, modeling coronal plasma requires extrapolating magnetic fields at the photosphere in the coronal region. Typically, a potential field source surface solution [PFSS (Altschuler and Newkirk, 1969), is adopted to extend photospheric magnetic fields up-to the source surface, usually set at $\sim 2.5R_{\odot}$]. Further, solutions from PFSS is augmented with magnetic fields obtained from the Schatten current sheet model [SCS, (Schatten, 1972)]. This ensures confining heliospheric currents into a very thin sheet in accordance to *Ulysees* measurements of latitude independent radial interplanetary field component (Wang and Sheeley, Jr., 1995). Field extrapolation techniques present an alternative approach to more computationally demanding magneto-hydrodynamic (MHD) simulations for estimating coronal properties from input photospheric magnetic field data (Lionello et al., 2009) and references therein). On comparing the properties of open magnetic field lines at the source surface with observed solar wind velocity, empirical relations have been formulated viz., Wang–Sheeley model (Wang and Sheeley, Jr., 1989) and its improvement Wang–Sheeley–Arge model (Arge and Pizzo, 2000; Arge et al., 2003) to calculate velocity at that surface. A state-of-the-art solar wind forecasting framework combines the coronal model described above with the inner-heliospheric model to estimate wind parameters at L1. Kinematic extrapolation methods that rely on 1D stream propagation like Heliospheric Upwind eXtrapolation (Reiss et al., 2019) and its time dependent variant HUXt (Owens et al., 2020) provides a computationally efficient solution without providing physical insight as done by the 3D MHD physics based models like ENLIL (Odstrcil et al., 2004), SWMF (Tóth et al., 2012), EUHFORIA (Pomoell and Poedts, 2018). The different approaches adopted for forecasting solar wind along with their quality assessment are presented in a review by MacNeice et al. (2018).

The various forecasting models over time have shown considerable progress in our understanding of modeling the macro-physical solar wind properties. One of the key ingredients that is critical for space weather modeling is the interplay of micro-physical turbulent and particle acceleration processes with macro-physical dynamics. Several attempts have been made to include effects of energy contained in sub-grid turbulence and multi-fluid aspects in modeling of solar wind [CORHEL (Downs et al., 2016), AWSoM (Sokolov et al., 2016), CRONOS (Usmanov et al., 2014; Wiengarten et al., 2016; Usmanov et al., 2018)]. In general, handling of large separation of scales required to consistently model such an interplay of length scales is a challenging task. Such a multi-scale nature of problem is also experienced in astrophysical plasma modeling and several astrophysical codes are working in direction of developing a hybrid framework that bridges this wide gap. In particular, recent development of hybrid particle module for PLUTO code (Mignone et al., 2018; Vaidya et al., 2018) to model particle acceleration at shocks and its subsequent non-thermal emission. Further, PLUTO code supports adaptive mesh refinement and various non-ideal MHD processes including magnetic resistivity (Mignone et al., 2012) and Hall-MHD. The code also has support for anisotropic thermal conduction (Vaidya et al., 2017) and optical thin cooling. In last 5 years, problems pertaining to solar and magnetospheric physics have also been tackled with PLUTO code (Reale et al., 2016; Sarkar et al., 2017; Bharati Das et al., 2019; Réville et al., 2020). The goal of this work is to develop a space weather modeling framework in conjunction with PLUTO code aiming to utilize the additional functionalities of the code for modeling the micro-physical aspects of Sun–Earth environment.

In this first study, our focus is to compare the various coronal and inner heliospheric models for solar wind forecasting and the assessment of their predictive performance. The paper is arranged in the following manner—the details of the methods implemented for the forecasting framework are described in **Section 2**. The results from various models adopted for forecasting of solar wind velocity for a couple of case studies along with statistical assessment of their accuracy are elaborated in **Section 3**. Finally, **Section 4** discusses the various features of the forecasting framework along with limitations and future outlook.

2. METHODOLOGY

The region between the solar photosphere and the Lagrangian point L1 is divided into two zones. The inner coronal zone extends from the photosphere up-to $5R_{\odot}$, followed by inner-heliosphere zone that extends from $5R_{\odot}$ up-to L1 point. Data driven prediction of solar wind parameters at L1 point requires the following steps:

- To calculate the magnetic fields in the coronal region through various extrapolation methods of the input observed photospheric magnetic field.
- Applying the velocity empirical relations based on the field line properties obtained from extrapolation at the outer boundary of the coronal region.
- Extending the velocity estimates from the outer boundary of the coronal region up-to Lagrangian point L1 for comparison with observations.

Detailed procedure followed for each of the above steps is described in this section.

2.1. Magnetic Field Extrapolation

Forecasting of solar wind across the domain requires accurate magnetic field solutions extrapolated from the solar surface to the outer boundaries of the coronal domain. The magnetic field extrapolations are carried out up to a distance of $5R_{\odot}$. The inner boundary conditions for the magnetic fields at the solar surface are specified by the input magnetograms (synoptic maps) taken from the Global Oscillations Network Group (GONG) (https://gong.nso.edu/data/magmap/crmap.html). Once the inner boundary conditions are specified, the extrapolation of the magnetic fields are then carried out in a twofold manner.

Just above the photospheric region, the magnetic energy density is greater than the plasma energy density and magnetic effects dominate. One can assume this region to be current free and thus, use the potential formulation for the magnetic fields (Schatten et al., 1968). This current free assumption is valid inside a sphere of radius of about $2.5R_{\odot}$, the outer boundary of which is known as the *source surface*. The magnetic fields inside the source surface can be solved using the Potential Field Source Surface (PFSS) model. The outer boundary condition for this model dictates that the magnetic fields at the source surface is approximately radial (Schatten and Wilcox, 1968). For the PFSS solution, we used the python module *pfsspy*, which is an open source, finite difference PFSS solver. Using the observed magnetogram data as an input, potential field equations are solved in radial direction on a logarithmic grid, whereas for latitude and longitude the grid is regularly spaced in terms of $\cos\theta$ (-1.0 to 1.0) and ϕ (0–2π) (Yeates, 2018; Stansby, 2019). Field line tracing using the field solutions is done via Runge Kutta 4th order method.

In the region outside the source surface, the magnetic fields are extrapolated using the Schatten Current Sheet (SCS) model (Schatten, 1972). The SCS model extends the magnetic fields from the source surface to a distance of $5R_{\odot}$, i.e, the outer boundary of the coronal zone. The input to the SCS model is the re-oriented output from *pfsspy*, i.e, if at the source surface, $B_r \geq 0$, the field remains unchanged, but if $B_r \leq 0$, B_r, B_θ, B_ϕ are replaced by $-B_r, -B_\theta, -B_\phi$. Using the same resolution in $\cos\theta$ and ϕ plane as that of the output from *pfsspy*, all magnetic field components beyond the source surface can be expressed in the form of a Legendre polynomial expansion (Schatten, 1972; Reiss et al., 2019). Following the formulations presented in the appendix of (Reiss et al., 2019), we construct the matrices of coefficient of spherical harmonics g_n^m and h_n^m, where n and m are degree and order of the associated Legendre polynomial $P_n^m(\cos\theta)$. A rather modest value of $n = 15$ is used to approximate the magnetic field values using the SCS model. The accuracy of SCS approximation improved only marginally with doubling the choice of n, but the computational time increased significantly. Thus, the order of Legendre polynomial used in the present work was carried out by optimizing both accuracy and computational time. While tracing the field lines, one should note that the boundary conditions of PFSS and SCS are not compatible with each other. A direct combination of the PFSS solution with the SCS model at $2.5R_{\odot}$ results in kinks and discontinuities at the model boundary which is a consequence of the different boundary requirements for the two models. To avoid this non-physical discrepancy, the input to the SCS model is given by the field values at $2.3R_{\odot}$ rather than $2.5R_{\odot}$. The field values in the thin radial slice between $2.3R_{\odot}$and $2.5R_{\odot}$is then overwritten by the values obtained by the SCS model. This leads to a smooth transition and a more desirable coupling between the PFSS and the SCS models (McGregor et al., 2008). The SCS model then extrapolates the fields upto $5R_{\odot}$. The PFSS + SCS solution together gives us a good approximation of the magnetic field structure up-to a distance of $5R_{\odot}$.

2.2. Velocity Empirical Relations

Based on the magnetic field structure (Reiss et al., 2019) obtained by from the field extrapolation methods, we generate a velocity map for the solar wind using some empirical velocity mapping models. We employ two different empirical models for the velocity calculations described in the sections below.

2.2.1. Wang–Sheeley Model

The Wang–Sheeley (WS) model depends on a parameter, called the *expansion factor* of the coronal flux tubes to calculate Solar Wind velocities. The expansion factor (f_s) is given by

$$f_s = (R_{\odot}/\mathrm{R_{ss}})^2 \left[\mathrm{B^P}(\mathrm{R_{\odot}})/\mathrm{B^P}(\mathrm{R_{ss}})\right] \tag{1}$$

where $B^P(R_{ss})$ denotes the radial field strength at a sub-earth point P on the source surface and $B^P(R_{\odot})$is the foot-point of the flux tube traversing P on the photosphere (Wang and Sheeley Jr, 1989). The *expansion factor* measures the amount of change in cross section of a flux tube between the photosphere and the source surface compared to a purely radial expansion. It is observed that there is a correlation between the expansion factor and the solar wind velocities. Based on this, an empirical formula for calculating the solar wind velocities can be devised

$$v_{sw}^{ws}(f_s) = v_{\mathrm{slow}} + \frac{v_{\mathrm{fast}} - v_{\mathrm{slow}}}{f_s^{\alpha}} \tag{2}$$

where, $v_{\mathrm{slow}}$is the lowest expected speed as $f_s \to \infty$ and v_{fast} is the fastest solar wind expected as $f_s \to 1$. For our calculations, we have used the values of $v_{\mathrm{slow}} = 200\,\mathrm{km}^{-1}$, $v_{\mathrm{fast}} = 750\,\mathrm{km}^{-1}$ and $\alpha = 0.5$ (Arge and Pizzo, 2000).

2.2.2. Wang–Sheeley–Arge Model

The Wang–Sheeley–Arge (WSA) (Arge et al., 2003) is a model that also incorporates the effect of minimum angular distance of foot point of the field line from coronal hole, along with the expansion factor. It is believed that coronal holes produce fast streams of solar wind. So the position of the field line's foot point in coronal hole plays a very important role. The empirical relation from the WSA model (Riley et al., 2015) used in the present work is

$$v_{sw}^{wsa}(f_s, \theta_b) = v_{\mathrm{slow}} + \frac{v_{\mathrm{fast}} - v_{\mathrm{slow}}}{(1 + f_s)^{\alpha}} \left(1 - 0.8 e^{-(\theta_b/\mathrm{w})^{\delta}}\right)^{3.5} \tag{3}$$

The parameters v_{slow} and v_{fast} corresponds to the velocity of fastest and slowest solar wind stream. $\theta_b$is the minimum angular distance for the foot point of the field line from a coronal hole boundary at the Solar surface. In the present work, we have used $v_{\mathrm{slow}} = 250\,\mathrm{km}^{-1}$, $v_{\mathrm{fast}} = 900\,\mathrm{km}^{-1}$, $\alpha = 1.5/9$, $w = 0.03$, and $\delta = 1.5$.

2.3. Extrapolation Into the Heliospheric Domain

The WS and WSA model gives us the solar wind maps at the outer boundary of the coronal domain i.e., at $2.5R_\odot$ or $5R_\odot$based on the choice of magnetic field extrapolation method. For comparison with the observed velocities at L1 point, it is required to extrapolate these velocities into the inner heliosphere zone. This requires coupling of the coronal velocity models with heliosperic velocity extrapolation models. We have employed two such extrapolation methods, a) Heliospheric Upwind eXtrapolation (HUX) (Riley and Lionello, 2011) and b) Physics based Modeling using PLUTO code. We describe these methods in the following sections.

2.3.1. Heliospheric Upwind eXtrapolation

The Heliospheric Upwind eXtrapolation (HUX) model assumes the solar-wind flow at the outer boundary of the coronal domain to be time-ϕstationary. The extrapolation of the solar wind velocities in an r-grid can be then be kinetically approximated using

$$v_{r+1,\phi} = v_{r,\phi} + \frac{\Delta r \Omega_\odot}{v_{r,\phi}} \left(\frac{v_{r,\phi+1} - v_{r,\phi}}{\Delta \phi} \right) \tag{4}$$

where $\Delta r = 1R_\odot$ and $\Delta\phi = 1°$ represent the grid spacings in r and ϕ directions, respectively. $\Omega_\odot$ is the angular velocity of the Sun calculated assuming a rotation time period of 27.3 days. The HUX is essentially a 1D extrapolation that neglect the effects of magnetic fields, pressure gradients and gravity. The advantage being that such an extrapolation method is computationally inexpensive when compared to state-of-the-art 3D MHD models.

2.3.2. Physics Based Modeling Using PLUTO Code

With an aim to incorporate the effects of some of the physical aspects in solar wind extrapolation, we describe a physics based modeling approach that involves solving a set of conservative equations using the Godunov scheme based Eulerian grid code, PLUTO (Mignone et al., 2007).

For this pilot study, we assume the solar wind to be hydrodynamic and solve the following set of compressible equations in 2D polar co-ordinates (r, ϕ):

$$\frac{\partial \rho}{\partial t} + \nabla \cdot \left(\rho \vec{v} \right) = 0 \tag{5}$$

$$\frac{\partial \rho v}{\partial t} + \nabla \cdot \left(\rho \vec{v}\,\vec{v} + P\mathcal{I} \right) = \rho \vec{g} \tag{6}$$

$$\frac{\partial E}{\partial t} + \nabla \cdot \left((E + P) \vec{v} \right) = \rho \vec{v} \cdot \vec{g} \tag{7}$$

where, ρ is the density of the fluid, P being the isotropic thermal pressure, v is the fluid velocity, $\mathcal{I}$ is an identity matrix and the total energy $E = \frac{1}{2}\rho v^2 + \rho\epsilon$ is sum of the kinetic energy and the internal energy. The acceleration due to gravity $g = -GM_\odot/r^2$ is included as a source term in the conservative momentum equation. A poly-tropic equation of state is adopted with the value of adiabatic index $\gamma = 1.5$ (Odstrcil et al., 2004; Pomoell and Poedts, 2018).

The above equations are solved in a non-inertial frame where the inner radial boundary rotates with the rate equal to the solar rotation rate. Further to simplify we neglect the Coriolis and centrifugal terms as their contribution is rather small in determining the steady flow structure of the solar wind (Pomoell and Poedts, 2018). The computational grid in polar co-ordinates ranges in the radial direction from $5R_\odot$ to $435R_\odot$ with a resolution of 512 grid cells. Same number of grid cells are used to resolve the azimuthal (ϕ) direction.

Initially, the computational domain is filled with a static gas with number density of $1\,\mathrm{cm}^{-3}$ and thermal sound speed of $180\,\mathrm{km\,s}^{-1}$. The choice of initial conditions does not affect final steady state wind solution as the material injected from the inner boundary wash away these initial values to obtain a new steady state. Radial velocity is prescribed at the inner boundary from the WSA mapping. The inner boundary is also made to rotate with respect to the computational domain with a rate equal to the solar rotational time period which is 27.3 days. As a general rule, boundary conditions can be specified for only those characteristics that are outgoing (away from the boundary). Since we have a supersonic inflow boundary condition, all the characteristics are pointing away from the boundary and therefore, along with the prescription of solar wind velocity, one would need to prescribe the density and pressure at the inner radial boundary as well. Following (Pomoell and Poedts, 2018), we prescribe the number density (n) and pressure at the inner radial boundary in following manner:

$$n(r) = n_0 \left(\frac{v_0}{v_r} \right)^2 \tag{8}$$

$$P = P_0 \tag{9}$$

where P_0 is set to be a constant value of 2.75 nPa and $n_0 = 100\,\mathrm{cm}^{-3}$ resulting in a proton temperature of 2 MK. The scaling velocity v_0 is set to be $675\,\mathrm{km\,s}^{-1}$. The outer radial boundary is set to have free flowing outflow conditions. For each Carrington rotation, we carry out the simulations using velocities obtained from sub-earth points with the magnetic field parameters obtained at 5 $R_\odot$ and employing WSA empirical relation for velocity. The results are presented in **Section 3.4**.

2.4. Model Definitions

Using the combination of various magnetic field extrapolation, velocity empirical relations and method of extrapolating velocity field within the inner heliosphere, we have defined 6 different models. The combinations used for each of these models are shown in **Figure 1**. Models 1 and 2 involves magnetic field extrapolation using PFSS (without SCS) and velocity extrapolation in inner heliosphere using the HUX model. The difference between them is the choice of velocity empirical relation. In the other set of models 3 and 4a, the magnetic fields are extrapolated using PFSS+SCS. The empirical velocity relation employed for Model 3 is WS and that for Model 4a is WSA. Velocity field in both these models are extrapolated from 5 $R_\odot$ to L1 using HUX. Model 4b is a variant obtained by considering an ensemble values using the same combinations as that of Model 4a (see **Section 3.2**). Model 4c uses the

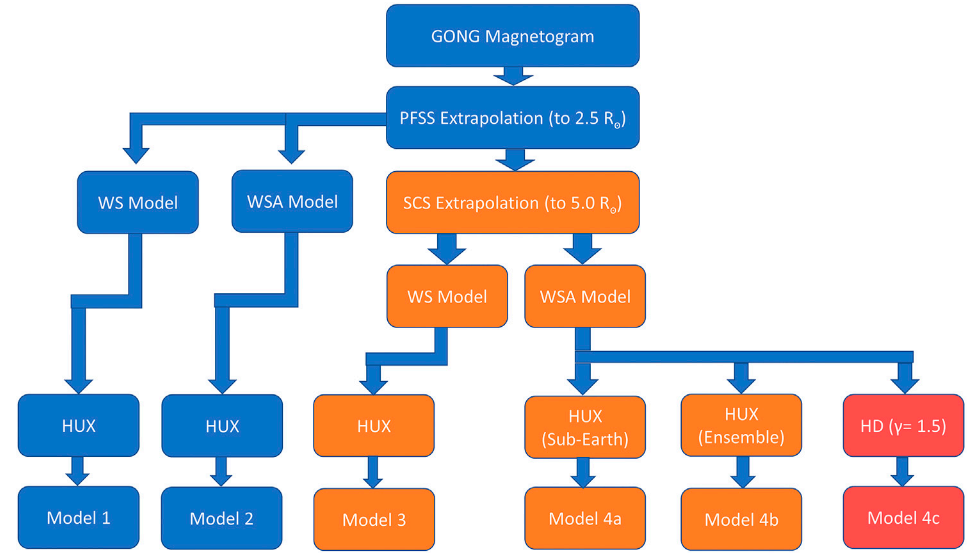

FIGURE 1 | A flowchart of the models that have been utilized in the present work. The various combinations of coronal and inner heliospheric models have been categorized into six different models: 1, 2, 3, 4a, 4b, and 4c.

PFSS+SCS field extrapolation model and WSA velocity empirical relation similar to that used by Model 4a, however, the extrapolation of velocity field is done using physics based hydrodynamic simulations.

2.5. Statistical Measures of Forecast Performance

The performance of a forecast can be determined by comparing the forecast outcome of continuous variables (e.g., velocity) to the observed values. We calculated several scalar measures of forecast accuracy which has previously been used to determine forecast performances by (Reiss et al., 2016; Wu et al., 2020). Given a set of modeled values m_n and a set of corresponding observed values o_n, the Mean Absolute Error (MAE) is given as the arithmetic mean of the absolute values of the differences between the model output and the observed values at each observed data point.

$$MAE = \frac{1}{N}\sum_{n=1}^{N}\left|m_n - o_n\right| \tag{10}$$

The Mean absolute error can be considered as a measure of the overall error in forecast of a model. Another such measure is the Mean Absolute Percentage error (MAPE) which is given by

$$MAPE = \frac{100}{N}\sum_{n=1}^{N}\left|\left(\frac{m_n - o_n}{o_n}\right)\right| \tag{11}$$

The Root Mean Square Error or RMSE is also used sometimes as a performance statistic for a model and is given by

$$RMSE = \sqrt{\frac{1}{N}\sum_{n=1}^{N}\left(m_n - o_n\right)^2} \tag{12}$$

Another important measure in determining the forecast performance is the Pearson Correlation Coefficient (CC) which is a parameter used to estimate the correlation between the observed values and the model values. In addition to this, another measure is the standard deviation of the time series of each of the individual model outputs and its comparison with the estimate from observed data. These measures are estimated for all the models considered and discussed in **Section 3.5** for the three Carrington rotations CR2053, CR2082 and CR2104 considered in our study.

3. RESULTS

In this section, we present our results using the methodology described above for the three case studies spanning the declining phase of cycle 23, near the solar minimum and the rising phase of solar cycle 24. In particular, we consider CR 2053 (from 2007/02/04 to 2007/03/04), CR 2082 (from 2009/04/05 to 2009/05/03) and CR 2104 (from 2010/11/26 to 2010/12/24).We also demonstrate the assessment of performance of the different forecasting models considered for these cases.

3.1. Case Studies

CR2053 represents a relatively quiet phase of the Sun during the decline of the solar cycle number 23. Six active regions were identified regions during the period of CR2053 (Fazakerley et al., 2016) that can also be seen in our input synoptic magnetogram (**Figure 2A**). All the active region lie close to the L1 footprint and thus are expected to have pertinent effects on the solar wind velocities.

As a first step, we calculated the PFSS solution for this Carrington rotation. The GONG magnetogram data which is

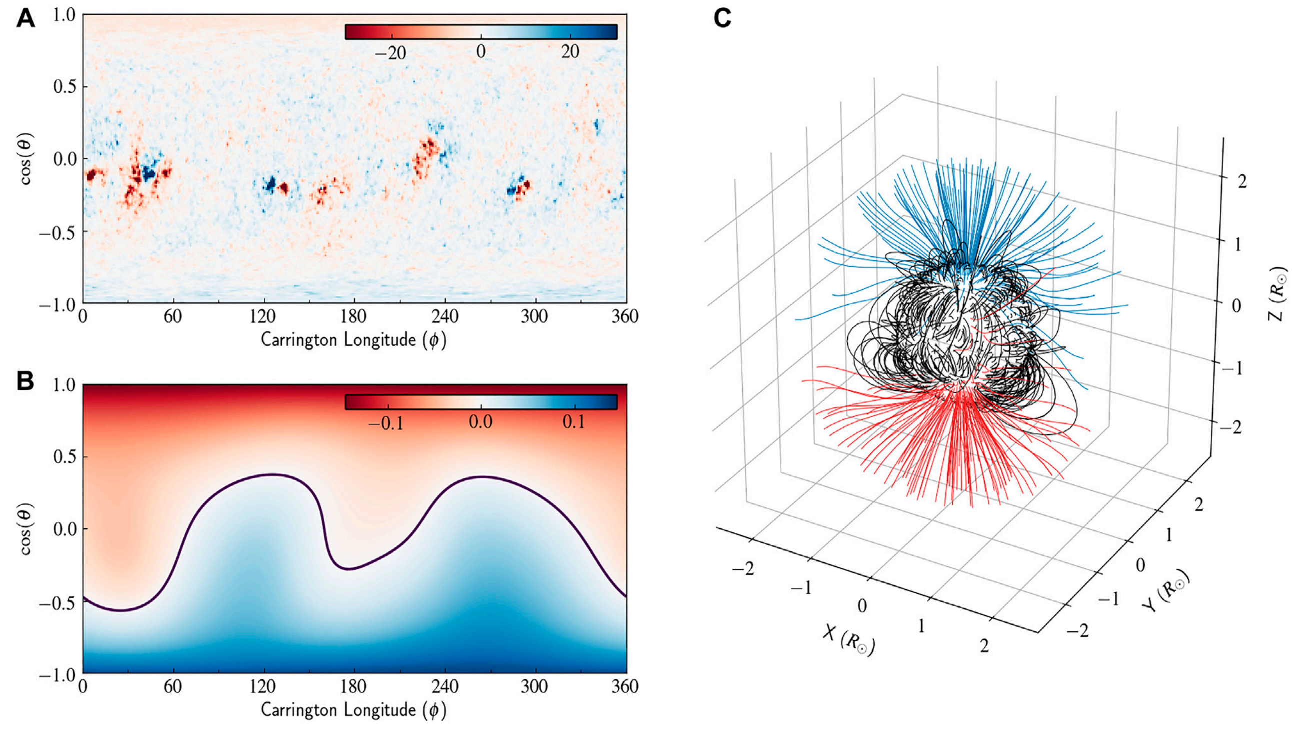

FIGURE 2 | Panel **(A)** shows the photspheric magnetic flux density (in Gauss) from a standard synoptic magnetogram obtained from GONG for CR 2053, panel **(B)** shows the magnetic flux density measured in Gauss obtained from PFSS extrapolation at the source surface (2.5$R_\odot$) with the polarity inversion line shown in violet. The distribution of magnetic field lines obtained from the PFSS solution is plotted in panel **(C)**. The field lines having negative polarity are shown in *blue* and the field lines having positive polarity are shown in *red*. The closed field lines are represented in *black*. The magnetic fields have units in Gauss and the distances on the radial axis are normalized to $R_\odot$.

given as input to PFSS and the output solution obtained using *pfsspy* are shown in **Figure 2**. A 3D map of field lines joining the photosphere to the PFSS source surface at 2.5$R_\odot$ is shown in panel (C) of the same figure. The angle θ on the Y-axis of panels (A) and (B) is related to Carrington latitude (θ_{cr}) as $\theta = -\theta_{\mathrm{cr}} + 90°$. It is evident from the distribution of field lines that few open field lines with both positive (red) and negative (blue) polarities have their foot points located on the photosphere that are close to solar equator. On extending these field lines from source surface up-to 5$R_\odot$ incorporating the SCS model, we obtain a distribution of magnetic field lines at the boundary of coronal domain. Sub-earth field lines are selected from such a distribution and the parameters like the expansion factor (f_s) and their distance to a nearby coronal hole boundary (θ_b) are estimated. These parameters obtained at 5$R_\odot$ are shown in **Figures 3A,B** as a function of Carrington longitude (ϕ). The solar wind velocity obtained from using these parameters in the empirical velocity relations of WS (Model 3) and WSA (Model 4a) are shown in panel (C) in comparison with the observed data. As the models 1 and 2 only rely on the magnetic fields interpolated using PFSS solution, the field parameters are estimated at 2.5$R_\odot$ and used in the empirical relations to estimate the velocity at L1 after HUX extrapolation.

We observe that the WS model gives an inaccurate representation of the solar wind velocities and the contrast between the slow wind and the fast streams are not satisfactorily reproduced. For example, during the first phase of high speed stream peaking on 2007-02-15, variations are observed in values of θ_b of the order of 0.03 radians, while the variation in the expansion factor (f_s) is not significant. This translates into a change in the estimate of the empirical velocity at 5$R_\odot$. The WS extrapolation that is solely dependent on value of f_s do not show appreciable variation resulting in poor prediction for models 1 and 3. Whereas, models 2 and 4a capture the high speed stream due to its dependence on θ_b.

The case of CR2082 also illustrates the quiet phase of the Sun, in-fact it lies at the solar minimum at the end of cycle 23. The input GONG magnetogram is shown in **Figure 4A**. The solution obtained from PFSS at the source surface shows a rather bipolar structure, where the polarity inversion line is relativity straight lying around the co-latitude $\cos(\theta) \sim 0$. The bipolar structure is also evident from the 3D distribution of magnetic field lines connecting the photosphere with the source surface shown in panel (C) of the same figure.

Extrapolated field lines from PFSS solution and ones that are augmented with SCS model are used to obtain the values of the expansion factor $f_s$and coronal hole boundary distance θ_b at sub-earth points. **Figures 5A,B** shows these parameters for the model where field line is extrapolated up-to 5$R_\odot$ using PFSS + SCS. The predicted velocity at L1 using HUX extrapolation is presented in panel (C) of the same figure (magenta line) along with observed value as black dashed line. We note here that the free parameters

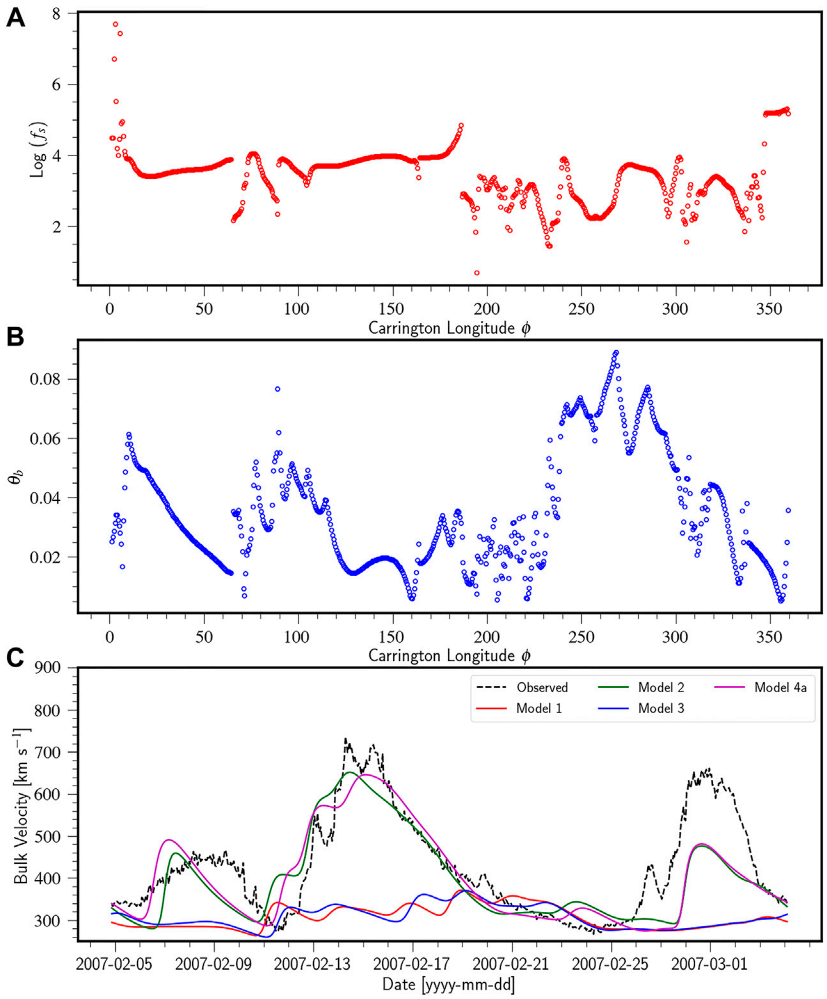

FIGURE 3 | Panel **(A)** and panel **(B)** show plots of θ_b and f_s with respect to the Carrington longitude (ϕ) for CR 2053. These values are estimated for field lines extrapolated using PFSS+SCS upto a reference sphere of radius $5R_{\odot}$. Panel **(C)** shows a comparison of the observed solar wind velocities (taken from OMNI database) and the relative differences between the various outputs of the numerical models at L1 ($\approx 215R_{\odot}$). A comparison with the physics based model (HD) has been shown later on in the results.

needed for empirical relations are kept to be the same as in case of CR2053. Predictions of solar wind flow velocity at L1 from other models 1 (red line), 2 (green line) and 3 (blue line) are also shown in panel (C). Models with WSA extrapolation (models 2, 4a) show a better match with observed values as compared to their counterparts using WS extrapolation (models 1, 3). The predicted velocity for this case shows an offset of about 1–2 days in predicting the high speed streams observed on 2009-04-19.

We have also carried out the same analysis using the same set of model parameters (see **Eq. 3**) for the case of CR 2104 that represents the rising phase of the solar cycle 24. We find similar trend even for this case as solar wind velocity estimates from Model 2 and Model 4a that involves WSA empirical relation presents a better match with observations as compared those obtained from Model 1 and Model 3.

3.2. Ensemble Forecasting

Numerical extrapolation models like HUX are computationally less demanding than HD or 3D MHD models. Such numerical models are thus used to study a large set of initial conditions by a method known as *ensemble forecasting*. Ensemble forecasting has been widely used to constrain terrestrial weather and is an important tool to determine model performance and also helps to set uncertainty bounds to the model output. A solar wind forecast model is considered to be a very uncertain one if the ensemble members produce drastically different results (Reiss et al., 2019).

To study the variations introduced in our model output due to an uncertainty in determining source that contribute to solar wind measured at L1, we created an ensemble of latitudes centered around our expected sub-earth latitude at a distance of ±1°, ±2.5°, ±5°, ±10°, and ±15°. The change in sub-earth latitude

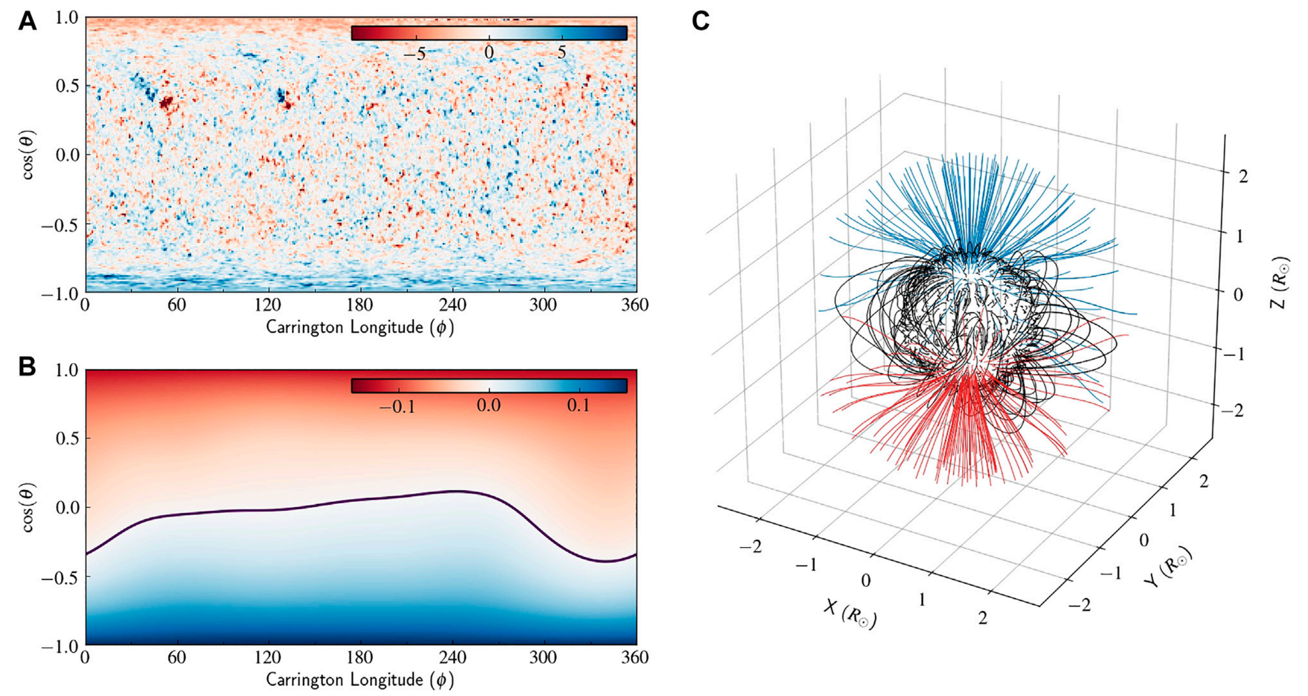

FIGURE 4 | The PFSS input and output in a similar layout as **Figure 2** for CR 2082.

changes the field lines under consideration which in turn effects the parameters associated with the field lines (e.g., θ_b, f_s) that are used as input to the WSA model. This reflects as a change in the final output velocities at L1. Our ensemble of sub-earth points provides us with a set of 11 different velocities at each Carrington longitude. We consider the ensemble median to be the preferred average as an ensemble of sub-earth points are known to produce highly skewed solutions and thus the ensemble mean may not be an accurate representation of the results (Reiss et al., 2019). One should note that the goal of ensemble forecasting in this case is to provide a measure of the uncertainty in the obtained model velocities rather than the ensemble results leading toward a better forecast (Henley and Pope, 2017; Owens and Riley, 2017; Reiss et al., 2019).

Figure 6 shows the forecast obtained from the ensemble of sub-earth latitudes by using Model 4a for all three cases CR 2053, CR 2082, and CR 2104 The dashed line in the figures represent the ensemble median for the respective cases. We have also plotted the velocity obtained by considering zero uncertainties in the the sub-earth latitudes and the same is plotted as a black solid line. The dark and light shades around the median represent the 1σ and 2σvariations, respectively, around the ensemble average. A wider spread in the 2σ values indicates a larger uncertainly in the velocities forecast by the model. In the case of CR2053 and CR2082, a large portion of the observed velocity profile lies within the 2σ error bounds indicating an excellent forecast performance. For the case of CR 2104, the high speed stream is not predicted well with any of our models and some portion of the observed values lie outside of the 2σ error bounds. This is mainly due to the underestimation of standard deviation from the models as compared to observations. However, the structure is well correlated as evident from high CC (**Section 3.5**).

3.3. Assessing Interplanetary Magnetic Field Polarity

In addition to predicting the solar wind velocity, we also assess the polarity of the magnetic field lines at L1 assuming a Parker spiral magnetic field configuration between Sun and Earth [see (Jian et al., 2015)] We evaluate the corresponding longitude at L1 for each CR longitude at $5R_{\odot}$ using the standard streamline equation. The solar wind velocity is assumed to be constant and corresponds to the value obtained using WSA formulation. The polarity of radial magnetic field obtained at $5R_{\odot}$ from PFSS + SCS extrapolation is then coverted to GSE/GSM co-ordinate frame to compare with the observed polarity of B_x component of interplanetary magnetic field at L1 from OMNI database for all three Carrington rotations. The convention of polarity followed at L1 in this case is -1 (outward) and +1 (inward). **Figure 7** shows the observed polarity (daily averaged) of inter-planetary magnetic field B_x in GSE/GSM co-ordinates and its comparison with that obtained for all three cases CR 2053, CR 2082, and CR 2104 using the field extrapolations and velocity from Model 4a. The inter-planetary magnetic field polarity obtained for all three cases show a good agreement with observed daily averaged values. In particular for the case of CR 2104 shown in

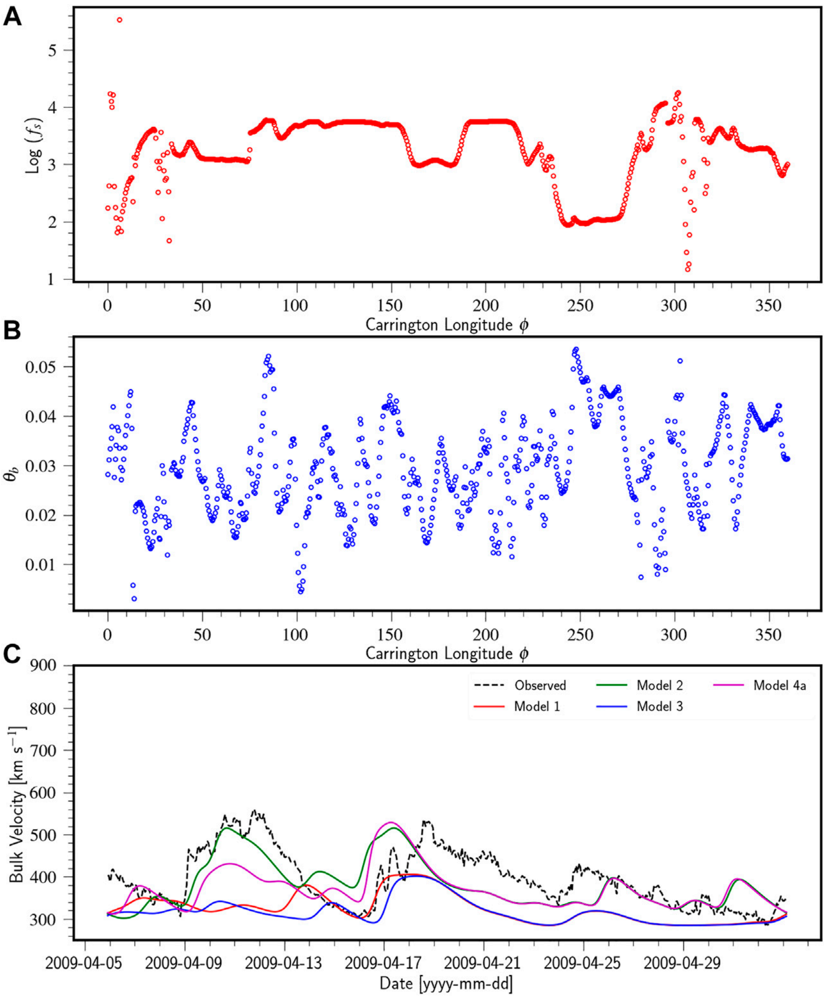

FIGURE 5 | Panel **(A)** and panel **(B)** show plots of θ_b and f_s as a function of the Carrington longitude (ϕ). These values are estimated for field lines extrapolated using PFSS + SCS up-to the reference sphere of radius $5R_\odot$ for CR 2082. Panel **(C)** shows a comparison of the observed solar wind velocities (taken from OMNI database) and the relative differences between the various outputs of the numerical models at L1 ($\approx 215R_\odot$).

Figure 7C, significant agreement exists between model prediction and observation.

3.4. Forecasting From Physics Based Modeling

Two dimensional hydrodynamic simulation runs with initial conditions described in **Section 2.3.2** provide a time dependent solar wind forecasting framework. Plasma is injected in the computational domain from the inner rotating radial boundary at each time step. Empirical values of velocities obtained from the WSA model using the sub-earth point field lines are used as input conditions for the hydrodynamic simulations in the inner boundary placed at $5R_\odot$.

In the initial transient phase, the plasma propagates outwards toward the outer boundary from where it leaves the domain. Subsequent to this transient phase, a steady state solar wind is established in the domain. The steady state radial velocity [X-Y plane] in units of km s^{-1} from the simulation after a one solar rotation time period of 27.3 days is shown in the **Figure 8A** for CR2053. The black dashed circle represents the radial distance corresponding to L1 point (~ $1AU$). Panels (B) and (C) shows the proton temperature in units of MK and number density (cm^{-3}) map for the same time step, respectively. One can distinctively observe a spiral pattern whereby high velocity streams tend to have higher proton temperature and lower density values than its surrounding low or moderate velocity streams. The velocity measured at L1 from simulations during the considered Carrington rotation period is shown as blue solid line in panel D. In comparison, hourly averaged observed values are shown in black dashed lines, while velocity estimates from models 4a and 4b are shown in magneta solid and green dashed lines, respectively, for comparison. The velocity estimate from the simulation runs have more variations as compared to its counterparts from model 4a and 4b. This comparison of models for velocity prediction demonstrates that addition of

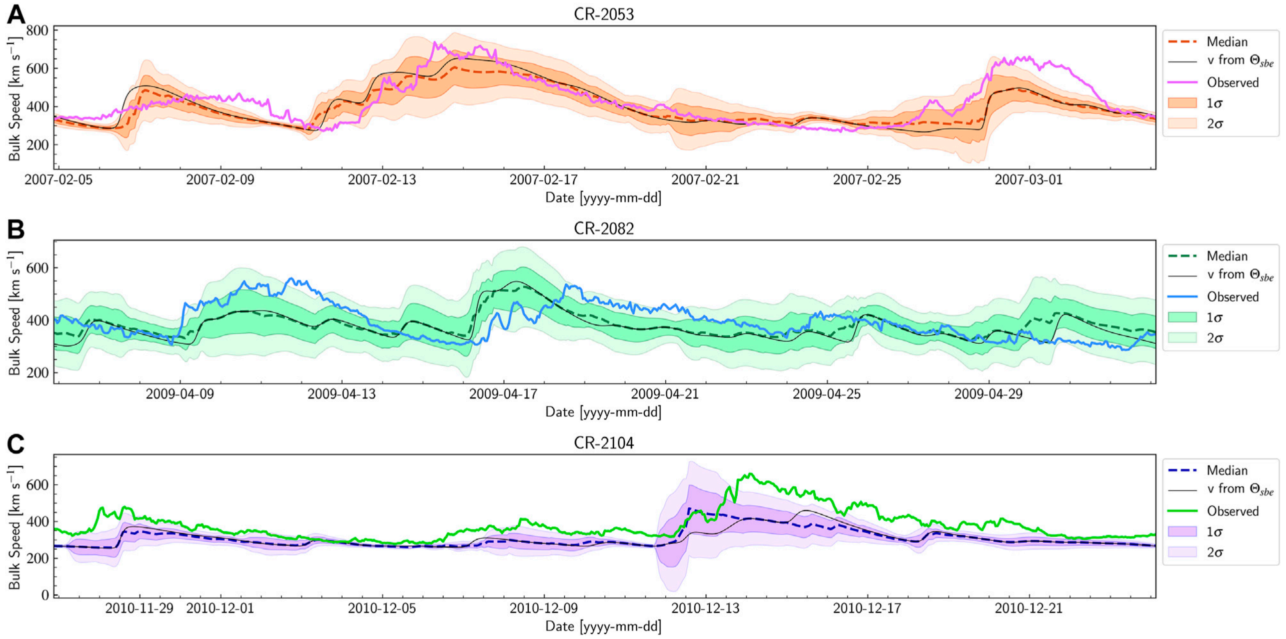

FIGURE 6 | A plot of the ensemble forecast for CR 2053 (panel **(A)**), CR 2082 (panel **(B)**) and CR 2104 (panel **(C)**) along with the observed velocities. The black solid line in each plot represents the velocities obtained without incorporating the uncertainty. The dashed line in each of the plots represent the respective ensemble median values and the darker and lighter shades around the median values represent the 1σ and 2σ error expected during the forecast, respectively.

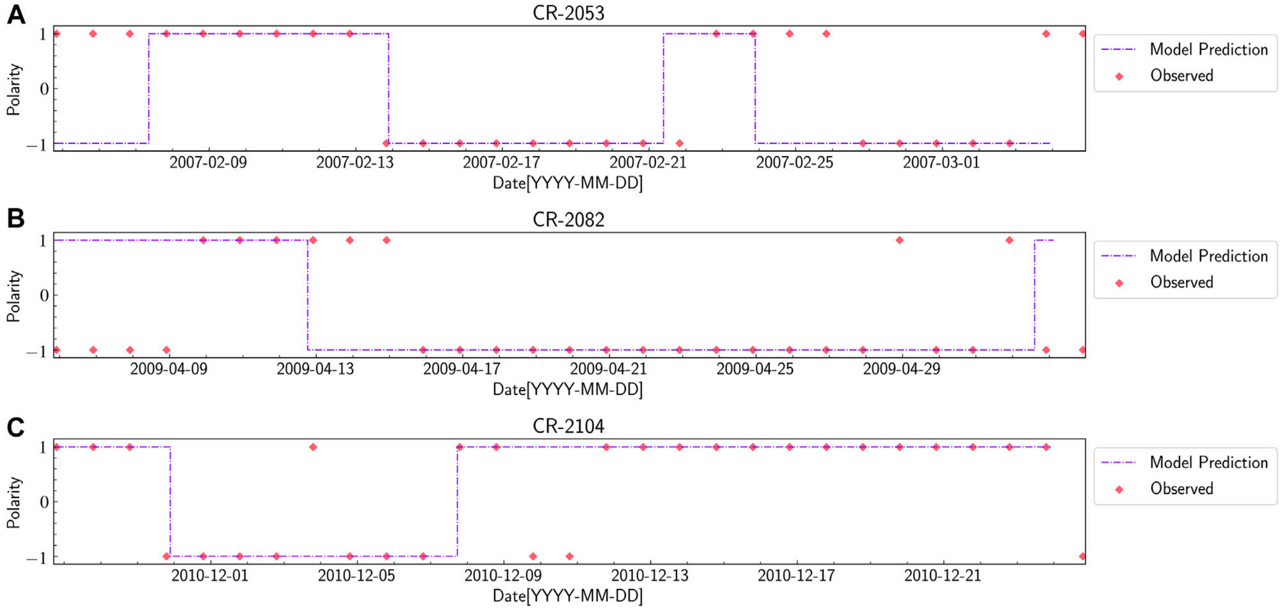

FIGURE 7 | A plot showing the magnetic field polarity forecast at L1 for CR 2053 **(A)**, CR 2082 **(B)** and CR 2104 **(C)** along with the observed values from OMNI database. The red diamonds represent the daily average value of polarity of radial component of the interplanetary magnetic field at L1. The purple dashed line are the polarity of the transformed radial component of field lines at L1 in the GSE/GSM co-ordinate frame.

pressure gradient term and incorporating the energy equation captures the interaction of streams leading to intermittent variable patterns. Such patterns do not appear for velocities obtained from model 4a and 4b as the kinematic extrapolation disregards physical effects due to presence of velocity shear and pressure gradient terms. Statistical analysis of velocity pattern at

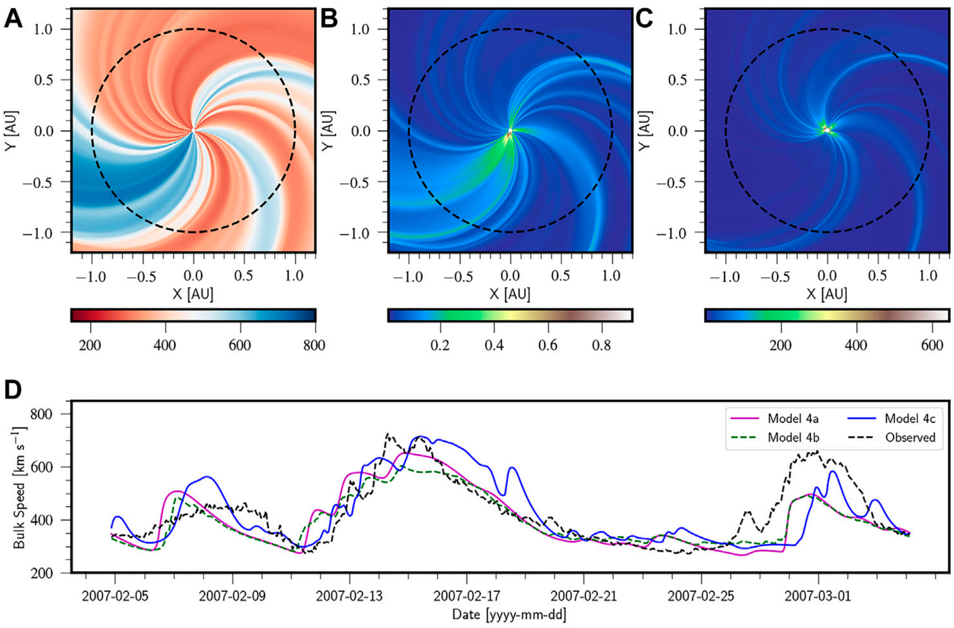

FIGURE 8 | Quantities of the solar wind obtained from the physics based model **(A)** radial velocity, **(B)** proton temperature in MK, and **(C)** number density in cm^{-3}, the black dashed line in each of these panels represents the L1 position at 1 AU. Panel **(D)** shows comparison of variation in bulk speed in km s^{-1} at L1 point for CR 2053 for Models 4a, 4b and 4c with hourly averaged observed values. The *X*-axis in panel **(D)** represents the time in yyyy-mm-dd format.

TABLE 1 | Performance of various forecast models for CR 2053.

σ_{obs} =119.4 km s^{-1}	Model 1	Model 2	Model 3	Model 4a	Model 4b	Model 4c
σ	31.1	105.8	30.1	109.9	90.8	123.6
MAE	131.1	60.8	125.0	59.2	57.8	66.9
MAPE	26.5	14.2	24.8	13.5	12.9	14.9
RMSE	171.8	79.4	169.5	77.9	75.5	88.8
CC	0.00	0.79	0.04	0.79	0.81	0.73

TABLE 2 | Performance of various forecast models for CR 2082.

σ_{obs} = 66.0 km s^{-1}	Model 1	Model 2	Model 3	Model 4a	Model 4b	Model 4c
σ	37.1	60.8	32.2	51.7	42.9	59.4
MAE	73.0	52.1	79.3	56.4	54.6	52.8
MAPE	17.1	13.3	18.7	13.8	13.6	13.3
RMSE	92.1	63.3	95.8	69.3	66.5	65.3
CC	0.42	0.52	0.54	0.39	0.34	0.46

L1 obtained from HD simulations indicate a good match with observed values (see **Table 1**). Similar variable velocity pattern is also obtained after using the empirical velocity values from CR2082 in the inner boundary (figure not shown). Statistical comparison with other models and observed values is presented in **Table 2**. The advantage of such physics based model is that it accounts for solar wind acceleration and other physical effects which the HUX model lacks. Further as the 2D simulations also solves the energy conservation equation with appropriate polytropic equation of state, it has the ability to estimate the proton temperature of the flow at each point in the computational domain. A comparison of proton temperature in MK obtained from simulation run for CR2053 (red solid line) with hourly averaged observed values (black dashed lines) is shown in **Figure 9A**. The statistical measures assessing the forecasting performance are mentioned in the panel. The curves show a considerable match with a correlation coefficient 0.53 and a RMSE of 0.08 MK. For the case of CR2082 shown in panel (B) of the same figure, the correlation coefficient is 0.32 and RMSE of 0.04 MK. The estimates of standard deviation from modeled and observed data are comparable for the case of CR2082 as well.

3.5. Quantifying Predictive Performance Using Statistical Analysis

Statistical measures (see **Section 2.5**) quantifying forecast performance for CR 2053, CR 2082, and CR 2104 are presented in **Table 1**, **2**, and **3**, respectively. The standard deviation of the observed time series for CR2053 is 119.4 km s^{-1}. Model 4c was able to reproduce this standard deviation quite satisfactorily (123.6 km s^{-1}). All models for CR 2053 involving the WS model failed to produce reasonable agreement with the observations, which can be inferred from the extremely low value of the correlation coefficient (~0). We believe that this is due to the proximity of the coronal holes to the equator, whereby open field lines emerging from these holes drive high speed streams. The WS empirical model disregards the size of coronal holes in its empirical relation and fails to capture this effect. The presence of a significant number of coronal holes on

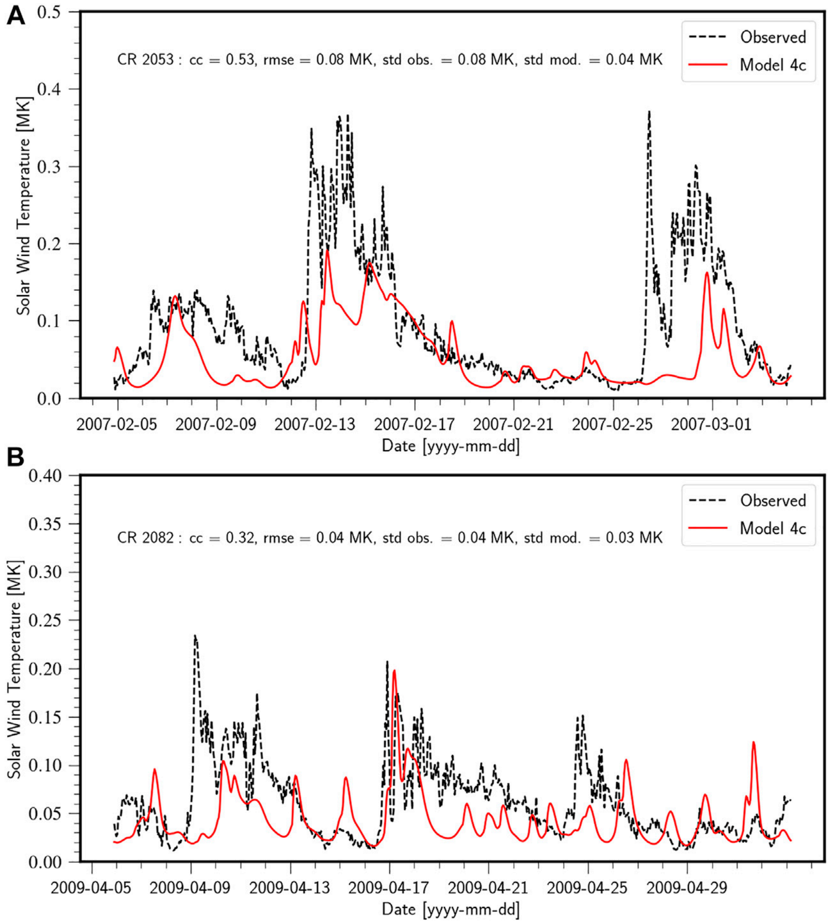

FIGURE 9 | (A) Comparison of the proton temperature estimated from the model 4c (red solid line) at Lagrangian point L1 with hourly averaged observed values (black dashed line) obtained from OMNI database for CR2053. The statistical analysis of the forecast performance are mentioned in the panel. **(B)** Comparison of proton temperature estimates from model 4c and observations for the case of CR 2082. The color scheme is same as the panel above.

TABLE 3 | Performance of various forecast models for CR 2104.

σ_{obs} = 82.2 km s^{-1}	Model 1	Model 2	Model 3	Model 4a	Model 4b	Model 4c
σ	26.0	57.0	27.9	47.4	47.6	49.1
MAE	93.6	68.7	94.3	72.3	74.0	65.7
MAPE	21.9	17.2	22.4	17.8	18.1	16.0
RMSE	123.6	79.2	118.6	87.2	90.0	81.1
CC	0.00	0.88	0.35	0.84	0.79	0.85

the magnetogram that are close to the sub-earth latitudes thus necessitates the use of the WSA model for velocity mapping on the inner boundary. CR2082 on the other hand has a significantly lesser number of coronal holes (Petrie and Haislmaier, 2013). And thus even the models involving the WS velocity mapping show acceptable CC values (0.42–0.54). The highest CC for CR 2053 is produced by model 4b (CC = 0.81) which represents the ensemble median of the sub-earth latitude variations, however the same cannot be said for CR 2082 as all the other models produce a greater CC and lower error values than that of the ensemble median. This reinforces the statement that the ensemble average does not always produce a more accurate representation of the velocity profile.

A graphical representation and analysis of various forecasting models implemented in this work are represented in a Taylor diagram (Taylor, 2001). The Taylor plots for CR 2053, CR 2082, and CR 2104 are given in **Figure 10** The radial distance from the origin represents the standard deviation, the azimuthal coordinate represent the correlation coefficient (CC). In addition to this, one more set of arcs are drawn, centered at the reference (observed) standard deviation on the X axis that represent the RMS error for the models. In general a solar wind model is considered to be a good model if it has a high correlation coefficient (CC), low RMS error, and having a similar standard deviation to the observed time series of velocities (Reiss et al., 2016) and in a Taylor plot it would lie close to the smallest circle on the X axis. For the case of CR 2053, Model 1 and Model 3 lie very close to the vertical axis indicating very low CC value and thus are considered to have poor forecast performance. Model 4b has the highest CC value and comparatively low errors, but it lies relatively far from the observed standard deviation curve. The

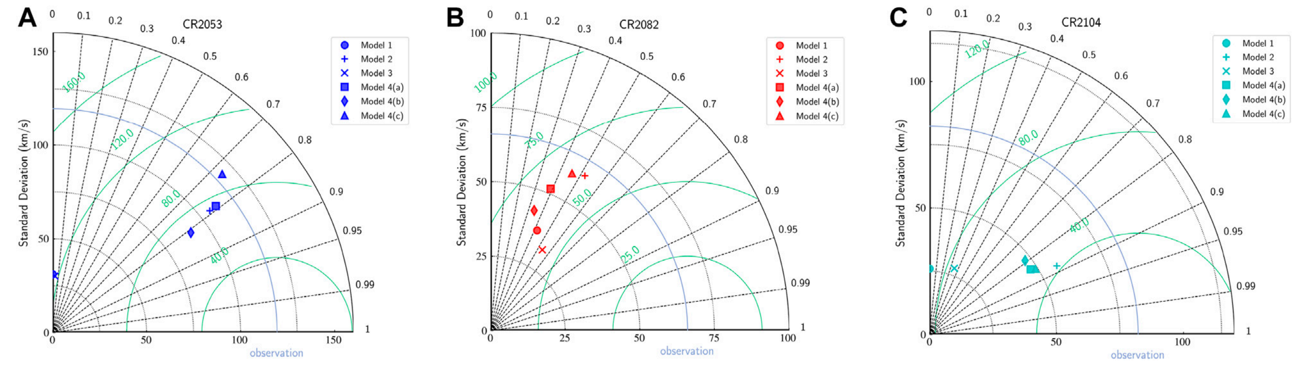

FIGURE 10 | Taylor Plots for CR 2053 **(A)**, CR 2082 **(B)** and CR 2104 **(C)** summarizing the performance of various models in each case. The blue curve concentric to the standard deviation curves represents the standard deviation of the observed time series. The green curves with centers on the *X* axis serve as ticks for the RMSE.

physics based models, Model 4c is seen to have standard deviation profiles well in agreement with the observed values along with a good CC. We thus assert that Model 4b and 4c are the best representations of the velocity profiles for CR 2053. For the case of CR 2082, Model 4c and Model 2 has a standard deviation closest to that of the observed value of ~60 km s^{-1} and Model 2 has the lowest error values (in terms of RMSE, MAE and MAPE). The CC of model 3 is one of the highest in the models considered followed closely by Model 2. Model 3 however has larger values of all the errors considered showing that even though its correlated well with the observed values, the model is prone to errors which would result in inaccurate output solar wind velocity profiles. Model 4a, 4b, and 4c have similar but low values of MAE, MAPE and RMSE, and CC lying in the range of (~0.34–0.46). Based on the above analysis for the assumed set of WSA parameters, Model 2 performs better for CR2082 closely followed by models 4c and 4a. For the case of CR 2104, the predicted standard deviation is less as compared to the observed values for all the models. The predictions from model 1 and 3 have low CC value and RMSE around 120 km/s and indicating a poor forecast performance. The CC of models 2, 4a, 4b, and 4c is as high as 0.8 and the RMSE for these models ranges between 80 and 90 km s. This suggests these models have a better forecast performance as was the case in CR 2053.

4. DISCUSSIONS AND SUMMARY

In this pilot study, we have developed a python module toward constructing a robust framework for accurate predictions of a steady state background solar wind model using various empirical and extrapolation formulations. This framework is also integrated with physics based modeling using PLUTO code. The entire workflow is a combination of a) extrapolating the magnetic fields to the outer coronal domain using magnetic models such as PFSS and SCS, b) mapping the velocities in the outer coronal domain using models such as WS and WSA, and c) extrapolating the velocities to L1 using extrapolation techniques such as HUX as well as hydrodynamic propagation of the velocities using PLUTO. We have studied various combinations of the coronal magnetic models as well as velocity extrapolation models in view of three different Carrington rotations, CR 2053, CR 2082, and CR 2104. We were successfully able to generate velocity profiles well in agreement with the observed values.

Even though the the models involving the WS velocity mapping performed relatively well for the case of CR 2082 when compared to the equivalent models of the other CRs in this study, it performed very poorly when applied to CR 2053 and CR 2104. The WSA model on the other hand has shown consistently superior performance for all the CRs with lesser error measures in these cases than the WS model. The WS model also failed to capture the contrast between the slow and fast solar wind streams and thus produced velocity profiles with significantly lesser standard deviation than the observed profile. We infer from this that the WSA model is superior to the WS model for the cases and parameters considered in this work.

In general, the models with a combination of PFSS + SCS for magnetic field extrapolation paired with the WSA model for velocity mapping (models 4a, 4b, and 4c) had the best performance in all the cases, CR 2053, CR 2082 as well as CR 2104. This can be seen as near identical standard deviations of the output velocity pattern in Model 4a and Model 4c paired with a very high correlation coefficient (~0.73–0.81) and relatively low errors for the case of CR 2053 (**Table 1**) and CR 2104 (**Table 3**). For CR 2082, Model 4a and Model 4c had standard deviations which are close to that of the observed profile. We note that Model 3 performed quite well in case of CR 2082 with a high CC (~0.53) but with higher errors than the other models. However, it showed a lack of consistency in performance with very poor results in case of CR 2053. We observe that Model 2 also performed well for all three CRs which can be seen in its high CC values and low errors.

Model 4c that employs PFSS+SCS and WSA velocity empirical relation with physics based extrapolation, gives us an additional advantage of being able to determine the thermal properties of the solar wind which also showed good correlation with the observed values (see **Figure 9**). This model also naturally takes into account the acceleration of the solar wind during its propagation. The standard deviation of the Model 4c velocity profile also had good agreement with the observations with high CC values (0.73 for CR 2053, 0.46 for CR 2082 and 0.85 for CR 2104). The Model 4c thus has its own pros and cons. The pros being the ability to determine additional solar wind properties than what HUX or HUXt can offer, and the cons being that it takes significantly more computational resources.

Ensemble forecasting helps provide a rather clear quantification of the uncertainty associated with the predictions. We have chosen a total of 11 realisations covering a latitude range of $\pm 15°$ about the expected sub-earth latitude. We can assert that the variation helped us accurately capture the uncertainty in the predictions as a bulk of the observed velocity curve was entirely within the 2σ bounds of the model output for CR 2053 as well as CR 2082 (**Figure 6**). Underestimation in the solar wind velocity is seen in case of CR 2104 particularly for the high speeds streams. We also note that the ensemble median did not necessarily provide a better estimate of the model velocity and in general, had sub-par performance when compared to some of the other models (Model 4a and Model 4c). The radial magnetic field polarity obtained at $5R_{\odot}$ has also been extrapolated to L1 assuming a Parker spiral field profile for Model 4a. A good agreement between the observed and predicted field polarity is seen in all three cases with CR 2082 showing misses only for three data points obtained from observations.

Even though ensemble forecasting can provide a rather clear statistical uncertainty prediction of the model, it has been seen that various other uncertainties can creep in that are solely dependent on the choice of the input magnetograms. Riley et al. (2014) highlighted that magnetograms from various observatories show significant differences in magnetic field measurements. In-spite of the fact that one can quantify the conversion factors between various independent datasets, there is no particular observatory that can produce a *ground truth* dataset for the input magnetograms. Additionally, one can improve the WSA model performance using time-dependent flux transport model based magnetograms (e.g., Schrijver and De Rosa, 2003; Arge et al., 2010; Arge et al., 2013). Quantifying the effects of input magnetograms on model performance is beyond the scope of this paper and shall be addressed in a future study.

The statistical parameters represented in the Taylor diagrams indicate the accuracy of our current forecasting framework. Typically, for an accurate forecasting model, low RMSE, high CC and similar standard deviation with observed values are expected. The forecasting presented in this paper uses the same set of parameters (except θ_b and f_s) for empirical velocity estimate of all the Carrington rotations. We find that these parameters give a more accurate forecast of the bulk solar wind speeds at L1 for the case of CR 2053. Even though the same parameters result in good forecast for CR 2082 and CR 2104 as well, we believe that the performance may be improved with a changes in the free parameters and radial distance of reference sphere (Wu et al., 2020).

We would like to point out that the free parameters used for the WS and WSA empirical relations cannot be universally applied for all CRs and must be individually tuned for a particular case scenario. This is evident from our use of the same set of free parameters for all the CRs which results in significantly different performances. Additionally, the statistical estimates have indicated that in case of CR 2082, the model with PFSS+WSA have performed slightly better than its counterpart including SCS. In this particular case, this could perhaps be related to over-estimation of magnetic field lines contributing to solar wind speeds at L1 by SCS. However, through the ensemble modeling we have demonstrated the estimation from Model 4a is within the 2σ bounds. Improving the accuracy and performance of SCS extrapolation will be considered in our further studies.

The caveat of hydrodynamic models (Model 4c) is that it solves the equations on a plane and does not contain the magnetic information of the Sun–Earth system on which state-of-the-art 3D MHD model are based. However, even without the magnetic field information and having a 2D geometry, the HD models capture many important aspects of the solar wind. Model 4c facilitate better physical insight in the behavior of solar wind than the HUX models (4a and 4b). Model 4c (HD) can thus be seen as a halfway point between HUX and full MHD models.

In summary, we have successfully produced velocity maps for the cases considered and also matched our results with additional observable eg, proton temperature. This pilot study is the first step in developing an indigenous space weather framework which is an absolute need of hour as Indian Space Research Organization (ISRO) is coming up with Aditya-L1 to study the properties of Sun at L1 (https://www.isro.gov.in/aditya-l1-first-indian-mission-to-study-sun). A full-fledged 3D-MHD run of solar wind using PLUTO code will be carried out in our subsequent paper for predicting other observable quantities like the number density and IMF magnetic field. Further, including the propagation of CMEs in such a realistic solar wind background would be carried out with an aim to study its impact on space weather.

DATA AVAILABILITY STATEMENT

The original contributions presented in the study are included in the article/supplementary materials, further inquiries can be directed to the corresponding author.

AUTHOR CONTRIBUTIONS

SK developed the python pipeline that was able to obtain the velocity of solar wind at L1 for various models following the flowchart described in the paper. AP utilised the data and formulated the statistical framework for quantifying the performance of forecasting. He also contributed significantly in writing the text. BV did the overall supervision of the work and contributed in integrating the data from python pipeline into PLUTO code for physics based simulations runs.

ACKNOWLEDGMENTS

The authors acknowledge the comments from the referees that have helped in significantly improving the manuscript. We also thank the support from Indian Institute of Technology Indore. The calculations are done using the computational resources available in the institute. BV is heading the Max Planck Partner Group at IIT Indore and would like to thank the same for financial support.

REFERENCES

Altschuler, M. D., and Newkirk, G. (1969). Magnetic fields and the structure of the solar corona. I: Methods of calculating coronal fields. *Sol. Phys.* 9, 131–149. doi:10.1007/BF00145734

Arge, C. N., and Pizzo, V. J. (2000). Improvement in the prediction of solar wind conditions using near-real time solar magnetic field updates. *J. Geophys. Res. Space Phys.* 105, 10465–10480. doi:10.1029/1999JA000262

Arge, C. N., Odstrcil, D., Pizzo, V. J., and Mayer, L. R. (2003). "Improved method for specifying solar wind speed near the sun," in Solar wind ten of American Institute of Physics conference series. Editors M. Velli, R. Bruno, F. Malara, and B. Bucci. Vol. 679, 190–193. doi:10.1063/1.1618574

Arge, C. N., Henney, C. J., Koller, J., Compeau, C. R., Young, S., MacKenzie, D., et al. (2010). "Air force data assimilative photospheric Flux transport (ADAPT) model," in Twelfth international solar wind conference of American Institute of Physics conference series. Editors M. Maksimovic, K. Issautier, N. Meyer-Vernet, M. Moncuquet, and F. Pantellini, Vol. 1216, 343–346. doi:10.1063/1.3395870

Arge, C. N., Henney, C. J., Hernandez, I. G., Toussaint, W. A., Koller, J., and Godinez, H. C. (2013). "Modeling the corona and solar wind using ADAPT maps that include far-side observations," in Solar wind 13 of American Institute of Physics conference series. Editors G. P. Zank, J. Borovsky, R. Bruno, J. Cirtain, S. Cranmer, H. Elliott, et al., Vol. 1539, 11–14. doi:10.1063/1.4810977

Bharati Das, S., Basak, A., Nandy, D., and Vaidya, B. (2019). Modeling star-planet interactions in far-out planetary and exoplanetary systems. *Astrophys. J.* 877, 80. doi:10.3847/1538-4357/ab18ad

Downs, C., Lionello, R., Mikić, Z., Linker, J. A., and Velli, M. (2016). Closed-field coronal heating driven by wave turbulence. *Astrophys. J.* 832, 180. doi:10.3847/0004-637X/832/2/180

Fazakerley, A. N., Harra, L. K., and van Driel-Gesztelyi, L. (2016). An investigation of the sources of earth-directed solar wind during Carrington rotation 2053. *Astrophys. J.* 823, 145. doi:10.3847/0004-637X/823/2/145

Henley, E. M., and Pope, E. C. D. (2017). Cost-loss analysis of ensemble solar wind forecasting: space weather use of terrestrial weather tools. *Space Weather* 15, 1562–1566. doi:10.1002/2017SW001758

Jian, L. K., MacNeice, P. J., Taktakishvili, A., Odstrcil, D., Jackson, B., Yu, H.-S., et al. (2015). Validation for solar wind prediction at earth: comparison of coronal and heliospheric models installed at the ccmc. *Space Weather* 13, 316–338. doi:10.1002/2015SW001174

Lionello, R., Linker, J. A., and Mikić, Z. (2009). Multispectral emission of the sun during the first whole sun month: magnetohydrodynamic simulations. *Astrophys. J.* 690, 902–912. doi:10.1088/0004-637X/690/1/902

MacNeice, P., Jian, L. K., Antiochos, S. K., Arge, C. N., Bussy-Virat, C. D., DeRosa, M. L., et al. (2018). Assessing the quality of models of the ambient solar wind. *Space Weather* 16, 1644–1667. doi:10.1029/2018SW002040

McGregor, S. L., Hughes, W. J., Arge, C. N., and Owens, M. J. (2008). Analysis of the magnetic field discontinuity at the potential fieldsource surface and schatten current sheet interface in the Wang–Sheeley–Arge model. *J. Geophys. Res.* 113, 23–27. doi:10.1029/2007ja012330

Mignone, A., Bodo, G., Massaglia, S., Matsakos, T., Tesileanu, O., Zanni, C., et al. (2007). PLUTO: a numerical code for computational astrophysics. *Astrophys. J. Suppl. Ser.* 170, 228–242. doi:10.1086/513316

Mignone, A., Bodo, G., Vaidya, B., and Mattia, G. (2018). A particle module for the PLUTO code. I. an implementation of the MHDPIC equations. *Astrophys. J.* 859, 13. doi:10.3847/1538-4357/aabccd

Mignone, A., Zanni, C., Tzeferacos, P., van Straalen, B., Colella, P., and Bodo, G. (2012). The PLUTO code for adaptive mesh computations in astrophysical fluid dynamics. *Astrophys. J. Suppl. Ser.* 198, 7. doi:10.1088/0067-0049/198/1/7

Odstrcil, D., Riley, P., and Zhao, X. P. (2004). Numerical simulation of the 12 May 1997 interplanetary CME event. *J. Geophys. Res. Space Phys.* 109, A02116. doi:10.1029/2003JA010135

Owens, M. J., and Forsyth, R. J. (2013). The heliospheric magnetic field. *Living Rev. Sol. Phys.* 10, 5. doi:10.12942/lrsp-2013-5

Owens, M. J., and Riley, P. (2017). Probabilistic solar wind Forecasting using large ensembles of near-sun conditions with a simple one-dimensional "upwind" scheme. *Space Weather* 15, 1461–1474. doi:10.1002/2017SW001679

Owens, M., Lang, M., Barnard, L., Riley, P., Ben-Nun, M., Scott, C. J., et al. (2020). A computationally efficient, time-dependent model of the solar wind for use as a surrogate to three-dimensional numerical magnetohydrodynamic simulations. *Sol. Phys.* 295, 43. doi:10.1007/s11207-020-01605-3

Petrie, G. J. D., and Haislmaier, K. J. (2013). Low-latitude coronal holes, decaying active regions, and global coronal magnetic structure. *Astrophys. J.* 775, 100. doi:10.1088/0004-637X/775/2/100

Pomoell, J., and Poedts, S. (2018). EUHFORIA: European heliospheric forecasting information asset. *J. Space Weather Space Clim.* 8, A35. doi:10.1051/swsc/2018020

Reale, F., Orlando, S., Guarrasi, M., Mignone, A., Peres, G., Hood, A. W., et al. (2016). 3D MHD modeling of twisted coronal loops. *Astrophys. J.* 830, 21. doi:10.3847/0004-637X/830/1/21

Reiss, M. A., Temmer, M., Veronig, A. M., Nikolic, L., Vennerstrom, S., Schöngassner, F., et al. (2016). Verification of high-speed solar wind stream forecasts using operational solar wind models. *Space Weather* 14, 495–510. doi:10.1002/2016SW001390

Reiss, M. A., MacNeice, P. J., Mays, L. M., Arge, C. N., Möstl, C., Nikolic, L., et al. (2019). Forecasting the ambient solar wind with numerical models. I. on the implementation of an operational framework. *Astrophys. J. Suppl.* 240, 35. doi:10.3847/1538-4365/aaf8b3

Réville, V., Velli, M., Rouillard, A. P., Lavraud, B., Tenerani, A., Shi, C., et al. (2020). Tearing instability and periodic density perturbations in the slow solar wind. *Astrophys. J.* 895, L20. doi:10.3847/2041-8213/ab911d

Richardson, I. G., Cliver, E. W., and Cane, H. V. (2000). Sources of geomagnetic activity over the solar cycle: relative importance of coronal mass ejections, high-speed streams, and slow solar wind. *J. Geophys. Res.: Space Phys.* 105, 18203–18213. doi:10.1029/1999JA000400

Riley, P., and Lionello, R. (2011). Mapping solar wind streams from the sun to 1 au: a comparison of techniques. *Sol. Phys.* 270 (2), 575–592. doi:10.1007/s11207-011-9766-x

Riley, P., Ben-Nun, M., Linker, J. A., Mikic, Z., Svalgaard, L., Harvey, J., et al. (2014). A multi-observatory inter-comparison of line-of-sight synoptic solar magnetograms. *Astrophys. J.* 289, 769–792. doi:10.1007/s11207-013-0353-1

Riley, P., Linker, J. A., and Arge, C. N. (2015). On the role played by magnetic expansion factor in the prediction of solar wind speed. *Space Weather* 13, 154–169. doi:10.1002/2014SW001144

Sarkar, A., Vaidya, B., Hazra, S., and Bhattacharyya, J. (2017). Simulating coronal loop implosion and compressible wave modes in a flare hit active region. ArXiv e-prints.

Schatten, K. H. (1972). Current sheet magnetic model for the solar corona. *NASA Special Publ.* 308, 44.

Schatten, K. H., Wilcox, J. M., and Ness, N. F. (1968). A model of interplanetary and coronal magnetic fields. *Sol. Phys.* 6, 442–455. doi:10.1007/BF00146478

Schrijver, C. J., and De Rosa, M. L. (2003). Photospheric and heliospheric magnetic fields. *Astrophys. J.* 212, 165–200. doi:10.1023/A:1022908504100

Schwenn, R. (2006). Space weather: the solar perspective. *Living Rev. Sol. Phys.* 3, 2. doi:10.12942/lrsp-2006-2

Sokolov, I. V., van der Holst, B., Manchester, W. B., Ozturk, D. C. S., Szente, J., Taktakishvili, A. R., et al. (2016). *Threaded-field-lines model for the low solar corona powered by the Alfven wave turbulence.* arXiv:1609.04379.

Stansby, D. (2019). dstansby/pfsspy: pfsspy 0.1.2. Zenodo doi:10.5281/zenodo.2566462

Taylor, K. E. (2001). Summarizing multiple aspects of model performance in a single diagram. *J. Geophys. Res.: Atmosphere* 106, 7183–7192. doi:10.1029/2000JD900719

Tóth, G., van der Holst, B., Sokolov, I. V., De Zeeuw, D. L., Gombosi, T. I., Fang, F., et al. (2012). Adaptive numerical algorithms in space weather modeling. *J. Comput. Phys.* 231, 870–903. doi:10.1016/j.jcp.2011.02.006

Usmanov, A. V., Goldstein, M. L., and Matthaeus, W. H. (2014). Three-fluid, three-dimensional magnetohydrodynamic solar wind model with eddy viscosity and turbulent resistivity. *Astrophys. J.* 788, 43. doi:10.1088/0004-637X/788/1/43

Usmanov, A. V., Matthaeus, W. H., Goldstein, M. L., and Chhiber, R. (2018). The steady global corona and solar wind: a three-dimensional MHD simulation with turbulence. *Transp. Heat.* 865, 25. doi:10.3847/1538-4357/aad687

Vaidya, B., Prasad, D., Mignone, A., Sharma, P., and Rickler, L. (2017). Scalable explicit implementation of anisotropic diffusion with Runge-Kutta-Legendre super-time stepping. *Astrophys. J.* 472, 3147–3160. doi:10.1093/mnras/stx2176

Vaidya, B., Mignone, A., Bodo, G., Rossi, P., and Massaglia, S. (2018). *A particle module for the PLUTO code: II-hybrid framework for modeling non-thermal emission from relativistic magnetized flows*. ArXiv e-prints

Wang, Y. M., and Sheeley, N. R., Jr. (1989). Solar wind speed and coronal flux-tube expansion. *Astrophys. J.* 355, 726–732. doi:10.1086/168805.

Wang, Y. M., and Sheeley, N. R., Jr. (1995). Solar implications of ULYSSES interplanetary field measurements. 447, L143. doi:10.1086/309578

Wiengarten, T., Oughton, S., Engelbrecht, N. E., Fichtner, H., Kleimann, J., and Scherer, K. (2016). A generalized two-component model of solar wind turbulence and ab initio diffusion mean-Free paths and drift lengthscales of cosmic rays. *Astrophys. J.* 833, 17. doi:10.3847/0004-637X/833/1/17

Wu, C.-C., Liou, K., Wood, B. E., Plunkett, S., Socker, D., Wang, Y. M., et al. (2020). Modeling inner boundary values at 18 solar radii during solar quiet time for global three-dimensional time-dependent magnetohydrodynamic numerical simulation. *J. Atmos. Sol. Terr. Phys.* 201, 105211. doi:10.1016/j.jastp.2020.105211

Yeates, A. (2018). antyeates1983/pfss: first release of pfss code. *Zenodo* 19, 23–29. doi:10.5281/zenodo.1472183

Conflict of Interest: The authors declare that the research was conducted in the absence of any commercial or financial relationships that could be construed as a potential conflict of interest.

frontiers
in Astronomy and Space Sciences

ORIGINAL RESEARCH
published: 14 January 2021
doi: 10.3389/fspas.2020.579585

Significance of Cooling Effect on Comprehension of Kink Oscillations of Coronal Loops

*Daria Shukhobodskaia[1], Alexander A. Shukhobodskiy[2], Chris J. Nelson[3], Michael S. Ruderman[1,4] and Robert Erdélyi[1,5]**

[1]Solar Physics and Space Plasma Research Centre (SP2RC), School of Mathematics and Statistics, University of Sheffield, Sheffield, United Kingdom, [2]School of Build Environment, Engineering and Computing, Leeds Beckett University, Leeds, United Kingdom, [3]Astrophysics Research Centre (ARC), School of Mathematics and Physics, Queen's University, Belfast, United Kingdom, [4]Laboratory of Interplanetary Medium, Space Research Institute (IKI) Russian Academy of Sciences, Moscow, Russia, [5]Department of Astronomy, Eötvös Loránd University, Budapest, Hungary

Edited by:
Valery M. Nakariakov,
University of Warwick,
United Kingdom

Reviewed by:
Pankaj Kumar,
Goddard Space Flight Center,
National Aeronautics and Space
Administration, United States
David James Pascoe,
KU Leuven, Belgium

***Correspondence:**
Robert Erdélyi
robertus@sheffield.ac.uk

Specialty section:
This article was submitted to
Stellar and Solar Physics,
a section of the journal
Frontiers in Astronomy and
Space Sciences

Received: *02 July 2020*
Accepted: *24 November 2020*
Published: *14 January 2021*

Citation:
Shukhobodskaia D,
Shukhobodskiy AA, Nelson CJ,
Ruderman MS and Erdélyi R (2021)
Significance of Cooling Effect on
Comprehension of Kink Oscillations of
Coronal Loops.
Front. Astron. Space Sci. 7:579585.
doi: 10.3389/fspas.2020.579585

Kink oscillations of coronal loops have been widely studied, both observationally and theoretically, over the past few decades. It has been shown that the majority of observed driven coronal loop oscillations appear to damp with either exponential or Gaussian profiles and a range of mechanisms have been proposed to account for this. However, some driven oscillations seem to evolve in manners which cannot be modeled with purely Gaussian or exponential profiles, with amplification of oscillations even being observed on occasions. Recent research has shown that incorporating the combined effects of coronal loop expansion, resonant absorption, and cooling can cause significant deviations from Gaussian and exponential profiles in damping profiles, potentially explaining increases in oscillation amplitude through time in some cases. In this article, we analyze 10 driven kink oscillations in coronal loops to further investigate the ability of expansion and cooling to explain complex damping profiles. Our results do not rely on fitting a periodicity to the oscillations meaning complexities in both temporal (period changes) and spatial (amplitude changes) can be accounted for in an elegant and simple way. Furthermore, this approach could also allow us to infer some important diagnostic information (such as, for example, the density ratio at the loop foot-points) from the oscillation profile alone, without detailed measurements of the loop and without complex numerical methods. Our results imply the existence of correlations between the density ratio at the loop foot-points and the amplitudes and periods of the oscillations. Finally, we compare our results to previous models, namely purely Gaussian and purely exponential damping profiles, through the calculation of χ^2 values, finding the inclusion of cooling can produce better fits in some cases. The current study indicates that thermal evolution should be included in kink-mode oscillation models in the future to help us to better understand oscillations that are not purely Gaussian or exponential.

Keywords: solar corona, coronal loop oscillations, magnetohydrodynamics, kink oscillations, waves

1 INTRODUCTION

Standing, driven kink-mode oscillations within coronal loops have been extensively studied by the community ever since they were detected in the solar atmosphere at the end of the 20th Century (Aschwanden et al., 1999; Nakariakov et al., 1999) and for reviews see e.g. Andries et al. (2009); Ruderman and Erdélyi (2009). It is now known that, typically, flare-driven kink-mode oscillations are observed to damp within only a few periods, faster than would routinely be expected given the large amplitudes present (see, for example, Aschwanden and Terradas 2008), implying the presence of complex physics during these relatively routine events. The damping profiles of the majority of driven kink-mode oscillations can be well fitted by either Gaussian or exponential profiles (as shown in the statistical study of Goddard et al., 2016) and numerous physical mechanisms have been proposed to account for such decay. Resonant absorption is one such mechanism and has been widely analyzed in numerous analytical works with the aim of better understanding damping within kink-mode oscillations. (e.g., Goossens et al., 2002; Ruderman and Roberts 2002; Dymova and Ruderman 2006; Shukhobodskiy and Ruderman 2018). Interestingly, resonant absorption was proposed well before the first direct detection of kink-modes in coronal loops in the solar atmosphere (Hollweg and Yang 1988; Goossens et al., 1992; Erdelyi and Goossens 1994, Erdelyi and Goossens 1995). The potential transition from Gaussian to exponential damping during the course of a single coronal loop oscillation for propagating kink waves was derived by Hood et al. (2013) in the absence of cooling and for standing kink waves by Ruderman and Terradas (2013). For a review on resonant absorption without complex profiles in a solar context see Goossens et al. (2011).

The improvement in both the spatial and temporal resolutions of coronal imaging which resulted from the launch of the Solar Dynamics Observatory's Atmospheric Imaging Assembly (SDO/AIA; Lemen et al., 2012) in 2010 has facilitated major advances in understanding of coronal loop oscillations over the past decade. For example, it is now known that multiple harmonics can be present in kink-mode oscillations (Pascoe et al., 2016a), that decay-less observations are present in some coronal loops (Anfinogentov et al., 2013), and that coronal loops can be multi-thermal in nature (Krishna Prasad et al., 2017). One of the main benefits of the continuous, full-disk observations provided by the SDO/AIA instrument is that large statistical studies of coronal loop oscillations can now be conducted (see, e.g., Zimovets and Nakariakov 2015; Goddard et al., 2016). Goddard et al. (2016), for example, studied 120 kink-mode oscillations finding parameters such as amplitudes, damping times, and periods. Ground-based facilities also enable such statistical investigations in chromospheric wave-guides, as were conducted by Kuridze et al. (2012), Morton et al. (2012) who studied the properties of transverse oscillations in mottles. Furthermore, for the example of undamped kink oscillations presented by Aschwanden and Schrijver (2011), Kumar et al. (2013) showed that such phenomena could be triggered by the combination of fast and slow MHD waves present within the system. Moreover, Wang et al. (2012) suggested that amplification could occur due to additional energy input, potentially associated with flaring during the lifetime of the initial oscillation (Pascoe et al., 2020).

Such studies are highly valuable and provide important constraints which can help with the verification of numerical and analytical theories. Interestingly, although the evolution of the majority of coronal loop oscillations analyzed by Goddard et al. (2016) could be modeled using Gaussian, exponential, or Gaussian followed by exponential fits, 21 decaying kink-mode oscillations were identified which had combinations of both exponential and non-exponential damping profiles co-temporally. The presence of these complex or non-standard damping profiles, which cannot be approximated by a few Gaussian profiles and exponential profiles attached to each other in a definite order, sometimes including amplification of the oscillations through time, implies further work is required to fully understand what effects are important in defining the evolution of kink-modes in some coronal loops.

The first analytical models of kink oscillations of coronal loops were simple and considered homogeneous magnetic flux tubes (e.g. Ryutov and Ryutova 1976; Edwin and Roberts 1983). More recently, the idea of analytically studying cooling effect on MHD waves (see e.g. Morton et al., 2010) and in particular on the seismological properties for kink oscillations of coronal loops (see Morton and Erdélyi 2009; Morton and Erdélyi 2010) was proposed. Morton and Erdélyi (2010); Ruderman (2011a) concluded that in the absence of damping due to resonant absorption cooling can cause amplification of coronal loops. Furthermore Ruderman (2011b) concluded that combining cooling and resonant damping can result in the amplitude not varying in time (i.e., the oscillation being decay-less). Ruderman et al. (2017) studied the combination of cooling and expansion for non damped kink oscillation, it was shown that expansion of coronal loops acts in favor of amplification. Shukhobodskiy et al. (2018) considered the similar problem in the presence of damping due to resonant absorption and found that the combination of cooling and expansion can lead to an increase in the oscillation amplitude even in presence of resonant damping. The theory was later tested observationally by Nelson et al. (2019) on one kink-mode oscillation. It was found that increases in the amplitude of the oscillation through time could be explained if cooling was considered, without the need of external forces (e.g., additional flaring) affecting the oscillating system in order to sustain oscillation.

Cooling has been observed in many coronal loops during their lifetimes and has numerous observational signatures, both direct and indirect. The most direct signature is the visible transition of the loops from channels sampling hotter plasma to channels sampling cooler plasma through time (as was shown by, for example, Winebarger and Warren 2005; López Fuentes et al., 2007; Aschwanden and Terradas 2008). More indirect mechanisms include coronal rain (e.g., Antolin et al., 2015) and associated process such as downflows in transition region spectra at the foot-points of coronal loops (Kleint et al., 2014; Ishikawa et al., 2020). Both coronal rain and transition region downflows have been shown to be stable (Antolin et al., 2015;

Straus et al., 2015) and variable (Antolin et al., 2015; Nelson et al., 2020a) over short time-scales meaning the thermal evolution of coronal loops may be an on-going and variable process throughout their lifetimes. It is known that transition region downflows occur above almost all sunspots (Samanta et al., 2018; Nelson et al., 2020b) implying that a high number of coronal loops do not maintain constant temperatures through time. The effects of thermal evolution (both heating and cooling) within loops should, therefore, be considered when analyzing the oscillations of coronal loops (see e.g., Morton et al., 2010; Erdélyi et al., 2011; Al-Ghafri and Erdélyi 2013; Al-Ghafri et al., 2014 to name a few studies).

In this article, we analyze 10 examples of kink mode oscillations in coronal loops which damp with non-Gaussian and non-exponential profiles, as identified in the statistical study of Goddard et al. (2016). Our aim is to understand whether a range of damping profiles can be explained using the theories develop in Shukhobodskiy et al. (2018) which accounts for cooling within the loops during the oscillations. We are not claiming that cooling occurs in the studied loops (this would need to be studied in more detail in a separate study) but are, instead, displaying the flexibility of the theory and offering a discussion of when it may be useful in understanding the solar atmosphere. Our work is laid out as follows: In **Section 2** we detail the coronal loops studied here and the data used to analyze them; In **Section 3** we present our results; Before in **Section 4** we draw our conclusions.

2 OBSERVATIONS—EVENT SELECTION AND MODEL FITTING

The aim of this article is to understand whether a range of damping profiles of kink mode oscillations can be explained by the effects of cooling and to compare this model to several other previously studied models. To tackle this aim, we selected 10 events randomly from the sample identified to damp with both exponential and non-exponential components in the statistical study of Goddard et al. (2016) for analysis. The combination of exponential and non-exponential components implies a level of complexity in the amplitude profiles through time which could be an observational signature of cooling. Each of these 10 examples of kink-mode oscillations were sampled by the SDO/AIA instrument at discrete times between November 3, 2010 and July 18, 2013, with the periods of these oscillations ranging from slightly over 2 min up to nearly 16 min. Here, we specifically study data from the 171 Å filter which samples the coronal plasma at temperatures of around 0.6 MK with a cadence of 12 s and a pixel scale of 0.6″. A 300″×300″ field-of-view (FOV) around each oscillation was downloaded for a 1-h time-series beginning 15 min before the oscillation was deemed to have begun in Goddard et al. (2016) using the *ssw_cutout_service.pro* routine. Frames from the SDO/AIA instrument can have reduced exposure times during flares resulting in frames being dropped during download. Therefore, we filled any gaps in the time-series with synthetic images generated by averaging the intensities in the previous and following frames at each pixel. Since no consecutive frames were dropped, this should have no effect on the identification and analysis of oscillations with periods of the order minutes. Time-distance diagrams were then constructed to mimic the slits studied in Goddard et al. (2016), with a width of five pixels. In **Table 1**, we detail the basic information of the 10 oscillations studied in this article. We should also note that Pascoe et al. (2017) have extensively studied density contrast for the event 40 02. Furthermore, comprehensive temporal analysis was performed by Goddard and Nisticò (2020) for the event 03 01.

In **Figure 1**, we plot the time-distance diagrams constructed for each of the events studied here (using the routine detailed in Krishna Prasad et al., 2012) over the course of 1 h. Each slit has a different length, however, they have all been scaled to the same y-axis to emphasize the oscillations. The blue dots over-laid on each panel indicate the edges of the loop, identified using the Canny edge-detection method in Wolfram Mathematica 12. The red dots in each panel indicate the mid-points between the detected edges that we infer to be the central axis of the oscillating loop here. The background trend was then accounted for by fitting a function, using spline fitting, through the averages between local extremum points, similar to the method described in Pascoe et al. (2016b). Once the background trend had been subtracted, the amplitudes of the oscillations were normalized and fitted with a sum of Gaussian profiles of the form:

$$f\left(\mathrm{amp}\right) = \sum_{i=1}^{n} A_i \exp\left[-\left(\mu_i + t\right)^2 \big/ \left(2\sigma_i^2\right)\right] \big/ \sqrt{2\pi}/\sigma_i^2, \qquad (1)$$

where A_i and μ_i, and σ_i are the amplitude, shift, and width of the profile fitted to each peak. The value of n corresponds to the number of extrema identified for each oscillation. To ensure that the summed functions maintain continuity, we used the Wolfram Mathematica 12 function *Non-linearModelFit*. The benefit of fitting Gaussians to each extrema profile independently is that no implicit periodicity needs to be assumed for the oscillations. All of these steps allow us now to estimate the damping profile of each oscillation that can be modeled using the theories described in Shukhobodskiy et al. (2018). The procedure described here is essentially similar to that used in Nelson et al. (2019), but with the exception of an updated background trend approximation.

3 RESULTS

3.1 Theoretical Model

In this article, we expand on the work of Nelson et al. (2019) by applying the model proposed by Shukhobodskiy et al. (2018) to analyze 10 complex kink-mode oscillations. Here, let us provide a brief summary of the theoretical model for completeness. We consider an expanding and cooling loop of semi-circular shape surrounded by an annulus layer which is fixed in the dense photosphere. We note that the effects of curvature are only applied to the density distribution meaning, essentially, we consider the loop to be a straight magnetic flux tube with radius $R(z)$ (including the annulus layer) and length L. The

TABLE 1 | Properties of the kink-mode oscillations studied here.

Event ID	Loop ID	Slit position [x1, y1, x2, y2] (arcsec)	Date	Time UT	Period (min)	Osc amp (mm)
03	01	−977, −383, −988, −368	2010-Nov-03	12:13:48	2.46 ± 0.03	4.7
03	02	−970, −416, −1001, −393	2010-Nov-03	12:14:35	3.62 ± 0.08	9.7
04	01	912, 405, 889, 433	2011-Feb-09	01:30:02	2.29 ± 0.03	4.4
26	01	1098, 13, 1126, 51	2012-Jan-16	00:08:28	11.95 ± 0.13	9.2
40	02	−1077, −121, −1065, −96	2012-Oct-20	18:09:33	5.61 ± 0.03	4.4
40	04	−1045, −114, −1020, −110	2012-Oct-20	18:10:08	5.53 ± 0.04	2.5
40	07	−1107, −153, −1094, −121	2012-Oct-20	18:11:11	5.72 ± 0.06	3.4
40	08	−1036, −217, −1066, −194	2012-Oct-20	18:08:39	4.33 ± 0.08	12.1
43	05	801, 608, 812, 631	2013-Jan-07	06:37:11	4.5 ± 0.02	2.2
48	01	−1076, 77, −1044, 111	2013-Jul-18	17:59:56	15.28 ± 0.16	22

*The information given is in the same format as in Table A1 from Goddard et al. (2016) for consistency with the previous literature. Note the estimation of period and apparent oscillation amplitude (later in the text we do not use the word "apparent" in front of the amplitude) are from Goddard et al. (2016) and are not estimated directly in this article. These are included for comparison with **Figure 2**.*

temperature of the loop is assumed to decay exponentially through time (similarly to, for example, Aschwanden and Terradas 2008; Morton and Erdélyi 2010; Ruderman et al., 2017; Ruderman et al., 2019) following:

$$T(t) = T_0 \exp(-t/t_{\mathrm{cool}}), \tag{2}$$

where T_0 is the constant external temperature and t_{cool} is the cooling time. We assume that the cooling time is equal to the total lifetime of the oscillation in each case studied.

The variation of the loop cross-section, $R(z)$, is defined by the relation:

$$R(z) = R_f \lambda \sqrt{\frac{\cosh(L/2L_c) - 1}{\cosh(L/2L_c) - \lambda^2 + (\lambda^2 - 1)\cosh(z/L_c)}}, \tag{3}$$

where z is the height of the tube (set to be equal to 0 at the apex), R_f is the radius of the magnetic flux tube at the foot-point, $\lambda = R(0)/R_f$ is the expansion factor of the loop, and L_c is an arbitrary constant. This radius profile was also considered by Ruderman et al. (2008), Ruderman et al. (2017) and Nelson et al. (2019). The density is set to transition from the internal value to the external value in the annulus layer. We follow Goossens et al. (2002) and Shukhobodskiy and Ruderman (2018) and assume that density in the annulus region where resonant absorption can occur, ρ_t, can be modeled linearly as:

$$\rho_t = \frac{\rho_i + \rho_e}{2} + (\rho_i - \rho_e)\frac{R - r}{lR}, \tag{4}$$

where ρ_i is internal density, ρ_e is external density, r is the radial component, where $r = 0$ at the center of the magnetic flux tube, and l is a dimensionless parameter, such that $lR(z)/2$ is the radius of the transitional layer.

With the aid of **Eqs 2–4**, Shukhobodskiy et al. (2018) derived the relation for the dimensionless amplitude, $A(t)$, where $A(0) = 1$, of the kink mode under the thin tube and thin boundary approximation. In addition to λ, below are the most important parameters in the model:

$$\zeta = \frac{\rho_i(\pm L/2)}{\rho_e(\pm L/2)}, \qquad \kappa = \frac{L}{\pi H_0} \text{ and } \alpha = \frac{\pi l C_f t_{\mathrm{cool}}}{4L}, \tag{5}$$

where H_0 is the scale height in the exterior plasma and C_f is the kink speed at the foot-points of the loop. The parameter ζ corresponds to the ratio between the internal and external densities at the loop foot-points, κ corresponds to the ratio between the coronal loop length and the plasma scale height in the region outside the loop, and, finally, α represents the relative strength between damping due to resonant absorption and amplification due to cooling. In the case where $\alpha = 0$ there is no damping. Furthermore, the ratio of densities at any point of the loop is defined by Eqs 71–73 derived by Shukhobodskiy et al. (2018).

We note that to obtain results for comparison with observed amplitude profiles, the arbitrary constant, L_c should be carefully selected such that the expansion factor be in line with observed values ($1 < \lambda < 1.5$; Klimchuk 2000; Watko and Klimchuk 2000). Here, we set $L/L_c = 6$ (similarly to Ruderman et al., 2008; Shukhobodskiy et al., 2018 and Nelson et al., 2019) to achieve this aim. We also set $A_t = A(0)A_{Ob}(0)$, where A_{Ob} is the initial amplitude measured of the observed oscillation and A_t is the scaling factor for the dimensionless amplitude. This would enable us to compare analytical and theoretical results within comparable scale.

3.2 Results of the Model Fitting

In order to fit these observations with the model, we first need to obtain the damping profiles for each of the 10 events studied here. In **Figure 2**, we plot each of the oscillations identified in **Figure 1** with red dots. Each of these oscillations appears to be qualitatively different with different periods and amplitudes, with some having large amplitudes and some only appearing to have small amplitudes (only several pixels). This variety in the studied oscillations allows us to test the model in a more dynamic

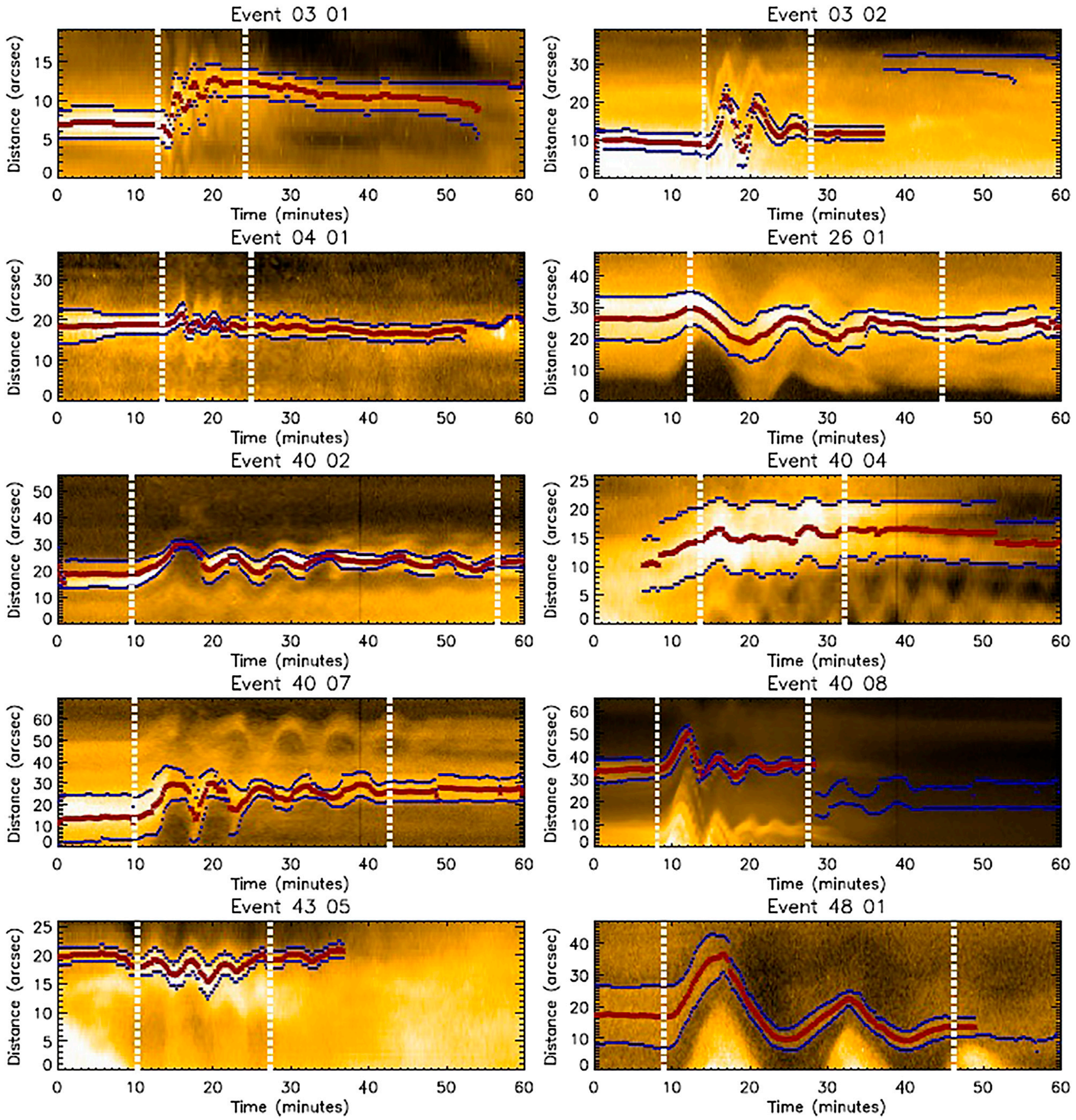

FIGURE 1 | Time-space diagrams for each of the selected events studied here. The *x*-axis of each panel corresponds to 1 h. The *y*-axes are all different in lengths but are scaled independently to improve the visibility of the oscillations. Exact timing and distance information is provided in **Table 1**. The results of the Canny edge-detection algorithm are over-laid as blue crosses. The central position between these points, assumed to be the center of the loop axis through time, is signified by the red crosses. The vertical white dashed lines denote the time-period plotted in **Figure 2**. We note that Event 40 04 could correspond to two individual loops over-lying each other, however, we do not remove it as the complex amplitude profile allows us to show-case both the strengths and limitations of the method.

way than if all oscillations displayed similar behavior. With this in mind, we keep the fitting of Event 40 04 despite the apparent overlap between two independent loops in the slit and label this as a "low-confidence" [LC] event in the remainder of this article. The green and blue lines in **Figure 2** mark the spline fits (following the method of Pascoe et al., 2016b) and the results of applying **Eq. 1**, respectively, for each of the events. The dashed black vertical lines indicate the temporal regions of interest within which the oscillations were studied in the remainder of this article. The next step in our analysis was

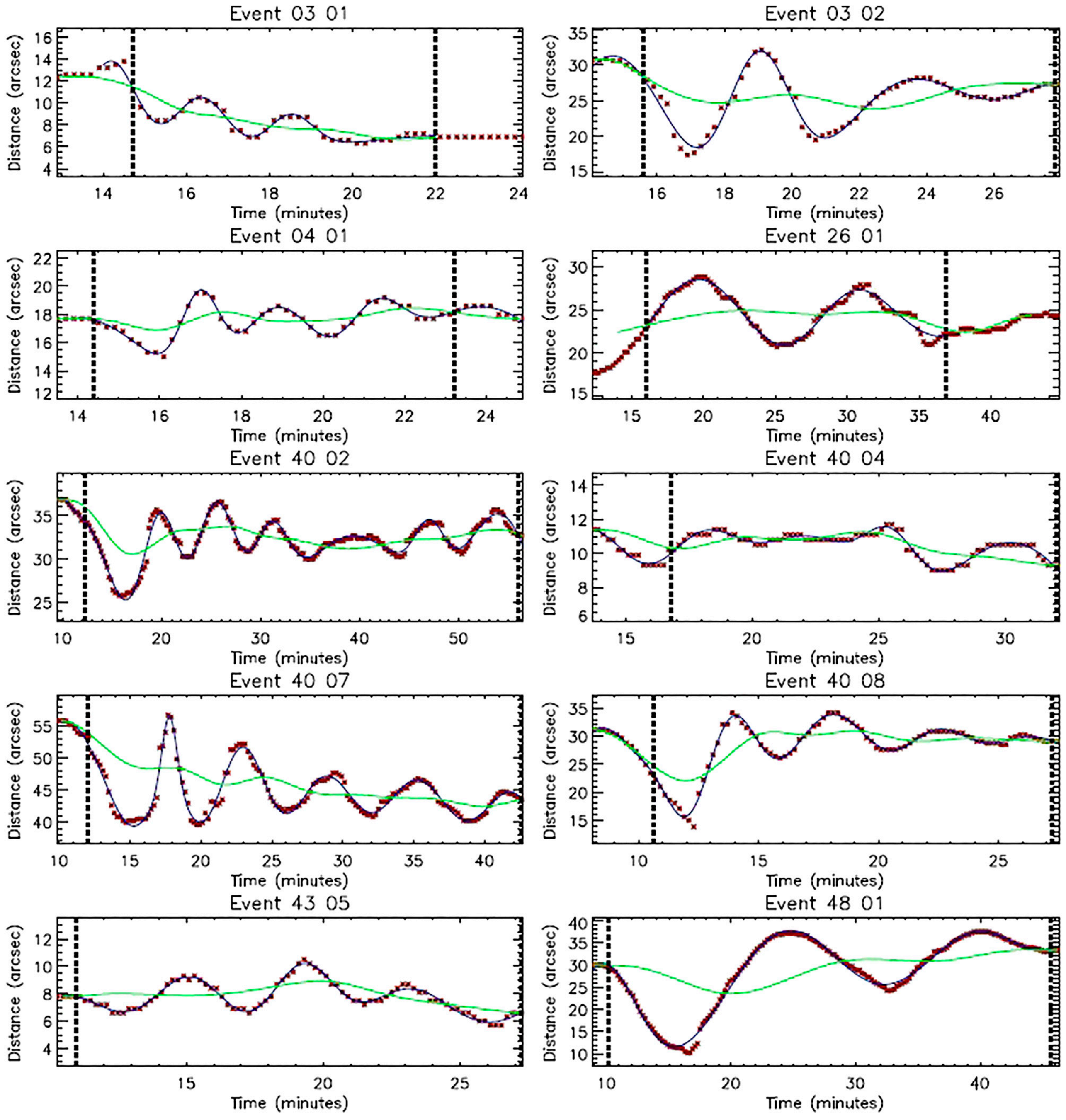

FIGURE 2 | Displacement profile of each coronal loop studied in this article. The red points correspond to the red points over-laid on **Figure 1** and track the measured amplitudes of the oscillation. The green lines display the background trend estimated using spline fitting. The blue lines are the results of fitting **Eq. 1** to each oscillation. Note the ability of this method to deal with variable periodicities, best seen in Events 40 02 and 40 07. The dashed black vertical lines on each panel outline the time-period plotted in Figure 3.

to remove the effects of the background trends and normalize the amplitudes such that the damping profiles could be calculated. The results of this procedure are plotted in **Figure 3**. It is immediately evident that the damping profiles of Events 03 01, 04 01, 40 02, 40 04 (LC), 40 07, 40 08 and 43 05 clearly deviate from both typical exponential and Gaussian damping. Some of these events display an increase in the amplitude through time whilst some others have stagnation periods where the amplitude remains constant for a while before further amplitude reduction takes place. Such damping profiles are difficult to explain using standard methods.

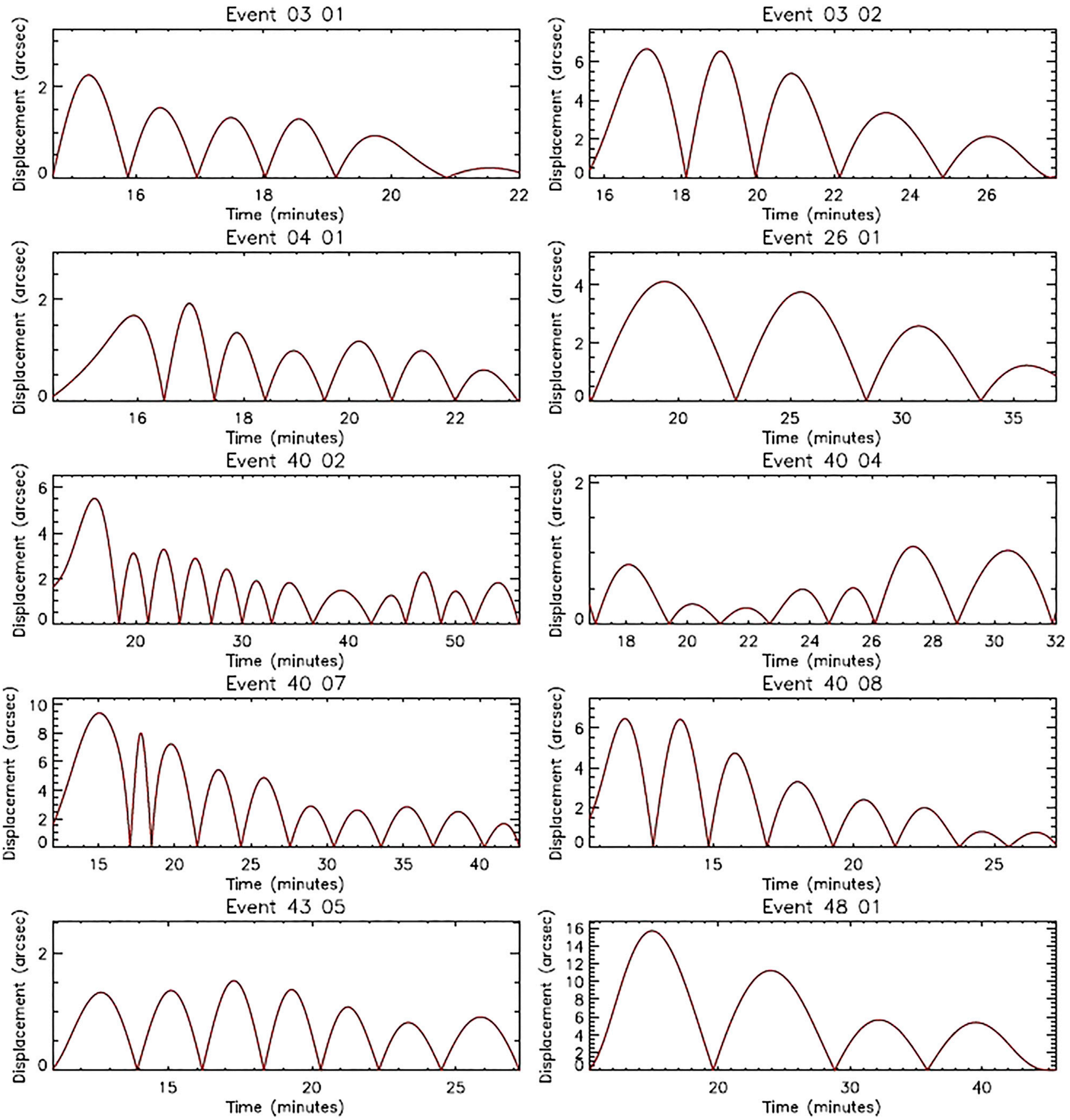

FIGURE 3 | The absolute value of the displacement of the Gaussian fitted position profiles (blue line from **Figure 2**) from the spline fitted background trend (green line from **Figure 2**) through time for each of the events studied here.

Next, we applied the model proposed by Shukhobodskiy et al. (2018) to the damping profiles, varying the four parameters discussed in the previous section to minimize the departure from the measured amplitude profile (as was previously done by Nelson et al., 2019). In **Figure 4** we plot the amplitudes of each peak of each oscillation as green dots, with spline fits over-laid as blue lines. The optimized results of the model fitting are over-laid as red lines. In order to compare with other single models, we also plot fits calculated using both exponential (dashed) and Gaussian (dot-dashed) profiles, as discussed in Pascoe et al. (2016b), which study the damping of a fundamental mode. The parameters used for the cooling model provide sufficiently good fits in a qualitative sense in the majority of cases, as can be seen in **Figure 4**, with only Event 40 04 (LC) being visually poorly fitted. Essentially, including the effects of cooling in the fitting of kink-mode damping profiles can produce good fits for a wide variety of

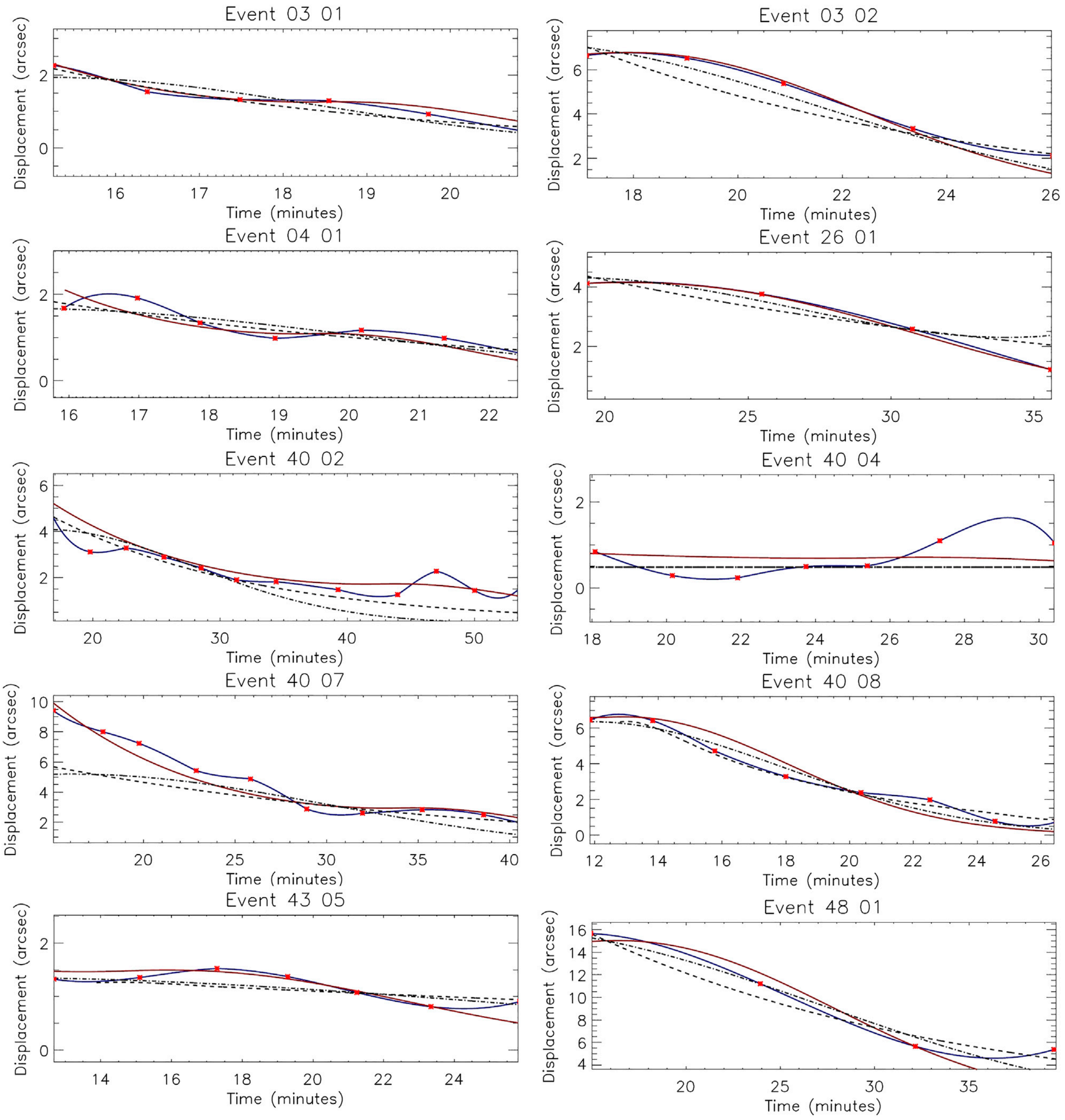

FIGURE 4 | The fitting of the model, introduced by Shukhobodskiy et al. (2018), to the coronal loop oscillations studied here. The blue lines plot spline fits through the maxima of each peak plotted in **Figure 3**. The red lines plot the approximation of the oscillations obtained through fitting the theoretical model. Reasonable fits are achieved for all events except Event 40 04 (LC). The dot-dashed lines represents Gaussian fit and the dashed lines correspond to exponential fits. Finally, the red crosses indicate the peaks from **Figure 3**.

profiles but even this method can struggle when low amplitude, highly variable damping profiles are considered. Deviations from standard Gaussian or exponential damping profiles are most prominent in Events 03 01, 03 02, 04 01, 26 01, 40 07 and 43 05 where several saddle points are evident in the fits. It is worth noting that this model is also capable of capturing features of both the Gaussian and exponential damping profiles by varying its parameters, with near-Gaussian damping profiles being returned for Events 40 08 and 48 01 and near-exponential damping being returned for Event 40 02. We note that Gaussian damping profiles can only be obtained for low values of ζ (<1.2) whereas exponential damping profiles can only be obtained with values

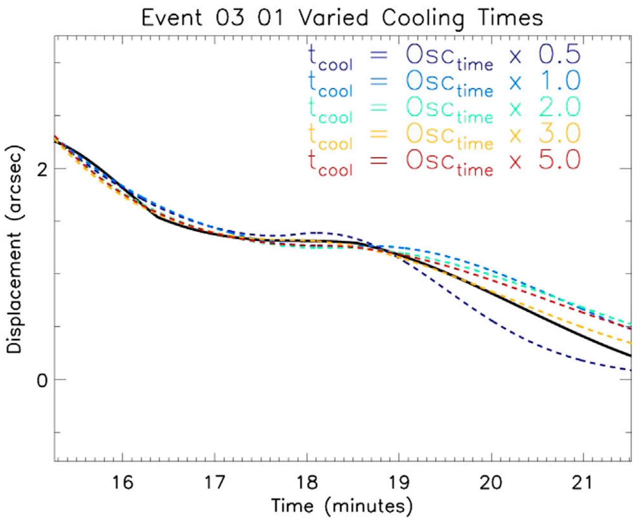

FIGURE 5 | Examination of the effect of cooling time on the fits of the analytical model to observations. The κ values for each of the cooling times (from quickest to slowest) are 1.3, 2.9, 5.6, 5.7, 10.9, respectively, and the corresponding ζ values are 3.7, 3, 1.7, 1.35, 1.2. We should note the condition of applicability of Shukhobodskiy et al. (2018) is $t_{cool} \gg P/6$, where t_{cool} is the cooling time and P is oscillation period.

of ζ higher than 4.5 when values of κ, λ, and α are not extreme. For values of α closer to 0, the effect of damping due to resonant absorption would be completely canceled out by the amplification due to cooling with overall amplification present. On the other hand, high values of α would result in profiles very similar to exponential decay, due to strong damping accountable for resonant absorption and weak cooling, though small increases in amplitude would be still present. The specific value of α that would make this change is dependent on the loop itself. Lowering the loop length by making κ smaller will compensate the increase in α. Furthermore, higher loop expansion favors amplification, therefore, to reduce the damping profile to an exponential profile one would need to consider values of $\zeta > 7$.

Highly complex amplitude profiles, for example Event 43 05, display both decreases and increases in the amplitude through time. Fortunately, this complexity can be explained by theory once cooling is considered. For lower values of ζ less than 1.2 the theoretical profile reduces to Gaussian decay. Whereas, for higher values of density ratios, the initial part would start with exponential decrease first and then after some time the local increase may appear after which the Gaussian decay profile appears. This behavior provides higher degrees of freedom in fitting the observations meaning more amplitude profiles are now theoretically permitted. This fact makes it ultimately both convenient and useful to consider the evolution of temperature during oscillations for accurate approximation of seismological parameters. Goddard and Nakariakov (2016) discussed the importance of the projection angle in order to obtain more accurate information about coronal loops, which could cause a cascade of associated errors and require the need to perform multiple angle analysis of the same phenomena. Despite this fact, the model used in this article is not dependent of the absolute values of the damping profile, rather it depends on the normalized shape of oscillation, making it resistant to the above errors in obtaining the dimensionless parameters. As such, that could lead to faster analysis of kink oscillations of coronal loops. However, such an error does limit the estimation of parameters with dimensions in the model used here.

We should note that ζ is responsive to the position where the analytical solution changes it shape (e.g., where amplitude increases are detected). Any increases in the assumed cooling time results in a stretching of the analytical solution and lowers the value of ζ, however, such effects becomes slower or negligible as ζ becomes closer to 1 as seen in **Figure 5**. Additionally, increases in the cooling time lead to increases of κ in order to fit the observed shape. Nevertheless, in all occasions the model is able to capture the observed profile for various lengths of cooling. Essentially, this introduces some degeneracy in our solutions which will need to be further studied through future research. Moreover, oscillations with low values of ζ are barely affected by the cooling time, where kink oscillations with high values of ζ could lead to overestimation of this parameter and require additional measurements to determine t_{cool} or κ. Once t_{cool} or κ is known or measured the model provides quick and accurate estimate for ζ. Furthermore, in the case where values of ζ are in the range 1–1.7 existing estimates of damping profiles are sufficiently good even without knowing t_{cool} and κ. We should note that the theoretical model studied here explains deviations from typical exponential or Gaussian damping profiles due to cooling, which causes plasma flows toward footpoints of the coronal loop. As a result, the upper parts of the coronal loops become lighter, however the impulse is preserved. The lighter the loop with comparison to

TABLE 2 | Comparative analysis for goodness of fit from the observed data for the theoretical model presented by Shukhobodskiy et al. (2018) and for Gaussian and exponential fits presented by Pascoe et al. (2016b).

Event	χ_t^2	χ_g^2	χ_e^2	$\tilde{\chi}_t^2$	$\tilde{\chi}_g^2$	$\tilde{\chi}_e^2$
03 01	0.5692	0.6857	0.4702	3.8990	5.6609	4.1022
03 02	0.5312	1.1218	1.3095	7.7526	26.8841	26.8841
04 01	0.4909	0.2764	0.2810	5.4039	7.3583	5.3894
26 01	0.0086	0.0446	0.1781	0.9976	38.5140	33.9762
40 02	1.5567	9.7141	7.0435	110.7415	646.3610	242.6087
40 04	3.6473	2.7641	2.7642	150.7310	99.0152	99.0189
40 07	1.0192	9.4239	7.9315	50.3733	314.3506	292.3057
40 08	2.2148	0.9184	0.6627	68.0517	25.3550	28.0358
43 05	0.3280	0.2262	0.3118	4.6998	8.6158	12.9752
48 01	3.9506	2.5507	1.1667	168.46012	61.3025	89.8005
Event 03 01					χ_t^2	$\tilde{\chi}_t^2$
Cooling time is equal to oscillation time × 0.5					0.2277	4.8311
Cooling time is equal to oscillation time × 2.0					0.7294	3.0602
Cooling time is equal to oscillation time × 3.0					0.1180	0.2628
Cooling time is equal to oscillation time × 5.0					0.5357	1.8411

χ_t^2, χ_g^2, and χ_e^2, correspond to χ^2 goodness of fit calculations for the cooling, Gaussian, and exponential models, respectively, only by comparing extremum points (i.e. peaks of the amplitudes). $\tilde{\chi}_t^2$, $\tilde{\chi}_g^2$, and $\tilde{\chi}_e^2$, correspond to $\tilde{\chi}^2$ goodness of fit for the cooling, Gaussian, and exponential models comparing overall fit at all times during the damping. The top panel exhibit the analysis for all studied events with cooling time being equal to oscillation time and bottom panel corresponds to the event 03 01 for various cooling times.

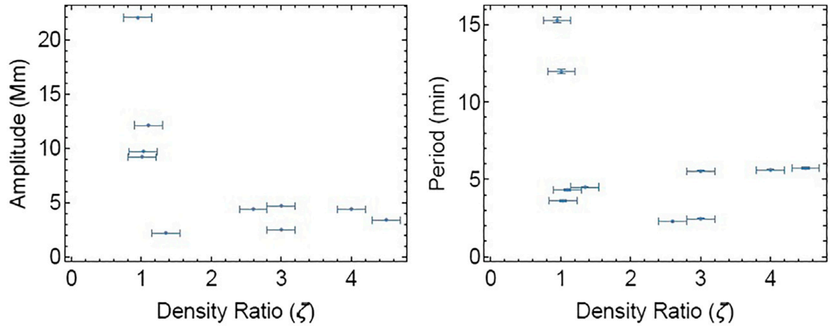

FIGURE 6 | Scatter plots displaying the apparent relationships between the amplitude and period of the coronal loop oscillations (as measured by Goddard et al., 2016) and the density ratio inferred here.

surroundings the less affect will be visible by cooling. That could be seen that for values of $\zeta < 1.2$ the damping profile is almost Gaussian. Furthermore the effect on heavier loops with $\zeta > 7$ is the similar, since the cooling time is not sufficient to affect the initial impulse of the oscillation. As a result, an exponential damping profile is preserved. Despite that, the introduction of cooling to the system might still provide better approximation for oscillations, however, at this time it is difficult to test this observationally. Furthermore, the most interesting analysis occurs for values of $1.2 \le \zeta \le 7$, where cooling plays a significant role in determining oscillation profiles. It is in this density range that future analyses could be focused.

The inferred, best fit, parameters (defined in the previous section) for each of the oscillations are presented in **Table 2**. To obtain accurate approximations for ζ, care should be taken in accurately positioning the dashed black lines in **Figure 2** due to its high sensitivity to temporal variations. In **Figure 6**, we plot the relationship between the density ratio at the loop foot-points, ζ, and the oscillation amplitudes (left panel) and periods (right panel) as measured by Goddard et al. (2016). It is immediately evident that the higher amplitude and longer period oscillations appear to have lower density ratios between the loop and the external environment at the foot-points. Although we are hesitant to draw strong conclusions about this due to the small statistical size and lack of direct density diagnostics, this result does suggest further research should be done to investigate such links in the future. Some important steps forward could come through analyzing the ratios between the O IV lines sampled by the Interface Region Imaging Spectrograph (IRIS; De Pontieu et al., 2014) at the foot-points of oscillating loops. Some limitations of this model are evident in **Figure 4** where deviations between the fitted theoretical model and the measured observed values are evident. It is unclear at this stage whether these limitations are caused by differences in the observed and modeled structures or due to measurement errors. It should be noted that the recent work of Goddard et al. (2017) shows that some of the loops might not have thin boundaries, with Pascoe et al. (2019) discussing the possible limitations of the thin boundary approximation used within theoretical approach. This could possibly lead to underestimation of ζ, with the current model supporting $l \le 0.5$. However, the effect of the transitional layer changes have not yet being studied in this configuration for cooling loops to provide accurate estimates of possible errors for kink oscillations of cooling coronal loops with $l \ge 0.5$. Future observational and analytical work will be needed to better understand this. We also note that since the analytical model is very sensitive in a non-linear way to the position of local oscillation amplification, without significant improvement in image resolution, it would be impossible to obtain the estimate of an error of given ζ and consequently all other parameters. Thus an upper bound of general error estimates for fixed values of ζ are applied here. However, once the spatial resolution of obtained data increases and the shape observed oscillation is more certain, quantification of these errors will be paramount for correct estimates.

TABLE 3 | Best-fit parameters fitted by the theoretical model for each of the loop oscillations studied here.

Event	03 01	03 02	04 01	26 01	40 02	40 04	40 07	40 08	43 05	48 01
ζ	3	1.03	2.6	1.01	4	3	4.5	1.1	1.35	1.01
λ	1.01	1.21	1.01	1.05	1.1	1.05	1.01	1.05	1.3	1.05
κ	2.9	2.6	2	1.7	1.6	1.8	2.5	3.5	2.2	2.95
α	1	0.9	1.6	1	1.6	0.5	1.1	1.1	1.01	0.8

Note that ζ is rather sensitive to the selection of the starting time of the oscillation and we assume that the cooling time is equal to oscillation time. Whilst conducting the fits, virtually any values of $\zeta \pm 0.2$, $\lambda \pm 0.05$, $\kappa \pm 0.2 \pm \varepsilon_\kappa$, $\alpha \pm 0.1 \pm \varepsilon_\alpha$, where ε with subscript denotes the errors associated with variation of ζ provided sufficiently good approximations to the observed values, however, the above particular values were chosen to follow the measured damping trend better. Given that there might be an error in the estimation of the starting time of damping, one should pay extra care of determining ζ in the vicinity of $\zeta = 1$, due to the ratio of internal and external densities being susceptible to changes in this interval. The combination of λ, κ, and α are key for the speed of decay of the amplitude. In this study, these values were treated as parameters and further measurements should be made to accurately determine κ and α in the future. We note that Event 40 02 was studied previously by Nelson et al. (2019), however, here we analyzed a longer time-period, therefore, explaining the difference in ζ.

Table 3 provides the comparison with previous models, we could see that inclusion of cooling to Events 03 02, 26 01, 40 02, 40 07 with oscillation time been equal to the oscillation time could lead the cooling theoretical model to have better approximations to the damping profiles than exponential and Gaussian fits, in case only extremum points (i.e. amplitude maxima) are taken as the point of reference. If instead we analyze the overall damping profile (i.e. calculate the χ^2 values at all time-steps), then Events 03 01, 03 02, 04 01, 26 01, 40 02, 40 07, 43 05 are approximated better by the cooling model, rather than exponential or Gaussian fits. We should note that the goodness of fit could be further improved in the cooling model if we were to put more stress on deviation from the observed data instead of focusing on finding the turning points. However, we should mention that position of turning point is crucial for estimation for values of ζ. Furthermore, changing the ration between oscillation time and cooling time could improve significantly the goodness of fit as was described in Event 03 01.

4 CONCLUSION

In this article, we have further demonstrated the promise of the theory developed by Shukhobodskiy et al. (2018) by applying it to 10 driven kink-mode oscillations. These events were sampled by the SDO/AIA instrument and were randomly selected from the population identified to have complex damping profiles in the statistical study of Goddard et al. (2016). Space-time diagrams were constructed for each oscillation before the edges of the loops through time were determined by employing the Canny edged-detection method (see **Figure 1**). The mid-point between the edges was defined as the central axis of the oscillating loop for each time-step. The background trends were then subtracted from each oscillation using spline fitting before the detrended data were then fitted with a series of Gaussian functions. The results of the application of these steps to the oscillations can be seen in **Figure 2**.

Next, we plotted the absolute values of the amplitude variation of the kink-mode oscillations through time in **Figure 3**. Some oscillations displayed clear deviations from the usual Gaussian or exponential damping profiles even at this stage. Specifically, five (Events 04 01, 40 02, 40 04 (LC), 40 07, and 43 05) of the 10 oscillations studied here displayed evidence of increases in amplitude through time. Such amplification was shown to be possible during oscillations of cooling loops by Ruderman (2011b), Shukhobodskiy and Ruderman (2018) and has been reported before in observations by Nelson et al. (2019). Using an iterative approach, we then constructed best fits for the parameters defined in **Eq. 5** such that the difference between the observed and theoretical damping profiles was minimized. In **Figure 4** it was shown that this theoretical model provides qualitatively reasonable approximations for the damping of kink oscillations of coronal loops for nine of the 10 cases (all except Event 40 04 [LC]). This result indicates that cooling should be studied in more detail in future research. Additionally, we have also shown that the model is capable of capturing the properties of fitting both simple Gaussian and exponential profiles, depending on the ratio of external and internal densities, ζ, at the loop foot-points. Furthermore, for sufficiently large loops with $\kappa \geq 1.6$, the shape of the damping profile is determined by this ratio. In the case where cooling is present, for the small values of ζ the profile would be Gaussian, while for large values of ζ it would be exponential. All values in-between would be a combination of both.

It was shown by Shukhobodskiy et al. (2018) that higher expansion factors of coronal loops could result in overall amplification of the first part of the oscillation eventually resulting in Gaussian decay of the amplitude profile. Thus studying complex damping profiles could allow us to extract interesting seismological information, such as the ratios of densities at foot-points. Furthermore, the information presented in **Figure 6** suggests, that lower ratios of internal and external densities have higher amplitude and period. One of the reasons why this could happen is that the coronal loops investigated are lighter and less disturbance created by the flare is needed to disturb the system more prominently. A larger statistical study and more targeted observations with spectral instruments suitable for providing density diagnostics (such as IRIS) should be used to study this potenatial result in more detail in the future.

Overall, we presented an alternative approach to model more complex damping profiles that deviate from the widely studied Gaussian and exponential decays. A number of examples of such deviation were addressed in this study, thus strengthening the claim made by Nelson et al. (2019) that the effect of cooling should be further considered for analyzing oscillations of coronal loops. This is in agreement with some earlier studies, e.g. by Morton and Erdélyi (2009), Morton and Erdélyi (2010). Furthermore, in the case of strong damping the theoretical model proposed by Shukhobodskiy et al. (2018) is able to provide seismological information, just from the damping profile alone. For some events, the cooling model demonstrated significant improvement over standard Gaussian on exponential fitting when χ^2 goodness of fits were calculated. We should note that results employed from Shukhobodskiy et al. (2018) model was only studied on the fundamental mode only. However, additional studies with inclusion of mode mixing would allow comparison with other fitting techniques that allowed multiple harmonics to be present, which could further unveil details regarding kink oscillations of coronal loops. Unfortunately, for less dominant damping more parameters need to be determined from observation in order to extract the information about the kink oscillations of coronal loops.

Although little evidence is presented about the actual cooling for the events studied here, it is possible that the gradual fading of the intensity of several coronal loops presented in **Figure 1** (specifically for Events 03 01, 04 01, and 43 05) may imply that some thermal evolution (either heating or cooling) is present. In a future work, it would be worthwhile to analyze oscillations within loops which are undergoing specific processes linked to cooling, such as coronal rain (Antolin et al., 2015) or the associated high velocity transition region downflows (see, for example, Nelson et al., 2020b, Nelson et al., 2020a and literature within), to understand whether abnormal amplitude profiles through time (such as those studied here) are present. Additionally, it would be worthwhile to develop further the analytical methods, which then could help to extract additional information about the kink oscillation of coronal loops, in order to optimize this theory for the application of solar magneto-seismology to kink-mode oscillations.

DATA AVAILABILITY STATEMENT

Publicly available datasets were analyzed in this study. This data can be found here: https://jsoc.stanford.edu.

AUTHOR CONTRIBUTIONS

AS and CN conceived the study. DS and AS conducted the data analysis, with DS having a major contribution to the analysis. All authors consulted on the interpretation of results. DS, AS, and CN drafted the manuscript. All authors read, discussed and commented on the draft. RE lead the research overall.

FUNDING

DS is grateful to the University of Sheffield for the support received. AS is thankful to Interreg Northwest Europe for the support received to conduct this research through grant number: NWE847. CN is thankful to the Science and Technology Facilities Council (STFC) for the support received to conduct this research through grant number: ST/P000304/1. RE is grateful to STFC (UK, grant number ST/M000826/1). RE also acknowledges support from the Chinese Academy of Sciences President's International Fellowship Initiative (PIFI, grant number 2019VMA0052) and The Royal Society (grant nr IE161153).

ACKNOWLEDGMENTS

SDO/AIA data are courtesy of NASA/SDO and the AIA science team. We thank S. Krishna Prasad for making their slit creation code available to us.

REFERENCES

Al-Ghafri, K. S., and Erdélyi, R. (2013). Effect of variable background on an oscillating hot coronal loop. *Sol. Phys*. 283, 413–428. doi:10.1007/s11207-013-0225-8

Al-Ghafri, K. S., Ruderman, M. S., Williamson, A., and Erdélyi, R. (2014). Longitudinal Magnetohydrodynamics oscillations in dissipative, cooling coronal loops. *Astrophys. J*. 786, 36. doi:10.1088/0004-637X/786/1/36

Andries, J., van Doorsselaere, T., Roberts, B., Verth, G., Verwichte, E., and Erdélyi, R. (2009). Coronal seismology by means of kink oscillation overtones. *Space Sci. Rev*. 149, 3–29. doi:10.1007/s11214-009-9561-2

Anfinogentov, S., Nisticò, G., and Nakariakov, V. M. (2013). Decay-less kink oscillations in coronal loops. *Astron. Astrophys*. 560, A107. doi:10.1051/0004-6361/201322094

Antolin, P., Vissers, G., Pereira, T. M. D., Rouppe van der Voort, L., and Scullion, E. (2015). The multithermal and multi-stranded nature of coronal rain. *Astrophys. J*. 806, 81. doi:10.1088/0004-637X/806/1/81

Aschwanden, M. J., Fletcher, L., Schrijver, C. J., and Alexander, D. (1999). Coronal loop oscillations observed with the transition region and coronal explorer. *Astrophys. J*. 520, 880–894. doi:10.1086/307502

Aschwanden, M. J., and Schrijver, C. J. (2011). Coronal loop oscillations observed with atmospheric imaging assembly—kink mode with cross-sectional and density oscillations. *Astrophys. J*. 736, 102. doi:10.1088/0004-637X/736/2/102

Aschwanden, M. J., and Terradas, J. (2008). The effect of radiative cooling on coronal loop oscillations. *Astrophys. J. Lett*. 686, L127. doi:10.1086/592963

De Pontieu, B., Title, A. M., Lemen, J. R., Kushner, G. D., Akin, D. J., Allard, B., et al. (2014). The Interface region imaging Spectrograph (IRIS). *Sol. Phys*. 289, 2733–2779. doi:10.1007/s11207-014-0485-y

Dymova, M. V., and Ruderman, M. S. (2006). Resonantly damped oscillations of longitudinally stratified coronal loops. *Astron. Astrophys*. 457, 1059–1070. doi:10.1051/0004-6361:20065051

Edwin, P. M., and Roberts, B. (1983). Wave propagation in a magnetic cylinder. *Sol. Phys*. 88, 179–191. doi:10.1007/BF00196186

Erdélyi, R., Al-Ghafri, K. S., and Morton, R. J. (2011). Damping of longitudinal magneto-acoustic oscillations in slowly varying coronal plasma. *Sol. Phys*. 272, 73–89. doi:10.1007/s11207-011-9795-5

Erdelyi, R., and Goossens, M. (1995). Resonant absorption of Alfven waves in coronal loops in visco-resistive MHD. *Astron. Astrophys*. 294, 575–586. doi:10.1063/1.1343090

Erdelyi, R., and Goossens, M. (1994). Viscous computations of resonant absorption of MHD waves in flux tubes by fem. *Astrophys. Space Sci*. 213, 273–298. doi:10.1007/BF00658215

Goddard, C. R., and Nakariakov, V. M. (2016). Dependence of kink oscillation damping on the amplitude. *Astron. Astrophys*. 590, L5. doi:10.1051/0004-6361/201628718

Goddard, C. R., Nisticò, G., Nakariakov, V. M., and Zimovets, I. V. (2016). A statistical study of decaying kink oscillations detected using SDO/AIA. *Astron. Astrophys*. 585, A137. doi:10.1051/0004-6361/201527341

Goddard, C. R., and Nisticò, G. (2020). Temporal evolution of oscillating coronal loops. *Astron. Astrophys*. 638, A89. doi:10.1051/0004-6361/202037467

Goddard, C. R., Pascoe, D. J., Anfinogentov, S., and Nakariakov, V. M. (2017). A statistical study of the inferred transverse density profile of coronal loop threads observed with SDO/AIA. *Astron. Astrophys*. 605, A65. doi:10.1051/0004-6361/201731023

Goossens, M., Andries, J., and Aschwanden, M. J. (2002). Coronal loop oscillations. An interpretation in terms of resonant absorption of quasi-mode kink oscillations. *Astron. Astrophys*. 394, L39. doi:10.1051/0004-6361:20021378

Goossens, M., Erdélyi, R., and Ruderman, M. S. (2011). Resonant MHD waves in the solar atmosphere. *Space Sci. Rev*. 158, 289–338. doi:10.1007/s11214-010-9702-7

Goossens, M., Hollweg, J. V., and Sakurai, T. (1992). Resonant behavior of MHD waves on magnetic-flux tubes. 3. Effect of equilibrium-flow. *Sol. Phys*. 138, 233–255. doi:10.1007/BF00151914

Hollweg, J. V., and Yang, G. (1988). Resonant-absorption of compressible magnetohydrodynamic waves at thin surfaces. *Comput. Phys. Rep*. 93, 5423–5436. doi:10.1029/JA093iA06p05423

Hood, A. W., Ruderman, M., Pascoe, D. J., De Moortel, I., Terradas, J., and Wright, A. N. (2013). Damping of kink waves by mode coupling. I. Analytical treatment. *Astron. Astrophys*. 551, A39. doi:10.1051/0004-6361/201220617

Ishikawa, R. T., Katsukawa, Y., Antolin, P., and Toriumi, S. (2020). Temporal and spatial scales in coronal rain revealed by UV imaging and spectroscopic observations. *Sol. Phys*. 295, 53. doi:10.1007/s11207-020-01617-z

Kleint, L., Antolin, P., Tian, H., Judge, P., Testa, P., De Pontieu, B., et al. (2014). Detection of supersonic downflows and associated heating events in the transition region above sunspots. *Astrophys. J. Lett*. 789, L42. doi:10.1088/2041-8205/789/2/L42

Klimchuk, J. A. (2000). Cross-Sectional properties of coronal loops. *Sol. Phys*. 193, 53–75. doi:10.1023/A:1005210127703

Krishna Prasad, S., Banerjee, D., and Singh, J. (2012). Oscillations in active region fan loops: observations from EIS/hinode and AIA/SDO. *Sol. Phys*. 281, 67–85. doi:10.1007/s11207-012-0098-2

Krishna Prasad, S., Jess, D. B., Klimchuk, J. A., and Banerjee, D. (2017). Unravelling the components of a multi-thermal coronal loop using magnetohydrodynamic seismology. *Astrophys. J*. 834, 103. doi:10.3847/1538-4357/834/2/103

Kumar, P., Cho, K. S., Chen, P. F., Bong, S. C., and Park, S. H. (2013). Multiwavelength study of a solar eruption from AR NOAA 11112: II. Large-scale coronal wave and loop oscillation. *Sol. Phys.* 282, 523–541. doi:10.1007/s11207-012-0158-7

Kuridze, D., Morton, R. J., Erdélyi, R., Dorrian, G. D., Mathioudakis, M., Jess, D. B., et al. (2012). Transverse oscillations in chromospheric mottles. *Astrophys. J.* 750, 51. doi:10.1088/0004-637X/750/1/51

Lemen, J. R., Title, A. M., Akin, D. J., Boerner, P. F., Chou, C., Drake, J. F., et al. (2012). The atmospheric imaging assembly (AIA) on the solar dynamics observatory (SDO). *Sol. Phys.* 275, 17–40. doi:10.1007/s11207-011-9776-8

López Fuentes, M. C., Klimchuk, J. A., and Mandrini, C. H. (2007). The temporal evolution of coronal loops observed by GOES SXI. *Astrophys. J.* 657, 1127–1136. doi:10.1086/510662

Morton, R. J., and Erdélyi, R. (2010). Application of the theory of damping of kink oscillations by radiative cooling of coronal loop plasma. *Astron. Astrophys.* 519, A43. doi:10.1051/0004-6361/201014504

Morton, R. J., and Erdélyi, R. (2009). Transverse oscillations of a cooling coronal loop. *Astrophys. J.* 707, 750–760. doi:10.1088/0004-637X/707/1/750

Morton, R. J., Hood, A. W., and Erdélyi, R. (2010). Propagating magneto-hydrodynamic waves in a cooling homogenous coronal plasma. *Astron. Astrophys.* 512, A23. doi:10.1051/0004-6361/200913365

Morton, R. J., Verth, G., Jess, D. B., Kuridze, D., Ruderman, M. S., Mathioudakis, M., et al. (2012). Observations of ubiquitous compressive waves in the Sun's chromosphere. *Nat. Commun.* 3, 1315. doi:10.1038/ncomms2324

Nakariakov, V. M., Ofman, L., Deluca, E. E., Roberts, B., and Davila, J. M. (1999). TRACE observation of damped coronal loop oscillations: implications for coronal heating. *Science*. 285, 862–864. doi:10.1126/science.285.5429.862

Nelson, C. J., Krishna Prasad, S., and Mathioudakis, M. (2020a). Evolution of downflows in the transition region above a sunspot over short time-scales. *Astron. Astrophys.* 640, 13. doi:10.1051/0004-6361/202038155

Nelson, C. J., Krishna Prasad, S., and Mathioudakis, M. (2020b). Evolution of supersonic downflows in a sunspot. *Astron. Astrophys.* 636, A35. doi:10.1051/0004-6361/201937357

Nelson, C. J., Shukhobodskiy, A. A., Erdélyi, R., and Mathioudakis, M. (2019). The effect of cooling on driven kink oscillations of coronal loops. *Frontiers in Astronomy and Space Sciences*. 6, 45. doi:10.3389/fspas.2019.00045

Pascoe, D. J., Goddard, C. R., and Nakariakov, V. M. (2016a). Spatially resolved observation of the fundamental and second harmonic standing kink modes using SDO/AIA. *Astron. Astrophys.* 593, A53. doi:10.1051/0004-6361/201628784

Pascoe, D. J., Goddard, C. R., Nisticò, G., Anfinogentov, S., and Nakariakov, V. M. (2016b). Damping profile of standing kink oscillations observed by SDO/AIA. *Astron. Astrophys.* 585, L6. doi:10.1051/0004-6361/201527835

Pascoe, D. J., Hood, A. W., and Van Doorsselaere, T. (2019). Coronal loop seismology using standing kink oscillations with a lookup table. *Frontiers in Astronomy and Space Sciences*. 6, 22. doi:10.3389/fspas.2019.00022

Pascoe, D. J., Russell, A. J. B., Anfinogentov, S. A., Simões, P. J. A., Goddard, C. R., Nakariakov, V. M., et al. (2017). Seismology of contracting and expanding coronal loops using damping of kink oscillations by mode coupling. *Astron. Astrophys.* 607, A8. doi:10.1051/0004-6361/201730915

Pascoe, D. J., Smyrli, A., and Van Doorsselaere, T. (2020). Tracking and seismological analysis of multiple coronal loops in an active region. *Astrophys. J.* 898, 126. doi:10.3847/1538-4357/aba0a6

Ruderman, M. S., and Erdélyi, R. (2009). Transverse oscillations of coronal loops. *Space Sci. Rev.* 149, 199–228. doi:10.1007/s11214-009-9535-4

Ruderman, M. S. (2011b). Resonant damping of kink oscillations of cooling coronal magnetic loops. *Astron. Astrophys.* 534, A78. doi:10.1051/0004-6361/201117416

Ruderman, M. S., and Roberts, B. (2002). The damping of coronal loop oscillations. *Astrophys. J.* 577, 475–486. doi:10.1086/342130

Ruderman, M. S., Shukhobodskaya, D., and Shukhobodskiy, A. A. (2019). Resonant damping of propagating kink waves in non-stationary, longitudinally stratified, and expanding solar waveguides. *Front. Astron. Space Sci.* 6, 10. doi:10.3389/fspas.2019.00010

Ruderman, M. S., Shukhobodskiy, A. A., and Erdélyi, R. (2017). Kink oscillations of cooling coronal loops with variable cross-section. *Astron. Astrophys.* 602, A50. doi:10.1051/0004-6361/201630162

Ruderman, M. S., and Terradas, J. (2013). Damping of coronal loop kink oscillations due to mode conversion. *Astron. Astrophys.* 555, A27. doi:10.1051/0004-6361/201220195

Ruderman, M. S. (2011a). Transverse oscillations of coronal loops with slowly changing density. *Sol. Phys.* 271, 41–54. doi:10.1007/s11207-011-9772-z

Ruderman, M. S., Verth, G., and Erdélyi, R. (2008). Transverse oscillations of longitudinally stratified coronal loops with variable cross section. *Astrophys. J.* 686, 694–700. doi:10.1086/591444

Ryutov, D. A., and Ryutova, M. P. (1976). Sound oscillations in a plasma with "magnetic filaments". *J. Exp. Theor. Phys.* 43, 491.

Samanta, T., Tian, H., and Prasad Choudhary, D. (2018). Statistical investigation of supersonic downflows in the transition region above sunspots. *Astrophys. J.* 859, 158. doi:10.3847/1538-4357/aabf37

Shukhobodskiy, A. A., Ruderman, M. S., and Erdélyi, R. (2018). Resonant damping of kink oscillations of thin cooling and expanding coronal magnetic loops. *Astron. Astrophys.* 619, A173. doi:10.1051/0004-6361/201833714

Shukhobodskiy, A. A., and Ruderman, M. S. (2018). Resonant damping of kink oscillations of thin expanding magnetic tubes. *Astron. Astrophys.* 615, A156. doi:10.1051/0004-6361/201732396

Straus, T., Fleck, B., and Andretta, V. (2015). A steady-state supersonic downflow in the transition region above a sunspot umbra. *Astron. Astrophys.* 582, A116. doi:10.1051/0004-6361/201525805

Wang, T., Ofman, L., Davila, J. M., and Su, Y. (2012). Growing transverse oscillations of a multistranded loop observed by SDO/AIA. *Astrophys. J. Lett.* 751, L27. doi:10.1088/2041-8205/751/2/L27

Watko, J. A., and Klimchuk, J. A. (2000). Width variations along coronal loops observed by TRACE. *Sol. Phys.* 193, 77–92. doi:10.1023/A:1005209528612

Winebarger, A. R., and Warren, H. P. (2005). Cooling active region loops observed with SXT and TRACE. *Astrophys. J.* 626, 543–550. doi:10.1086/429817

Zimovets, I. V., and Nakariakov, V. M. (2015). Excitation of kink oscillations of coronal loops: statistical study. *Astron. Astrophys.* 577, A4. doi:10.1051/0004-6361/201424960

Conflict of Interest: The authors declare that the research was conducted in the absence of any commercial or financial relationships that could be construed as a potential conflict of interest.

frontiers
in Astronomy and Space Sciences

ORIGINAL RESEARCH
published: 18 January 2021
doi: 10.3389/fspas.2020.571186

Testing and Validating Two Morphological Flare Predictors by Logistic Regression Machine Learning

M. B. Korsós[1,2,3], **R. Erdélyi**[2,3,4]*, **J. Liu**[5] **and H. Morgan**[1]

[1]Department of Physics, Aberystwyth University, Ceredigion, United Kingdom, [2]Department of Astronomy, Eötvös Loránd University, Budapest, Hungary, [3]Gyula Bay Zoltán Solar Observatory (GSO), Hungarian Solar Physics Foundation (HSPF), Gyula, Hungary, [4]Solar Physics and Space Plasma Research Center (SP2RC), School of Mathematics and Statistics, University of Sheffield, Sheffield, United Kingdom, [5]Astrophysics Research Centre (ARC), School of Mathematics and Physics, Queen's University, Belfast, United Kingdom

Whilst the most dynamic solar active regions (ARs) are known to flare frequently, predicting the occurrence of individual flares and their magnitude, is very much a developing field with strong potentials for machine learning applications. The present work is based on a method which is developed to define numerical measures of the mixed states of ARs with opposite polarities. The method yields compelling evidence for the assumed connection between the level of mixed states of a given AR and the level of the solar eruptive probability of this AR by employing two morphological parameters: 1) the separation parameter S_{l-f} and 2) the sum of the horizontal magnetic gradient G_S. In this work, we study the efficiency of S_{l-f} and G_S as flare predictors on a representative sample of ARs, based on the SOHO/MDI-Debrecen Data (SDD) and the SDO/HMI - Debrecen Data (HMIDD) sunspot catalogues. In particular, we investigate about 1,000 ARs in order to test and validate the joint prediction capabilities of the two morphological parameters by applying the logistic regression machine learning method. Here, we confirm that the two parameters with their threshold values are, when applied together, good complementary predictors. Furthermore, the prediction probability of these predictor parameters is given at least 70% a day before.

Keywords: morphological parameters, validation, binary logistic regression, machine learning, flare prediction

OPEN ACCESS

Edited by:
Peng-Fei Chen,
Nanjing University, China

Reviewed by:
Sergei Zharkov,
University of Hull, United Kingdom
Keiji Hayashi,
Stanford University, United States

****Correspondence:***
R. Erdélyi
robertus@sheffield.ac.uk

Specialty section:
This article was submitted to Stellar and Solar Physics, a section of the journal Frontiers in Astronomy and Space Sciences

Received: *10 June 2020*
Accepted: *11 December 2020*
Published: *18 January 2021*

Citation:
Korsós MB, Erdélyi R, Liu J and Morgan H (2021) Testing and Validating Two Morphological Flare Predictors by Logistic Regression Machine Learning.
Front. Astron. Space Sci. 7:571186.
doi: 10.3389/fspas.2020.571186

1 INTRODUCTION

A solar flare is a sudden flash observed in the solar atmosphere which is able to rapidly heat the plasma to megakelvin temperatures, while the electrons, protons and other heavier ions are accelerated to very large speeds (Benz, 2008). The associated accelerated particle clouds may reach the Earth, typically within a few hours or a day following a solar flare eruption. The flares produce radiation across the electromagnetic spectrum at all wavelengths. Most of the released energy is spread over frequencies outside the visible range. For this reason, the majority of flares must be observed with instruments which measurements in these wavelength ranges, as e.g., the Geostationary Operational Environmental Satellite (GOES). Therefore, the most generally known flare classification scheme is GOES flare-class. Measurements of the maximum x-ray flux at wavelengths from 0.1 to 0.8 nm near Earth are classed as A, B, C, M, or X type flares back from 1975[1]. These five GOES flare intensity

---

[1] http://hesperia.gsfc.nasa.gov/goes/goes_event_listings/

categories are further divided into a logarithmic scale labeled from 1 to 9. The A-, B- and C-classes are the lowest energy release classes of solar flares and they also occur frequently in the solar atmosphere. The A to C-class range has no or hardly any detectable effect on Earth based on current instrumentations and understanding. The M-class medium flare category may cause smaller or occasionally more serious disruptions, e.g., radio blackouts. However, the X-intensity flares may cause strong to extreme hazardous events, facility break-downs (e.g., radio blackouts, etc.) on the daylight side of the Earth (Hayes et al., 2017). The major solar flares (M- and X-class) are often accompany with accelerated solar energetic particles and coronal mass ejections (CMEs) (see, e.g.,, Tziotziou et al., 2010).

For solar activity modeling, a key ingredient is to determine the role of the associated observable magnetic field. Waldmeier (1938) proposed the first classification scheme to examine the connection between the size and morphology of active regions (ARs) and the capacity of their flare-productivity. This classification scheme is known today as the Zürich classification (see also Kiepenheuer, 1953). This scheme contains eight types thought to be representative of consecutive states in the evolution of a sunspot group. The classification system was further developed by McIntosh (1990). McIntosh introduced three more components based on characteristics including the Zürich class, the largest sunspot, and the sunspot distribution in an AR. Although the classification uses white-light observations only, it is still widely used.

The first magnetic classification scheme, known as the Mount Wilson classification, was introduced by Hale et al. (1919). It is simpler than the Zürich-McIntosh system, as it only distinguishes unipolar, bipolar, mixed configurations and very close and mixed configurations within a common penumbral feature, denoted by the letters α, β, γ and δ-class, respectively. Künzel (1960) added the δ-class configurations for the McIntosh system which refer to the most productive sources of energetic flares (see, e.g.,, Schrijver, 2016, and references therein). All these classification schemes are useful in revealing potential connections between the morphological properties of sunspot groups and their flare-productivity. However, it is somewhat ambiguous that these classification schemes rely on a number of rather subjective elements to be identified by visual inspection besides some more objective measures.

The McIntosh and Mount Wilson classifications have been shown to be useful for grouping ARs by their expected flare productivity (Gallagher et al., 2002; Ireland et al., 2008; Bloomfield et al., 2012). However, further quantities derived from AR observations allow a physical comparison and deeper understanding of the actual causes of the solar eruptions. In this sense, different morphological parameters have been introduced to characterised the magnetic field configuration or highlight the existence of polarity-inversion-lines (PILs) in ARs, with varying sophistication (see e.g., Barnes et al., 2016; Leka et al., 2018; Campi et al., 2019; Leka et al., 2019a, Leka et al., 2019b; Park et al., 2020, and references therein). Furthermore, Kontogiannis et al. (2018) investigated and tested some of those parameters, which were identified as efficient flare predictors. These parameters include, e.g.,, a quantity denoted as B_{eff} that measures the coronal magnetic connectivity between the opposite magnetic field elements (Georgoulis and Rust, 2007), Ising energy E_{Ising} of a distribution of interacting magnetic elements (Ahmed et al., 2010), the sum of the horizontal magnetic field gradient G_S (Korsós and Erdélyi, 2016), and the total unsigned non-neutralized currents, $I_{NN,tot}$ (Kontogiannis et al., 2017).

The observed magnetic properties of an AR can be processed for the purpose of prediction by machine learning (ML) computational methods for data analysis (Camporeale, 2019), such as neural networks (Ahmed et al., 2013), support vector machines (Bobra and Couvidat, 2015; Boucheron et al., 2015), relevance vector machines (Al-Ghraibah et al., 2015), ordinal logistic regression (Song et al., 2009), decision trees (Yu et al., 2009), random forests (Liu et al., 2017; Domijan et al., 2019), and deep learning (Nishizuka et al., 2018). Notably, parameters B_{eff}, E_{Ising}, G_S, and $I_{NN,tot}$ were used by the FLARECAST project[2], where the prediction capabilities of almost 200 parameters were tested by the LASSO and Random Forest ML techniques (Campi et al., 2019). From these 200 parameters, the FLARECAST project found that the four morphological parameters were ranked as good flare predictors.

The content of the paper is as follows: **Section 2** overviews in detail the two morphological parameters used for flare prediction in this work. **Section 3** describes the data preparation process and key aspects of the adopted ML method. **Section 4** shows the results of the analysis focusing on two morphological parameters in particular, while our conclusions are in **Section 5**.

2 TWO MORPHOLOGICAL PARAMETERS

Korsós and Erdélyi (2016) introduced and tested, as a trial, an advantageous scheme that may be used as new prediction indicators besides the Zürich, McIntosh and Mount Wilson classification systems. This scheme includes two morphological parameters, namely:

- The separation parameter S_{l-f}, which characterises the separation of opposite polarity subgroups in an AR, given by the formula:

$$S_{l-f} = \frac{D_{lc-fc}}{2\sqrt{\sum A_g \big/ \pi}}, \tag{1}$$

where l and f refer to the leading and following polarities. The numerator denotes the distance between the area-weighted centers (therefore the index c) of the spots of leading and following polarities. **Figure 1A** gives a visual representation. The denominator is the diameter of a hypothetic circle (2 times the radius ($\sqrt{\sum A_g/\pi}$)). The $\sum A_g$ is the sum of individual umbrae areas in a sunspot group.

---

[2] http://flarecast.eu

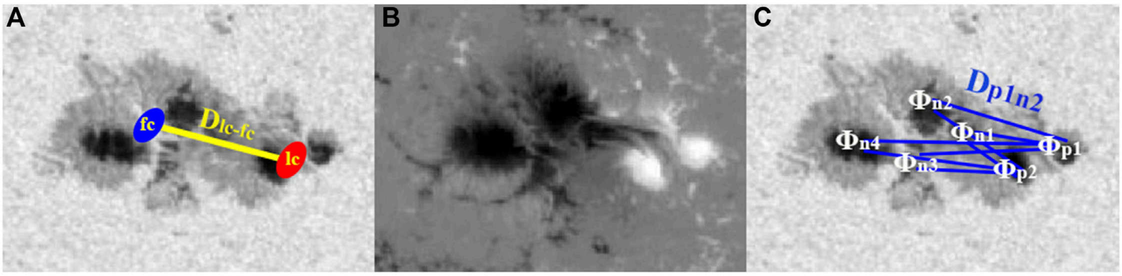

FIGURE 1 | Figures illustrating the determination of the $S_{l\text{–}f}$ and G_S morphological parameters. Panel **(A)** demonstrates, for $S_{l\text{–}f}$, how the distance $D_{lc\text{–}fc}$ is taken between the area-weighted centers (therefore the index *c*) of the spots of leading *l* and following *f* polarities. Panel **(B)** is the corresponding magnetogram of the continuum image of AR 11775, which were taken at 00:59 on 20 June 2013. Panel **(C)** present how the G_S parameter is calculated. Φ is the magnetic flux in a positive *p* or negative *n* umbra. *D* is the distance between two opposite-polarity umbrae.

The second introduced morphological parameter is the sum of the horizontal magnetic gradient G_S, defined by

$$G_S = \sum_{i,j} \frac{\left|\Phi_{p,i} - \Phi_{n,j}\right|}{D_{i,j}}, \qquad (2)$$

- where Φ is the magnetic flux of the umbra based on Korsós et al. (2014). The indices p and n denote positive and negative polarities, and i and j are their running indices in the entire sunspot group. D is the distance between two opposite-polarity umbrae with indices i and j, respectively. Panel c of **Figure 1** gives a visual presentation of the G_S parameter.

The $S_{l\text{–}f}$ and G_S can be determined from the moment of first available observation of sunspot groups, because the applied umbrae data are suitably corrected for geometrical foreshortening in the SOHO/MDI-Debrecen Data (SDD[3,]) and the SDO/HMI—Debrecen Data (HMIDD[4]) catalogues (Baranyi et al., 2016). Furthermore, these two morphological parameters were shown to be potential indicators for upcoming flares on a smaller number of typical test cases (Korsós and Erdélyi, 2016). The test cases included 116 ARs, which were selected from SDD. Their selection was based on that about a third of the ARs produced only B- and C-class flares, another third produced M-class flares, and the remaining third produced X-class flares. For the statistical analysis, the considered values of $S_{l\text{–}f}$ and G_S were determined 24, 48, and 72 hr before flare onset to test the conditional flare probability (CFP) of these two parameters. The CFPs were calculated as empirical probabilities, which measure the studied flare intensities and adequate recordings of the happening of events.

Korsós and Erdélyi (2016) found that if $S_{l\text{–}f} \leq 1$ for a flaring AR then the CFP of the expected largest intensity flare being X-class is over at least 70%. If $1 \leq S_{l\text{–}f} \leq 3$ the CFP is more than 45% for the largest-intensity flare(s) to be the M-class, and, if $3 \leq S_{l\text{–}f} \leq 13$ there is larger than 60% CFP that C-class flare(s) may occurs within a 48-hr interval. Next, Korsós and Erdélyi (2016) found also that from analysing G_S independently for determining the associated CFPs: if $7.5 \leq \log(G_S)$ then there is at least 70% chance for the strongest energy release to be X-class; if $6.5 \leq \log(G_S) \leq 7.5$ then there is ∼45% CFP that M-class could be the highest-intensity flares; finally, if $5.5 \leq \log(G_S) \leq 6.5$, then it is very likely that C-class flare(s) may be the main intensity flares in the coming 48 h. ARs are unlikely to produce X-class flare(s) if $13 \leq S_{l\text{–}f}$ and $\log(G_S) \leq 5.5$.

3 DATA AND DATA PREPARATION

In this study, we further explore test and validate, the joint prediction capabilities of the $S_{l\text{–}f}$ and G_S morphological parameters. The analysis is based on the binary logistic regression algorithm, using the Scikit-Learn module in Python (Pedregosa et al., 2011). The adopted ML technique requires appropriate historical datasets for training. Logistic regression is one of simplest and widely-used ML algorithms for two-class classification. Logistic regression is a special case of linear regression where the target variable is dichotomous in nature. Dichotomous means that there are only two possible classes, e.g., yes/no or true/false. Logistic regression also predicts the probability of occurrence of a binary event utilising a logit function.

Four training sets were constructed to enforce consistency in time and test robustness, each one corresponding to 6-, 12-, 18- and 24-hr forecast issuing time interval, because within a day the forecast reliability becomes more pronounced. The study takes as a reference the time of the largest flare event for each AR. For each issuing time interval, we consider the calculated $S_{l\text{–}f}$ or G_S values of an AR before this reference time, as input data for the logistic regression. This framework allows us to quantify the prediction capabilities of the two morphological parameters.

Similarly to Korsós and Erdélyi (2016), this study uses information on around 1,000 ARs extracted from the Debrecen Sunspot Data Catalogue between 1996 and 2015 (Baranyi et al., 2016). The catalogue contains information including centroid position in various coordinate systems,

---

[3] http://fenyi.solarobs.csfk.mta.hu/en/databases/SOHO/

[4] http://fenyi.solarobs.csfk.mta.hu/en/databases/SDO/

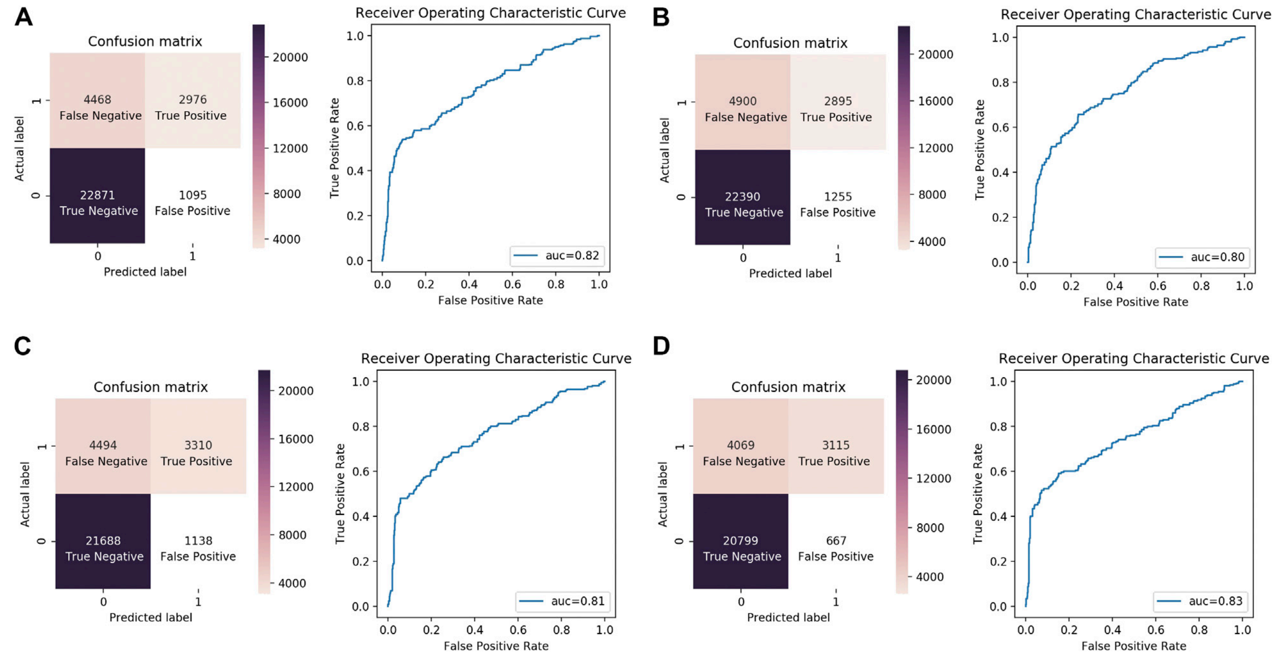

FIGURE 2 | The result of the binary logistic regression of the 1st model with 6-, 12-, 18-, and 24-hr forecast issuing times for panels **(A)**, **(B)**, **(C)**, and **(D)** respectively. The right side of each panel presents the corresponding Receiver Operating Characteristic (ROC) curves.

area, and magnetic field of sunspots and sunspot groups. Derived from spacecraft observations, the catalogue has entries at each 1 hr for SDD[5], and 1.5 hr for HMIDD[6]. The GOES[7] flare catalogue is used for information on the largest-intensity flare eruption of each AR.

For each issuing time interval, two thirds of the ARs were randomly extracted to create a training set. These ARs are labeled as true(1) and false(0) events, under two different binary classification definition models:

- 1st model: When the largest intensity flare of an AR is M- or X-class then this case is classified as true(1), otherwise B- or C-class flares are false(0).
- 2nd model: Based on the results of Korsós and Erdélyi (2016), an event is true(1) if an AR is host to a M/X-class flare, satisfying $3 \le S_{l-f}$, and $6.5 \le \log(G_S)$. Or, an event is true(1) if an AR was host to a B/C-class flare, satisfying $S_{l-f} > 3$, and $\log(G_S) < 6.5$. Otherwise the cases are all labeled false(0).

The two different classification models were chosen to study whether the two morphological parameters perform better, either with or without (2nd or 1st model) thresholds. Often, a well-chosen threshold adjustment(s) could improve prediction capabilities of a method, as a warning level or as a warning sign. Furthermore, in the case of both model approaches as described above, the set of S_{l-f} and G_S values associated with the remaining 1/3 ARs are not labeled and are provided as a test set only for the logistic regression algorithm training. In this manner, there is no overlap between training and testing. To ensure robustness of the results, we replicated 100 times the training and test datasets for 6/12/18 and 24-hr issuing time intervals, like e.g., Campi et al. (2019).

4 ANALYSIS

Solar flare prediction is affected by strong class imbalances, in that there are far more negative examples (labeled as N) than positive ones (labeled as P.) Therefore, we apply different metrics to measure the performance of the 1st and 2nd models. The performances of the two binary classifiers can be characterised by confusion matrixes in **Figures 2**, **3**. Those confusion matrixes summarise the True Positive (TP), True Negative (TN), False Positive (FP), and False Negative (FN) predictions, we adopt different metrics to quantify the impact performance of the S_{l-f} and G_S parameters in the case of both model approaches (1st and 2nd). The applied metrics are summarised in **Table 1** for 6-, 12-, 18- and 24-hr forecast issuing times, and are:

- Accuracy is the ratio of true positives plus true negatives over all events, or how often the TRUE prediction is correct: (TP + TN)/(P + N)
- Recall, also called the true positive rate or sensitivity, measures the proportion of actual positives that are correctly identified: TP/P

---

[5] http://fenyi.solarobs.csfk.mta.hu/en/databases/SOHO/

[6] http://fenyi.solarobs.csfk.mta.hu/en/databases/SDO/

[7] https://www.ngdc.noaa.gov/stp/space-weather/solar-data/solar-features/solar-flares/x-rays/goes/xrs/

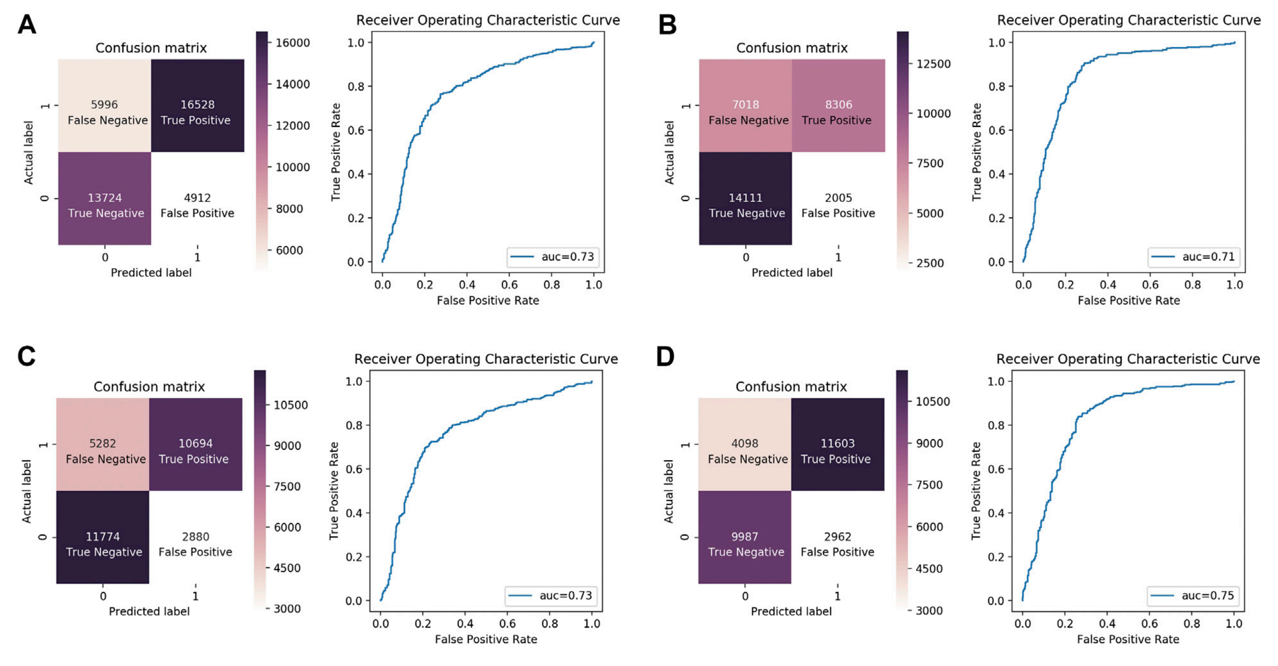

FIGURE 3 | Same as **Figure 2**, but in the case of the 2nd model.

TABLE 1 | Flare prediction capabilities with six metrics in the case of the two model approaches i.e., for 1st model and 2nd model.

Metrics	**1st model**				**2nd model**			
	6 h	**12 h**	**18 h**	**24 h**	**6 h**	**12 h**	**18 h**	**24 h**
Accuracy	0.82	0.81	0.82	0.83	0.73	0.71	0.73	0.75
Recall	0.41	0.37	0.43	0.43	0.73	0.54	0.67	0.74
Specificity	0.95	0.95	0.95	0.97	0.74	0.87	0.80	0.77
Precision	0.73	0.70	0.74	0.82	0.77	0.81	0.79	0.80
NPV	0.83	0.82	0.83	0.84	0.70	0.67	0.69	0.71
F1	0.52	0.48	0.52	0.56	0.75	0.65	0.73	0.77
TSS	0.36	0.32	0.35	0.40	0.47	0.42	0.47	0.51

- Specificity, also called the true negative rate, measures the proportion of actual negatives that are correctly identified: TN/N
- Precision, also called positive predictive value. This is the ratio of true positives over all positive predictions: TP/(TP + FP).
- Negative predictive value (NPV) is the ratio of true negatives over all negative predictions: TN/(TN + FN).
- F1 score is the harmonic mean between sensitivity (or recall) and precision (or). It tells us how precise our two classifiers are, as well as how robust these are. A greater F1 score means that the performance of our model is better. Mathematically, F1 can be expressed as: 2 (1/Recall + 1/Precision)
- True Skill Statistic (TSS) is widely used to test the performance of forecasts (McBride and Ebert, 2000). TSS will be the preferred performance metric when comparing results of the 1st and 2nd model approaches with different N/P ratios because this metric is independent from the imbalance ratio (Woodcock, 1976; Bloomfield et al., 2012). TSS takes into account both omission and commission errors. The TSS parameter is similar to Cohen's kappa approach (Shao and Halpin, 1995), and compares the predictions against the result of random guesses. TSS ranges from −1 to +1, where +1 indicates perfect agreement. The zero or less value indicates that a performance no better than random (Landis and Koch, 1977). TSS = TP/P−FP/N = Recall + Specificity-1

These seven metric parameters are plotted as a function of forecast issuing times in **Figure 4**, where the blue/red lines stand for the 1st/2nd model. Based on the values of **Table 1** and **Figure 4**, the two models have high accuracy for all forecast issuing times. In both models, the best accuracy is gained by the 24-hr prediction window. We emphasise that the accuracy is a meaningful measure only if the values of FP and FN would be similar in the confusion matrices of **Figures 2**, **3**. For dissimilar values, the other metrics must be considered in evaluating the prediction performance of the two models.

Next, we focus on the recall and specificity metrics, which show the probability whether a model captures the correct classification during all four intervals. The values of the specificity metric show that the two models are capable to correctly classify TN cases during all four intervals, especially in the case of the 1st model, which is greater than 90%. Based on recall values, the TP classification of the 2nd model is 20% more accurate than the 1st model for 6/12/18/24-hr forecast issuing times.

However, when the two models classify a new AR, then we do not know the true outcome until after an event. Therefore, we are likely to be more interested in the question what is the probability of a true decision of the two models. This is measured by precision and NPV metrics. For the 1st model, the precision

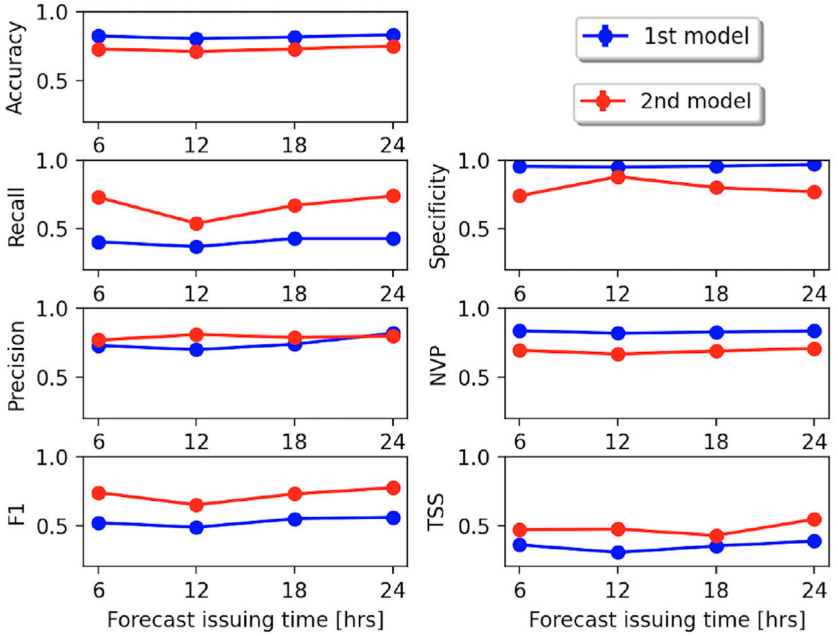

FIGURE 4 | The evolution of selected metrics as a function of forecast issuing times for the 1st **(blue)** and 2nd **(red)** model.

of the 24-hr prediction time is $\sim 10\%$ better than the other issuing time intervals, while the NPV values are $\sim 80\%$ in the case of four issuing time. The precision and NPV values of the 2nd model are almost the same over all four prediction windows. Based on precision and NPV metrics, the 2nd model predict a TP event with higher probability than the 1st model, while the 1st model is better with the case of TN event. This is because the 2nd model discards some X- and M-class flares which do not satisfy the threshold conditions. Despite this, the 2nd model still could fairly predict a TN event with about 70% probability.

The F1 and TSS metrics show that the 2nd model performs better than the 1st in the case of all of the prediction windows. This is an important aspect because the F1 and TSS are the most reliable scores in the presence of class imbalance. Intuitively, the F1 score is not as easy to understand as that of the accuracy, but it is usually more useful than accuracy, especially in our case, where we have an uneven class distribution. Namely, 77% of the F1 score shows that the 24-hr flare prediction window is the most efficient in the case of the 2nd model approach. Furthermore, the above 0.4 values of TSS score of the 2nd model show that this method is a good prediction scheme, and, the defined accuracy values of the 2nd model can be considered as correct.

We also use Receiver Operating Characteristic Curves (ROCs) to evaluated the results of the binary logistic regression method for both models. In the ROC plots in **Figures 2**, **3**, the sensitivity (the proportion of true positive results) is shown on the y-axis, ranging from 0 to 1 (0–100%). The specificity (the proportion of false positive results) is plotted on the x-axis, also ranging from 0 to 1 (0–100%). The area under the curve (AUC) is a measure of the test's performance at distinguishing positive and negative classes. In **Figures 2**, **3**, AUCs are above 0.7, or a capability to distinguish between positive class and negative class with more than 70% likelihood over the 6-, 12-, 18- and 24-hr prediction time windows. From **Figure 2**, the 1st model shows similar AUC values during the four prediction windows. In the case of the 2nd model, the predicting probabilities are also similar based on the AUC values of **Figure 3**. On further note that the predicting probabilities of the 2nd model are 10% less than the 1st one, based on AUC values during the four prediction windows.

5 CONCLUSION

Korsós and Erdélyi (2016) introduced the separation parameter $S_{l\text{–}f}$ and the sum of the horizontal magnetic gradient G_S as potential indirect indicators of the measure of non-potentiality of the magnetic fields of solar active regions. They also proposed these two morphological parameters as potential new prediction proxy indicators complementing the traditional Zürich, McIntosh or Mount Wilson classification schemes.

In this work, a binary logistic regression machine learning approach is used to test and validate the flare prediction capability of the G_S and $S_{l\text{–}f}$ morphological parameters. Two binary classification schemes are used. One scheme is based on a simple approach while implementing solely flare intensity, the second approach is a more sophisticated model based on both flare intensity and threshold values of the morphological parameters. This experimental approach is applied to a large set of ~1,000 ARs, with 100 repeats the datasets, over different forecast issuing time intervals of 6-, 12-, 18-, and 24-hr. Analysis of various performance metrics shows the following:

- The morphological parameters give more than 70% flare prediction accuracy, based on logistical regression analysis.

This result supports the findings of Kontogiannis et al. (2018) and (Campi et al., 2019), who conclude that the G_S parameter has potential as an efficient predictor.

- Based on the F1 scores and the True Skill Statistic metrics, the joint flare prediction efficiency of the S_{l-f} and G_S parameters is improved when the previously identified threshold values by Korsós and Erdélyi (2016) were also imposed. However, the 2nd model discards some X- and M-class flares which do not satisfy the threshold conditions. Despite of it, the 2nd model still could predict/classify an upcoming event with at least 70% probability, based on the precision and NPV metrics.
- The best flare prediction capability of the two parameters is available with 24-hr forecast issuing time. This latter means that the S_{l-f} and G_S parameters with their thresholds are capable to predict an upcoming flare with 75% accuracy a day before flare occurrence.
- However, not just the 24 hrs prediction window has good metric scores, but also the ones with 6/12 and 18 hrs. This means that the S_{l-f} and G_S are together applicable for prediction purpose in a short- and long-term one.
- The limitation of this study is that the applied data are extracted from a given sunspot database. Therefore, an other ML method (e.g., Convolutional Neural Network) that is trained on the same SDO/HMI intensity and magnetogram data, may assess further parameters to increase the predictive capability of the two morphological parameters.

We are aware that the two tested models are not perfect and so a natural question to ask is: how can we improve further them? In the future, we intend to further explore the application of these two warning parameters both from machine learning and physics perspectives: 1) fine tune the threshold conditions of 2nd model, 2) extend the application of the S_{l-f} and G_S parameters at different solar atmosphere heights, 3) train the employed machine learning model at different atmospheric heights for an even more accurate estimation of flare event time and flare event intensity, and 4) identify an optimal height range giving the earliest possible flare prediction, similar to the concept described by Korsos et al. (2020).

DATA AVAILABILITY STATEMENT

Publicly available datasets were analyzed in this study. This data can be found here: http://fenyi.solarobs.csfk.mta.hu/ftp/pub/SDO/data/. http://fenyi.solarobs.csfk.mta.hu/ftp/pub/SDD/data/

AUTHOR CONTRIBUTIONS

MK, RE, JL, and HM contributed to the conception and design of the study. MK performed the statistical analysis and wrote the first draft of the manuscript. All authors contributed to manuscript revision, read, and approved the submitted version.

FUNDING

MK and HM are grateful to the Science and Technology Facilities Council (STFC), (United Kingdom, Aberystwyth University, grant number ST/S000518/1), for the support received while carrying out this research. RE is grateful to STFC (United Kingdom, grant number ST/M000826/1) and EU H2020 (SOLARNET, grant number 158538). RE also acknowledges support from the Chinese Academy of Sciences President's International Fellowship Initiative (PIFI, grant number 2019VMA0052) and The Royal Society (grant nr IE161153). JL acknowledges the support from STFC under grant No. ST/P000304/1.

ACKNOWLEDGMENTS

The authors are grateful to the Referees for constructive comments and recommendations which helped to improve the readability and quality of the paper.

REFERENCES

Ahmed, O. W., Qahwaji, R., Colak, T., Dudok De Wit, T., and Ipson, S. (2010). A new technique for the calculation and 3D visualisation of magnetic complexities on solar satellite images. *Vis. Comput.* 26, 385–395. doi:10.1007/s00371-010-0418-1

Ahmed, O. W., Qahwaji, R., Colak, T., Higgins, P. A., Gallagher, P. T., and Bloomfield, D. S. (2013). Solar flare prediction using advanced feature extraction, machine learning, and feature selection. *Sol. Phys.* 283, 157–175. doi:10.1007/s11207-011-9896-1

Al-Ghraibah, A., Boucheron, L. E., and McAteer, R. T. J. (2015). An automated classification approach to ranking photospheric proxies of magnetic energy build-up. *Astron. AstroPhys.* 579, A64. doi:10.1051/0004-6361/201525978

Baranyi, T., Győri, L., and Ludmány, A. (2016). On-line tools for solar data compiled at the debrecen observatory and their extensions with the Greenwich sunspot data. *Sol. Phys.* 291, 3081–3102. doi:10.1007/s11207-016-0930-1

Barnes, G., Leka, K. D., Schrijver, C. J., Colak, T., Qahwaji, R., Ashamari, O. W., et al. (2016). A comparison of flare forecasting methods. I. Results from the all-clear workshop. *Astrophys. J.* 829, 89. doi:10.3847/0004-637X/829/2/89

Benz, A. O. (2008). Flare observations. *Living Rev. Sol. Phys.* 5, 1. doi:10.12942/lrsp-2008-1

Bloomfield, D. S., Higgins, P. A., McAteer, R. T. J., and Gallagher, P. T. (2012). Toward reliable benchmarking of solar flare forecasting methods. *Astrophys. J. Lett.* 747, L41. doi:10.1088/2041-8205/747/2/L41

Bobra, M. G., and Couvidat, S. (2015). Solar flare prediction using SDO/HMI vector magnetic field data with a machine-learning algorithm. *Astrophys. J.* 798, 135. doi:10.1088/0004-637X/798/2/135

Boucheron, L. E., Al-Ghraibah, A., and McAteer, R. T. J. (2015). Prediction of solar flare size and time-to-flare using support vector machine regression. *Astrophys. J.* 812, 51. doi:10.1088/0004-637X/812/1/51

Campi, C., Benvenuto, F., Massone, A. M., Bloomfield, D. S., Georgoulis, M. K., and Piana, M. (2019). Feature ranking of active region source properties in solar flare forecasting and the uncompromised stochasticity of flare occurrence. *Astrophys. J.* 883, 150. doi:10.3847/1538-4357/ab3c26

Camporeale, E. (2019). The challenge of machine learning in space weather: nowcasting and forecasting. *Space Weather* 17, 1166–1207. doi:10.1029/2018SW002061

Domijan, K., Bloomfield, D. S., and Pitié, F. (2019). Solar flare forecasting from magnetic feature properties generated by the solar monitor active region tracker. *Sol. Phys.* 294, 6. doi:10.1007/s11207-018-1392-4

Gallagher, P. T., Moon, Y.-J., and Wang, H. (2002). Active-region monitoring and flare forecasting I. Data processing and first results. *Sol. Phys.* 209, 171–183. doi:10.1023/A:1020950221179

Georgoulis, M. K., and Rust, D. M. (2007). Quantitative forecasting of major solar flares. *Astrophys. J. Lett.* 661, L109–L112. doi:10.1086/518718

Hale, G. E., Ellerman, F., Nicholson, S. B., and Joy, A. H. (1919). The magnetic polarity of sun-spots. *Astrophys. J.* 49, 153. doi:10.1086/142452

Hayes, L. A., Gallagher, P. T., McCauley, J., Dennis, B. R., Ireland, J., and Inglis, A. (2017). Pulsations in the Earth's lower ionosphere synchronized with solar flare emission. *J. Geophys. Res.* 122, 9841–9847. doi:10.1002/2017JA024647

Ireland, J., Young, C. A., McAteer, R. T. J., Whelan, C., Hewett, R. J., and Gallagher, P. T. (2008). Multiresolution analysis of active region magnetic structure and its correlation with the Mount Wilson classification and flaring activity. *Sol. Phys.* 252, 121–137. doi:10.1007/s11207-008-9233-5

Kiepenheuer, K. O. (1953). *Solar activity*. Chicago, IL: The University of Chicago Press, 322.

Kontogiannis, I., Georgoulis, M. K., Park, S.-H., and Guerra, J. A. (2017). Non-neutralized electric currents in solar active regions and flare productivity. *Sol. Phys.* 292, 159. doi:10.1007/s11207-017-1185-1

Kontogiannis, I., Georgoulis, M. K., Park, S.-H., and Guerra, J. A. (2018). Testing and improving a set of morphological predictors of flaring activity. *Sol. Phys.* 293, 96. doi:10.1007/s11207-018-1317-2

Korsós, M. B., and Erdélyi, R. (2016). On the state of a solar active region before flares and CMEs. *Astrophys. J.* 823, 153. doi:10.3847/0004-637X/823/2/153

Korsós, M. B., Baranyi, T., and Ludmány, A. (2014). Pre-flare dynamics of sunspot groups. *Astrophys. J* 789, 107. doi:10.1088/0004-637X/789/2/107

Korsos, M. B., Georgoulis, M. K., Gyenge, N., Bisoi, S. K., Yu, S., Poedts, S., et al. (2020). Solar flare prediction using magnetic field diagnostics above the photosphere. *Astrophys. J.* 896 (2), 119. doi:10.3847/1538-4357/ab8fa2

Künzel, H. (1960). Die Flare-Häufigkeit in Fleckengruppen unterschiedlicher Klasse und magnetischer Struktur. *Astron. Nachr.* 285, 271. doi:10.1002/asna.19592850516

Landis, J. R., and Koch, G. G. (1977). The measurement of observer agreement for categorical data. *Biometrics* 33, 159–174. doi:10.2307/2529310

Leka, K. D., Barnes, G., and Wagner, E. (2018). The NWRA classification infrastructure: description and extension to the discriminant analysis flare forecasting system (DAFFS). *J. Space Weather and Space Clim.* 8, A25. doi:10.1051/swsc/2018004

Leka, K. D., Park, S.-H., Kusano, K., Andries, J., Barnes, G., Bingham, S., et al. (2019a). A comparison of flare forecasting methods. II. Benchmarks, metrics, and performance results for operational solar flare forecasting systems. *Astrophys. J.* 243, 36. doi:10.3847/1538-4365/ab2e12

Leka, K. D., Park, S.-H., Kusano, K., Andries, J., Barnes, G., Bingham, S., et al. (2019b). A comparison of flare forecasting methods. III. Systematic behaviors of operational solar flare forecasting systems. *Astrophys. J.* 881, 101. doi:10.3847/1538-4357/ab2e11

Liu, C., Deng, N., Wang, J., and Wang, H. (2017). "Predicting solar flares using SDO/HMI vector magnetic data product and random forest algorithm," *Astrophys. J.* 843 (2), 104. doi:10.3847/1538-4357/aa789b

McBride, J. L., and Ebert, E. E. (2000). Verification of quantitative precipitation forecasts from operational numerical weather prediction models over Australia. *Weather Forecast* 15, 103–121. doi:10.1175/1520-0434(2000)015<0103:VOQPFF>2.0.CO;2

McIntosh, P. S. (1990). The classification of sunspot groups. *Sol. Phys.* 125, 251–267. doi:10.1007/BF00158405

Nishizuka, N., Sugiura, K., Kubo, Y., Den, M., and Ishii, M. (2018). Deep flare net (DeFN) model for solar flare prediction. *Astrophys. J.* 858, 113. doi:10.3847/1538-4357/aab9a7

Park, S.-H., Leka, K. D., Kusano, K., Andries, J., Barnes, G., Bingham, S., et al. (2020). A comparison of flare forecasting methods. IV. Evaluating consecutive-day forecasting patterns. *Astrophys. J.* 890, 124. doi:10.3847/1538-4357/ab65f0

Pedregosa, F., Varoquaux, G., Gramfort, A., Michel, V., Thirion, B., Grisel, O., et al. (2011). Scikit-learn: machine learning in Python. *J. Mach. Learn. Res.* 12, 2825–2830. doi:10.1016/j.patcog.2011.04.006

Schrijver, C. J. (2016). The nonpotentiality of coronae of solar active regions, the dynamics of the surface magnetic field, and the potential for large flares. *Astrophys. J.* 820, 103. doi:10.3847/0004-637X/820/2/103

Shao, G., and Halpin, P. N. (1995). Climatic controls of eastern north american coastal tree and shrub distributions. *J. Biogeogr.* 22, 1083–1089. doi:10.2307/2845837

Song, H., Tan, C., Jing, J., Wang, H., Yurchyshyn, V., and Abramenko, V. (2009). Statistical assessment of photospheric magnetic features in imminent solar flare predictions. *Sol. Phys.* 254, 101–125. doi:10.1007/s11207-008-9288-3

Tziotziou, K., Sandberg, I., Anastasiadis, A., Daglis, I. A., and Nieminen, P. (2010). Using a new set of space-borne particle monitors to investigate solar-terrestrial relations. *Astron. AstroPhys.* 514, A21. doi:10.1051/0004-6361/200912928

Waldmeier, M. (1938). Chromosphärische eruptionen. I. Mit 6 abbildungen. *Z. AstroPhys.* 16, 276.

Woodcock, F. (1976). The evaluation of yes/no forecasts for scientific and administrative purposes. *Mon. Weather Rev.* 104, 1209. doi:10.1175/1520-0493(1976)104<1209:TEOYFF>2.0.CO;2

Yu, D., Huang, X., Wang, H., and Cui, Y. (2009). Short-term solar flare prediction using a sequential supervised learning method. *Sol. Phys.* 255, 91–105. doi:10.1007/s11207-009-9318-9

Conflict of Interest: The authors declare that the research was conducted in the absence of any commercial or financial relationships that could be construed as a potential conflict of interest.

ORIGINAL RESEARCH
published: 17 May 2021
doi: 10.3389/fphy.2021.646750

MHD Modeling of Solar Coronal Magnetic Evolution Driven by Photospheric Flow

Chaowei Jiang, Xinkai Bian, Tingting Sun and Xueshang Feng*

Institute of Space Science and Applied Technology, Harbin Institute of Technology, Shenzhen, China

It is well-known that magnetic fields dominate the dynamics in the solar corona, and new generation of numerical modeling of the evolution of coronal magnetic fields, as featured with boundary conditions driven directly by observation data, are being developed. This paper describes a new approach of data-driven magnetohydrodynamic (MHD) simulation of solar active region (AR) magnetic field evolution, which is for the first time that a data-driven full-MHD model utilizes directly the photospheric velocity field from DAVE4VM. We constructed a well-established MHD equilibrium based on a single vector magnetogram by employing an MHD-relaxation approach with sufficiently small kinetic viscosity, and used this MHD equilibrium as the initial conditions for subsequent data-driven evolution. Then we derived the photospheric surface flows from a time series of observed magentograms based on the DAVE4VM method. The surface flows are finally inputted in time sequence to the bottom boundary of the MHD model to self-consistently update the magnetic field at every time step by solving directly the magnetic induction equation at the bottom boundary. We applied this data-driven model to study the magnetic field evolution of AR 12158 with SDO/HMI vector magnetograms. Our model reproduced a quasi-static stress of the field lines through mainly the rotational flow of the AR's leading sunspot, which makes the core field lines to form a coherent S shape consistent with the sigmoid structure as seen in the SDO/AIA images. The total magnetic energy obtained in the simulation matches closely the accumulated magnetic energy as calculated directly from the original vector magnetogram with the DAVE4VM derived flow field. Such a data-driven model will be used to study how the coronal field, as driven by the slow photospheric motions, reaches a unstable state and runs into eruptions.

Keywords: magnetic field, magnetohydodynamic, numerical modeling, solar corona, photospheric flow

Edited by:
Peng-Fei Chen,
Nanjing University, China

Reviewed by:
Yang Guo,
Nanjing University, China
Shin Toriumi,
Japan Aerospace Exploration Agency (JAXA), Japan
Yuhong Fan,
University Corporation for Atmospheric Research (UCAR), United States

***Correspondence:**
Chaowei Jiang
chaowei@hit.edu.cn

Specialty section:
This article was submitted to Stellar and Solar Physics, a section of the journal Frontiers in Physics

Received: 28 December 2020
Accepted: 13 April 2021
Published: 17 May 2021

Citation:
Jiang C, Bian X, Sun T and Feng X (2021) MHD Modeling of Solar Coronal Magnetic Evolution Driven by Photospheric Flow. Front. Phys. 9:646750. doi: 10.3389/fphy.2021.646750

1. INTRODUCTION

Magnetic fields dominate the dynamics in the Sun's upper atmosphere, the solar corona. On the solar surface, i.e., the photosphere, magnetic fields are seen to change continuously; magnetic flux emergence brings new flux from the solar interior into the atmosphere, and meanwhile the flux is advected and dispersed by surface motions such as granulation, differential rotation, and meridional circulation. Consequently, the coronal field evolves in response to (or driven by) the changing of the photospheric field, and thus complex dynamics occur ubiquitously in the corona, including the interaction of newly emerging field with the pre-existing one, twisting and shearing of the magnetic arcade fields, magnetic reconnection, and magnetic explosions which are manifested as flares and coronal mass ejections (CMEs).

As we are still not able to measure directly the three-dimensional (3D) coronal magnetic fields, numerical modeling has long been employed to reconstruct or simulate the coronal magnetic fields based on different assumption of the magnetohydrodynamic (MHD) equations, such as the most-frequently used force-free field model [1], which has been developed for over four decades. However, the force-free field assumption is only valid for the equilibrium of the corona, and it cannot be used to follow a continual and dynamic evolution of the magnetic fields. In recent years, with vector magnetogram data in the photosphere measured routinely with high resolution and cadence, data-driven modeling is becoming a viable tool to study coronal magnetic field evolution, which can self-consistently describe both the quasi-static and the dynamic evolution phases [e.g., 2–10]. Still, due to the limited constraint from observation, data-driven models are developed with very different settings from each other [11]. For simplicity, some used the magneto-frictional model [4, 10], in which the Lorentz force is balanced by a fictional plasma friction force. As such, the magnetic field evolves mainly in a quasi-static way [12], although in some case an eruption can be reproduced but it evolves in a much slower rate than the realistic one [10], because the dynamic is strongly reduced by the frictional force. Some used the so-called zero-β model [7, 9, 13], in which the gas pressure and gravity are neglected. The zero-β model might fail when there is fast reconnection in the field, in which the thermal pressure could play an important role in the dynamics in weak-field region of magnetic field dissipation. Therefore, it is more realistic and accurate to solve the full MHD equations to deal with the non-linear interaction of magnetic fields with plasma.

To drive the full MHD model, one needs to specify all the eight variables (namely plasma density, temperature, and three components of velocity and magnetic field, respectively) in a self-consistent way at the lower boundary. Previously, with only the magnetic field obtained from observations, we employed the projected-characteristic method [2, 14–17] to specify the other variables according to the information of characteristics based on the wave-decomposition principle of the full MHD system [e.g., 5, 18]. Specifically, the full MHD equations are a hyperbolic system that can be eigen-decomposed into a set of characteristic wave equations (i.e., compatibility equations), which are independent with each other; on the boundary, these waves may propagate inward or outward of the computational domain because the wave speeds (the eigenvalues) of both signs generally exist at the boundary. If the wave goes out of the computational domain through the boundary, it carries information from the inner grid to the boundary, and thus the corresponding compatibility equation should be used to constrain the variables on the boundary surface. Thus, if there are five waves going out, and with three components of magnetic field specified by observed data, the eight variables are fully determined. Ideally and in principle, the projected-characteristic method is the most self-consistent one with inputting data that is partially available (for example, in our case, only the data of magnetic field). However, such conditions, i.e., exactly five waves going out, are often not satisfied in the whole boundary and other assumptions are still necessary. Even worse, in areas near the magnetic polarity inversion line (PIL) where the normal magnetic field component is small, the Alfvén wave information goes mainly in the transverse direction rather than the normal one, and the projected-characteristic approach may fail. Another shortcoming of the method lies in its difficulty in code implementation, which needs to perform eigen-decomposition and solve a linear system of the compatibility equations on every grid point on the boundary to recover the primitive variables from the characteristic ones.

In this paper we test another way of specifying the bottom boundary conditions, which uses the surface velocity derived by the DAVE4VM method [19] to drive the MHD model. The differential affine velocity estimator (DAVE) was first developed for estimating velocities from line-of-sight magnetograms, and was then modified to directly incorporate horizontal magnetic fields to produce a differential affine velocity estimator for vector magnetograms (thus called DAVE4VM). It is generally accepted that the coronal magnetic fields are line tied in the dense photosphere and are advected passively by the surface motions of the photosphere, such as the shearing, rotational, and converging flows [20]. Thus, with the surface velocity in hand, we can solve the magnetic induction equation on the bottom boundary to update self-consistently the magnetic field to implement such a line-tying boundary condition, which is a much simpler way than using the projected-characteristic method. To illustrate the approach, we take the solar AR 12158 as an example to simulate its two-day evolution from 2014 September 8 to 10 during its passage of the solar disk. This AR is of interest since it produced an X1.6 eruptive flare accompanied with a fast CME with speed of $\sim$ 1300 km s^{-1}, which is well-documented in the literature [21–23]. The AR is well-isolated from neighboring ARs, thus is suited for our modeling focused on a single AR. Within a few days prior to this major eruption, the AR developed from a weakly sheared magnetic arcade into a distinct sigmoidal configuration, indicating a continual injection of non-potential magnetic energy into the corona through the photospheric surface motion. Indeed, prior to the eruption, the major sunspot of the AR showed a significant rotation of over 200° in 5 days [21]. Based on the sigmoidal hot coronal loop seen immediately before the flare, many authors have interpreted it as a pre-existing magnetic flux rope which erupted and resulted in the flare and CME [e.g., 21–23], while some non-linear force-free field extrapolations appear not to support this [24, 25]. Thus, a fully data-driven MHD simulation can provide valuable insight in addressing this issue by following the dynamic evolution of the coronal magnetic field, although the main objective of this paper is to describe the methods.

In the following we first describe our model equation in section 2. The data-driven simulation consists of three steps, and first we constructed an MHD equilibrium based on a single vector magnetogram observed for the start time of our simulation, which is described in section 3. Then in section 4 we calculated the surface flow field using the DAVE4VM code with the time series of vector magnetograms. Finally, we input the flow field in

TABLE 1 | Parameters used for non-dimensionalization.

Variable	Expression	Value
Density	$\rho_s = nm$	2.29×10^{-15} g cm^{-3}
Temperature	T_s	1×10^6 K
Length	L_s = 16 arcsec	11.52 Mm
Pressure	$p_s = 2nk_B T_s$	2.76×10^{-2} Pa
Magnetic field	$B_s = \sqrt{\mu_0 p_s}$	1.86 G
Velocity	$v_s = \sqrt{p_s/\rho_s}$	110 km s^{-1}
Time	$t_s = L_s/v_s$	105 s
Gravity	$g_s = v_s/t_s$	1.05 km s^{-2}

n is a typical value of electron number density in the corona given by n = 1 × 10^9 cm^{-3} and m is the mean atomic mass.

the model to drive the evolution of the MHD system, as described in section 5. Summary and discussion are given in section 6.

2. MHD EQUATIONS

We numerically solve the full MHD equations in a 3D Cartesian geometry by an advanced conservation element and solution element (CESE) method [26]. Before describing the model equations in the code, it is necessary to specify the quantities used for non-dimensionalization. Here we use typical values at the base of the corona for non-dimensionalization as given in **Table 1**. In the rest of the paper all the variables and quantities are written in non-dimensionalized form if not mentioned specially.

In non-dimensionalized form, the full set of MHD equations are given as

$$\begin{aligned}
\frac{\partial \rho}{\partial t} + \nabla \cdot (\rho \mathbf{v}) &= -\nu_\rho(\rho - \rho_0), \\
\rho \frac{D\mathbf{v}}{Dt} &= -\nabla p + \mathbf{J} \times \mathbf{B} + \rho \mathbf{g} + \nabla \cdot (\nu \rho \nabla \mathbf{v}), \\
\frac{\partial \mathbf{B}}{\partial t} &= \nabla \times (\mathbf{v} \times \mathbf{B}), \\
\frac{\partial T}{\partial t} + \nabla \cdot (T\mathbf{v}) &= (2-\gamma) T \nabla \cdot \mathbf{v}. \qquad (1)
\end{aligned}$$

where $\mathbf{J} = \nabla \times \mathbf{B}$, ν is the kinetic viscosity, and γ is the adiabatic index.

Note that we artificially add a source term $-\nu_\rho(\rho - \rho_0)$ to the continuity equation, where ρ_0 is the density at the initial time $t = 0$ (or some prescribed form), and ν_ρ is a prescribed coefficient. This term is used to avoid a ever-decreasing of the density in the strong magnetic field region, which we often encounter in the very low-β simulation. It can maintain the maximum Alfvén speed in a reasonable level, which may otherwise increase and make the iteration time step smaller and smaller and the long-term simulation unmanageable. Specifically, this source term is a Newton relaxation of the density to its initial value by a time scale of

$$\tau_\rho = \frac{1}{\nu_\rho} = 20\tau_\mathrm{A}, \qquad (2)$$

where $\tau_\mathrm{A} = 1/v_\mathrm{A}$ is the Alfvén time with length of 1 (the length unit) and the Alfvén speed $v_\mathrm{A} = B/\sqrt{\rho}$. Thus, it is sufficiently large to avoid its influence on the fast dynamics of Alfvénic time scales. As a result, we used $\nu_\rho = 0.05 v_\mathrm{A}$ in all the simulation in this paper.

No explicit resistivity is used in the magnetic induction equation, but magnetic reconnection is still allowed through numerical diffusion when a current layer is sufficiently narrow such that its width is close to the grid resolution. In the energy (or temperature) equation, we set $\gamma = 1$ for simplicity, such that the energy equation describes an isothermal process[1]. The kinetic viscosity ν will be given with different values when needed, which is described in the following sections.

3. CONSTRUCTION OF AN INITIAL MHD EQUILIBRIUM

We first constructed an initial MHD equilibrium based on a single vector magnetogram taken for time of 00:00 UT on 2014 September 8 by SDO/HMI. Such an equilibrium is assumed to exist when the corona is not in the eruptive stage, and is crucial for starting our subsequent data-driven evolution. The vector magnetogram is preprocessed to reduce the Lorentz force and is further smoothed to filter out the small-scale structures that are not sufficiently resolved in our simulation. Reduction of the Lorentz force is helpful for reaching a more force-free equilibrium state [e.g., 27], and smoothing is also necessary to mimic the magnetic field at the coronal base rather directly the photosphere, because the lower boundary of our model is placed at the base of the corona [28]. The preprocessing is done using a code developed by Jiang et al. [29], which is originally designed for NLFFF extrapolation using the HMI data [30]. Specifically, the total Lorentz force and torque are quantified by two surface integrals associated with three components of the photospheric magnetic field, and an optimization method is employed to minimize these two functions by modifying the magnetic field components within margins of measurement errors. Then Gaussian smoothing with FWHM of 8 arcsec is applied to all the three components of the magnetic field. **Figure 1** compares the original HMI vector magnetogram with the preprocessed one as well as the final smoothed version. Using the vertical component B_z of this preprocessed and smoothed magnetogram, a potential field is extrapolated and used as the initial condition of the magnetic field in the MHD model.

In addition to the magnetic field, an initial plasma as the background atmosphere is also needed to start the MHD simulation. We used an isothermal plasma in hydrostatic equilibrium. It is stratified by solar gravity with a density $\rho = 1$ at the bottom and a uniform temperature of $T = 1$. Using this typical coronal plasma, we did not directly input the magnetic field into the model but multiplies it with a factor of 0.05 such that the maximum of magnetic field strength in normalized value is

---

[1] Although in this case we can simply discard the energy equation by setting the temperature as a constant, we still keep the full set of equations in our code which can thus describe either the isothermal or adiabatic process by choose different value of γ.

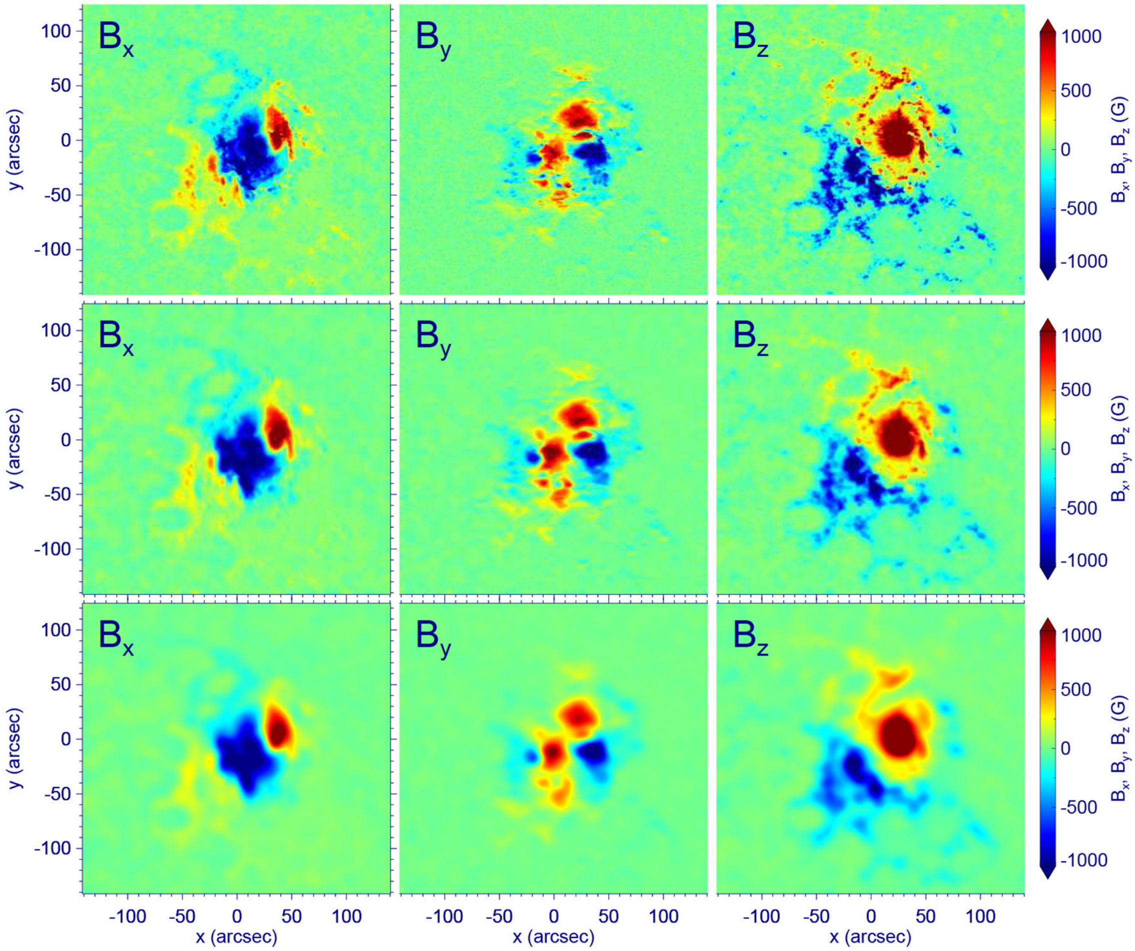

FIGURE 1 | Comparison of the original HMI vector magnetogram for time of 00:00 UT on 2014 September 8 **(Top)**, the preprocessed one **(Middle)**, and the final smoothed one **(Bottom)**. From left to right are shown for magnetic field components B_x, B_y, and B_z, respectively.

approximately 50 $\sim$ 100 in the model. If using the original values of magnetic field, its strength (and the characteristic Alfvén speed) near the lower surface is too larger, which will be a too heavy burden on computation as the time step of our simulation is limited by the CFL condition. With the reduced magnetic field, we further modified the value of solar gravity to avoid an unrealistic large plasma β (and small Alfvén speed) in the corona. This is because if using the real number of the solar gravity ($g_{\odot} = 274$ m s$^{-2}/g_s = 0.26$), it results in a pressure scale height of $H_p = 3.8$, by which the plasma pressure and density decay with height much slower than the magnetic field. With the weak magnetic field strength we used, the plasma β will increase with height very fast to above 1, which is not realistic in the corona. To make the pressure (and density) decrease faster in the lower corona, we modified the gravity as

$$g = \frac{1.5 H_p g_{\odot}}{(1 + 0.15z)^2}. \tag{3}$$

By this, we got a plasma with $\beta < 1$ mainly within $z < 10$ and the smallest value is 5×10^{-3}.

Then we input the transverse field of the smoothed magnetogram to the model. This is done by modifying the transverse field on the bottom boundary incrementally using linear extrapolation from the potential field to the vector magetogram in time with a duration of 1 t_s until it matches the vector magnetogram. This will drive the coronal magnetic field to evolve away from the initial potential state, since the change of the transverse field will inject electric currents and thus Lorentz forces, which drive motions in the computational volume. Note that in this phase all other variables on the bottom boundary are simply fixed, thus the velocity remaining zero. This is somewhat un-physical since the Lorentz force will introduce non-zero flows on the bottom boundary, but it provides a simple and "safe" way (avoiding numerical instability) to bring the transverse magnetic field into the model. Once the magnetic field on the bottom surface is identical to that of the vector magnetogram, the system is then left to relax to equilibrium with all the variables (including the magnetic field) on the bottom boundary fixed. To avoid a too large velocity in this phase such that the system can relax faster, we set the kinetic viscosity coefficient as $\nu = 0.5\Delta x^2/\Delta t$, where Δx is the local grid spacing and Δt the local time step, determined by the CFL condition with the fastest magnetosonic speed. Actually this is the largest viscosity one can use with given grid size Δx and time step Δt, because the CFL condition for a purely diffusive equation with diffusion coefficient ν requires $\Delta t \leq 0.5\Delta x^2/\nu$.

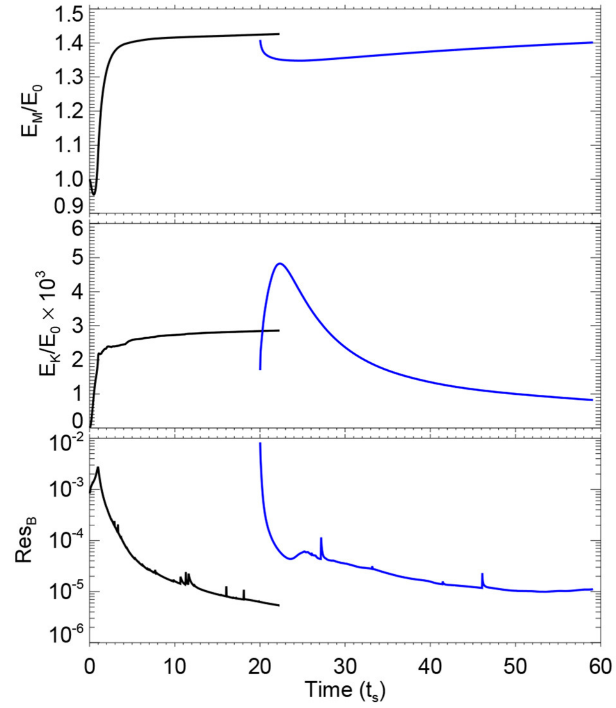

FIGURE 2 | Evolutions of the total magnetic energy, kinetic energy, and residual of magnetic field in the process of the constructing the initial MHD equilibrium. The black curves show the results for the first evolution phase, and the blue ones show that for the second, "deeper" evolution phase.

For the purpose of minimizing the numerical boundary influences introduced by the side and top boundaries of the computational volume, we used a sufficiently large box of $(-32, -32, 0) < (x, y, z) < (32, 32, 64)$ embedding the field of view of the magnetogram of $(-8.75, -8.25) < (x, y) < (8.75, 8.25)$. The full computational volume is resolve by a non-uniform block-structured grid with adaptive mesh refinement (AMR), in which the highest and lowest resolution are $\Delta x = \Delta y = \Delta z = 1/16$ (corresponding to 1 arcsec or 720 km, matching the resolution of the vector magnetogram) and $1/2$, respectively. The AMR is controlled to resolve with the smallest grids the regions of strong magnetic gradients and current density. The magnetic field outside of the area of the magnetograms on the lower boundary is given as zero for the vertical component and simply fixed as the potential field for the transverse components. On the side and top boundaries, we fixed the plasma density, temperature, and velocity. The horizontal components of magnetic field are linearly extrapolated from the inner points, while the normal component is modified according to the divergence-free condition to avoid any numerical magnetic divergence accumulated on the boundaries.

In **Figure 2**, the curves colored in black show the evolution of the magnetic and kinetic energies integrated for the computational volume, and the residual of the magnetic field of two consecutive time steps which is defined as

$$\mathrm{Res}_B = \sqrt{\frac{1}{3}\sum_{\delta=x,y,z}\frac{\sum_i\left(B^k_{i\delta} - B^{k-1}_{i\delta}\right)^2}{\sum_i\left(B^k_{i\delta}\right)^2}}, \tag{4}$$

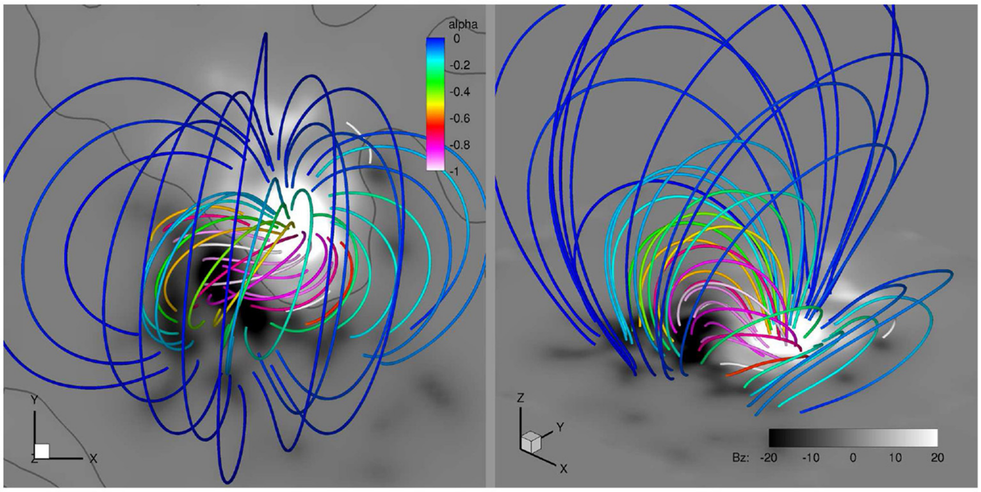

FIGURE 3 | 3D magnetic field of the MHD equilibrium based on the magnetogram taken for 00:00 UT on 2014 September 8. The thick lines are magnetic field lines and are pseudo-colored by value of the force-free parameter α. The background is shown with the magnetic flux distribution (i.e., B_z) on the bottom surface of the model.

where the indices k and $k-1$ refer to the two consecutive time steps and i goes through all the mesh points. It can be seen that the magnetic energy increases sharply in a few time units[2], reaching $\sim$ 1.4 of the potential field energy E_0 (here $E_0 = 1.2 \times 10^{33}$ erg when scaled to the realistic value in the corona), and then keeps almost constant during the relaxing phase with bottom boundary fixed. Very similar, the kinetic energy first increases and later keeps on the level of 3×10^{-3} of E_0. The residual of the magnetic field increases in the first t_s as we continually modified the transverse field at the bottom boundary which drives quickly the evolution of the field in the corona. Then it decreases to below 10^{-5} with a time duration of 20 t_s, which indicates that the magnetic field reaches a quasi-equilibrium state.

To make the field even closer to equilibrium, we carried out a "deeper" relaxation by running the model again, which is started with the relaxed magnetic field obtained at $t = 20\ t_s$ and the initially hydrostatic plasma. Now we reduce the kinetic viscosity to $\nu = 0.05\Delta x^2/\Delta t$, i.e., an order of magnitude smaller than the previously used one, which will let the magnetic field relax further. Furthermore, the magnetic field at the boundary boundary is allowed to evolve in a self-consistent way by assuming the bottom boundary as a perfectly line-tying and fixed (i.e., $\mathbf{v} = 0$) surface of magnetic field lines. However, such a line-tying condition does not indicate that all magnetic field components on the boundary are fixed, because even though the velocity $\mathbf{v}$ is given as zero on the bottom boundary, it is not necessarily zero in the neighboring inner points. To self-consistently update the magnetic field, we solve the magnetic induction equation on the bottom boundary. Slightly different from the one in the main Equations (1), the induction equation at the bottom surface is given as

$$\frac{\partial \mathbf{B}}{\partial t} = \nabla \times (\mathbf{v} \times \mathbf{B}) + \eta_{\rm stable} \nabla_{\perp}^2 \mathbf{B}, \tag{5}$$

where we added a surface diffusion term defined by using a surface Laplace operator as $\nabla_{\perp}^2 = \frac{\partial^2}{\partial x^2} + \frac{\partial^2}{\partial y^2}$ with a small resistivity for numerical stability near the PIL $\eta_{\rm stable} = 1 \times 10^{-3} e^{-B_z^2}$, since the magnetic field often has the strongest gradient on the photosphere around the main PIL. The surface induction Equation (5) in the code is realized by second-order difference in space and first-order forward difference in time. Specifically, on the bottom boundary (we do not use ghost cell), we first compute $\mathbf{v} \times \mathbf{B}$, and then use central difference in horizontal direction and one-sided difference (also 2nd order) in the vertical direction to compute the convection term $\nabla \times (\mathbf{v} \times \mathbf{B})$. The surface Laplace operator is also realized by central difference.

The curves colored in blue in **Figure 2** show the evolution of different parameters during this relaxation phase[3]. Initially one can see a fast decrease of the magnetic energy because the magnetic field becomes more relaxed. As the viscosity is reduced significantly, the kinetic energy first increases, as driven by the residual Lorentz force of the magnetic field, to almost $5 \times 10^{-3}\ E_0$. Then as the magnetic field relaxed, the kinetic energy decreases fast to eventually less than $10^{-3}\ E_0$, which is a very low level. The residual of magnetic field of two consecutive time steps also decreases to 10^{-5}. These values show that the magnetic field reaches an excellent equilibrium.

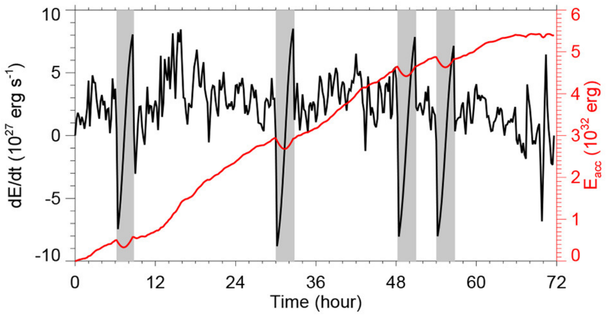

FIGURE 4 | Evolution of Poynting flux (black line) and the accumulated energy (red line) which is time integration of the Poynting flux. The gray bars denote the data gaps of the vector magnetograms for which a simple linear interpolation in time is used to fill.

Figure 3 shows the 3D magnetic field lines of the final relaxed MHD equilibrium. Note that the field lines are false-colored by the values of the force-free factor defined as $\alpha = \mathbf{J} \cdot \mathbf{B}/B^2$, which indicates how much the field lines are non-potential. For a force-free field, this parameter is constant along any given field line. As can be seen, the magnetic field is close to a perfect force-free one since the color is nearly the same along any single field line. In the core of the configuration, the field lines are sheared significantly along the PIL, and thus have large values of α and current density. On the other hand, the overlying field is almost current-free or quasi-potential field with $\alpha \sim 0$, which plays the role of strapping field that confines the inner sheared core. Such a configuration is typical for eruption-productive ARs [e.g., 5, 31–34].

4. DERIVE THE SURFACE FLOW FIELD

Based on the time sequence of vector magnetograms, it is straightforward to derive the surface velocity by employing the DARE4VM code developed by [19]. The differential affine velocity estimator (DAVE) was first developed for estimating velocities from line-of-sight magnetograms, and was then modified to directly incorporate horizontal magnetic fields to produce a differential affine velocity estimator for vector

---

[2] Note that at the very beginning the magnetic energy actually decreases shortly for about 0.5 t_s, which is unphysical as the potential field energy is in principle the lowest energy with a given magnetic flux distribution on the bottom boundary. Such an unphysical evolution is a result of the fact that we modified directly the transverse magnetic field on the bottom boundary in an unphsyical way.

[3] Note that the initial values of the blue curves (the deeper relaxation phase) do not equal to the values of the black curves at $t = 20t_s$ although the deeper relaxation phase starts from that time point. This is because in the deeper relaxation process, there are three ways different from the initial relaxation one: (1) the velocity is reset to zero and the plasma is reset to hydrostatic state, thus the kinetic energy is reset to zero; (2) the viscosity is abruptly reduced by an order of magnitude; (3) the boundary condition is changed. Furthermore, not data of every time step in the run is recorded, thus small difference is shown in the magnetic energy of the initial value of the blue line (which is not exactly for the time of $t = 20t_s$) from the $t = 20t_s$ of the black line.

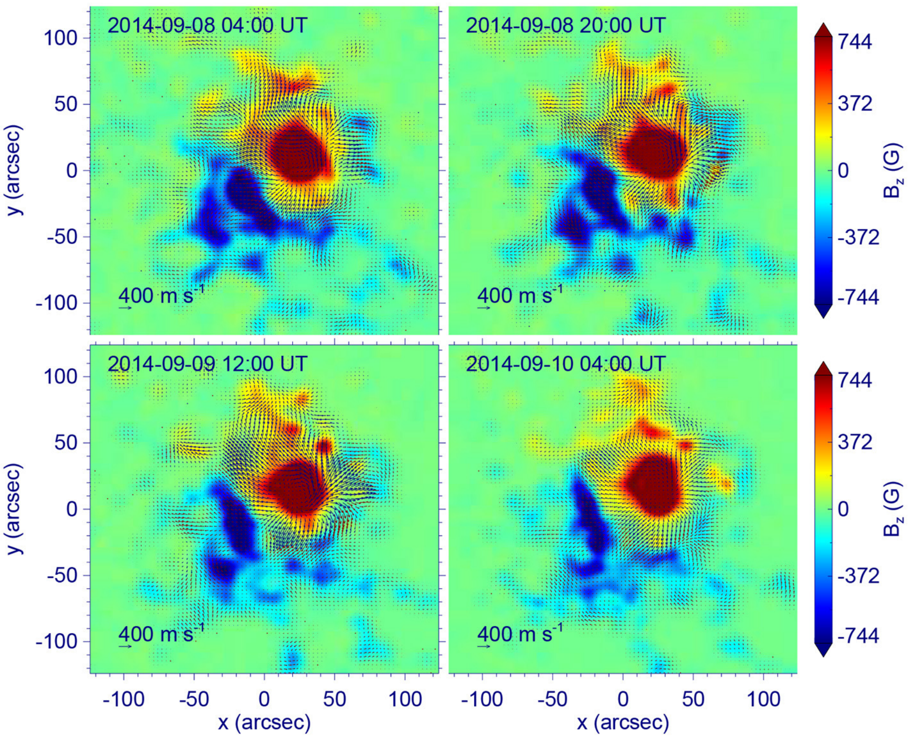

FIGURE 5 | Four snapshots of the surface flows (the final smoothed version) as derived using the DAVE4VM code.

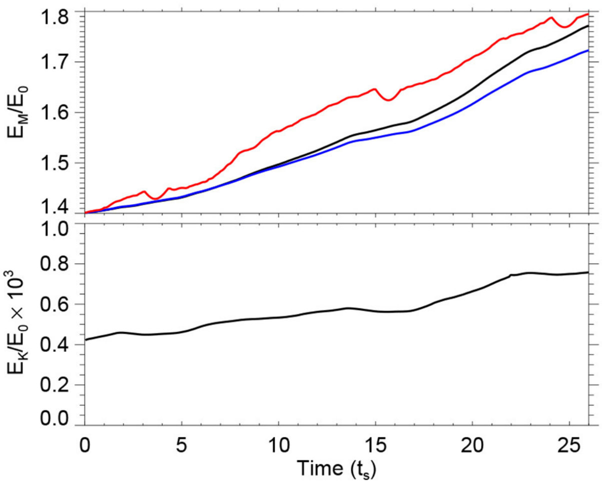

FIGURE 6 | Magnetic energy **(Top)** and kinetic energy **(Bottom)** evolution of the MHD system as driven by the photospheric flows. The black lines represent the values of the volume-integrated energies. The blue line in the top panel shows the time integration of the total Poynting flux on the bottom surface from the simulation. The red line shows the accumulated magnetic energy from directly the observation data, i.e., the same one shown in **Figure 4**.

magnetograms (DAVE4VM). We use the SHARP data with cadence of 12 min and pixel size of 1 arcsec (by rebinning the original data with pixel size of 0.5 arcsec), and first of all, we fill the data gap using a linear interpolation in the time domain to generate a complete time series of 3 days from 00:00 UT on 2014 September 8 to 24:00 UT on September 10 with cadence of 12 min. Then we input the time series of vector magnetogram (rebinned as 1 arcsec per pixel) in the DAVE4VM code. A key parameter needed by the DAVE4VM code is the window size, and here we use 19 pixels, following [35] and [36]. After obtaining the surface velocity, we first reset those in the weak-field region (with total magnetic field strength below 100 G) as zero, because there are large errors and unresolved scales in these regions. **Figure 4** shows evolution of the Poynting flux $\mathrm{d}E/\mathrm{d}t$, which is defined by

$$\frac{\mathrm{d}E}{\mathrm{d}t} = \frac{1}{\mu_0} \int_S \left[(B_x^2 + B_y^2) v_z - (B_x v_x + B_y v_y) B_z \right] \mathrm{d}x\mathrm{d}y, \qquad (6)$$

where S is the photospheric surface, and its time accumulation E_{acc}, as computed by using the surface flow (v_x, v_y, v_z) and the magnetic field. It can be seen that, except the data gap intervals[4], the magnetic energy is continually injected in the corona through the photosphere, and in the 3 days, it gains $\sim 5 \times 10^{32}$ erg.

Before being input into the model, the flow data are also needed to be smoothed. We smoothed the time series of flow maps in both the time and space domains, with a Gaussian FWHM of 6 h (i.e., 30 time snapshots) and 8 arcsec, respectively,

---

[4] During the data gaps the Poynting flux is found to become negative adruptly, which might be a result of our simple linear interpolation in filling the gaps of the magnetograms. More optimized method for filling the data gaps will be considered to recover a more consistent evolution of Poynting flux.

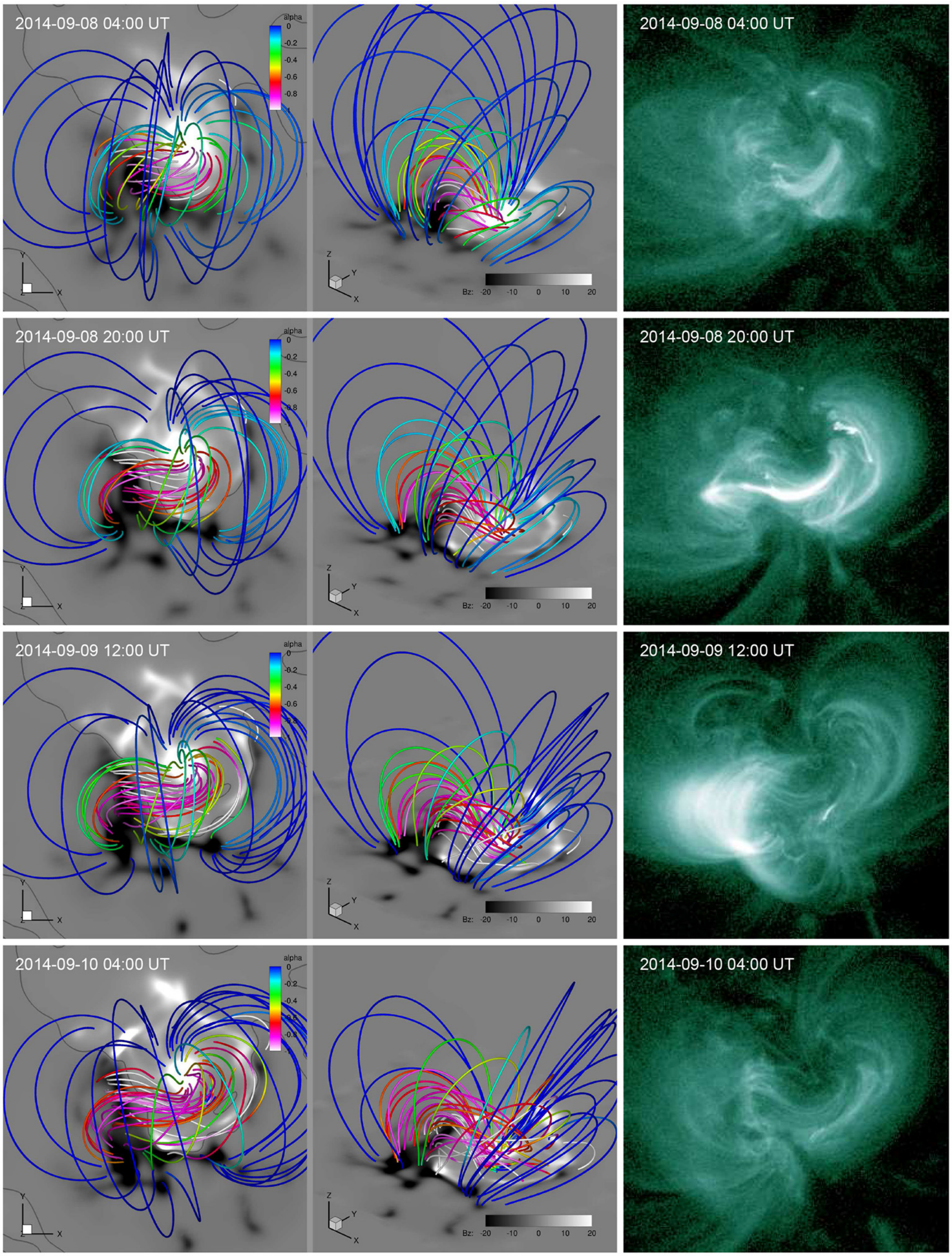

FIGURE 7 | Evolution of the magnetic field lines (shown in different view angles in the left and middle columns) and their comparison with observed coronal loops observed in EUV wavelength of 94 Å by SDO/AIA (right column). The field lines are shown in the same format in **Figure 3**. An animation of the magnetic field evolution is attached for this figure.

which is finally input to the data-driven model. **Figure 5** shows 4 snapshots of the surface velocity after smoothing. The speed of the flow is generally a few hundreds of meters per second and the main feature is a clear and persistent rotation of the main sunspot. Note that during the 3 days the basic configuration of the photospheric magnetic flux distribution is rather similar with only somewhat dispersion. So the magnetic energy injection should come mainly from the transverse rotational flows. In addition to the rotational flow, we can see very evident diverging flow existing persistently near the boundary of the sunspot.

5. DATA-DRIVEN SIMULATION

We input the surface velocity at the bottom boundary to drive the evolution of the model, by starting the simulation from the solution obtained from the time point of $t = 58$ in the relaxation phase (see **Figure 2**) as described in section 3. Here to save computing time, the cadence of the input flow maps, which is originally 12 min, was increased by 68.6 times when inputting into the MHD model. As a result, an unit of time in the simulation, t_s, corresponds to actually $t_s \times 68.6 = 7200$ s, i.e., 2 h, in the HMI data. Compressing of the time in HMI data is justified by the fact that the speed of photospheric flows is often a few 100 m s^{-1}. So in our model settings, the evolution speed of the boundary field, even enhanced by a factor of 68.6, is still smaller by two orders of magnitude than the coronal Alfvén speed (on the order of 10^3 km s^{-1}), and the quick reaction of the coronal field to the slow bottom changes should not be affected. The implementation of the bottom boundary conditions is the same as that for the deeper relaxation phase described in section 3. That is, on the bottom surface, we solved the Equation (5) to update all the three components of magnetic field with the flow field prescribed by those derived in section 4, while the plasma density and temperature are simply fixed. In the driven-evolution phase, the kinetic viscosity is also used as the smaller one $\nu = 0.05\Delta x^2/\Delta t$, which corresponds to a Reynolds number of 10 for the length of a grid cell Δx.

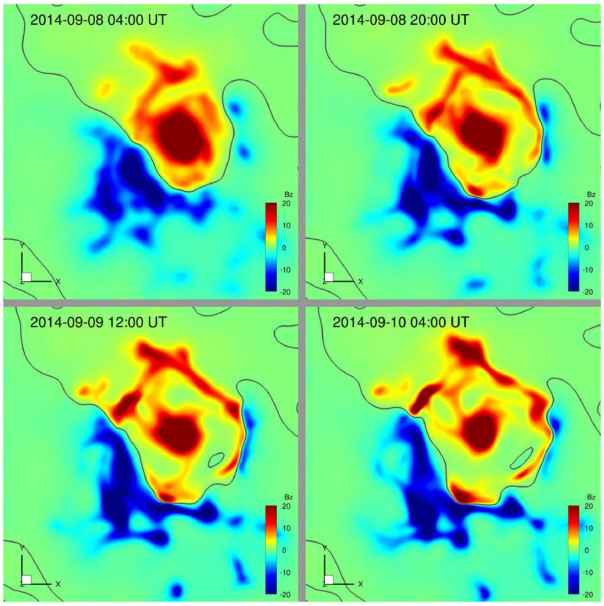

FIGURE 8 | Evolution of magnetic flux distribution on the bottom surface in the simulation, shown for 4 snapshots of the same times shown in **Figure 5**.

We show an approximately 2-day (a duration of 26 t_s or 52 h in reality) evolution of the MHD system as an example, while the further evolution associated with an eruption and the physical mechanisms will be left for future study. **Figure 6** presents the global energy evolutions. It can be seen the magnetic energy (the black line in the top panel) increases monotonously as driven by the surface flows. By the end of our simulation, it reaches approximately 1.8 times of the initial potential energy, and thus the total magnetic energy obtained in this driving phase is $(1.8 - 1.4) \times E_0 \approx 4.8 \times 10^{32}$ erg. On the other hand, the kinetic energy (bottom panel of **Figure 6**) keeps below the level of $1 \times 10^{-3} E_0$ with a mild increase, which indicates that the system remains a stable, quasi-static evolution. In the top panel of **Figure 6** we also plots the time integration of total Poynting flux (the blue line), using the magnetic field and the flow field on the bottom boundary of the simulation, which is the energy injected into the volume from the bottom boundary through the surface flow. If our boundary condition is accurately implemented, the energy injected from the bottom surface should match the magnetic energy obtained in the computational volume, since other energies are negligible if compared with the magnetic energy. As can be seen, the trend of magnetic energy evolution (the black line) matches rather well that of the energy input by the surface flow (the blue line), albeit a small numerical error that increases slowly the total magnetic energy, which is also seen in the relaxation phase as shown in **Figure 2**. It is worthy noting that the magnetic energy evolution is also in good agreement with the accumulated magnetic energy as derived from directly the observation data (the red line, which is the same value shown in **Figure 4** but multiplied by a factor of 0.05^2 because the field input to the model is multiplied by 0.05) as calculated in section 4, which suggests that our data-driven model can reliably reproduce the magnetic energy injection into the corona through the photospheric motions. The small difference between the observation-derived and simulated energies might be due to the smoothing of the velocity since it filters out the small-scale flows that also contribute to the total Poynting flux.

Figure 7 (and its attached animation) shows the 3D magnetic field lines and their evolution in comparison with SDO/AIA image of coronal loops in the 94 Å wavelength which highlights the hot, core coronal loops in the AR. Overall, we can see a slow stressing of the field lines mainly through the sunspot rotational flow. It renders the core field lines to form a more and more coherent S shape, which resembles the observed sigmoid structure in the core of the AR. The increase of non-potentiality can also be seen from the increase of the force-free factor α in the core region. **Figure 8** shows evolution of the surface magnetic flux distribution (see also the animation attached to **Figure 7**). The four snapshots are taken for the same times given in **Figure 5**, and thus comparing **Figure 8** with **Figure 5** shows the difference between the simulated magnetograms and the observed ones. In addition to the rotation of the main sunspot, an evident feature is the enhancement of the field strength along the PIL. This is owing to the divergence flow from the edge of the sunspot, which continually convect the magnetic flux to the PIL. Such pileup of magnetic flux near the PIL, however, is not seen in the observed magnetograms (**Figure 5**), which rather show field decaying. Such decaying of magnetic flux is likely due to the global turbulent diffusion of photospheric magnetic field by granular and supergranular convection [37] and other small-scale turbulence and flux cancellations in the photosphere, which is not being recovered by the DAVE4VM code and thus not reproduced in our simulation.

6. CONCLUSIONS

This paper is devoted to the description of a new approach of data-driven modeling of solar AR magnetic field evolution, in which, we have for the first time utilized directly the photospheric velocity field from DAVE4VM to drive a full-MHD model. To setup the initial conditions, we used a special MHD relaxation approach with sufficiently small kinetic viscosity to construct a true MHD equilibrium based on a single vector magnetogram. Then we derived the photospheric surface flows from a time series of observed magentograms based on the DAVE4VM method. The surface flows were finally inputted, again in time sequence, to the bottom boundary of the MHD model to self-consistently update the magnetic field at every time step, which is implemented by solving directly the magnetic induction equation at the bottom boundary using finite difference method.

We applied this data-driven model to study the magnetic field evolution of AR 12158 with SDO/HMI vector magnetograms. The initial MHD equilibrium is calculated using magnetogram observed for 00:00 UT on 2014 September 8, and a 2-day duration of the AR evolution is then simulated using the data-driven MHD model. Overall, the evolution is characterized by a slow stress of the field lines mainly through the rotational flow of the AR's leading sunspot, which makes the core field lines to forms an coherent S shape consistent with the sigmoid structure as seen in the AIA images. Such evolution proceeds in a quasi-static way since the kinetic energy of the system remains less than its magnetic energy by three orders of magnitude, while the magnetic energy increases monotonously as driven by the surface flow, and reaches approximately double of the initial potential energy by the end of the simulation. The magnetic energy obtained in the simulation during the surface driving phase matches closely the accumulated magnetic energy as calculated directly from the original vector magnetogram with the DAVE4VM derived flow field.

With the surface flow specified at the bottom boundary, the magnetic field can be updated self-consistently by solving the induction equation at the surface boundary. However, our simulation shows that discrepancy arises between the simulated magnetic field at the bottom surface with the original magnetograms. That is, in the simulation, magnetic flux are significantly enhanced along the PIL, owing to the divergence flow from the edge of the sunspot, whereas in the observed magnetograms such pileup of magnetic flux near the PIL is not seen, which rather shows field decaying. In the next step, we will try to use some *ad-hoc* flux cancellation near the PIL, for which a straightforward way is to increase the value of η_{stable} in Equation (5), such that the flux diffusion speed is comparable to that of the flux pileup. In the future, we will consider to include the global diffusion of photospheric magnetic field by granular and supergranular convection to simulate more realistically the magnetic field evolution. On the other hand, the discrepancy might result from errors in the vector magnetograms, since these errors can introduce spurious flows with the DAVE4VM code and thus influences our simulation. To elucidate this, we will test our model with error-free magnetograms from recent convective flux-emergence simulations [e.g., 38–40] as the ground-truth data.

Our ultimate purpose is to use the model to study how the coronal field, as driven by the slow photospheric motions, reaches a unstable state and runs into eruption. From this, we will be able to investigate in details the topology of the evolving magnetic field leading to the eruption, to see whether it forms a magnetic flux rope and becomes ideally unstable [e.g., 41, 42], or, a simply sheared arcade with a interally-formed current sheet to trigger flare reconnection [43], which would be helpful for resolving the long-standing debates on the triggering mechanism of solar eruptions [44].

DATA AVAILABILITY STATEMENT

The original contributions presented in the study are included in the article/supplementary material, further inquiries can be directed to the corresponding author/s.

AUTHOR CONTRIBUTIONS

CJ developed the numerical model, performed the result analysis, and wrote the draft. All authors participated in discussions and revisions on the manuscript.

ACKNOWLEDGMENTS

This work is jointly supported by National Natural Science Foundation of China (NSFC 41822404, 41731067, 41574170, and 41531073), the Fundamental Research Funds for the Central Universities (Grant No. HIT.BRETIV.201901), and Shenzhen Technology Project JCYJ20190806142609035. Data from observations are courtesy of NASA SDO. The computational work was carried out on TianHe-1(A), National Supercomputer Center in Tianjin, China. We are grateful to the reviewers for helping to improve the paper.

REFERENCES

1. Wiegelmann T, Sakurai T. Solar force-free magnetic fields. *Liv Rev Solar Phys.* (2012) 9:5. doi: 10.12942/lrsp-2012-5
2. Wu ST, Wang AH, Liu Y, Hoeksema JT. Data-driven magnetohydrodynamic model for active region evolution. *Astrophys J.* (2006) 652:800–11. doi: 10.1086/507864
3. Feng X, Jiang C, Xiang C, Zhao X, Wu ST. A data-driven model for the global coronal evolution. *Astrophys J.* (2012) 758:62. doi: 10.1088/0004-637X/758/1/62
4. Cheung MCM, DeRosa ML. A method for data-driven simulations of evolving solar active regions. *Astrophys J.* (2012) 757:147. doi: 10.1088/0004-637X/757/2/147
5. Jiang CW, Wu ST, Feng XS, Hu Q. Data-driven MHD simulation of a flux-emerging active region leading to solar eruption. *Nat Commun*. (2016) 7:11522. doi: 10.1038/ncomms11522
6. Leake JE, Linton MG, Schuck PW. Testing the accuracy of data driven MHD simulations of active region evolution. *Astrophys J.* (2017) 838:113. doi: 10.3847/1538-4357/aa6578

7. Inoue S, Kusano K, Büchner J, Skála J. Formation and dynamics of a solar eruptive flux tube. *Nat Commun.* (2018) 9:174. doi: 10.1038/s41467-017-02616-8
8. Hayashi K, Feng X, Xiong M, Jiang C. Magnetohydrodynamic simulations for solar active regions using time-series data of surface plasma flow and electric field inferred from helioseismic magnetic imager vector magnetic field measurements. *Astrophys J.* (2019) 871:L28. doi: 10.3847/2041-8213/aaffcf
9. Guo Y, Xia C, Keppens R, Ding MD, Chen PF. Solar magnetic flux rope eruption simulated by a data-driven magnetohydrodynamic model. *Astrophys J.* (2019) 870:L21. doi: 10.3847/2041-8213/aafabf
10. Pomoell J, Lumme E, Kilpua E. Time-dependent data-driven modeling of active region evolution using energy-optimized photospheric electric fields. *Sol Phys.* (2019) 294:41. doi: 10.1007/s11207-019-1430-x
11. Toriumi S, Takasao S, Cheung MCM, Jiang C, Guo Y, Hayashi K, et al. Comparative study of data-driven solar coronal field models using a flux emergence simulation as a ground-truth data set. *Astrophys J.* (2020) 890:103. doi: 10.3847/1538-4357/ab6b1f
12. Yang WH, Sturrock PA, Antiochos SK. Force-free magnetic fields – The magneto-frictional method. *Astrophys J.* (1986) 309:383. doi: 10.1086/164610
13. Inoue S. Magnetohydrodynamics modeling of coronal magnetic field and solar eruptions based on the photospheric magnetic field. *Prog Earth Planet Sci.* (2016) 3:19. doi: 10.1186/s40645-016-0084-7
14. Nakagawa Y. Evolution of solar magnetic fields - a new approach to mhd initial-boundary value problems by the method of near-characteristics. *Astrophys J.* (1980) 240:275. doi: 10.1086/158232
15. Nakagawa Y, Hu YQ, Wu ST. The method of projected characteristics for the evolution of magnetic arches. *Astron Astrophys.* (1987) 179:354–70.
16. Wu ST, Wang JF. Numerical tests of a modified full implicit continuous eulerian (FICE) Scheme with projected normal characteristic boundary conditions for MHD flows. *Comput Methods Appl Mech Eng.* (1987) 64:267–82. doi: 10.1016/0045-7825(87)90043-0
17. Hayashi K. magnetohydrodynamic simulations of the solar corona and solar wind using a boundary treatment to limit solar wind mass flux. *Astrophys J Suppl.* (2005) 161:480–94. doi: 10.1086/491791
18. Jiang C, Wu ST, Yurchyshyn VB, Wang H, Feng X, Hu Q. How did a major confined flare occur in super solar active region 12192. *Astrophys J.* (2016) 828:62. doi: 10.3847/0004-637X/828/1/62
19. Schuck PW. Tracking vector magnetograms with the magnetic induction equation. *Astrophys J.* (2008) 683:1134. doi: 10.1086/589434
20. Priest ER, Forbes TG. The magnetic nature of solar flares. *Astron Astrophys Rev.* (2002) 10:313–17. doi: 10.1007/s001590100013
21. Vemareddy P, Cheng X, Ravindra B. Sunspot rotation as a driver of major solar eruptions in the NOAA active region 12158. *Astrophys J.* (2016) 829:24. doi: 10.3847/0004-637X/829/1/24
22. Zhao J, Gilchrist SA, Aulanier G, Schmieder B, Pariat E, Li H. Hooked flare ribbons and flux-rope related QSL footprints. *Astrophys J.* (2016) 823:62. doi: 10.3847/0004-637X/823/1/62
23. Zhou GP, Zhang J, Wang JX. Observations of magnetic flux-rope oscillation during the precursor phase of a solar eruption. *Astrophys J.* (2016) 823:L19. doi: 10.3847/2041-8205/823/1/L19
24. Duan A, Jiang C, Hu Q, Zhang H, Gary GA, Wu ST, et al. Comparison of two coronal magnetic field models to reconstruct a sigmoidal solar active region with coronal loops. *Astrophys J.* (2017) 842:119. doi: 10.3847/1538-4357/aa76e1
25. Lee H, Magara T. MHD Simulation for investigating the dynamic state transition responsible for a solar eruption in active region 12158. *Astrophys J.* (2018) 859:132. doi: 10.3847/1538-4357/aabfe6
26. Jiang CW, Feng XS, Zhang J, Zhong DK. AMR Simulations of magnetohydrodynamic problems by the CESE method in curvilinear coordinates. *Sol. Phys.* (2010) 267:463–491. doi: 10.1007/s11207-010-9649-6
27. Wiegelmann T. Optimization code with weighting function for the reconstruction of coronal magnetic fields. *Sol Phys.* (2004) 219:87–108. doi: 10.1023/B:SOLA.0000021799.39465.36
28. Jiang C, Toriumi S. Testing a data-driven active region evolution model with boundary data at different heights from a solar magnetic flux emergence simulation. *Astrophys J.* (2020) 903:11. doi: 10.3847/1538-4357/abb5ac
29. Jiang C, Feng X. Preprocessing the photospheric vector magnetograms for an nlfff extrapolation using a potential-field model and an optimization method. *Sol Phys.* (2014) 289:63–77. doi: 10.1007/s11207-013-0346-0
30. Jiang C, Feng X. Extrapolation of the solar coronal magnetic field from SDO/HMI magnetogram by a CESE-MHD-NLFFF code. *Astrophys J.* (2013) 769:144. doi: 10.1088/0004-637X/769/2/144
31. Schrijver CJ, DeRosa ML, Metcalf T, Barnes G, Lites B, Tarbell T, et al. Nonlinear force-free field modeling of a solar active region around the time of a major flare and coronal mass ejection. *Astrophys J.* (2008) 675:1637–44. doi: 10.1086/527413
32. Sun X, Hoeksema JT, Liu Y, Wiegelmann T, Hayashi K, Chen Q, et al. Evolution of magnetic field and energy in a major eruptive active region based on SDO/HMI observation. *Astrophys J.* (2012) 748:77. doi: 10.1088/0004-637X/748/2/77
33. Toriumi S, Wang H. Flare-productive active regions. *Liv Rev Solar Phys.* (2019) 16:3. doi: 10.1007/s41116-019-0019-7
34. Duan A, Jiang C, He W, Feng X, Zou P, Cui J. A study of pre-flare solar coronal magnetic fields: magnetic flux ropes. *Astrophys J.* (2019) 884:73. doi: 10.3847/1538-4357/ab3e33
35. Liu Y, Zhao J, Schuck PW. Horizontal flows in the photosphere and subphotosphere of two active regions. *Sol Phys.* (2013) 287:279–91. doi: 10.1007/s11207-012-0089-3
36. Liu C, Deng N, Lee J, Wiegelmann T, Jiang C, Dennis B, et al. Three-dimensional magnetic restructuring in two homologous solar flares in the seismically active NOAA AR 11283. *Astrophys J.* (2014) 795:128. doi: 10.1088/0004-637X/795/2/128
37. Wang Y, Nash AG, Sheeley NR Jr. Magnetic flux transport on the sun. *Science.* (1989) 245:712–718. doi: 10.1126/science.245.4919.712
38. Chen F, Rempel M, Fan Y. Emergence of magnetic flux generated in a solar convective dynamo. I. the formation of sunspots and active regions, and the origin of their asymmetries. *Astrophys J.* (2017) 846:149. doi: 10.3847/1538-4357/aa85a0
39. Cheung MCM, Rempel M, Chintzoglou G, Chen F, Testa P, Martnez-Sykora J, et al. A comprehensive three-dimensional radiative magnetohydrodynamic simulation of a solar flare. *Nat Astron.* (2019) 3:160–6. doi: 10.1038/s41550-018-0629-3
40. Toriumi S, Hotta H. Spontaneous generation of -sunspots in convective magnetohydrodynamic simulation of magnetic flux emergence. *Astrophys J.* (2019) 886:L21. doi: 10.3847/2041-8213/ab55e7
41. Kliem B, Tr̈k T. Torus instability. *Phys Rev Lett.* (2006) 96:255002. doi: 10.1103/PhysRevLett.96.255002
42. Aulanier G, Tr̈k T, Démoulin P, DeLuca EE. Formation of torus-unstable flux ropes and electric currents in erupting sigmoids. *Astrophys J.* (2010) 708:314–33. doi: 10.1088/0004-637X/708/1/314
43. Moore RL, Sterling AC, Hudson HS, Lemen JR. Onset of the magnetic explosion in solar flares and coronal mass ejections. *Astrophys J.* (2001) 552:833–48. doi: 10.1086/320559
44. Chen PF. Coronal mass ejections: models and their observational basis. *Liv Rev Solar Phys.* (2011) 8:1. doi: 10.12942/lrsp-2011-1

Conflict of Interest: The authors declare that the research was conducted in the absence of any commercial or financial relationships that could be construed as a potential conflict of interest.

The reviewer YG declared a past co-authorship with one of the authors CJ to the handling editor.

Advantages of publishing in Frontiers

OPEN ACCESS
Articles are free to read
for greatest visibility
and readership

FAST PUBLICATION
Around 90 days
from submission
to decision

HIGH QUALITY PEER-REVIEW
Rigorous, collaborative,
and constructive
peer-review

TRANSPARENT PEER-REVIEW
Editors and reviewers
acknowledged by name
on published articles

Frontiers
Avenue du Tribunal-Fédéral 34
1005 Lausanne | Switzerland

Visit us: www.frontiersin.org
Contact us: frontiersin.org/about/contact

REPRODUCIBILITY OF RESEARCH
Support open data
and methods to enhance
research reproducibility

DIGITAL PUBLISHING
Articles designed
for optimal readership
across devices

FOLLOW US
@frontiersin

IMPACT METRICS
Advanced article metrics
track visibility across
digital media

EXTENSIVE PROMOTION
Marketing
and promotion
of impactful research

LOOP RESEARCH NETWORK
Our network
increases your
article's readership